SYNTHESIS, KINETIC AND COMPUTATIONAL CHEMISTRY OF THIOPHENE-CONTAINING BETA-DIKETONATO COMPLEXES OF RHODIUM(I) AND RHODIUM(III)

A dissertation submitted to meet the requirements for the degree of
Magister Scientiae

in the
Department of Chemistry
Faculty of Science

at the
University of the Free State

by
Marrigje Marianne Conradie

promotor
Dr. J. Conradie

January 2007

I can do all things through Christ who strengthens me.

Philippians 4:13

Acknowledgments

My further gratitude hereby expressed to:

Dr. J. Conradie,

my mother and promoter, thank you for your time and devotion

Mr. J.M.J. Koorts, Miss. W. Bubb and Mr. E.H.G. Langer,

my team of grammar experts

Prof. J.C. Swarts,

for helpful inputs

Prof. R. Carvallo,

for NMR expertise

Dr. A.F. Muller and Prof. A Roodt,

for X-ray data-collections

Dr. I. Kamara,

for organic expertise

friends, family and colleagues,

for support and understanding

the Chemistry Department at the University of the Free State,

for available facilities

the National Research Foundation,

for financial support

Table of contents

Chapter 4

List of abbreviations

Ligands

CO	carbonyl ligand or carbon monoxide
Fc	ferrocene, *bis*(pentahaptocyclopentadienyl)iron, $[(\eta^5\text{-}C_5H_5)_2Fe]$
fc	ferrocenyl ligand
Fc^+	ferrocenium.
Hacac	2,4-pentanedione, acetylacetone
Hba	1-phenyl-1,3-butanedione, benzoylacetone
Hbfcm	1-ferrocenyl-3-phenylpropane-1,3-dione, benzoylferrocenoylmethane
Hbth	1-phenyl-3-(2-thenoyl)-1,3-propanedione
Hcacsm	methyl(2-cyclohexylamino-1-cyclopentene-1-dithiocarboxylate)
Hcupf	N-hydroxy-N-nitroso-benzeneamine, cupferron
Hdbm	1,3-diphenyl-1,3-propanedione, dibenzoylmethane
Hdfcm	1,3-diferrocenylpropane-1,3-dione, diferrocenoylmethane
Hdmavk	dimethylaminovinylketone
Hdtm	1,3-di(2-thenoyl)-1,3-propanedione
Hfca	1-ferrocenylbutane-1,3-dione, ferrocenoylacetone
Hfctfa	1-ferrocenyl-4,4,4-trifluorobutane-1,3-dione, ferrocenoyltrifluoroacetone
Hhacsm	methyl(2-amino-1-cyclopentene-1-dithiocarboxylate)
Hhfaa	1,1,1,5,5,5-hexafluoro-2,4-pentanedione, hexafluoroacetylacetone
Hmacsm	methyl(2-methyl-amino-1-cyclopentene-1-dithiocarboxylate)
Hmnt	maleonitriledithiolate
Hneocup	N-nitroso-N-naphthylhydroxylamine, neocupferron
Hox	8-hydroxyquinoline, oxine
Hsacac	thioacetylacetone
Hstsc	salicylaldehydethiosemicarbazone
Htfaa	1,1,1-trifluoro-2,4-pentanedione, trifluoroacetylacetone
Htfba	1,1,1-trifluoro-4-phenyl-2,4-butanedione, trifluorobenzoylacetone
Htta	thenoyltrifluoroacetone, 4,4,4-trifluoro-1-(2-thenoyl)-1,3-propanedione
L,L'-BID	mono anionic bidentate ligand
L	one of two donor atoms of the bidentate ligand L,L'-BID
L'	the second donor atom of the bidentate ligand L,L'-BID
$P(OPh)_3$	triphenyl phosphite
PPh_3	triphenyl phosphine
PR_3	tertiary phosphine with substituents R
Th	thienyl

Solvents

DMF	dimethylformamide
DMSO	dimethylsulfoxide
THF	tetrahydrofuran

Groups

Et	ethyl
Me	methyl
Ph	phenyl
$LiNPr^i_2$	LDA

Other

A	absorbance
ε	molar extinction coefficient
ν_{CO}	infrared stretching frequency of carbonyl
IR	infrared spectroscopy
NMR	nuclear magnetic resonance
pK_a	$-\log K_a$, K_a = acid dissociation constant
T	temperature
UV	ultraviolet spectroscopy
χ_R	group electronegativity of group R

1 Introduction and aim of study

1.1 Introduction.

The formation and breaking of metal-carbon bonds has become an important and versatile tool in synthetic organic chemistry.[1,2,3] Transition metal assisted reactions used for the manufacture of organic compounds on an industrial scale include the oxidation, hydrogenation, hydroformylation, isomerization and polymerization of alkenes, diene cyclooligomerization and alcohol carbonylation. Other reactions, such as the asymmetric hydrogenation of prochiral alkenes, the activation of C-H bonds for hydrogen/deuterium exchange, the reduction of ketones by hydrosilation and the decarbonylation of aldehydes are also catalysed by complexes of transition metals. These reactions have a wide application in laboratory-scale preparations and some are also used in the manufacture of pharmaceuticals.

The reactions of the types just mentioned, and indeed, a majority of all organic reactions, are controlled by kinetic rather than thermodynamic factors. The addition of transition metal complexes that can become intimately involved in the reaction sequence is an effective way of increasing the reaction rates. The transition metal catalyst lowers the energy of activation for the reaction by changing the mechanism[4] and in some cases it relaxes restrictions imposed by orbital symmetry control.[5,6,7]

---

[1] H. Alper (Ed.), Transition Metal Organometallics in Organic Synthesis, vol. 2, Academic press, New York, 1978.

[2] D.C. Black, W.R. Jackson, J.M. Swan, in: D.N. Jones (Ed.), Comprehensive Organic Chemistry, vol. 3, Pergamon, Oxford, 1979, Parts 15 and 16.

[3] J.P. Collman, L.S. Hegedus, Principles and Applications of Organotransition Metal Chemistry, University Science Books, CA, 1980.

[4] J.K. Kochi, Organometallic Mechanisms and Catalysis, Academic Press, New York, 1978.

[5] J. Halpern, in: I. Wender, P. Pino (Eds.), Organic Synthesis via Metal Carbonyls, Wiley, New York, 1977.

[6] F.D. Mango, Coord. Chem. Rev. 15 (1975) 109.

[7] R.G. Pearson, Symmetry Rules for Chemical Reactions, Wiley, New York, 1976.

During the last 50 years, industrial organic chemistry has been based largely on petroleum products. Most petrochemical processes use heterogeneous rather than homogeneous catalysts. This is principally because heterogeneous catalysts are generally more stable at higher temperatures and are less troublesome to separate from the substrate phase. However, over the past 30 years, there has been a growing interest in homogeneous catalysts because they often show higher selectivity and greater catalytic activity and they also provide greater control of temperature on the catalyst site. For some commercial processes it has been determined that the advantage of soluble catalysts outweigh the economic problems associated with catalyst recovery. Examples include the hydroformylation of alkenes specifically to straight-chain aldehydes which are catalysed by $[HRh(CO)_2(PPh_3)_2]$, and the carbonylation of methanol to acetic acid with $[Rh(CO)_2I_2]^-$ as the active catalyst.[8]

Each catalytic cycle is composed of several steps; the hydroformylation of C_2H_4 by $[HRh(CO)_2(PPh_3)_2]$ to liberate ethyl aldehyde, $C_2H_5C(O)H$, can serve as an example:[9]

$$[HRh(CO)_2(PPh_3)_2] + C_2H_4 \rightleftharpoons [HRh(CO)_2(PPh_3)(C_2H_4)] + PPh_3 \quad 1$$

$$[HRh(CO)_2(PPh_3)(C_2H_4)] \rightleftharpoons [C_2H_5Rh(CO)_2(PPh_3)] \quad 2$$

$$[C_2H_5Rh(CO)_2(PPh_3)] + PPh_3 \rightleftharpoons [C_2H_5Rh(CO)_2(PPh_3)_2] \quad 3$$

$$[C_2H_5Rh(CO)_2(PPh_3)_2] \rightleftharpoons [C_2H_5C(O)Rh(CO)(PPh_3)_2] \quad 4$$

$$[C_2H_5C(O)Rh(CO)(PPh_3)_2] + H_2 \rightleftharpoons [C_2H_5C(O)Rh(CO)(PPh_3)_2(H_2)] \quad 5$$

$$[C_2H_5C(O)Rh(CO)(PPh_3)_2(H_2)] \rightarrow [HRh(CO)(PPh_3)_2] + C_2H_5C(O)H \quad 6$$

$$[HRh(CO)(PPh_3)_2] + CO \rightleftharpoons [HRh(CO)_2(PPh_3)_2] \quad 7$$

The above reactions may be classified as ligand addition to the sixteen electron metal complex (reactions 3 and 7), ligand substitution (reaction 1), insertion within the co-ordination sphere (reactions 2 and 4), oxidative addition (reaction 5) and reductive elimination (reaction 6). During catalysis, reactions such as 1 – 7 often occur so rapidly that they may not be individually observed. Thus, the importance of model complexes to demonstrate and study the individual steps of catalytic reactions is apparent. In South Africa, two world scale hydroformylation plants at Sasolburg and Secunda use rhodium catalysts for the production of alcohols for Sasol.

---

[8] R.S. Dickson, Homogeneous Catalysis with Compounds of Rhodium and Iridium, D. Reidel Publishing Company, Dordrecht, 1985, Chapter 1.

[9] J.D. Atwood, Coord. Chem. Rev. 83 (1988) 93.

Among the most representative examples of an industrial process catalyzed by a metal complex in solution is certainly the rhodium-iodide catalyzed carbonylation of methanol to acetic acid.[10] The original $[Rh(CO)_2I_2]^-$ catalyst, developed at the Monsanto laboratories[11,12] and studied in detail by Forster and co-workers,[13,14,15] is largely used for the industrial production of acetic acid with a selectivity greater than 99%. Acetic acid's global production in 2005 was about 9 million tons and the demand grows yearly with nearly 5%. More than 60% of this is being produced by the Monsanto process.[16] This process is illustrated in **Scheme 1.1**.

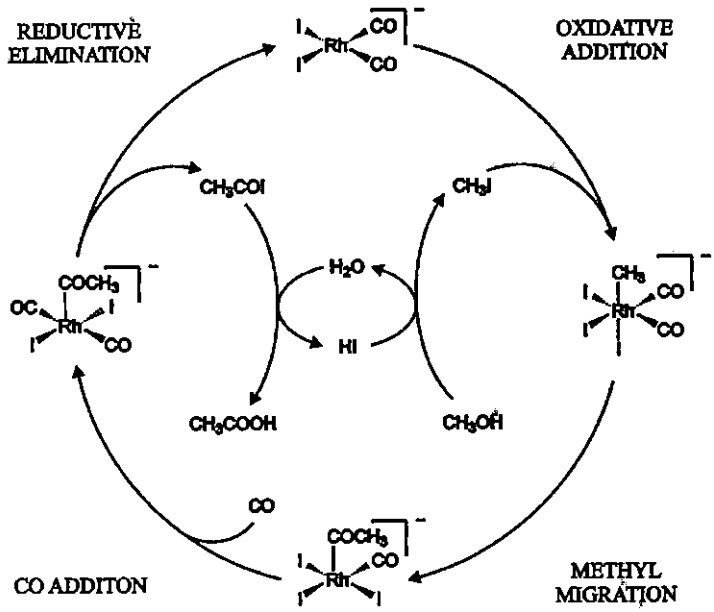

Scheme 1.1: The Monsanto process.

The conditions used industrially (30-60 atm and 150-200 °C)[17], however, have spurred the search for new catalysts, which could work in milder conditions.[18,19,20] The rate determining step of the

---

[10] P.M. Maitlis, A. Haynes, G.J. Sunley, M.J. Howard, J. Chem. Soc., Dalton Trans. (1996) 2187.

[11] K.K. Robinson, A. Hershman, J.H. Craddock, J.F. Roth, J. Mol. Catal. 27 (1972) 389.

[12] F.E. Paulik, J.F.J. Roth, Chem. Soc., Chem. Commun. (1968) 1578.

[13] D.J. Forster, J. Am. Chem. Soc. 98 (1976) 846.

[14] D. Forster, Adv. Organomet. Chem. 17 (1979) 255.

[15] D. Forster, T.C.J. Singleton, Mol. Catal. 17 (1982) 299.

[16] Annual report, Indian Petrochemicals Corporation Ltd, Baroda, 2005, p. 68.

[17] J.F. Roth, J.H. Craddock, A. Hershman, F.E. Paulik, Chem. Technol. (1971) 600.

[18] J.R. Dilworth, J.R. Miller, N. Wheatley, M.J. Baker, J.G. Sunley, J. Chem. Soc., Chem. Commun. (1995) 1579.

[19] T. Ghaffar, H. Adams, P.M. Maitlis, A. Haynes, G.J. Sunley, M. Baker, Chem. Commun. (1998) 1023.

catalytic cycle is the oxidative addition of MeI (**Scheme 1.1**), so catalyst design should focus on the improvement of this reaction. The basic idea is that ligands which increase the electron density at the metal should promote oxidative addition, and by consequence the overall rate of production. To this purpose, in the last years several other Rh compounds have been synthesized and have been demonstrated to be active catalysts of comparable or better performances compared to the original Monsanto catalyst.[18,21,22,23] One of the most important classes is based on Rh complexes containing simple phosphines,[24] biphoshine ligands[25] and more recently also mixed bidentate ligands.[20,22,23] Indeed, all these new ligands enhance oxidative addition but as a consequence they usually retard the subsequent CO migratory insertion because the increased electron density at the metal also leads to a stronger Rh-CO bond.

Due to the cost of rhodium (R3000 per gram), and the fact that rhodium catalysts can only be used in reactors made from hastaloy (much more expensive than stainless steel), the development of rhodium catalysts with a higher activity will be profitable – lower concentration rhodium catalyst and smaller reactor. In the catalyst design, it is also of economic importance that loss of rhodium due to decomposition must be minimized.

Effective catalyst design should focus on the acceleration off all steps in the catalytic cycle and stability over the long term. It is therefore necessary to study each step of a catalytic cycle in detail and to test the stability of the rhodium catalyst.

---

[20] R.W. Wegman, Chem. Abstr. 105 (1986) 78526g.

[21] J. Rankin, A.D. Poole, A.C. Benyei, D. Cole-Hamilton, Chem. Commun. (1997) 1835.

[22] K.V. Katti, B.D. Santarsiero, A.A. Pinkerton, R.G. Cavell, Inorg. Chem. 32 (1993) 5919.

[23] M.J. Baker, M.F. Giles, A.G. Orpen, M.J. Taylor, R.J. Watt, J. Chem. Soc., Chem. Commun. (1995) 197.

[24] J. Rankin, A.C. Benyei, A.D. Poole, D.J. Cole-Hamilton, J. Chem. Soc., Dalton Trans. (1999) 3771.

[25] K.G. Moloy, R.W. Wegman, Organometallics 8 (1989) 2883.

1.2 Aims of this study.

With this background the following goals were set for this study:

(i) The optimized synthesis of new and known thienyl (Th) containing β-diketones, $ThCOCH_2COR$ with R = Ph, Th.

(ii) The acid dissociation constant (pK_a) determinations of the thienyl (Th) containing β-diketones, $ThCOCH_2COR$ with R = Ph, Th, CF_3.

(iii) The optimized synthesis of new and known [Rh^I(β-diketonato)$(CO)_2$] complexes, where the β-diketonato ligand is of the form in (i) with R = Ph, Th, CF_3.

(iv) The optimized synthesis of new and known [Rh^I(β-diketonato)$(CO)(PPh_3)$] complexes, where the β-diketonato ligand is of the form in (i) with R = Ph, Th, CF_3.

(v) To characterize the synthesized β-diketones and rhodium complexes with a variety of methods such as NMR techniques, IR spectrophotometry, melting points, etc.

(vi) The use of X-ray crystallography to determine the molecular structure of representative examples of the synthesized β-diketones and rhodium complexes.

(vii) The determination of a general mechanism for the oxidative addition of MeI to [Rh(ThCOCHCOR)$(CO)(PPh_3)$] complexes (R = Ph, Th, CF_3) by means of detailed kinetic studies utilizing NMR techniques, IR and UV/vis spectrophotometry.

(viii) Using computational chemistry by means of density functional theory (DFT) to obtain an insight into the possible reaction products during oxidative addition of MeI to [Rh(ThCOCHCOR)$(CO)(PPh_3)$] complexes (R = Ph, Th, CF_3).

2 Survey of literature and fundamental aspects

2.1 Introduction.

This study is concerned with the rhodium(I) and rhodium(III) complexes of a β-diketone containing a thienyl group. This chapter provides a background of literature on the synthesis, properties, kinetics and computational studies of such β-diketones and their rhodium complexes.

2.2 β-diketone chemistry.

During the past decades there has been growing interest in the metal (and organometal) derivatives of β-diketones and the number of novel ligands employed for the purpose, as well as new compounds of previously known ligands, have multiplied dramatically.[1,2] It may be worthwhile at this stage to describe briefly the chemistry of β-diketone ligands themselves before going into a detailed account of their metal derivatives.

2.2.1 Synthesis.

A wide variety of β-diketones can be synthesized by the well known Claisen condensation reaction.[3] In this reaction a ketone containing an α-hydrogen atom undergoes acylation with an appropriate acylation reagent (acid anhydride, an acid chloride or an ester) in the presence of a base as illustrated in **Scheme 2.1**.

---

[1] R.C. Mehrotra, R. Bohra, D.P. Gaur, Metal β-diketonates and Allied Derivatives, Academic Press, London, 1978.

[2] C. Pettinari, F. Marchetti, A. Drozdov, Comprehensive Coordination Chemistry II, vol. 1, Elsevier Pergamon, Oxford, 2003, Chapter 1.6.

[3] C.R. Hauser, F.W. Swamer, J.T. Adams, Organic Reactions, vol. VIII, John Wiley & Sons, New York, 1954, Chapter 3.

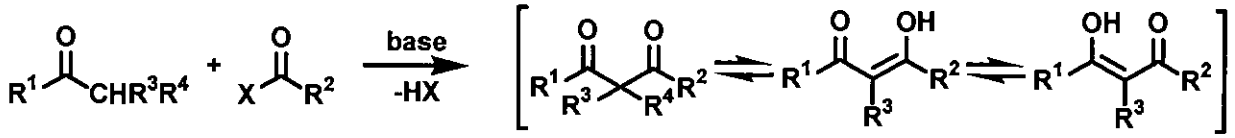

Scheme 2.1: Synthesis of β-diketones. For the enol forms there must be at least one α hydrogen (R^4 = H) present.

The acylation and acidification occurs in a four step[3] mechanism as illustrated in **Scheme 2.2.** For this illustration the base lithium diisopropylamide (LDA), the ketone R^1COCH_3 and the ester R^2COOEt are used. In the first step the α-hydrogen of the ketone is removed by the base to form a ketone anion, which is a hybrid of the resonance structures $R^1CO\bar{C}H_2$ and $R^1C(\bar{O})=CH_2$. The second step may be formulated as the addition of the ketone anion to the carbonyl carbon of the ester, accompanied by the release of ethoxide ion to form the β-diketone. The third step consists of the removal of an α hydrogen of the β-diketone as a proton to form a β-diketone anion, which is a resonance hybrid of structures $R^1CO\bar{C}HCOR^2$, $R^1C(\bar{O})=CHCOR^2$ and $R^1COCH=C(\bar{O})R^2$. The first three steps of the mechanism are reversible. In practice, the equilibrium of the over-all reaction is shifted in the direction of the condensation product by precipitation of the β-diketone as its lithium salt. The fourth step is the acidification of the β-diketonato anion to form the β-diketone.

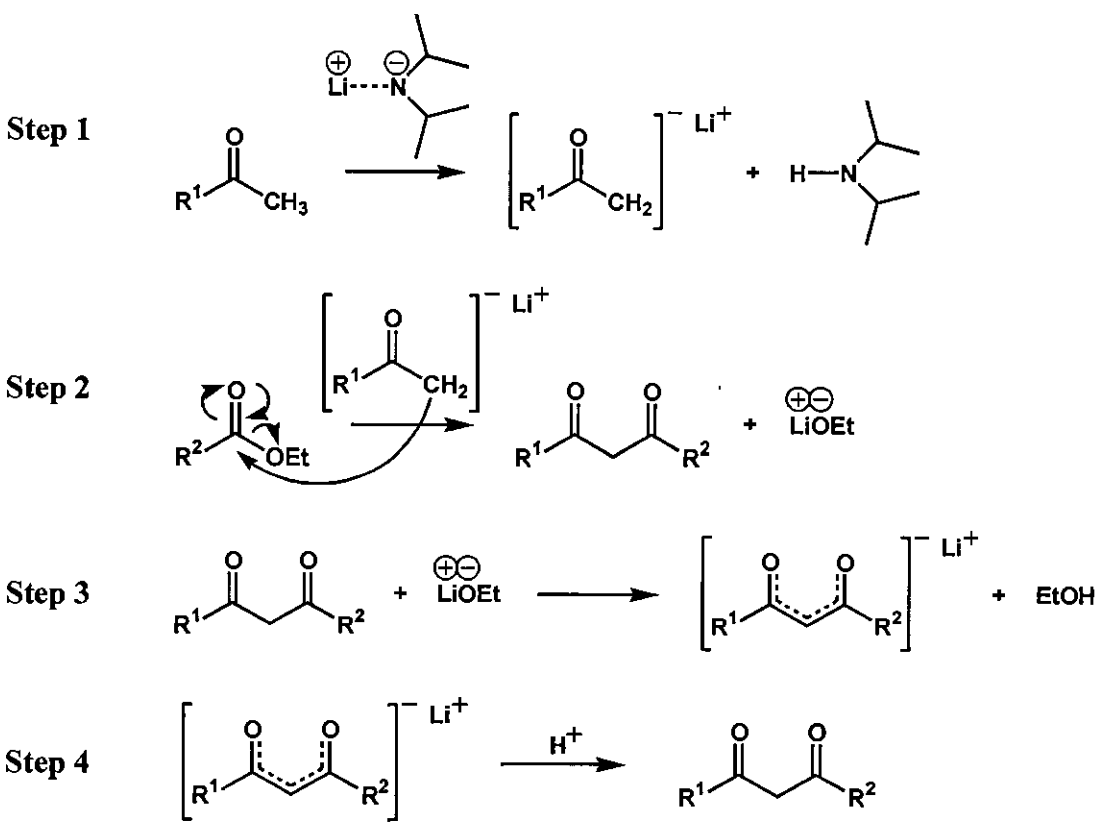

Scheme 2.2: Mechanism for the formation of a β-diketone.

For the synthesis of a β-diketone such as in **Scheme 2.3 path A**, one would ordinarily use the direct acylation as described above. The basic reagent can be replaced with BF_3 to form mainly the methylene derivative (**Scheme 2.3 path B**) rather than the methyl derivative (**Scheme 2.3 path A**).[3]

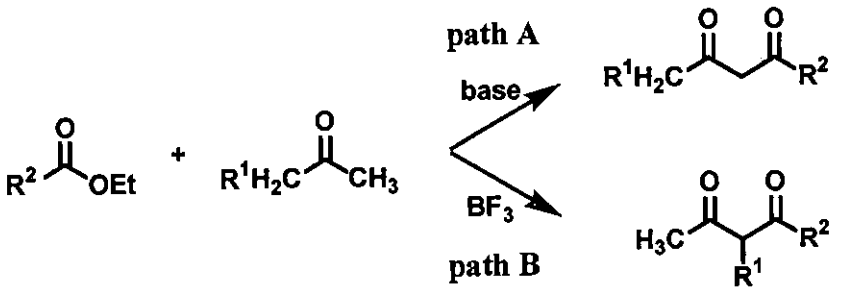

Scheme 2.3: Acylation synthesis of a β-diketone.

Another direct way to synthesize a β-diketone would be to effect a carbon-carbon condensation at position 1 or position 2 as indicated in **Figure 2.1**. Syntheses of this type have been accomplished by reaction of a Grignard reagent with either a β-keto acid chloride[4] or a β-keto nitrile[5,6] (followed by hydrolysis), and by the Friedel-Crafts reaction of benzene with either acetoacetyl chloride or diketene.[7] However, none of these methods appears to have been as satisfactory as the acylation of ketones (described above).[3]

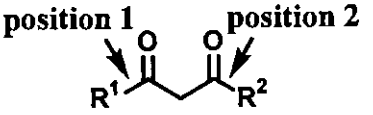

Figure 2.1: Carbon-carbon synthesis of a β-diketone.

[4] Hurd, Kelso, J. Am. Chem. Soc. 62 (1940) 2184.

[5] Renberg, Henze, J. Am. Chem. Soc. 62 (1941) 2785.

[6] Mavrodin, Bull. Soc. Chim. Romania 15 (1933) 99.

[7] Hurd, Kelso, J. Am. Chem. Soc. 62 (1940) 1548.

2.2.2 Tautomerism of β-diketones.

Although β-diketones are commonly represented in the ketonic form, most β-diketones exist in solution in an equilibrium involving keto- and enol forms provided that there is at least one methine hydrogen (R^4 = H, **Scheme 2.1**) present.

The hydrogen atom of the CHR^3 group (**Scheme 2.4**) is activated by the adjacent C=O groups and a conjugated system can arise by a phototropic shift. The enol isomer can exist as two tautomers that are stabilized by a hydrogen bridge as illustrated in **Scheme 2.4.** These tautomers exist in equilibrium with each other and structurally posses a *cis* configuration and a *syn* conformation. In the solid state the enol form is often the sole form observed.

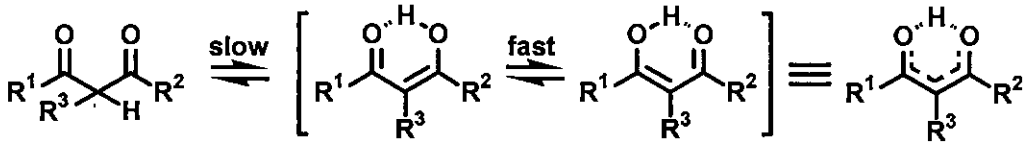

Scheme 2.4: Tautomerism of β-diketone.

The methine proton in the keto form and the hydroxyl proton in the enol form of the β-diketones are acidic and their removal generates 1,3-diketonate anions, which are the source of an extremely broad class of coordination compounds.

2.2.2.1 Enol-enol tautomerism.

The kinetics of conversion from one enol form to the other is very fast, with a rate constant approaching 10^6 s^{-1}.[8] Since the rate of proton transfer between the two enolic forms goes beyond the time-scale of the NMR, the peaks of NMR spectra of the two enolic forms are a weighted average of the two enolic forms. G. Sky *et al.*[9] developed a method for determining the relative concentrations of the two enol tautomers of an asymmetric β-diketone using ^{17}O NMR spectroscopy. Kwon and Moon[10] calculated the enol-enol equilibrium constant from theoretically determined ^{17}O shifts of frozen enols using Hartree-Fock and density functional

[8] G.F.G.C. Geraldes, M.T. Barros, C.D. Maycock, M.I. Silva, J. Mol. Struct. 238 (1990) 335.

[9] M. Gorodetsky, Z. Luz,Y. Mazur, J. Am. Chem. Soc. 89 (1967) 1183.

[10] S. Moon, Y. Kwon, Magn. Reson. Chem. 39 (2001) 89.

B3LYP levels of theory. It was concluded that the equilibrium constant is highly dependent on the character and position of the R groups.

2.2.2.2 Keto-enol tautomerism.

The keto-enol tautomerism of a wide variety of β-diketones has been studied over many years by techniques such as bromine titration,[11] exchange with deuterium,[12] polarographic measurements,[13] energy of enolization,[14] UV and [15] IR spectrophotometry[16] and NMR spectroscopy.[17] It has been generally accepted that the enolic form is favoured in non-polar solvents[18] and simultaneous conjugation and chelation through hydrogen bonding are responsible for the stability of the enol tautomer. The enol content generally decreases as the temperature increases, due to the disruption of hydrogen bonds (see **Scheme 2.5**).[19]

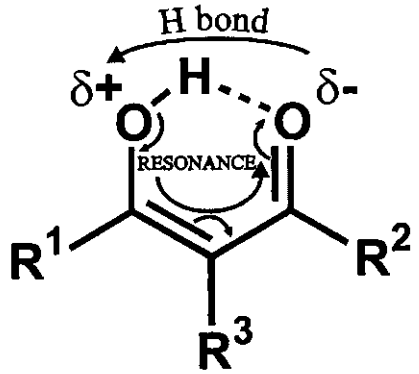

Scheme 2.5: Synergistic interplay of resonance and hydrogen bond (HB) formation, called resonance-assisted hydrogen bonding (RAHB), stabilizing the enol form of β-diketones.

---

[11] K.H. Meyer, Ann. Physik 380 (1911) 212.

[12] L.E. Marchi, Inorg. Synth. 2 (1946) 10.

[13] G. Semerano, A. Chisini, Gazz. Chim. Ital. 66 (1936) 504.

[14] J.B. Constant, A.F. Thompson Jr., J. Am. Chem. Soc. 54 (1932) 4039.

[15] R.J. Irving, M.A.V. Ribeiro da Silva, J. Chem. Soc. Dalton (1975) 798.

[16] J. Powling, H. Bernstein, J. Am. Chem. Soc. 73 (1951) 4353.

[17] L.W. Reeves, Canad. J. Chem. 35 (1957) 1351.

[18] B. Floris, J. Toullec, in: Z. Rappoport (Ed.), The Chemistry of Enols, John Wiley & Sons, Chichester, 1990, pp. 270, 361.

[19] G. Gilli, V. Bertolasi, in: Z. Rappoport (Ed.), The Chemistry of Enols, John Wiley & Sons, Chichester, 1990, pp. 714, 724.

A rescent ^{1}H NMR study by Du Plessis *et al.*[20] showed that the percentages of enolized tautomers in deutorated chloroform solutions of some β-diketones were found to be very high (>85%). These findings along with the pK_a' (observed pK_a) values are tabulated in **Table 2.1**.

Table 2.1: pK_a' values and % enol tautomers of various β-diketones of the type $R^1COCH_2COR^2$.

β-diketones		R^1	R^2	pK_a' [a]	% Enol [b]
Acetylacetone	Hacac	CH_3	CH_3	8.95[21]	91[20,22]
Trifluoroacetylacetone	Htfaa	CH_3	CF_3	6.3[21]	>99[20]
Benzoylacetone	Hba	CH_3	Ph [c]	8.7[21]	92[20]
Dibenzoylmethane	Hdbm	Ph	Ph	9.35[21]	>99[20]
Hexafluoroacetylacetone	Hhfaa	CF_3	CF_3	4.7[23]	
Dipivaloylmethane	Hhmaa	$C(CH_3)_3$	$C(CH_3)_3$	11.77[21]	
Ferrocenoylacetone	Hfca	Fc [d]	CH_3	10.01[20]	86[20,24]
Ferrocenoyltrifluoroacetone	Hfctfa	Fc	CF_3	6.53[20]	>99[20]
Benzoylferrocenoylmethane	Hbfcm	Fc	Ph	10.41[20]	≈95[20]
Diferrocenoylmethane	Hdfcm	Fc	Fc	13.1[20]	>99[20]
Thenoyltrifluoroacetone	Htta	Th [e]	CF_3	6.23[21]	
Trifluorobenzoylacetone	Htfba	CF_3	Ph	6.3[21]	>99[20]
Ferrocenoyltrichloroacetone	Hfctca	Fc	CCl_3	7.15[20]	≈95[20]

a At 21 °C, pK_a' refers to the pK_a of the conjugated keto-enol system
b In $CDCl_3$ at 25 °C
c Ph = phenyl = C_6H_5
d Fc = ferrocenyl = $C_5H_5FeC_5H_4$
e Th = thienyl = C_4H_3S

The proportion of the enol tautomers generally increases when an electron withdrawing group, for example fluorine, is substituted for hydrogen at an α-position relative to a carbonyl group in β-diketones, or when the ligands contain an aromatic ring.[25] Substitution by a bulky group (R^3), such as an alkyl, at the α-position tends to produce steric hindrance between the R^3 and R^1 or between the R^3 and R^2 groups (**Scheme 2.4**). This, together with inductive effects of the alkyl group, often brings about a large decrease in the enol proportion.[26] However, when looking for instance at β-diketones with a ferrocenyl group, enolization in solution was found to be

---

[20] W.C. Du Plessis, T.G. Vosloo, J.C. Swarts, J. Chem. Soc. Dalton Trans. (1998) 2507.

[21] J. Starý, The Solvent Extraction of Metal Chelates, MacMillan Company, New York, 1964, Appendix.

[22] J.L. Burdett, M.T. Rodgers, J. Am. Chem. Soc. 86 (1964) 2105.

[23] M. Ellinger, H. Duschner, K. Starke, J. Inorg. Nucl. Chem. 40 (1978) 1063.

[24] W. Bell, J. A Crayston, C. Glidewell, M.A. Mazid, M.B. Hursthouse, J. Organomet. Chem. 434 (1992) 115.

[25] J.D. Park, H.A. Brown, J.R. Lachen, J. Am. Chem. Soc. 75 (1953) 4753.

[26] G. Klose, P. Thomas, E. Uhlemann, J. Marki, Tetrahedron 22 (1966) 2695.

predominantly away from the aromatic ferrocenyl group. Two different driving forces that control the conversion of β-diketones to an enolic isomer were postulated by Du Plessis *et al.*[20] These forces were labelled as electronic- and resonance driving forces. In the former, the formation of the preferred enol isomer is controlled by the electronegativity of the R^1 and R^2 substituents on the β-diketone:

$$\underset{\textbf{(enol I)}}{R^1-C(OH)=CH-CO-R^2} \rightleftharpoons \underset{\textbf{(keto)}}{R^1-CO-CH_2-CO-R^2} \rightleftharpoons \underset{\textbf{(enol II)}}{R^1-CO-CH=C(OH)-R^2}$$

When the electronegativity of R^1 is greater than that of R^2, the carbon atom of the carbonyl group adjacent to R^2 on the β-diketone, **keto**, will be less positive in character than the carbon atom of the other carbonyl, implying that **enol II** will dominate. However, many β-diketones were described that did not follow the enolisation pattern predicted by the electronic driving force.[20,27,28] All the cited exceptions had aromatic R^1 or R^2 side groups and hence it was stated that the electronic driving force will always take second priority compared with the resonance driving force.

The resonance driving force implies that the formation of different canonical forms of a specific isomer will lower the energy of this specific isomer sufficiently to allow it to dominate over the existence of other isomers that may be favoured by electronic effects (**Scheme 2.6**).

---

[27] W.C. Du Plessis, W.L. Davis, S.J. Cronje, J.C. Swart, Inorg. Chim. Acta. 314 (2001) 97.

[28] W. Bell, C. Glidewell, J.A. Crayson, M.A. Mazid, M.B. Hursthouse, J. Organomet. Chem. 434 (1992) 115.

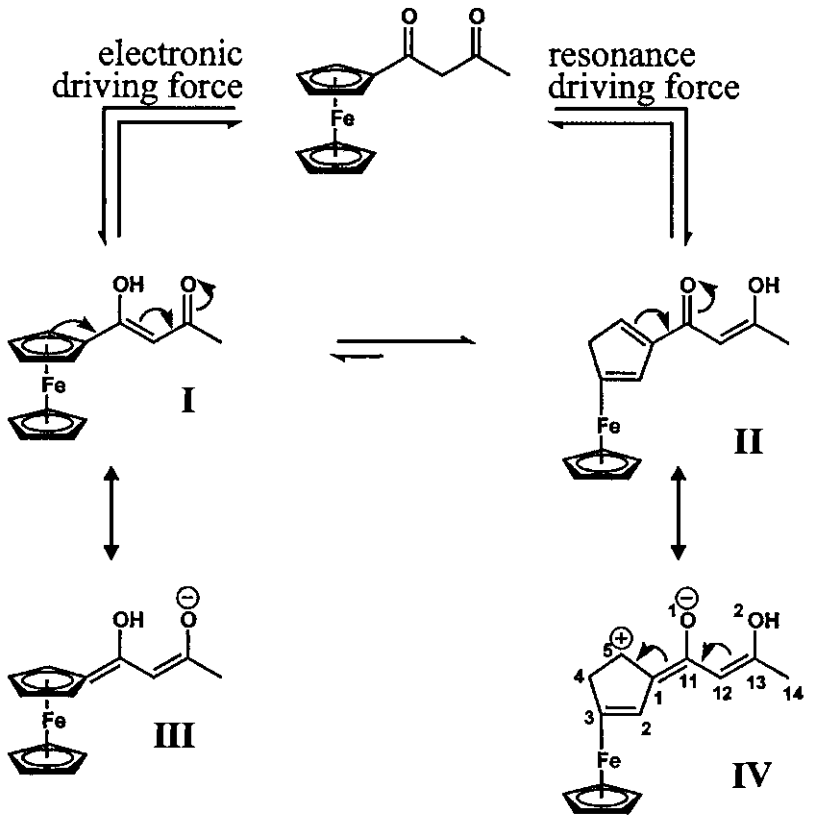

Scheme 2.6: Electronic considerations in terms of electronegativity, χ (χ_{methyl} = 2.34, $\chi_{ferrocenyl}$ = 1.87), favour **I** as the enol form of Hfca. However, structure **II** was shown by crystallography and NMR spectroscopy to be dominant, implying that the equilibrium between **I** and **II** lies far to the right. A dihedral angle of 4.9(2)° between the aromatic ferrocenyl group and the pseudo-aromatic β-diketone core implies that the energy lowering canonical forms such as **IV** make a noticeable contribution to the overall existence of Hfca. For clarity, the ferrocenyl group in **II** and **IV** is shown just in canonical forms, but in both cases the iron atom can be bound in any of the five cyclopentadienyl carbon atoms as indicated in **I**. Likewise, the positive charge of **IV** is not confined to the single position shown, but rather oscillates between C(2) and C(5) (it cannot be on C(1) – atom numbers are indicated to individual atoms) to give rise to four different canonical forms.

Indirect evidence for the existence of these canonical forms found in crystal structures determinations of the enol forms of Hfctfa[29] and Hfca,[28] where the enolization was away from the aromatic ferrocenyl group. The two cited examples cover the cases where the group electronegativity, χ_R, of R^1 and R^2 are fairly similar (χ_{Me} = 2.34; χ_{Fe} = 1.87 in Hfca) or very much different (χ_{CF3} = 3.01; χ_{Fe} = 1.87 in Hfctfa).[28] This resonance driving force is valid when both R^1 and R^2 groups are aromatic groups or if one or neither R^1 nor R^2 is aromatic, provided resonance stabilization via different canonical forms is still possible.

In addition, it was noted that under certain conditions the keto isomer of Hfca could be observed in large quantities by proton NMR, while under other conditions the keto isomer of the same

---

[29] W.C. Du Plessis, J.J.C. Erasmus, G.J. Lambrecht, J. Conradie, T.S. Cameron, M.A.S. Aquino, J.C. Swarts, Can. J. Chem. 77 (1999) 378.

compound is much less pronounced. The explanation for these apparent differences was postulated to be the β-diketone concentration of the solution studied, because at very low concentration hydrogen bonding stabilization of the enol form should be absent. Although it has been shown that very low concentrations slightly favour the keto form in solution, this did not adequately explain why in some cases the keto form is observed in appreciable quantities in concentrated solutions (>80%), while in other cases not (<5%).[27] In a follow-up kinetic investigation it was found that the rate of conversion from keto to enol isomers for simple ferrocene-containing β-diketones is very slow ($t_{1/2}$ = 4.4 hours for Hfca).[27] Many β-diketones are isolated by isolating the solid Li salt, $R^1COCHLi^+COR^2$ from solution, followed by acidification. This means that the first product that is obtained during a synthetic procedure, must be the keto isomer, because the lithium salt exists as a keto isomer. If the ^{1}H NMR is obtained very quickly after isolation and acidification (in other words, within minutes), it follows that the keto content will be high. However, if the ^{1}H NMR is obtained several days after synthesis, time would have elapsed to allow conversion of the keto form to the equilibrium content. Consequently the keto form will be much less dominant. It is interesting to observe that for old samples in the solid state, the enol form is the only stable isomer (in other words, almost no keto form) for the ferrocene-containing β-diketones studied in reference **27**, while in solution, the equilibrium positions allow keto isomers in percentages up to 32%.

2.2.2.3 Keto-enol equilibrium constants and kinetics.

From a kinetic point of view, the equilibrium constant, K_c, for the equilibrium shown in **Scheme 2.7**, can be expressed as the quotient of the rate of conversion of keto to enol isomers and the rate of conversion of enol to keto isomers.

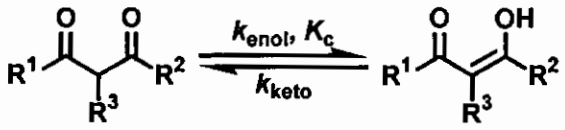

Scheme 2.7: Keto-enol tautomerism.

The keto-enol conversion of most β-diketones, which is solvent-sensitive, is generally a fast process. β-diketones that show this rapid tautomerism are illustrated in **Figure 2.2**.[30]

[30] E. Iglesias, J. Org. Chem. 68 (2003) 2680.

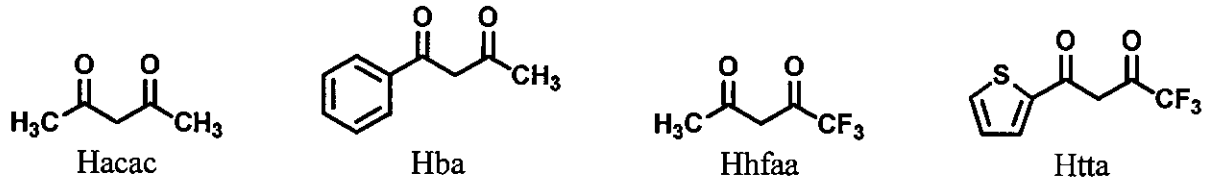

Figure 2.2: β-diketones with rapid keto-enol tautomerism.

By contrast, the keto-enol conversions of 2-acetylcyclohexanone (Hache)[30] and certain ferrocene-containing β-diketones,[27] are slow enough to be followed by conventional methods. These β-diketones that show slow tautomerism are illustrated in **Figure 2.3**.

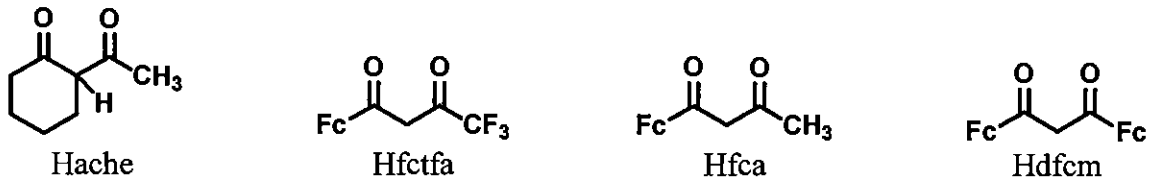

Figure 2.3: β-diketones with slow keto-enol tautomerism.

The enol-keto tautomerism of Hache was studied in water by monitoring the decrease of absorbance at λ = 291 nm due to the enol formation after addition of 10 μL of a 0.018 M solution of Hache in dioxane to a water sample (dilution factor higher than 250). Alternatively, Hache can be dissolved in an alkaline medium to yield the enolate quantitatively, which, after acidification, gives the enol form with a 100% yield. The enol then slowly tautomerizes to the keto form until equilibrium proportions are achieved. This reaction was followed by UV/vis spectrophotometry and the data collected are graphically represented in **Figure 2.4**.

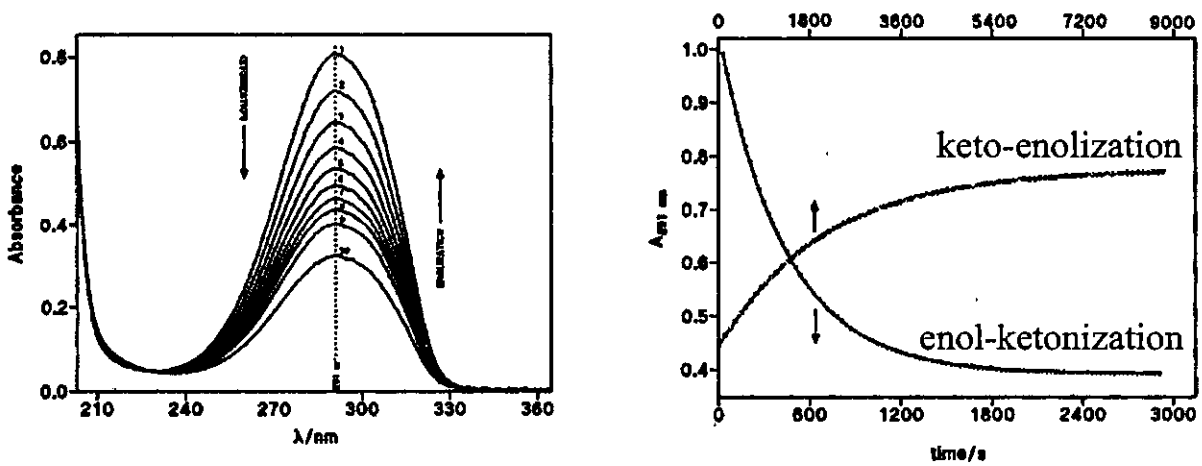

Figure 2.4: On the **left** are repetitive scans showing the decrease in absorbance due to ketonization of Hache-enol, [Hache] = 6.0 x 10^{-5} M, [H^+] = 0.050 M, T = 25 °C. Illustrated on the **right** is the variation of the absorbance at 291 nm as a function of time for enol-ketonization in water, [Hache] = 6.5 x 10^{-5} M, [H^+] = 0.015 M, 25 °C; and for keto-enolonization in 70% water v/v dioxane/water, [Hache] = 6.0 x 10^{-5} M, [H^+] = 0.013 M, 25 °C. (Figure is adopted from reference 30.)

Du Plessis *et al.*[27] have studied the keto-enol kinetics of ferrocene-containing β-diketones with the aid of ^{1}H NMR spectroscopy. To monitor the keto to enol conversion, freshly synthesized samples of Hfctfa, Hfca and Hdfcm were dissolved in $CDCl_3$ and were recorded at specific time intervals on the NMR. Aged samples in the solid state were found to be mainly in the enol form. Upon dissolving aged samples of Hfctfa, Hfca and Hdfcm in $CDCl_3$, the slow formation of keto isomers could be monitored, until the solution equilibrium position was reached.

The keto-enol equilibrium constant $K_c = k_{enol} / k_{keto}$, along with the rate constants k_{enol} and k_{keto}, for selected β-diketones are tabulated in **Table 2.2.**

Table 2.2: The keto-enol equilibrium constant (K_c) and rate constants (k_{enol} and k_{keto}) for selected β-diketones.

β-diketone	K_c	k_{enol} / s^{-1}	k_{keto} / s^{-1}	Solvent	Temperature / °C
Hache[30 a]	0.72	0.68×10^{-3}	1.0×10^{-3}	water	25
Hfctfa[27]	30	64×10^{-6}	2×10^{-6}	$CDCl_3$	20
Hfca[27]	3.4	44×10^{-6}	13×10^{-6}	$CDCl_3$	20
Hdfcm[27]	2.0	20×10^{-6}	10×10^{-6}	$CDCl_3$	20
Htta[31]	0.016	0.101	0.6	water	25
Htta[31]	-	-	17	benzene	25

a $[H^+]$ = 0.05 M and 0.08 M ionic strength (NaCl)

2.2.3 Acid dissociation constant (K_a).

2.2.3.1 Introduction.

According to the Brønsted theory[32] an acid (HA) is defined as a proton donor and a basis (B) as a proton acceptor. After the acid has donated a proton (H^+) it is called the conjugated base ($A:^-$) which still has the electron pair (**Scheme 2.8**). The acid dissociation constant, K_a can be determined according to **Equation 2.1**. Since K_a differs for each acid over many degrees of magnitude, the pK_a value, the additive inverse of K_a's common logarithm (pK_a, = -log K_a), is commonly used. The pK_a for an acid is expressed in **Equation 2.2.**

---

31 J.C. Reid, M. Calvin, J. Am. Chem. Soc. 72 (1950) 2948.

32 A. Albert, E.P. Serjeant, The Determination of Ionization Constants, Chapman and Hall, London, Third edition, 1984, p. 4.

Scheme 2.8: $HA \overset{K_a}{\rightleftharpoons} H^+ + A:^-$

Equation 2.1: $$K_a = \frac{[H^+][A:^-]}{[HA]}$$

Equation 2.2: $$pK_a = -\log K_a = pH + \log \frac{[HA]}{[A:^-]}$$

with K_a = dissociation constant.

The pK_a for a base, according to the reaction in **Scheme 2.9**, is given by **Equation 2.3**.

Scheme 2.9: $B + H^+ \overset{1/K_a}{\rightleftharpoons} BH^+$

Equation 2.3: $$pK_a = pH + \log \frac{[BH^+]}{[B]}$$

A bigger pK_a value implies a weaker acid and thus a stronger base. A table of acid strengths of increasing basicity can be set up and used to determine whether an acid or a base will react with one another.[33] Due to the practical pH-measurement restrictions, pK_a values $1 < pK_a < 13$, are more accurate. Though, the pK_a-values for different compounds can vary between -12 and 51 as illustrated by some examples in **Table 2.3**. Apparent pK_a values of selected β-diketones are included in **Table 2.1**.

Table 2.3: The pK_a-values for different compounds.

Compound (acid)	pK_a
$RCNH^+$[34]	-10
$HCOCH_2CHO$[35]	5
$ROOCCH_2R$[35]	24.5
RCH_2CN[35]	25
C_6H_6[36]	43

[33] J. March, Advanced Organic Chemistry, Reactions, Mechanisms and Structure, John Wiley & Sons, New York, Fourth edition, 1992, p. 248.

[34] N.C. Deno, R.W. Ganger, M.J. Wisotsky, J. Org. Chem. 31 (1966) 1967.

[35] R.G. Pearson, R.L. Dillon, J. Am. Chem. Soc. 75 (1953) 2439.

[36] A. Streitwieser, P.J. Scannon, H.M. Niemeyer, J. Am. Chem. Soc. 94 (1972) 7936.

The term "apparent" is used for the pK_a values of β-diketones, since the experimentally obtained pK_a' value was not partitioned between separate pK_a values for the enol and the keto tautomers, see **Scheme 2.10**.

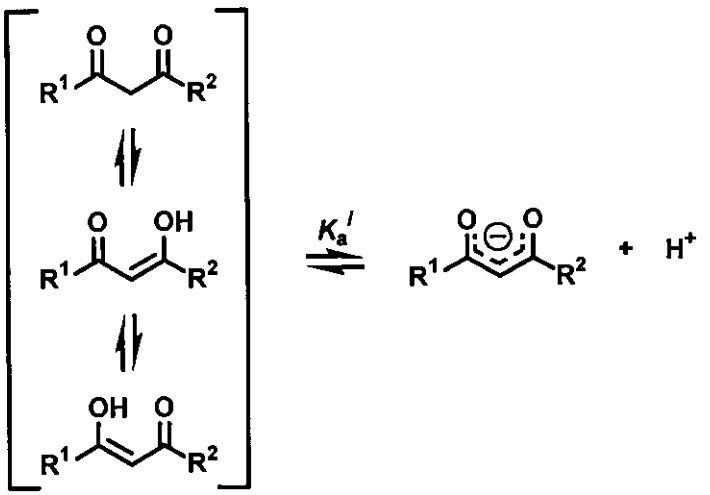

Scheme 2.10: K'_a value of β-diketones.

2.2.3.2 Methods of determining pK_a.

There are different ways to determine the pK_a of a compound. The most important methods include conductometry[37], potentiometry and spectroscopy.[38] Examples of spectroscopic methods are UV/vis[38], vibrational[39,40] and ^{1}H NMR spectroscopy.[39]

The UV/vis spectrophotometry method is useful if the acid or the base does not dissolve sufficiently at higher concentrations and the potentiometry method fails. This method can only be used when the protonation reaction has an effect on the chromophoric group in the compound.[38] In this method the proportion of the molecular species against the ionized species in a range of non-absorbent buffer solutions are directly determined as a function of the pH. The wavelength of the measurement (analytical wavelength) is chosen where the absorbance of the

---

[37] K.D. Purnendu, N. Osamu, Anal. Chem. 62 (1990) 1117.

[38] R.F. Cookson, Chem. Rev. 75 (1974) 5.

[39] G.A. Olah, A.M. White, Chem. Rev. 70 (1970) 561.

[40] S. Hoshino, H. Hosoya, S. Nagakura, Can. J. Chem. 44 (1966) 1961.

molecular species and the absorbance of the ionized species differ the most.[41] **Equation 2.4** is used to determine the pK_a spectrophotometrically.

Equation 2.4: $$pK_a = pH + \log\frac{A_{HA} - A}{A - A_{A^-}}$$

with A_{HA} = absorption of the molecular species, A_{A^-} = absorption of the ionized species and A = absorption of the solution at a specific pH, applicable to **Scheme 2.8**.

2.2.4 Crystallography of β-diketones.

The crystal structures of β-diketones can be divided into three classes:

a. enol with an asymmetric H-bond
b. enol with a symmetric H-bond
c. keto

A search on the Cambridge database[42] for β-diketones, resulted in more than 120 hits. A few representative examples of each class will be chosen to discuss the general geometrical features of β-diketones. Since the crystal structures of the β-diketone 1-phenyl-3-(2-thenoyl)-1,3-propanedione (Hbth) will be reported in this study, the majority of the β-diketones discussed will contain either a phenyl or a thienyl group.

Crystal data for selected β-diketones are summarized in **Table 2.4**. The typical bond lengths for selected bonds in the β-diketones are tabulated in **Table 2.5**. **Figure 2.5 (a-c)** gives the structures of the tabulated β-diketones.

---

[41] A. Albert, E.P. Serjeant, The Determination of Ionization Constants, Chapman and Hall, London, Third edition, 1984, pp. 71-73.

[42] The Cambridge Crystallographic Data Centre (CCDC), ConQuest Version 1.8, Copyright © 2005.

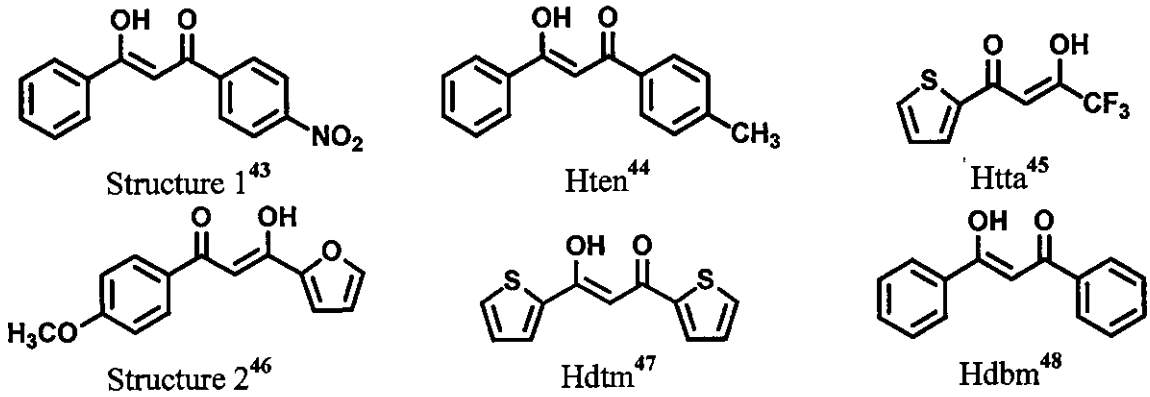

Structure 1[43] Hten[44] Htta[45]

Structure 2[46] Hdtm[47] Hdbm[48]

Figure 2.5.a: Examples of β-diketone structures: enol with an asymmetric H-bond.

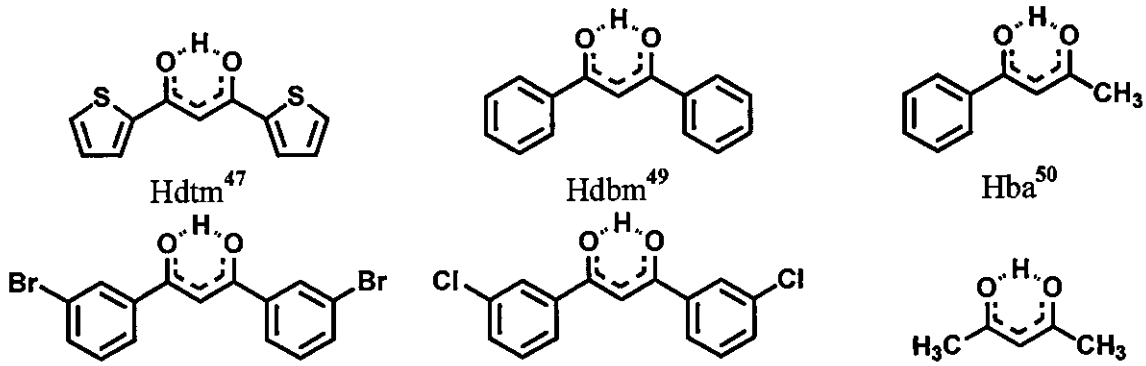

Hdtm[47] Hdbm[49] Hba[50]

Hdbrbm[51] Hdclbm[52] Hacac[53]

Figure 2.5.b: Examples of β-diketone structures: enol with a symmetric H-bond.

---

[43] V. Bertolasi, P. Gilli, V. Ferretti, G. Gilli, J. Am. Chem. Soc. 113 (1991) 4917.

[44] K. Kato, Acta Crystallogr., Sect. B: Struct. Crystallogr. Cryst. Chem. 27 (1971) 2028.

[45] R.D.G. Jones, Acta Crystallogr., Sect. B: Struct. Crystallogr. Cryst. Chem. 32 (1976) 1224.

[46] X Li, Y Zou, Z. Kristallogr. - New Cryst. Struct. 219 (2004) 281.

[47] L.A.M. Baxter, A.J. Blake, G.A. Heath, T.A. Stephenson, Acta Crystallogr., Sect. C: Cryst. Struct. Commun. 46 (1990) 508.

[48] S. Ozturk, M. Akkurt, S. Ide, Z. Kristallogr. 212 (1997) 808.

[49] B. Kaitner, E. Mestrovic, Acta Crystallogr., Sect. C: Cryst. Struct. Commun. 49 (1993) 1523.

[50] G.K.H. Madsen, B.B. Iversen, F.K. Larsen, M. Kapon, G.M. Reisner, F.H. Herbstein, J. Am. Chem. Soc. 120 (1998) 10040.

[51] D.E. Williams, W.L. Dumke, R.E. Rundle, Acta Crystallogr. 15 (1962) 627.

[52] G.R. Engebretson, R.E. Rundle, J. Am. Chem. Soc. 86 (1964), 574.

[53] R. Boese, M.Y. Antipin, D. Blaser, K.A. Lyssenko, J. Phys. Chem. B 102 (1998) 8654.

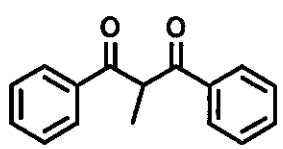
H2mdbm[54]

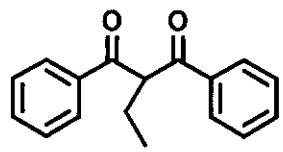
H2edbm[55]

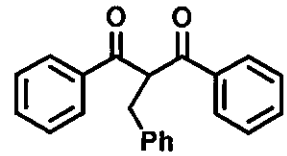

Hbzaa[56]

Figure 2.5.c: Examples of β-diketone structures: keto.

Table 2.4: Selected geometrical data for β-diketones. The typical range of bond lengths in enolized and non-enolized β-diketones are tabulated in **Table 2.5**. **Figure 2.5 (a-c)** gives the structures of the tabulated β-diketones. (See List of Abbreviates for different β-diketones.)

β-diketone	keto or enol	C=O bond length / Å	C-O (enol) bond length / Å	C=C bond length between carbonyl groups / Å	C-C bond length between carbonyl groups / Å	O···O distance / Å	Space group
Structure 1[43]	asym enol	1.288	1.313	1.391	1.397	2.465	$P2_1/c$
Hten[44]	asym enol	1.278	1.316	1.384	1.416	2.455	*Pbca*
Htta[45 a]	asym enol	1.269	1.307	1.343	1.432	2.522	$P2_1/n$
	asym enol	1.271	1.310	1.354	1.417	2.511	
Structure 2[46]	asym enol	1.286	1.298	1.376	1.400	2.495	*Pbca*
Hdtm[47 a]	asym enol	1.287	1.306	1.376	1.407	2.514	*Cc*
	sym enol	1.276	1.282	1.400	1.411	2.517	
Hdbm[48]	asym enol	1.292	1.314	1.373	1.412	2.459	*Pbca*
Hdbm[49]	sym enol	1.283	1.292	1.382	1.388	2.461	$P2_1/c$
Hba[50]	sym enol	1.284	1.291	1.405	1.413	2.502	$P2_1/c$
Hdbrbm[51]	sym enol	1.306	1.306	1.393	1.393	2.465	*Pnca*
Hdclbm[52]	sym enol	1.299	1.319	1.395	1.404	2.458	$Pca2_1$
Hacac[53]	sym enol	1.283	1.283	1.397	1.397	2.543	*Pnma*
H2mdbm[54]	keto	1.224 1.225			1.519 1.529	3.190	$P2_1/a$
H2edbm[55]	keto	1.218 1.221			1.519 1.520	3.169	$P2_1/a$
Hbzaa[56]	keto	1.216 1.217			1.524 1.527	3.130	$P2_1/n$

a Two molecules in the same asymmetric unit

[54] J. Emsley, N.J. Freeman, M.B. Hursthouse, P.A. Bates, J. Mol. Struct. 161 (1987) 181.

[55] D.F. Mullica, J.W. Karban, D.A. Grossie, Acta Crystallogr., Sect. C: Cryst. Struct. Commun. 43 (1987) 601.

[56] N. Judas, B. Kaitner, Acta Crystallogr., Sect. E: Struct. Rep. Online 61 (2005) o4008.

Table 2.5: The typical range of bond lengths in enolized and non-enolized β-diketones.

β-diketone	keto or enol	C=O bond length / Å	C-O (enol) bond length / Å	C=C bond length between carbonyl groups / Å	C-C bond length between carbonyl groups / Å	O····O distance / Å
typical range[24]	*enol*	*1.269 – 1.283*	*1.306 – 1.337*	*1.343 – 1.392*	*1.403 – 1.432*	*2.4 – 2.5*[57,58 a]
	keto	*1.212 – 1.211*			*1.507 – 1.537*	*2.7-3.2*[57,58 a, b]

a O····O distances in enol and keto forms, based on the enol and keto tautomers of acetylacetone (Hacac) are 2.381 and 2.767 Å respectively
b Results from **Table 2.4**

Most of the β-diketones isolated in the solid state, are in the enol form. As mentioned before, there are two extreme forms of intramolecular hydrogen bonding – symmetric and asymmetric. In asymmetric enolization the ring hydrogen is bound much more tightly to one oxygen atom than to the other. In general, one would expect symmetric hydrogen bonds when the β-diketone has identical substituens (*e.g.* Hdbrbm, Hdclbm and Hacac) and asymmetric hydrogen bonds when the β-diketone does not have identical substituens (*e.g.* Structure 1, Hten, Htta and Structure 2). Though, Hdtm, which has both a symmetrical hydrogen bond molecule and an asymmetric hydrogen bond molecule in one crystal system,[47] does not follow this general rule. A possible explanation for Hdtm deviating from the general rule, is that it contains a sulphur in the aromatic ring. Sulphur has an extra lone pair of electrons that can coordinate with nearby molecules, resulting in an asymmetric enolic arrangement rather than in a symmetric enolic arrangement. Baxter *et al.*[47] have found that when Hdtm is complexed with a metal (as discussed in **paragraph 3.4**), the thienyl ring, the S atom of which is not involved in primary coordination to the metal centre, can rotate 180° from the orientation found in **Figure 2.5 (a-b)** to form secondary S····M contact with another metal in the lattice.

Another example of the rotation of the thiophene ring in complexes was found by van der Watt **(Figure 2.6)**.[59] Two isomers were found for both the chromium and tungsten complexes. The major isomer (Cr 88.0 %, W 84.4 %) is the one with the sulphur atom on the same side as the ethoxy substituent and the minor isomer (Cr 12 %, W 15.6 %) exists with the sulphur on the

[57] S. Yamabe, N. Tsuchida, K. Kiyajima, J. Phys. Chem. A 108 (2004) 2750.

[58] A.H. Lowrey, C. George. P. D'Antonio, J. Karle, J. Am. Chem. Soc. 93 (1971) 6399.

[59] E. van der Watt, The Synthesis of Fischer Carbene Complexes with Metal-containing Substituents, M.Sc. Thesis, University of Pretoria, South Africa, 2006.

opposite side of the ethoxy substituent. These two isomers might be explained by free rotation around the C9-C10 bond in solution, but not in the solid state.

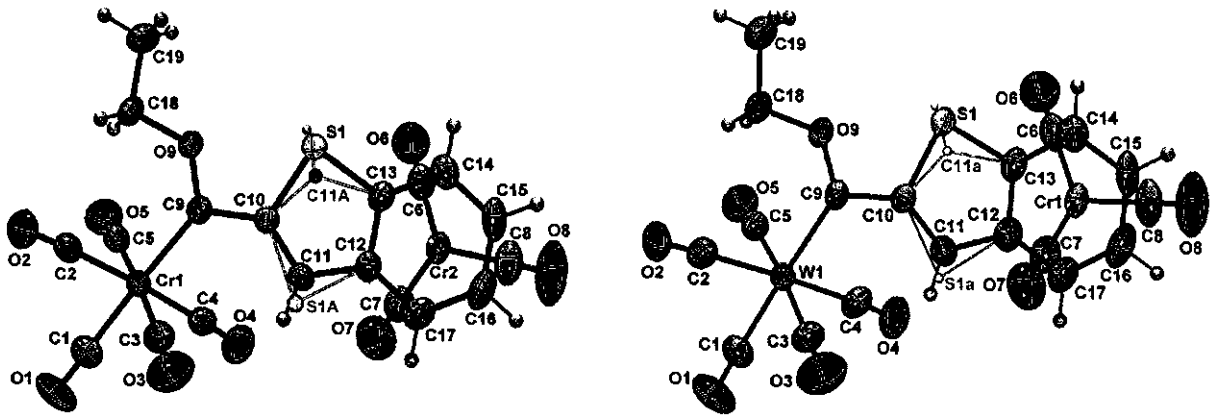

Figure 2.6: ORTEP + POV-Ray plot of the geometry of the chromium **(left)** and tungsten **(right)** complexes. (Figures are adopted from reference **59.**)

From the crystal structures[42] of the β-diketones displayed in **Figure 2.5 (a-c)** it has been observed that all the β-diketones in the enol form have a flat arrangement, while all the β-diketones in the keto form are twisted as illustrated in **Figure 2.7**.

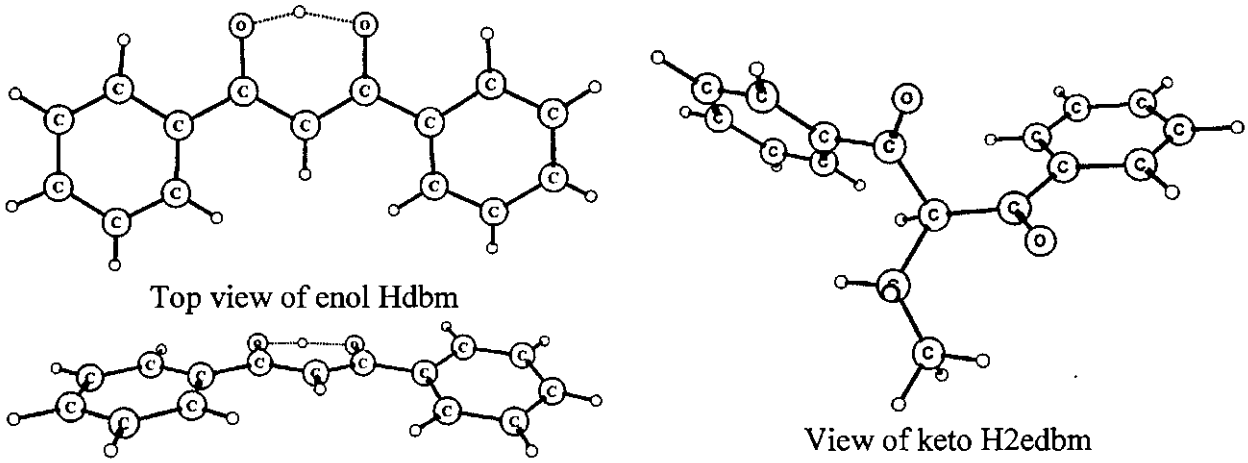

Figure 2.7: The flat arrangement **(left)** of the enol Hdbm and twisted arrangement **(right)** of the keto H2edbm.

2.3 Square planar Rh(I) and octahedral Rh(III) chemistry.

2.3.1 Introduction.

Under appropriate conditions the enolic hydrogen atom of a β-diketone can be replaced by a metal cation, M^{n+}, to produce a six-membered pseudo-aromatic chelate ring as illustrated in **Scheme 2.11**.[60]

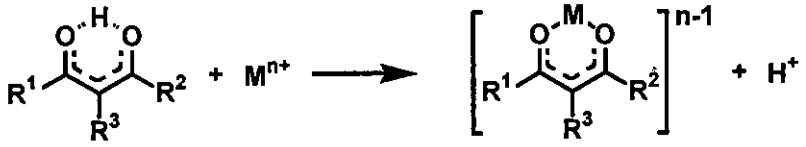

Scheme 2.11: Schematic representation of pseudo-aromatic chelate ring of metal β-diketonates.

The chemical behaviour of square planar Rh(I) complexes is very important in homogeneous catalysis. These complexes are coordinatively unsaturated and can take part in a series of elementary reactions that are steps in the catalytic synthesis of organic products.[61,62] To understand the process of homogeneous catalysis better, it is important to have extensive knowledge of each of these elementary key reactions as well as a thorough knowledge of the chemical properties of Rh(I) and Rh(III). In **paragraph 2.4**, we take a closer look at the theoretical aspects of oxidative addition, one of these elementary reactions. But first, lets have a look at the chemical properties of Rh(I) and Rh(III).

2.3.2 General properties.[63]

The chemistry of Rh(I) is almost entirely one involving π-bonding ligands such as CO, PR_3, RNC, alkenes, cyclopentadienyls and aryls. In complex, rhodium forms square planar,

---

[60] R.C. Mehrotra, R. Bohra, D.P. Gaur, Metal β-diketonates and Allied Derivatives, Academic Press, London, 1978, p. 2.

[61] L. Vaska, Acc. Chem. Res. 1 (1968) 335.

[62] J.P. Collman, Acc. Chem. Res. 1 (1968) 136.

[63] F.A. Cotton, G. Wilkinson, C.A. Murillo, M. Bochmann, Advanced inorganic chemistry, Sixth edition, John Wiley & Sons, New York, 1999, pp. 1041-1042.

tetrahedral, octahedral and five-coordinate species. The latter two are commonly produced by addition of neutral ligands to the first two. The criteria for relative stability of five- and four-coordinate species are by no means fully established. Substitution reactions of square species, which are often rapid, proceed by an associative pathway involving five-coordinate intermediates. Most of the square planar complexes undergo oxidative addition reactions and these lead to octahedral Rh(III) complexes with π-bonding ligands. These Rh(I)-Rh(III) oxidation changes are important in catalytic cycles.

2.3.3 Synthesis.

The Rh(I) complexes are usually prepared by reduction of similar Rh(III) complexes or of halide species such as $Rh^{III}Cl_3.3H_2O$ in the presence of the complexing ligand. Hundreds of complexes are known and only a few representative examples synthesized from $Rh^{III}Cl_3.3H_2O$ are shown in **Scheme 2.12**.[64,65,66]

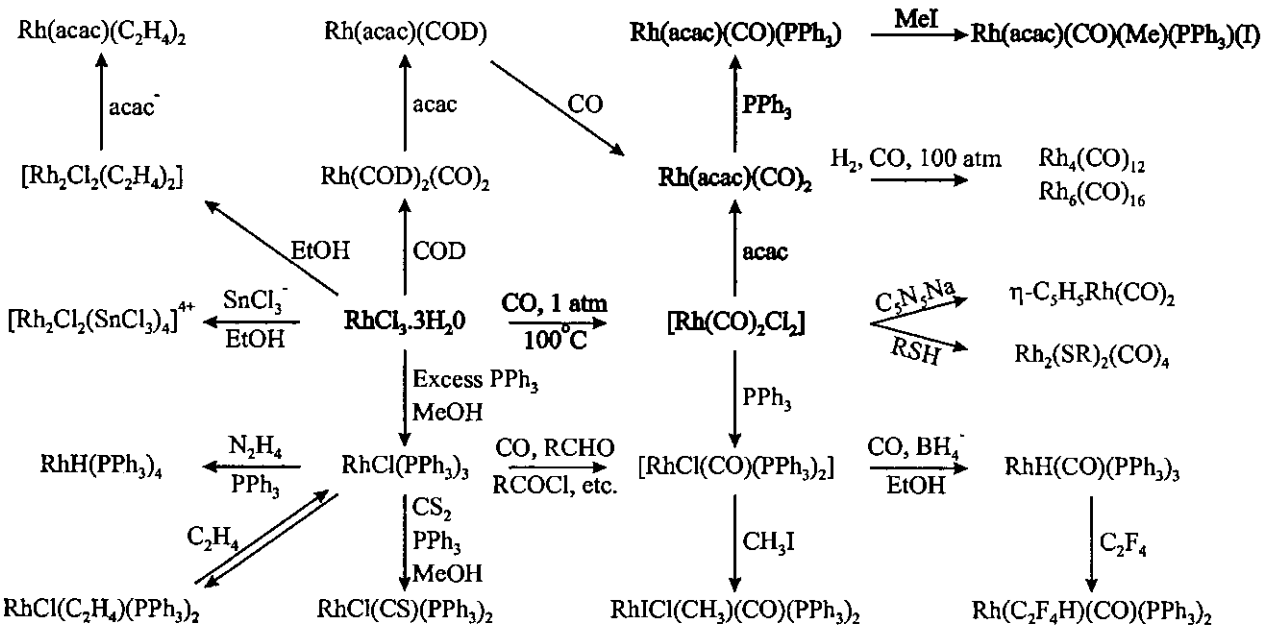

Scheme 2.12: Preparations and reactions of Rh(I) and Rh(III) compounds from $Rh^{III}Cl_3.H_2O$.

---

[64] F.A. Cotton, G. Wilkinson, C.A. Murillo, M. Bochmann, Advanced Inorganic Chemistry, Sixth edition, John Wiley & Sons, New York, 1999, p1042.

[65] Y.S. Varshavsky, T.G. Cherkosova, N.A. Buzina, L.S. Bresler, J. Organomet. Chem. 464 (1994) 239.

[66] J. Conradie, T.S. Cameron, M.A.S. Aquino, G.J. Lambrecht, J.C. Swarts, Inorg. Chim. Acta 358 (2005) 2530.

This study is concerned with compounds of the kind [Rh(β-diketonato)(CO)(PPh_3)] and its Rh(III) products that form after oxidative addition with MeI. [Rh(β-diketonato)(CO)(PPh_3)] is a member of the more general class of [Rh(L,L'-BID)(CO)(PPh_3)] complexes, where L,L'-BID is a monocharged bidentate ligand with donor atoms L and L' such as illustrated in **Figure 2.8**. This study will focus on the bold part in **Scheme 2.12**.

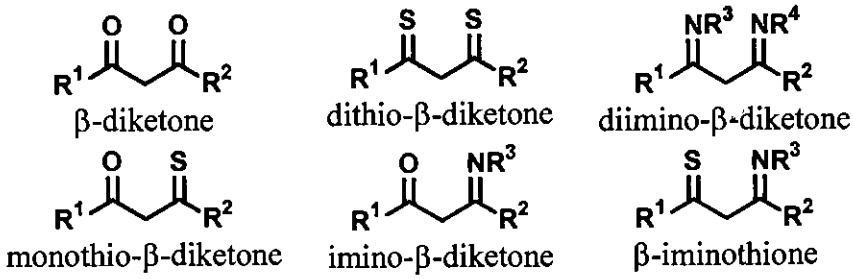

Figure 2.8: Structures of L,L-BID.

When L,L'-BID is an unsymmetrical ligand, it gives rise to two structural isomers of the [Rh(L,L'-BID)(CO)(PPh_3)] complex, as illustrated in **Figure 2.9**.

Figure 2.9: The two structural isomers of the [Rh(L,L'-BID)(CO)(PPh_3)] complex.

2.3.4 Carbonyl (CO) bonding to a metal.

The fact that refractory metals, with high heats of atomization (~400 kJ.mol^{-1}), and an inert molecule like CO are capable of uniting to form stable, molecular compounds is quite surprising, especially when the CO molecules retain their individuality. Moreover, the Lewis basicity of CO is negligible. The explanation lies in the multiple nature of the M-CO bond. The bonding is best explained by a molecular orbital diagram as illustrated in **Figure 2.10**.

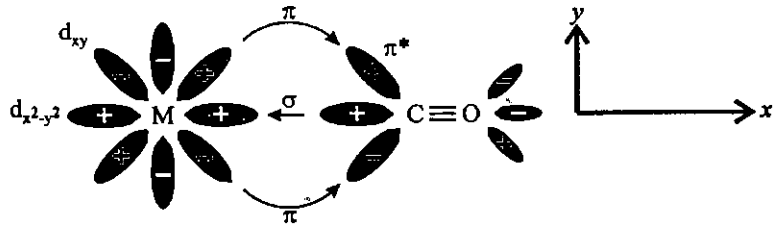

Figure 2.10: The formation of the metal←CO σ bond using a lone electron pair on the carbon and the formation of the metal→CO π back-bond. Other orbitals on the CO ligand are omitted for clarity.

Firstly, there is a dative overlap of the filled carbon σ orbital. The lone pair electrons of the carbon are donated to the empty metal d_{x2-y2} orbital to form a σ bond. Secondly, there is a dative overlap of the filled d_π orbital of the metal with an empty antibonding p_π orbital of the CO to form a π bond. This bonding mechanism is synergic, since the drift of metal electrons into the CO orbitals will tend to make the CO as a whole negative and, hence, will increase its electron donating property via the σ orbital of the carbon. Also, the drift of electrons to the metal in the σ bond tends to make the CO positive, thus enhancing the acceptor strength of the π^* orbitals. Thus, the effects of σ-bond formation strengthen the π bonding and vice versa.

The main lines of physical evidence showing the multiple nature of the M-CO bonds are bond lengths and vibrational spectra. According to the preceding description of the bonding, as the extent of back-donation from M to CO increases, the M-C bond becomes stronger and the C≡O bond becomes weaker which results in a lower CO-stretching frequency (ν_{CO}). Thus the multiple bonding should be evidenced by shorter M-C and longer C-O bonds as compared with M-C single bonds and C≡O triple bonds, respectively and the ν_{CO} will decrease as illustrated in **Scheme 2.13**. Although C-O bond lengths are rather insensitive to bond order, for M-C bonds in selected compounds there is an appreciable shortening consistent with the π-bonding concept.[67]

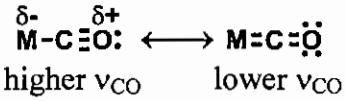

Scheme 2.13: Tighter bonded C-O bonds (left) has an higher ν_{CO} than weaker bonded C-O bonds (right).

Infrared spectra have been widely used in the study of metal carbonyls since the CO-stretching frequency (ν_{CO}) gives a very strong sharp band that is well separated from other vibrational modes of any other ligands also present. Where the free CO molecule has a $\nu_{CO} = 2143\ cm^{-1}$, it has a lower ν_{CO} when bonded to a Rh(I) complex. Although the oxidative addition of MeI to Rh(I) complexes of the form [Rh(L,L'-BID)(CO)(PPh_3)] will be thoroughly discussed in **paragraph 2.4**, **Scheme 2.14**[68] and **Scheme 2.15**[69] illustrate and explain the CO-stretching frequency (ν_{CO}) shifts during the reaction.

---

[67] F.A. Cotton, G. Wilkinson, P.L. Gaus, Basic Inroganic Chemistry, Third edition, John Wiley & Sons, New York, 1995, pp. 649-650.

[68] A. Roodt, G.J.J. Steyn, Recent Rs. Devel. Inorganic Chem. 2 (2000) pp. 1-23.

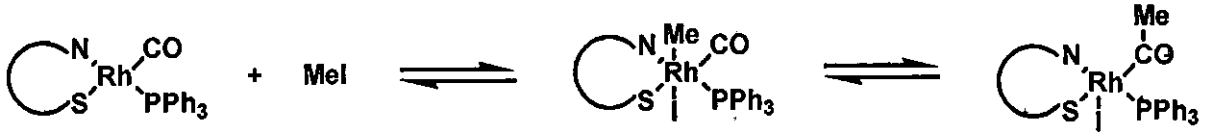

$\nu_{CO} \approx 2000$ cm^{-1}
Rh^{I} very electron rich
π backbonding
stronger M-C bond
weakened C≡O bond
∴ smaller ν_{CO}

$\nu_{CO} \approx 2050$ cm^{-1}
Rh^{III} less electron rich
less π backbonding
weakened M-C bond
stronger C≡O bond
∴ higher ν_{CO}

$\nu_{CO} \approx 1750$ cm^{-1}
no triple bond
C=O double bond (sp^2) even weakened
∴ smaller ν_{CO}

Scheme 2.14: CO-stretching frequency (ν_{CO}) shifts during oxidative addition reaction of MeI to a [Rh(L,L'-BID)(CO)(PPh_3)] complex where L, L' = N, S.[68]

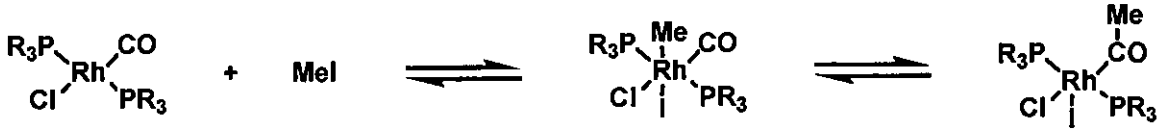

$\nu_{CO} \approx 1980$ cm^{-1}
Rh^{I} very electron rich
π backbonding
stronger M-C bond
weakened C≡O bond
∴ smaller ν_{CO}

$\nu_{CO} \approx 2060$ cm^{-1}
Rh^{III} less electron rich
less π backbonding
weakened M-C bond
stronger C≡O bond
∴ higher ν_{CO}

$\nu_{CO} \approx 1705$ cm^{-1}
no triple bond
C=O double bond (sp^2) even weakened
∴ smaller ν_{CO}

Scheme 2.15: CO-stretching frequency (ν_{CO}) shifts during oxidative addition reaction of MeI to *trans*-[RhCl(CO)(PR_3)$_2$] where PR_3 = triarylphosphine.[69]

2.3.5 Trivalent phosphine (PX_3) bonding to a metal.[70]

PX_3 compounds can be π-acceptor ligands when X is fairly electronegative (Ph, OR) or very electronegative (Cl, F). Tertiary phosphines and phosphates are much better Lewis bases than CO and can form many complexes where π acidity plays little or no role. This is observed with the phosphine complexes of the early transition metals and with metal atoms of any kind in their higher oxidation states where the M-P distances show no evidence of significant π bonding. In almost any CO-containing molecule, one or more CO groups can be replaced with a PX_3 or similar ligand. While the occurrence of π bonding from M to P is a generally acknowledged fact, the explanation for it entails controversy. The widely credited explanation is the figure that is

[69] S. Franks, F.R. Hartley, J.R. Chipperfield, Inorg. Chem. 20 (1981) 3238.

[70] F.A. Cotton, G. Wilkinson, C.A. Murillo, M. Bochmann, Advanced Inorganic Chemistry, Sixth edition, John Wiley & Sons, New York, 1999, p. 642.

shown in **Figure 2.11**, in which phosphorus specifically employs a pair of its d orbitals to accept metal electrons.

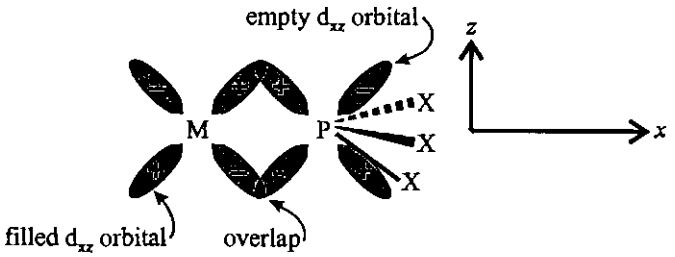

Figure 2.11: The back-bonding from a filled metal d orbital to an empty phosphorus 3d orbital in the PX_3 ligand taking the internuclear axis as the x axis. An exactly similar overlap occurs in the xy plane between the d_{xy} orbitals.

Of course, not all M-P bond properties can be explained by the π bond model in **Figure 2.11**. According to Pidcock[71] there are clearly two extremes: firstly, complexes containing the metal in oxidation states greater than +2 contain predominantly pure σ-bonds with phosphine ligands and secondly, those in low oxidation states, especially with such ligands as PF_3, PCl_3 and $P(OPh)_3$ form bonds with phosphines which contain a σ- as well as a π-component.[72,73] It has been proposed by Marynick[74], on the basis of quantum mechanical calculations that phosphorus p orbitals and the P-X σ^* orbitals may play a major role in accepting metal d_π electrons, even to the complete exclusion of the phosphorus d_π orbitals. Experimental evidence for or against such ideas is lacking. **Figure 2.12** shows the probability that a π bond will form between the phosphorus and the appropriate ligand.

---

[71] A. Pidcock, in: C.A. McAuliffe (Ed.), Transition Metal Complexes of Phosphorus, Arsenic and Antimony Ligands, Macmillan, London, 1973, Part 1.

[72] J. Emsly, D. Hall, The Chemistry of Phosphorus, Harper and Row Publishers, 1976, Chapter 5.

[73] C.A. McAuliffe, W. Levason, Phosphine, Arsine and Stibine Complexes of the Transition Elements, Elsevier Scientific Publishing Company, Amsterdam, 1979, Chapter 3.

[74] D.S. Marynick, J. Am. Chem. Soc. 106 (1984) 4064.

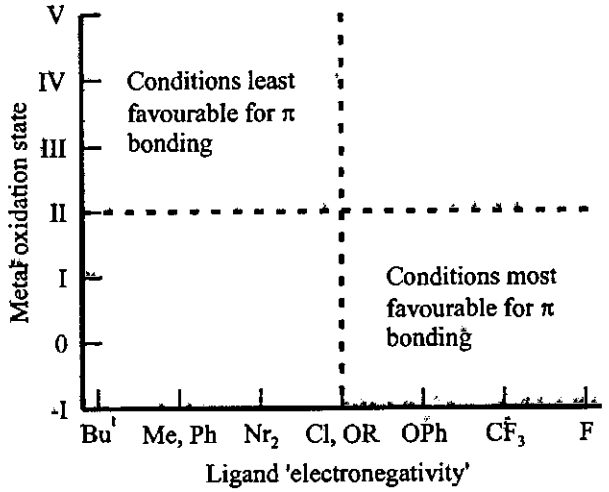

Figure 2.12: Dependence of π bonding on oxidation state of metal and 'electronegativity' of phosphorus ligands, based on tetracoordinate phosphorus.

Phosphines have steric and electronic influences on the metal complexes which influence the oxidative addition reaction. These influences will be discussed in **paragraph 2.3.6**.

2.3.6 Structural isomers of Rh(I) bidentate complexes.

The stereochemistry of the two structural isomers of Rh(I) bidentate complexes (**Figure 2.9**) are influenced by the following factors:

a. Thermodynamic trans-influence
b. Steric properties
c. Crystallization energy

Although the thermodynamic trans-influence is normally the more general influence, it can be dominated by the steric properties of the complex or by the crystallization energy. Each of these factors will be discussed in the following paragraphs.

2.3.6.1 Thermodynamic trans-influence.

The thermodynamic trans-influence[75] is a ground state phenomenon, which can be defined as the ability of a ligand to weaken the metal-ligand bond *trans* to it. This means that certain ligands give rise to the replacement of the ligands *trans* to it by weakening the metal-ligand bond *trans* to it. The trans-influence of a wide variety of ligands has been "measured" with techniques such as

[75] A. Pidcock, R.E. Richards, L.M. Venanzi, J. Chem. Soc. A (1966) 1707.

X-ray crystallography, IR, NMR, nuclear quadrupole resonance, photoelectron and Mössbauer spectroscopy.[76,77]

Grinberg[78] proposed that the thermodynamic trans-influence was purely electrostatic (polarization theory). A strong dipole interaction between a ligand and the central metal atom would tend to weaken the attachment of the ligand *trans* to it by a mis-match of dipoles (**Figure 2.13**).

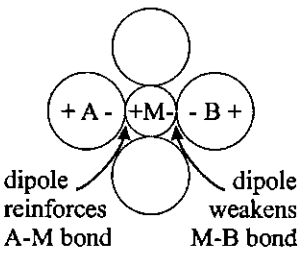

Figure 2.13: The polarization theory of Grinberg.

The trans-influence should not be confused with the trans-effect, which is a kinetic phenomenon and is defined as the effect of a coordinated ligand on the substitution rate of the ligand opposite to it.[79]

The thermodynamic trans-influence of bidentate ligands of compounds of the type [Rh(L,L'-BID)(CO)(PPh_3)] can be subdivided in the following categories:

a. The relative influence of PPh_3 and CO on the bidentate ligand L,L-BID
b. The relative influence of the ligand L,L'-BID on the Rh-P bond length with
   b.i. different donor atoms L and L' and a symmetrical backbone on the BID ligand
   b.ii. the same donor atoms L and L and an unsymmetrical backbone on the BID ligand

The relative thermodynamic trans-influence of PPh_3 and CO is best described when CO is replaced with PPh_3 in [Rh(L,L'-BID)($CO)_2$], where (L,L'-BID) is a symmetrical bidentate ligand. The different catagories of the trans-influence are schematically illustrated in **Scheme 2.16** and

---

[76] G.M. Bancroft, K.D. Butler, J. Am. Chem. Soc. 96 (1974) 7208.

[77] C.H. Langford, H.B. Gray, Ligand Substitution Processes, W.A. Benjamin Inc., New York, 1965.

[78] A.A. Grinberg, Acta Physiochim, USSR 3 (1935) 573.

[79] F.A. Cotton, G. Wilkinson, P.L. Gaus, Basic Inorganic Chemistry, Third edition, John Wiley & Sons, New York, 1995, p 201.

examples[80] of each category are given in **Figure 2.14**. Since the PPh_3 group has a larger trans-influence than the CO group, the Rh-L bonded *trans* to the PPh_3 group will be weakened.

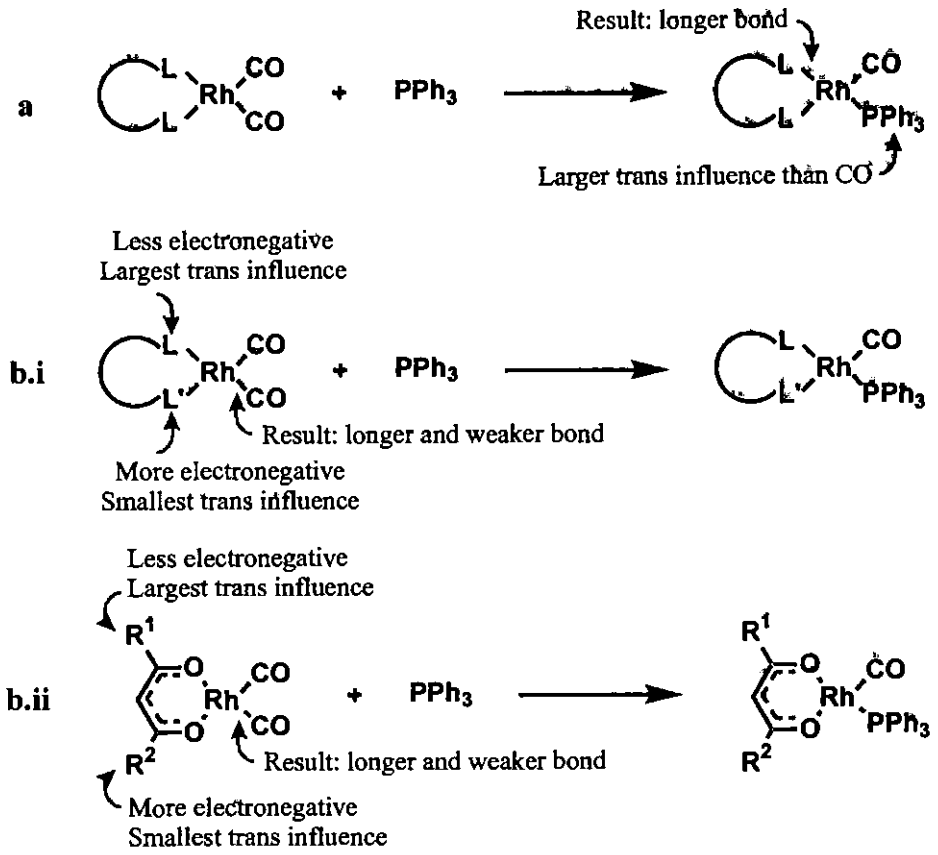

Scheme 2.16: a) The relative influence of PPh_3 and CO on the bidentate ligand L,L-BID. **b.i)** The relative influence of the L,L'-BID on the Rh-P bond length with different donor atoms L and L' and a symmetrical backbone on the BID ligand. **b.ii)** The relative influence of the L,L-BID on the Rh-P bond length with the same donor atoms L and L and a unsymmetrical backbone on the BID ligand.

From the examples in **Figure 2.14.a** it clear that the PPh_3 group, relative to the CO group, has a larger trans-influence on the bidentate ligand L,L-BID, which is demonstrated by the elongated bond *trans* to the PPh_3. To understand the examples in **Figure 2.14.b.** one needs to look at the electronegativities of the elements[81]/groups[82], which are as follow:

$$S\ (2.4) < C\ (2.5) < N\ (3.1) < O\ (3.5) \quad \text{and} \quad CH_3\ (2.34) < CF_3\ (3.01)$$

---

[80] Cambridge Crystallographic Data Centre (CCDC), ConQuest Version 1.8, Copyright © 2005.

[81] R.C. Weast, Handbook of Chemistry and Physics, Forty-ninth edition, The Chemical Rubber Co., Ohio.

[82] W.C. Du Plessis, J.J.C. Erasmus, G.J. Lambrecht, J. Conradie, T.S. Cameron, M.A.S. Aquino, J.C. Swarts, Can. J. Chem. 77 (1999) 378.

The element/group with a smaller electronegativity has a larger trans-influence on the CO group bonded *trans* to it, which results in a weaker bond and subsequently in the replacement of that CO group with a PPh_3 group.

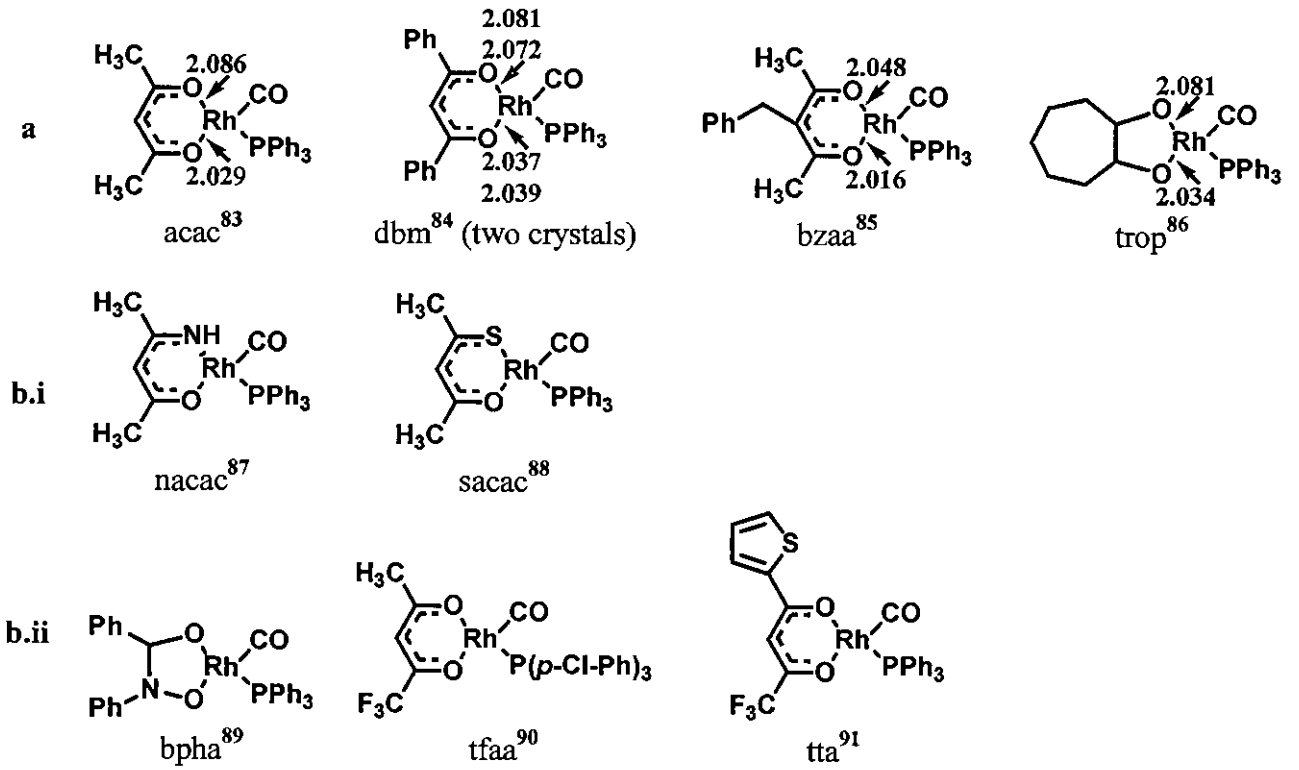

Figure 2.14: Examples of square planar complexes [Rh(L,L'-BID)(CO)(PPh_3)] containing L,L'-BID ligands with L, L' donor atoms as indicated illustrating **a)** The relative influence of PPh_3 and CO on the bidentate ligand L,L-BID. **b.i)** The relative influence of the L,L'-BID on the Rh-P bond length with different donor atoms L and L' and a symmetrical backbone on the BID ligand. **b.ii)** The relative influence of the L,L'-BID on the Rh-P bond length with the same donor atoms L and L and an unsymmetrical backbone on the BID ligand.

---

[83] J.G. Leipoldt, S.S. Basson, L.D.C. Bok, T.I.A. Gerber, Inorg. Chim. Acta 26 (1978) L35.

[84] D. Lamprecht, G.J. Lamprecht, J.M. Botha, K. Umakoshi, Y. Sasaki, Acta Crystallogr., Sect. C: Cryst. Struct. Commun. 53 (1997) 1403.

[85] A. Roodt, J.G. Leipoldt, J.C. Swarts, G.J.J. Steyn, Acta Crystallogr., Sect. C: Cryst. Struct. Commun. 48 (1992) 547.

[86] J.G. Leipoldt, L.D.C. Bok, S.S. Basson, H. Meyer, Inorg. Chim. Acta 42 (1980) 105.

[87] L.J. Damoense, W. Purcell, A. Roodt, J.G. Leipoldt, Rhodium Ex. 5 (1994) 10.

[88] L.J. Botha, S.S. Basson, J.G. Leipoldt, Inorg. Chim. Acta 126 (1987) 25.

[89] J.G. Leipoldt, E.C. Grobler, Inorg. Chim. Acta 60 (1982) 141.

[90] E.C. Steynberg, G.J. Lamprecht, J.G. Leipoldt, Inorg. Chim. Acta 133 (1987) 33.

[91] J.G. Leipoldt, L.D.C. Bok, J.S. van Vollenhoven, A.I. Pieterse, J. Inorg. Nucl. Chem. 40 (1978) 61.

Another example to demonstrate the trans-influence is $[Rh(CF_3COCHNOCH_3)(CO)_2]$, which had two crystals in the same asymmetric unit.[92] This complex has different donor atoms L and L' as well as an unsymmetrical backbone on the BID ligand (**Figure 2.15**). The less electronegative element and group (L = N and $R_1 = CH_3$) are located on the one side of the complex. Together they have a larger trans-influence on the CO group bonded *trans* to them than the more electronegative element and group (L' = O, $R_2 = CF_3$). This results in a longer Rh-CO bond (1.869 and 1.878 *vs.* 1.838 and 1.848) and subsequently in the replacement of that CO group with a PPh_3 group. Both the complexes in **Figure 2.15** were verified by X-ray crystallography.

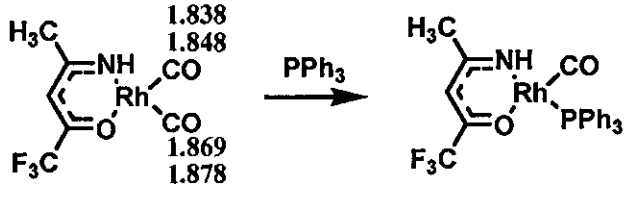

Figure 2.15: Structures of $[Rh(CF_3COCHNOCH_3)(CO)_2]$ (two crystals in the same asymmetric unit) and $[Rh(CF_3COCHNOCH_3)(CO)(PPh_3)]$. Note how the longer and weaker R-CO bond is broken to replace the CO group with a PPh_3 group.[92]

2.3.6.2 Steric properties.

Steric properties refer to the influence of different bulky ligands co-ordinated to the same metal centre. It has been observed that increasing sizes of reacting complexes and ligands lower the rate of reaction. In sterically crowded complexes, bulky ligands shield the metal centre, thereby blocking the approach of the incoming ligand.

A kinetic study of the replacement of the CO ligands in $[Rh(L,L'\text{-BID})(CO)_2]$ with cod (1,5-cyclooctadiene) where L'L-BID = β-diketonato, indicated an associative mechanism.[93] Square planar substitution reactions following an associative mechanism, for example **Reaction 2.1**, involve a trigonal bipyramidal transition state wherein the entering ligand (PPh_3), the leaving group (CO) and the group *trans* to the leaving group (oxygen) occupy the same trigonal plane of the trigonal bipyramid, with the other two remaining ligands in the apical positions.[77]

---

[92] Y.S. Varshavsky, M.R. Galding, T.G. Cherkasova, I.S. Podkorytov, A.B. Nikol'skii, A.M. Trzeciak, Z. Olejnik, T. Lis, J.J. Ziolkowski, J. Organomet. Chem. 628 (2001) 195.

[93] J.G. Leipoldt, S.S. Basson, J.J.J. Schlebush, E.C. Grobler, Inorg. Chim. Acta 62 (1982) 113.

Reaction 2.1: $[Rh(L,L'\text{-BID})(CO)_2] + PPh_3 \rightarrow [Rh(L,L'\text{-BID})(CO)(PPh_3)] + CO$

In the bulky complex $[Rh(tftma)(CO_2)]$ (**Figure 2.16**) the CF_3 group is more electronegative than the $C(CH_3)_3$ group. According to electronic considerations (the trans-influence) it is thus expected that the CO group *trans* to the oxygen nearest to the $C(CH_3)_3$ group will be replaced with PPh_3. If the expected isomers, according to electronic considerations, were to be formed, the oxygen nearest to the sterically hindered groups, the leaving CO and the incoming PPh_3 ligand would have to share the limited space of the trigonal plane, resulting in a relatively unstable intermediate (structure B in **Figure 2.16**). It is thus more likely that the other isomer, with PPh_3, CO and oxygen nearest to the less bulky group in the trigonal plane of the trigonal bipyramidal transition state will be formed. **Figure 2.16** gives a schematic presentation of the trigonal bipyramidal transition state of the associative mechanism of the replacement of the carbonyl group in $[Rh(tftma)(CO)_2]$ with PPh_3 illustrating the larger steric interaction expected between the PPh_3 and Bu^t if the expected isomers according to the electronic considerations were to be formed (structure B in **Figure 2.16**). Examples[80] of complexes where the substitution pattern is due to steric interactions, rather than electronic considerations, are given in **Figure 2.17**.

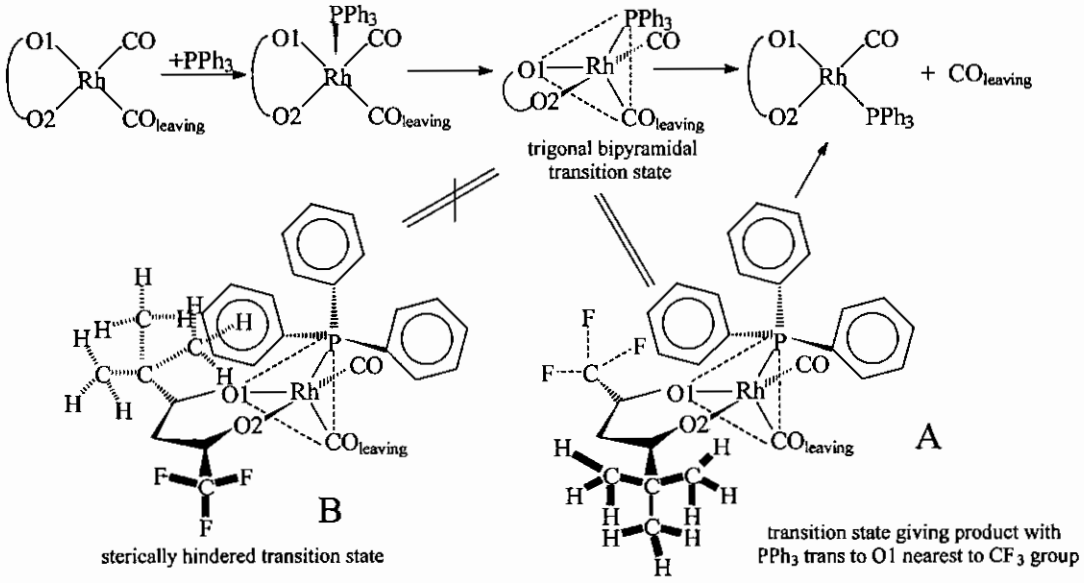

Figure 2.16: Schematic representation of the trigonal bipyramidal transition state of the replacement of the carbonyl group in $[Rh(tftma)(CO)_2]$ with PPh_3 following an associative mechanism. The trigonal bipyramidal transition state, TBP, is expected to have the sterically unhindered structure A with the tertiary butyl group Bu^t above the trigonal plane and far away from the PPh_3 substituents. The sterically crowded transition state B is not expected because of the larger steric interaction expected between the PPh_3 and Bu^t which are here either completely below the trigonal plane (Bu^t) or partially below the trigonal plane (the tetrahedrically PPh_3 group). H-atoms on the phenyl groups are omitted for clarity but in B they enhance steric interaction.

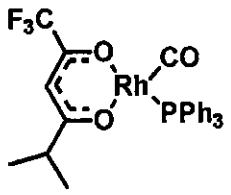

tfdma[94]

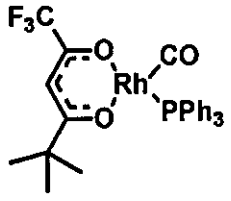

tftma[95]

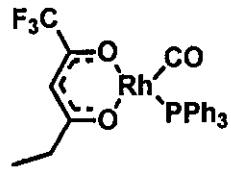

tfhd[90]

Figure 2.17: Structures of complexes with steric properties.

2.3.6.3 Crystallization energy.

It is known[96,97] that it is not necessarily always the thermodynamically stable isomer that crystallizes since the crystallization energy of a specific isomer will determine the solid state structure, specifically in labile rhodium systems.[68] The crystal structure of $[Rh(fctfa)(CO)(PPh_3)]$[98] (**Figure 2.18**) is a typical example.

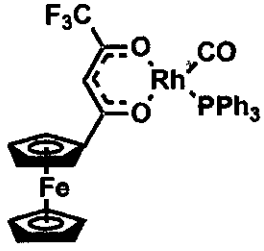

Figure 2.18: Structure of $[Rh(fctfa)(CO)(PPh_3)]$.[98]

The crystal structure of $[Rh(fctfa)(CO)(PPh_3)]$ showed that the carbonyl group *trans* to the oxygen atom nearest to the more electronegative CF_3-group was replaced with PPh_3. The dominance of the steric hindrance of the ferrocenyl group over the electronic influence, may be the reason for the unexpected substitution. However, the similar Rh-C bond lengths in the structure of the $[Rh(fctfa)(CO)_2]$ complex, 1.83(2) and 1.84(1) Å, showed no obviously weaker bonded carbonyl group. Therefore, there should not be a preferred CO group that should be replaced with PPh_3. Since both the isomers of $[Rh(fctfa)(CO)(PPh_3)]$ were observed on

---

[94] J.G. Leipoldt, S.S. Basson, J.T. Nel, Inorg. Chim. Acta 74 (1983) 85.

[95] J.G. Leipoldt, S.S. Basson, J.H. Potgieter, Inorg. Chim. Acta 117 (1986) L3.

[96] G.J.J. Steyn, A. Roodt, I. Poletaeva, Y.S. Varshavsky, J. Organomet. Chem. 536/7 (1997) 797.

[97] C.H. Langford, H.B. Gray, Ligand Substitution Processes, Benjamin, New York, 1965.

[98] G.J. Lamprecht, J.C. Swarts, J. Conradie, J.G. Leipoldt, Acta Crystallogr., Sect. C: Cryst. Struct. Commun. 49 (1993) 82.

^{1}H NMR, in solution of $CDCl_3$ in 2:3 ratio,[66] it is more probable that the lower crystallization energy of the obtained crystal, determined which isomer crystallized from solution.

2.3.6.4 Two different isomers in one asymmetric unit.

The discussion on the trans-influences, steric properties and crystallization energy of bidentate ligands was thus far based on single isomers that crystallized from solution and was characterized by X-ray crystallography. However, for [Rh(ba)(CO)(PPh_3)],[99] both the isomers crystallized out in the same asymmetric unit. This unusual occurrence might be explained by the similar group-electronegativities of the CH_3 and Ph groups (κ_{CH3} = 2.34 and κ_{Ph} = 2.21) resulting in a similar trans-influence on the CO groups in [Rh(ba)$(CO)_2$] which are to be replaced with PPh_3.

2.3.7 Crystallography of Rh(I) and Rh(III) complexes.

2.3.7.1 Crystal structures of square planar dicarbonyl-Rh(I) complexes.

The replacement of one of the carbonyl groups in [Rh(L,L'-BID)$(CO)_2$] with PPh_3 results in the complex [Rh(L,L'-BID)(CO)(PPh_3)] with the Rh-donor atom bond length *trans* to P (2.045 - 2.297 Å) being longer than the Rh-donor atom bond length *cis* to P (2.019 - 2.062 Å) (discussion follows in **paragraph 2.3.7.2**, summary in **Table 2.8**). This longer bond length is the result of the combined effect of the trans-influence of the substituents on the L,L'-BID and the trans-influence of the PPh_3. **Table 2.6** presents selected geometrical data[80] of Rh(I) complexes of the type [Rh(R^1-CL-CH-CL'-R^2)$(CO)_2$] containing the bidentate ligand (R^1-CL-CH-CL'-R^2) with R^1 and R^2 groups and donor atoms (L, L') = (O, N), (O, O) and (N, N). Since the CO ligands are the same, the Rh-donor atom bond lengths in the [Rh(R^1-CL-CH-CL'-R^2)$(CO)_2$] complexes can be used to study the effect of the influence of the different substituents R^1 and R^2 (*e.g.* CH_3, CF_3, Ph and Fc) on the donor atoms L and L' (*e.g.* O or N).

---

[99] W. Purcell, S.S. Basson, J.G. Leipoldt, A. Roodt, H. Preston, Inorg. Chim. Acta 234 (1995) 153.

Table 2.6: Selected geometrical data[80] for square planar complexes [Rh(R^1-CL-CH-CL'-R^2)$(CO)_2$] with R^1 and R^2 groups and L, L' donor atoms as indicated (see List of Abbreviations for different bidentate ligands).

L,L'-BID	L, L'	R^1	R^2	Rh-L distance / Å	Rh-L' distance / Å	Rh-C distance *trans* to R^2-CL' / Å	Rh-C' distance *trans* to R^1-CL / Å	L-Rh-L' angle / °	Space group
Complex 1[92 a, b]	O, N	CF_3	CH_3	2.034 2.046	2.030 2.038	1.869 1.878	1.838 1.848	89.5 89.5	$P\bar{1}$
acac[100]	O, O	CH_3	CH_3	2.040	2.044	1.831	1.831	90.8	$P\bar{1}$
tfba[101]	O, O	CF_3	Ph	2.025	2.026	1.78(3)	1.81(3)	89.8	*Pbca*
fctfa[66]	O, O	CF_3	Fc	2.016	2.049	1.84(1)	1.83(1)	90.1	*C2/c*
Complex 2[102 c]	N, N	CH_3	CH_3	2.036	2.045	1.864(5)	1.881(6)	86.7	$P2_1/c$

a $(CF_3COCHCNCH_3)^-$
b Two molecules in the same asymmetric unit
c $(CH_3CNCHCNCH_3)^-$

The [Rh(L,L'-BID)$(CO)_2$] complexes, where (L,L'-BID) = (R^1-CL-CH-CL'-R^2), presented in **Table 2.6** show that:

- In complex 1, the Rh-CO bond length (1.869 and 1.878 Å) of the CO *trans* to the N donor atom and the CH_3 group is longer than the Rh-CO bond length (1.838 and 1.848) *cis* to them. This indicates a larger trans-influence of the N donor atom (χ_N = 3.1) and the CH_3 group (χ_{CH3} = 2.34) than the O donor atom (χ_O = 3.5) and the CF_3 group (χ_{CF3} = 3.01). This result is in agreement with the crystal structure in **Table 2.7** where it was shown that the carbonyl *trans* to the N donor atom and the CH_3 group was replaced with the PPh_3 ligand as discussed in **paragraph 2.3.6.1**.
- When the L,L'-BID is symmetrical like in acac, the Rh-CO bonds should be chemically equivalent, as was confirmed by the structure determination of this complex where the equivalent bond lengths around the Rh were the same within experimental error. The crystal data of complex 2, which is a diimino-β-diketonato complex, were not consistent with this.
- In the tfba and fctfa crystals, the errors in the Rh-CO bond lengths are too large to interpret small differences in bond lengths in terms of trans-influence. These inaccurate Rh-C bond lengths are most probably due to the large thermal vibrations of the small CO ligands relative to the more rigid and large β-diketonato ligand with a Fc or a Ph group. Due to the similar,

[100] F. Huq, A.C. Skapski, J. Cryst. Mol. Struct. 4 (1974) 411.

[101] J.G. Leipoldt, L.D.C. Bok, S.S. Basson, J.S. van Vollenhoven, T.I.A. Gerber, Inorg. Chim. Acta 25 (1977) L63.

[102] P.W. De Haven, V.L. Goedken, Inorg. Chem. 18 (1979) 827.

inaccurate, Rh-C bond lengths, it is not possible to forecast which CO group will be replaced with a PPh_3 group in the substitution reaction: $[Rh(L,L'\text{-BID})(CO)_2] + PPh_3 \rightarrow [Rh(L,L'\text{-BID})(CO)(PPh_3)] + CO$.

2.3.7.2 Crystal structures of square planar monocarbonyl-Rh(I) complexes.

Table 2.7 presents selected geometrical data[80] of Rh(I) complexes of the type $[Rh(L,L'\text{-BID})(CO)(PPh_3)]$ containing L,L'-BID ligands with donor atoms (L, L') = (O, N), (O, O) and (O, S). The R^1 and L groups were selected *cis* to the PPh_3 group.

Table 2.7: Selected geometrical data[80] for square planar complexes $[Rh(L,L'\text{-BID})(CO)(PPh_3)]$ containing L,L'BID ligands with L, L' donor atoms as indicated (see List of Abbreviations for different L,L'-BID). R^1 and L were selected *cis* to the PPh_3 group.

L,L'-BID	L, L'	R^1	R^2	Rh-L distance / Å	Rh-L' distance / Å	Rh-P distance / Å	Rh-C distance / Å	L-Rh-L' angle / °	Space group
Complex 1[92 a]	O, N	CF_3	CH_3	2.045	2.045	2.281	1.804	88.0	$Pca2_1$
Complex 3[92 b]	O, N	CF_3	$C(CH_3)_3$	2.036	2.062	2.278	1.803	87.9	$P2_1$
dmavk[87]	O, N	CH_3	CH_3	2.044	2.045	2.275	1.784	87.4	$Pca2_1$
acac[83]	O, O	CH_3	CH_3	2.029	2.086	2.243	1.801	87.9	$P\bar{1}$
tfdma[94]	O, O	$CH(CH_3)_2$	CF_3	2.057	2.088	2.239	1.781	87.5	$P\bar{1}$
tftma[95]	O, O	$C(CH_3)_3$	CF_3	2.062	2.071	2.237	1.765	88.1	$P2_1/c$
tfhd[90]	O, O	CH_2CH_3	CF_3	2.047	2.094	2.252	1.796	87.6	$P\bar{1}$
fctfa[98]	O, O	Fc	CF_3	2.048	2.07	2.232	1.801	88.6	$P\bar{1}$
dbm[84 c]	O, O	Ph	Ph	2.037 2.039	2.081 2.072	2.236 2.245	1.813 1.794	88.5 89.1	Cc
tta[91]	O, O	CF_3	C_4H_3S	2.520	2.085	2.245	1.781	87.6	$P2_1/n$
ba[99 c]	O, O	CH_3, Ph	Ph, CH_3	2.019 2.032	2.057 2.078	2.245 2.249	1.768 1.739	86.2 88.1	$P\bar{1}$
sacac[88]	O, S	CH_3	CH_3	2.023	2.297	2.301	1.808	91.7	$P\bar{1}$

a $(CF_3COCHCNCH_3)^-$
b $(CF_3COCHCNC(CH_3)_3)^-$
c Two molecules in the same asymmetric unit

The average bond lengths of the $[Rh(L,L'\text{-BID})(CO)(PPh_3)]$ complexes presented in **Table 2.7**, as tabulated in **Table 2.8**, indicate a tendency of:

- the Rh-L' (donor atom *trans* to PPh_3) distance (2.045 – 2.297 Å) is longer than the Rh-L (donor atom *cis* to PPh_3) distance (2.019 – 2.062 Å) – in agreement with larger trans-influence of PPh_3 relative to CO,
- the Rh-P distances range between 2.232 – 2.301 Å,

- the Rh-C distances range between 1.739 – 1.813 Å,
- the L-Rh-L' angles range between 86.2 – 91.7°,
- Rh-P bond length *trans* to O atoms < Rh-P bond length *trans* to N atoms < Rh-P bond length *trans* to S atoms and
- Rh-C bond length *trans* to O atoms < Rh-C bond length *trans* to N atoms < Rh-C bond length *trans* to S atoms – this and the previous are in agreement with the increase in trans-influence as the electronegativity decreases O > N > S.

It should be realized, however, that the averages given in **Table 2.8** mathematically include any smaller effects on bond lengths that adjacent groups with different group electronegativity may have.

Table 2.8: Average bond lengths in complexes of the type [Rh(L,L'-BID)(CO)(PPh_3)] as tabulated in **Table 2.7**. R^1 and L were selected *cis* to the PPh_3 group.

L, L'	Rh-L distance / Å	Rh-L' distance / Å	Rh-P distance / Å	Rh-C distance / Å	L-Rh-L' angle / °
O, N	2.042	2.051	2.278	1.797	87.8
O, O	2.042	2.078	2.242	1.784	87.9
O, S	2.023	2.297	2.301	1.808	91.7
range	**2.019 - 2.062**	**2.045 - 2.297**	**2.232 - 2.301**	**1.739 - 1.813**	**86.2 - 91.7**

2.3.7.3 Crystal structures of octahedral and square pyramidal Rh(III) complexes.

Geometrical data[80] of the alkyl oxidative addition product of [Rh(L,L'-BID)(CO)(PPh_3)] and iodomethane, namely [Rh(L,L'-BID)(CH_3)(I)(CO)(PPh_3)], are given in **Table 2.9**. **Figure 2.19** gives the graphical representations of the alkyl complexes (hydrogens were removed for clarity). Data of the acyl complexes (formed from the insertion reaction of carbonyl after oxidative addition of iodomethane to [Rh(L,L'-BID)(CO)(PPh_3)] complexes) are given in **Table 2.10** and the graphical representations in **Figure 2.20** (hydrogens were removed for clarity).

Table 2.9: Selected geometrical data[80] for octahedral Rh(III) alkyl complexes [Rh(L,L'-BID)(CH_3)(I)(CO)(PPh_3)] containing L,L'-BID ligands with L, L' donor atoms as indicated (see List of Abbreviations for different L,L'-BID; **Figure 2.19** illustrates the structures of the alkyl complexes).

L,L'-BID	L, L'	Rh-L distance / Å	Rh-L' distance / Å	Rh-P distance / Å	Me and I *cis* or *trans*	Rh-CH_3 distance / Å	Rh-I distance / Å	L-Rh-L' angle / °	Space group
ox[103]	O, N	2.036 2.037	2.085 2.083	2.317 2.326	*trans*	2.104 2.111	2.085 2.083	81.6 80.8	$P\bar{1}$
Complex 4[104] a	O, P	2.079	2.318	2.418	*trans*	2.104	2.785	82.5	$P\,2_1/n$
dmavk[87]	O, N	2.042	2.035	2.356	*trans*	1.850	2.8489	89.5	$P\bar{1}$
cupf[105]	O, O	2.175	2.039	2.327	*cis*	2.082	2.708	74.9	$P\bar{1}$
fctfa[98]	O, O	2.075	2.158	2.32	*cis*	2.077	2.716	88.0	$P2_1/c$
Complex 5[106] b	O, N	2.039	2.223	2.334	*cis*	2.112	2.701	77.7	$P2_1/c$
neocupf[107]	O, O	2.074	2.128	2.307	*cis*	2.092	2.711	76.3	$P\bar{1}$

a $(PhCOCHPPh_2)^-$, see **Figure 2.19**
b $(OCO(C_9H_6N))^-$, see **Figure 2.19**

Type 1 - Me and I *trans*

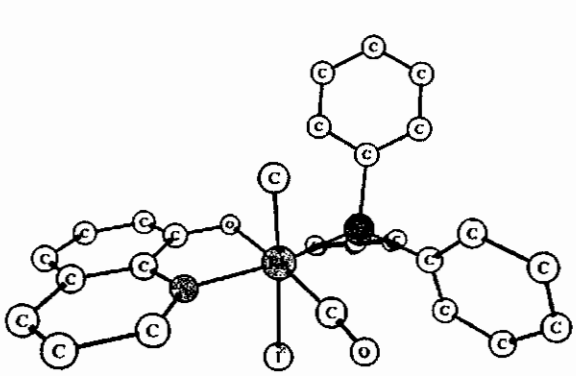

ox[103]

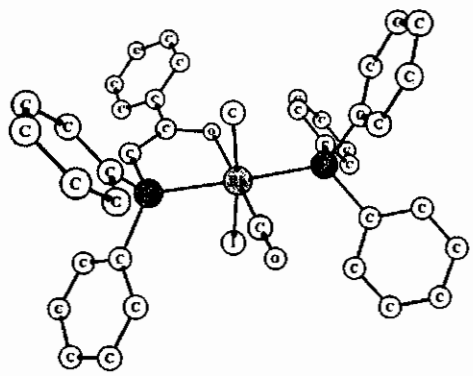

Complex 4[104]

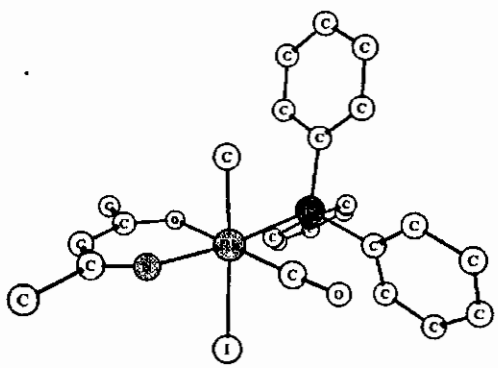

dmavk[87]

[103] K.G.van Aswegen, J.G. Leipoldt, I.M. Potgieter, G.J. Lamprecht, A. Roodt, G.J.van Zyl, Transition Met. Chem. 16 (1991) 369.

[104] P. Braunstein, Y. Chauvin, J. Fischer, H. Olivier, C. Strohmann, D.V. Toronto, New J. Chem. (Nouv. J. Chim.) 24 (2000) 437.

[105] S.S. Basson, J.G. Leipoldt, A. Roodt, J.A. Venter, Inorg. Chim. Acta 128 (1987) 31.

[106] M. Cano, J.V. Heras, M.A. Lobo, E. Pinilla, M.A. Monge, Polyhedron 11 (1992) 2679.

[107] S.S. Basson, J.A. Venter, A. Roodt, Manuscript in preparation.

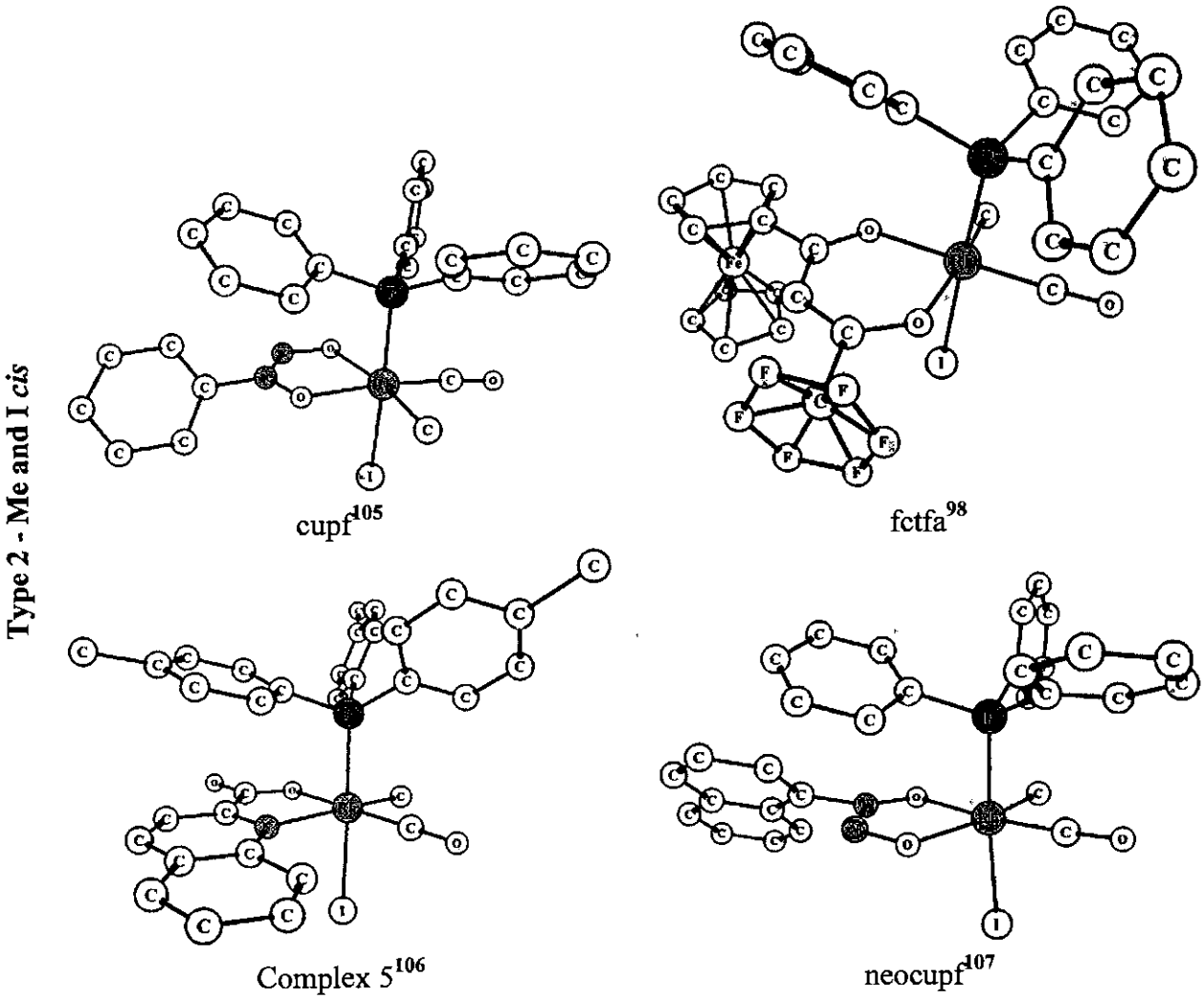

Figure 2.19: Structures of alkyl complexes [Rh(L,L'-BID)(CH_3)(I)(CO)(PPh_3)] where L,L'-BID is as indicated (hydrogens were removed for clarity).

Table 2.10: Selected geometrical data[80] for square pyramidal Rh(III) acyl complexes [Rh(L,L'-BID)($COCH_3$)(I)(PPh_3)] containing L,L'-BID ligands with L, L' donor atoms as indicated (see List of Abbreviations for different L,L'-BID; **Figure 2.20** illustrates the structures of the acyl complexes).

L,L'-BID	L, L'	Rh-L distance / Å	Rh-L' distance / Å	Rh-P distance / Å	PPh_3 *cis* or *trans* to L	Rh-C distance / Å	L-Rh-L' angle / °	Space group
Complex 6[108 a]	S, S	2.441	2.366	2.290	*trans*	1.956	82.5	$P2_1/c$
mnt[109]	S, S	2.323	2.269	2.324	*trans*	2.005	88.5	$P2_1/a$
dmavk[110]	O, N	2.054	2.031	2.254	*cis*	1.943	87.4	$P2_1/c$
stsc[111]	S, N	2.151	2.284	2.341	*cis*	1.992	81.4	$P2_1/c$

a $(PhCOCHPPh_2)^-$, see **Figure 2.20**

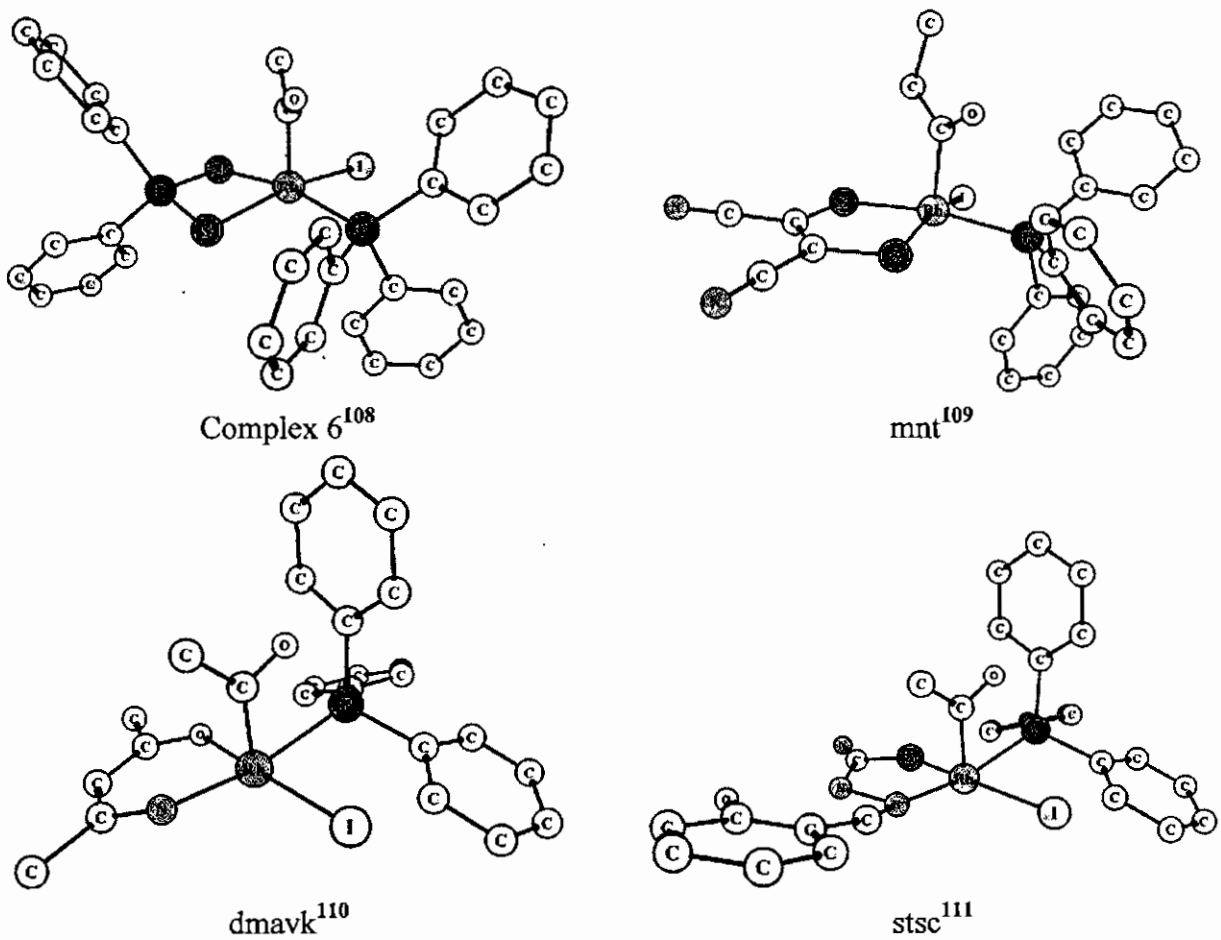

Figure 2.20: Structures of acyl complexes [Rh(L,L'-BID)($COCH_3$)(I)(PPh_3)] where L,L'-BID is as indicated (hydrogens were removed for clarity).

---

[108] J.A. Cabeza, V. Riera, M.A. Villa-Garcia, L. Ouahab, S. Triki, J. Organomet. Chem. 441 (1992) 323.

[109] C.H. Cheng, B.D. Spivack, R. Eisenberg, J. Am. Chem. Soc. 99 (1977) 3003.

[110] L.J. Damoense, W. Purcell, A. Roodt, Rhodium Ex. 14 (1995) 4.

[111] G.J.J. Steyn, Mechanistic study of Nitrogen/Sulphur Donor Atom Bidentate Ligand Influence on the Iodomethane Oxidative Addition to Carbonylphosphinerhodium(I) Complexes, Ph.D. Thesis, University of the Free State, South Africa., 1994.

According to the stereochemistry of the alkyl complexes (**Table 2.9** and **Figure 2.19**), they can be divided into two classes:

Type 1: Where the methyl and the iodide are above and below the square planar plane.

Type 2: Where the PPh_3 and the iodide are above and below the square planar plane.

In the acyl complexes (**Table 2.10** and **Figure 2.20**), the acyl moiety is in the apical position in all the crystal structures.

No general trends were found in the bond lengths and angles of the alkyl and acyl complexes.

The two classes of the Rh(III) alkyl complexes lead to some speculation as to the initial addition of the MeI molecule during the oxidative addition to the square planar Rh(I) complex. Does the same type always form during oxidative addition and does isomerization take place from the one type to the other? In this thesis, this question will be exploited by combining kinetic, spectrophotometric, spectroscopic and computational methods.

2.4 Oxidative addition and insertion (migration) reactions.

2.4.1 Oxidative addition.

2.4.1.1 Introduction.

The process oxidative addition in transition metal chemistry is used to describe the addition of neutral molecules (X-Y) to transition metal complexes having no more than 16 valence electrons.[112] Oxidative addition can be represented by **Scheme 2.17** below where the forward reaction is oxidative addition and the reverse reaction is reductive elimination.

---

[112] F. Mathey, A. Sevin, Molecular Chemistry of the Transition Elements, John Wiley & Sons, Chichester, 1996, pp. 28-50.

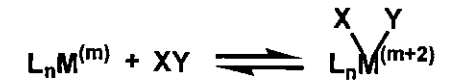

Scheme 2.17: Oxidative addition of the neutral molecule XY to the transition metal complex $L_nM^{(m)}$ with n = number of ligands (L) bonded to the metal (M) and m = the oxidation state of M before oxidative addition.

These terms merely describe a reaction and have no mechanistic implications. The mechanisms can be extremely complicated and vary with the nature of the metal-ligand system and the molecule that is oxidatively added.

For an oxidative addition reaction to proceed, there must be:[113]

a. nonbonding electron density on the metal,
b. two vacant coordination sites on the complex L_nM to allow the formation of two new bonds to X and Y and
c. the oxidation state of the central metal atom has to be two units lower than the most stable oxidation state of the metal.

Whether the equilibrium in **Scheme 2.17** lies on the reduced-metal or the oxidized-metal side, depends very critically on:

a. the nature of the metal,
b. the nature of the ligands L in the complex,
c. the nature of the added molecule XY and of the bonds M-X and M-Y so formed and
d. the medium in which the reaction is conducted.

For transition metals, the most common oxidative addition reactions involve complexes of the metals with d^8 and d^{10} electron configurations, for example Rh(I), Ir(I) and Pt(II). In general, the oxidative addition to unsaturated square planar, 16 electron, d^8 complexes gives saturated six-coordinate, 18 electron, d^6 complexes (**Scheme 2.18** (a)). Coordinatively saturated five-coordinate, 18 electron, d^8 complexes must loose one of the original ligands in the oxidative addition of two new ligands to give a saturated six-coordinate, 18 electron, d^6 complex as the final product (**Scheme 2.18** (b)).[114] Coordinatively saturated d^8 compounds are typically less

---

[113] F.A. Cotton, G. Wilkinson, P.L. Gaus, Basic Inroganic Chemistry, Third edition, John Wiley & Sons, New York, 1995, pp. 704-708.

[114] K.F. Purcell, J.C. Kotz, Inorganic Chemistry, W.B. Saunders Company, Philadelphia, 1977, pp. 938-948.

reactive and usually add only the stronger oxidizing addenda XY.[115] Frequently d^{10} complexes are coordinatively unsaturated, being only three or four-coordinate, so addition occurs readily (example in **Scheme 2.18** (c)).[116,117]

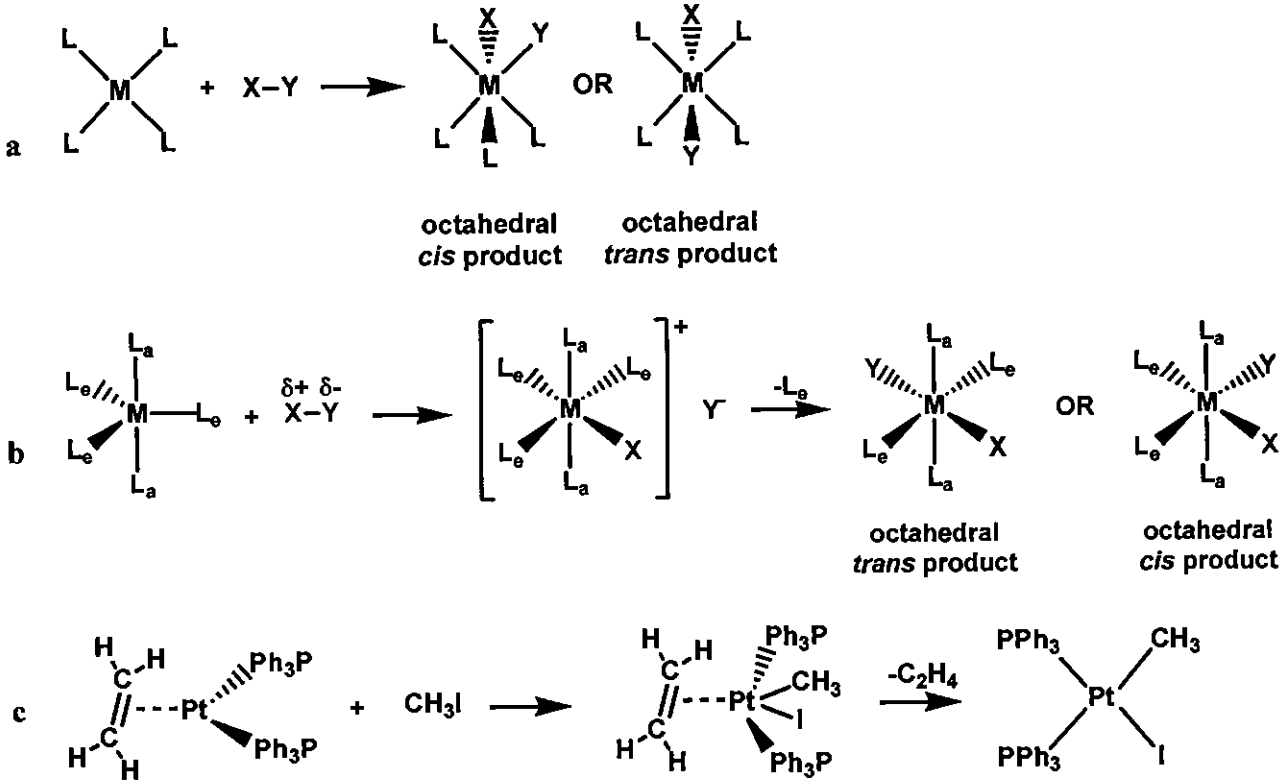

Scheme 2.18: Oxidative addition to d^8 and d^{10} complexes. **(a)** Oxidative addition to unsaturated square planar d^8 complex ML_4 with metal M and ligands L. **(b)** Oxidative addition to saturated trigonal bipyramidal d^8 complex (L_a = an axial ligand, L_e = an equatorial ligand).[114] **(c)** Oxidative addition to coordinatively unsaturated d^{10} complex.[116]

The final product of an oxidative addition reaction will be the isomer or mixture of isomers that is thermodynamically the most stable under the reaction conditions. The nature of the ligands, solvent, temperature, pressure, and the like, will have a decisive influence on this. The mechanism of oxidative addition determines the initial oxidative addition product. The nature of the final product, however, does not necessarily give a guide to the initial product or the mechanism of the addition, since isomerization of the initial product may occur.

---

115 J.P. Collman, L.S. Hegedus, Principles and Applications of Organotransition Metal Chemistry, University Science Books, Mill Valley, California, 1980, pp. 176-258.

116 J.P. Birk, J. Halpern, A.L. Pichard, J. Am. Chem. Soc. 90 (1968) 4491.

117 R. Ugo, Coord. Chem. Rev. 3 (1968) 319.

2.4.1.2 Mechanism of oxidative addition reactions.

Although it is still widely speculated what the intimate mechanism of oxidative addition is, two general types can be defined, that of one- and two-electron oxidative addition.[115,118] These two types differ from one another due to the fact that the intermediate of the one-electron mechanism is paramagnetic and the two-electron mechanism involves a paired electron process.[119,118] The one-electron mechanism can be described as a free-radical mechanism while the two-electron mechanism is dependent on the polarity of the proposed transition state and can be divided into three subcategories. These main mechanisms are listed below:[112,113,119,120]

a. the free-radical mechanism,

b.i. the three-centred concerted mechanism,

b.ii. the S_N2 mechanism and

b.iii. the ionic mechanism.

Pearson[121] has pointed out that reactions proceeding with reasonable low activation energies involve an electron flow between orbitals with the same symmetry properties. For oxidative addition, electrons must flow from a filled metal orbital into an anti-bonding X-Y orbital. This allows the X-Y bond to be broken and new bonds to the metal to be formed. The X-Y anti-bonding orbital must overlap in phase with a filled metal orbital, as illustrated in **Figure 2.21**.

---

[118] J.K. Kochi, Organometallic Mechanism and Catalysis, Academic Press, London (1978).

[119] R.J. Cross, Chem. Soc. Rev. 14 (1985) 197.

[120] R.S. Dickson, Organometallic Chemistry of Rhodium and Iridium, Academic Press, London, 1983, pp. 70-79.

[121] R.G. Pearson, Symmetry Rules for Chemical Reactions, Wiley, New York, 1976, pp. 405-413.

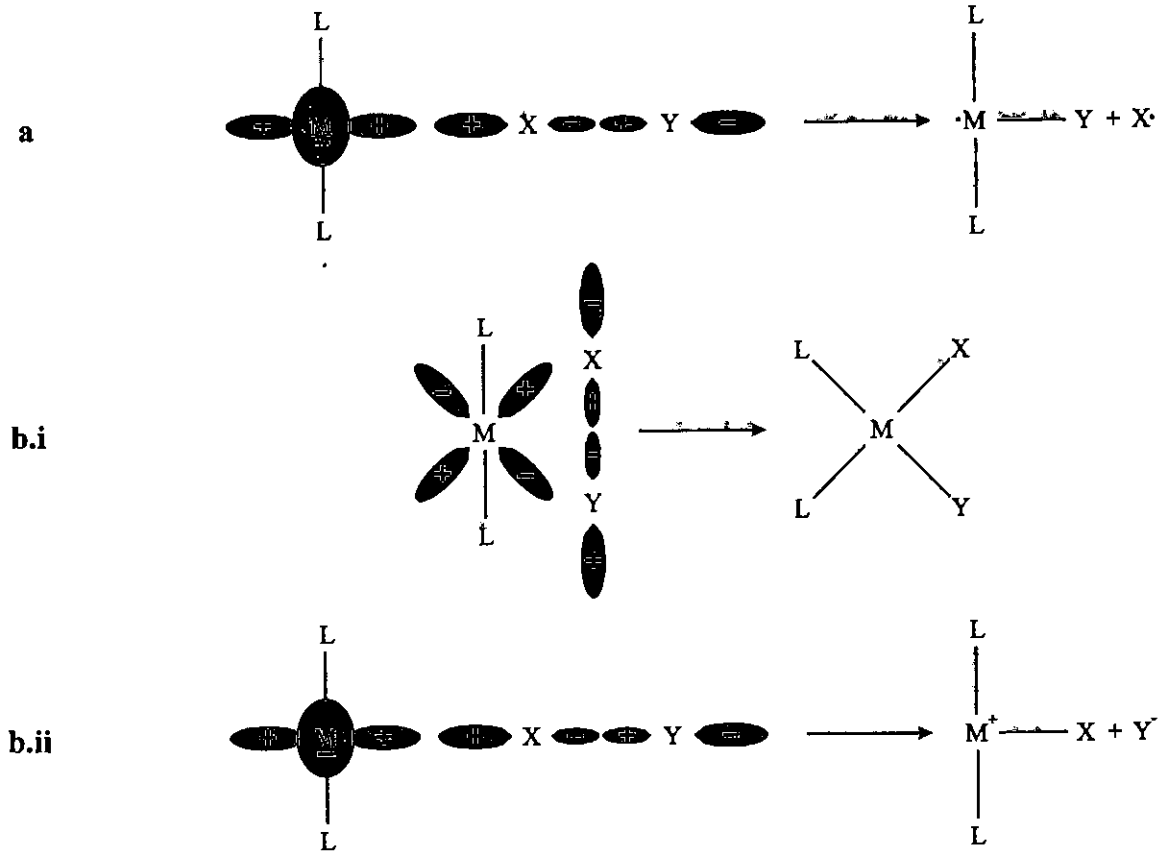

Figure 2.21: Symmetry-allowed overlap of orbitals for electron transfer in oxidative addition to 16 electron ML_4 complexes. Two ligands are above and below the plane of the page. **(a)** The free-radical mechanism. **(b.i.)** The three-centred concerted mechanism. **(b.ii.)** the S_N2 mechanism.

a. The free-radical mechanism.

Free-radical mechanisms are generally observed when the participating complex is a strong reducing agent and are favoured by increasing stability of the radical $[L_nM\text{-}X]^{\cdot}$ (see **Scheme 2.19**). In certain cases, radical-chain processes are observed. They are often initiated by O_2 or peroxides and can be blocked by inhibitors such as bulky phenols.[112]

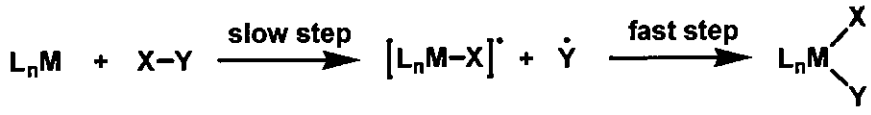

Scheme 2.19: The free-radical mechanism for oxidative addition.

Free-radical mechanisms are found for organic bromides and iodides reacting with Ir(I) and Pt(0) complexes.[122,123] Rh and Pd are less likely to give free-radical reactions.[124] Evidence shows that

---

[122] J.A. Labinger, A.V. Kramer, J.A. Osborn, J. Am. Chem. Soc. 95 (1973) 7908.

[123] M.F. Lappert, P.W. Ledner, J. Chem. Soc., Chem. Commun. (1973) 948.

trans addition products and racemates of optically active alkyl groups form. Although the *trans* products are most probable, rearrangements lead to *cis* products and therefore cannot be ruled out. Nonpolar solvents (or the absence of solvents) favour a free-radical mechanism.[121]

b.i. The three-centred concerted mechanism.

The three-centred concerted mechanism follows the scheme as illustrated in **Scheme 2.20.**[112]

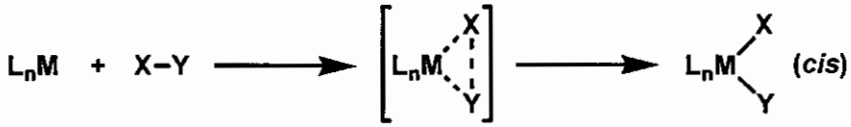

Scheme 2.20: The three-centred concerted mechanism for oxidative addition.

Here, filled d_{xz} and d_{xy} orbitals on the metal interact with antibonding orbitals of the substrate X-Y to produce a cyclic transition state (**Scheme 2.18 (b.i)**). The product formed by this route will have a *cis*-arrangement. As would be expected for a concerted process, the kinetics are second order.[120] As with the free-radical mechanism, nonpolar solvents (or the absence of solvents) favour a three-centred concerted mechanism.

b.ii. The S_N2 mechanism.

In the S_n2 mechanism the metal complex plays the role of a nucleophile to produce a polar intermediate as illustrated in **Scheme 2.21.**

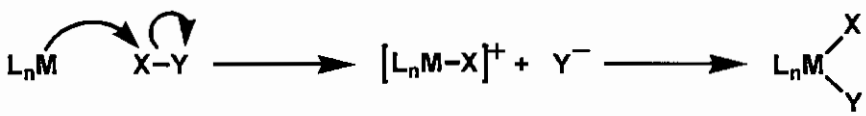

Scheme 2.21: The S_N2 mechanism for oxidative addition.

As in the three-centred concerted mechanism, the kinetics are second order and the entropy, ΔS, is negative. However, unlike the three-centred concerted mechanism, the product can have either

---

[124] J.K. Stille, R.W. Fries, J. Am. Chem. Soc. 96 (1974) 1514.

cis or *trans* geometry and the reaction is accelerated by polar solvents.[112] The S_N2 mechanism seems particularly appropriate to oxidative addition reactions with alkyl and acyl halides.[120]

b.iii. The ionic mechanism.

Ionic mechanisms generally require the presence of a strongly dissociated protic acid H-X as a reagent. This means that a polar solvent is necessary. Two cases have been recognized as illustrated in **Scheme 2.22.**

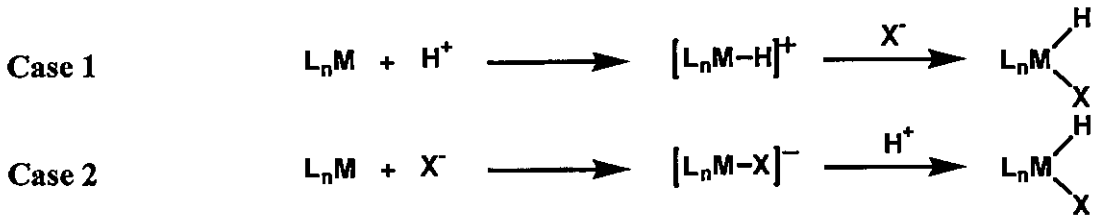

Scheme 2.22: The two variants of the ionic mechanism.

In the more common one (Case 1 in **Scheme 2.22**), the complex is sufficiently basic to protonate, after which the anion bonds to give the final product. The opposite case, in which the halide ion attacks first, followed by protonation of the intermediate, is rare. The first route is favoured by basic ligands and a low oxidation state, the second by electron acceptor ligands and by a positive charge on the metal.[112]

2.4.2 Carbonyl (CO) insertion and methyl (Me) migration.

2.4.2.1 Introduction.

An insertion reaction can be defined as the incorporation of an unsaturated two-electron ligand (A=B) into an M-X σ bond (X being a one-electron ligand) of a transition metal complex L_nM-X. Of the various classifications of insertion reactions two are considered here:

(i) Insertion types (1,1) and (1,2) etc. depending on how the addition between M and X to A=B takes place. Each proceeds through two distinct steps. The first involves incorporating A=B as a ligand within the metal coordination sphere. (L_nM-X must have no more than 16

electrons because the reaction requires a vacant coordination site.) The second step, often called migratory-insertion, incorporates A=B into the M-X bond.[112] See **Scheme 2.23.**

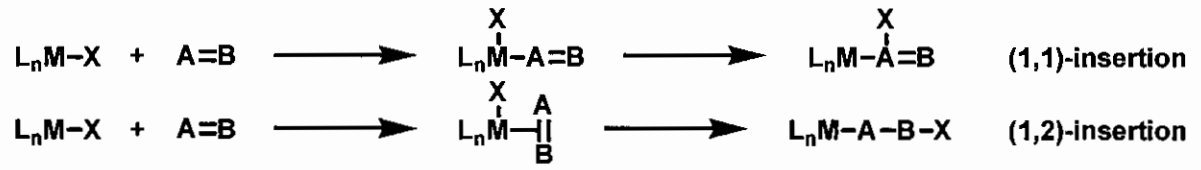

Scheme 2.23: (1,1) and (1,2) insertion reactions of an unsaturated two-electron ligand (A=B) into a M-X σ bond (X being a one-electron ligand).

In both the (1,1)- and (1,2)-insertion reactions the metal oxidation state remains unchanged. The migration of X to A=B (or A=B to X) requires that these ligands adopt a *cis* geometry within the metal sphere. During the migratory-insertion, the number of electrons and the metal coordination number decrease by two units and one unit respectively. The addition of a two-electron ligand is often required to stabilize the complex that is produced. Carbon monoxide CO is the ligand that most commonly undergoes (1,1) insertions. Alkenes and alkynes invariably give (1,2) insertions.

(ii) The insertion processes can also be classified as intramolecular "migratory insertions" or as intermolecular "nucleophilic additions". The intramolecular "migratory insertions" take place by the combination of X and A=B while both are coordinated to the metal[125] (the second step of both insertion reactions of **Scheme 2.23**). See **Scheme 2.24** for examples of intra-[126] and intermolecular[127] insertion reactions. The reaction $MeMn(CO)_5 + {}^{13}CO \rightarrow MeCOMn(CO)_4({}^{13}CO)$ is considered as an intramolecular "migratory insertion" since the carbonyl insertion took place at a CO group already coordinated to $MeMn(CO)_5$, and not at the ^{13}CO group.

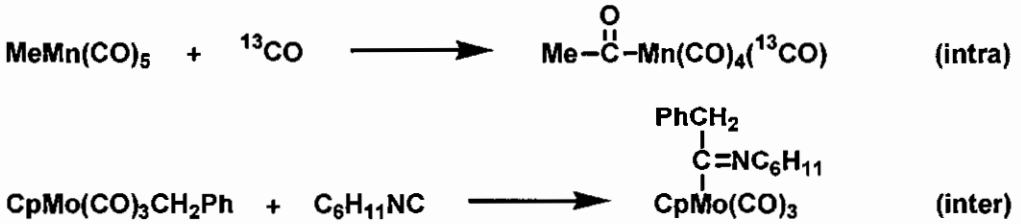

Scheme 2.24: Example of an intra- and an intermolecular insertion reaction.

---

[125] J.P. Collman, L.S. Hegedus, Principles and Applications of Organotransition Metal Chemistry, University Science Books, Mill Valley, California, 1980, p 259-298.

[126] K. Noack, F. Calderazzo, J. Organomet. Chem. 10 (1967) 10.

[127] Y. Yamamato, H. Yamazaki, J. Organomet. Chem. 10 (1967) 10.

2.4.2.2 Mechanism of insertion of CO.

Generally speaking, a carbonyl insertion reaction is regarded as known when any one of the following stoichiometric reactions has been fully characterized:[128]

a. R-M + CO → RCO-M — CO insertion into the metal-carbon σ-bond of a metal complex which may or may not contain carbonyl groups.

b. R-M(CO) → RCO-M — Conversion of a coordinated CO group into an acyl (or aroyl) group.

c. R-M(CO) + L → RCO-M(L) — CO insertion into a metal carbonyl complex promoted by a Lewis base L.

(L = two-electron ligand, R is an alkyl or related σ-bonded group.)

Carbonyl insertion reactions for square planar complexes may be represented as in **Scheme 2.25**, where [MR(CO)] is a reactant or an intermediate, R is an alkyl or related σ-bonded group and L stands for any ligand including CO and M represents a metal together with its ancillary ligands.

Scheme 2.25: Carbonyl (CO) insertion reactions for square planar complexes.

The insertion reaction is best considered as an intramolecular alkyl migration to a coordinated carbon monoxide ligand in a *cis*-position, and the migration probably proceeds through a three-centred transition state[129] as illustrated in **Scheme 2.26**.

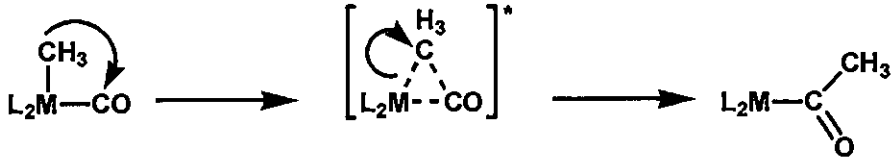

Scheme 2.26: Three-centred transition state proposed for carbonyl insertion reaction.

---

[128] F. Calderazzo, Angew. Chem. Int. Ed. Engl. 16 (1977) 299.

[129] F.A. Cotton, G. Wilkinson, C.A. Murillo, M. Bochmann, Advanced Inorganic Chemistry, Sixth edition, John Wiley & Sons, New York, 1999, pp. 1208-1212.

2.4.3 Addition of iodomethane (MeI) to Rh(I) complexes.

In this paragraph, selected examples of MeI addition to Rh(I) complexes will be discussed.

2.4.3.1 Example 1:[130] [Rh^{I}(tridentate ligand)(CO)(PMe$_3$)].

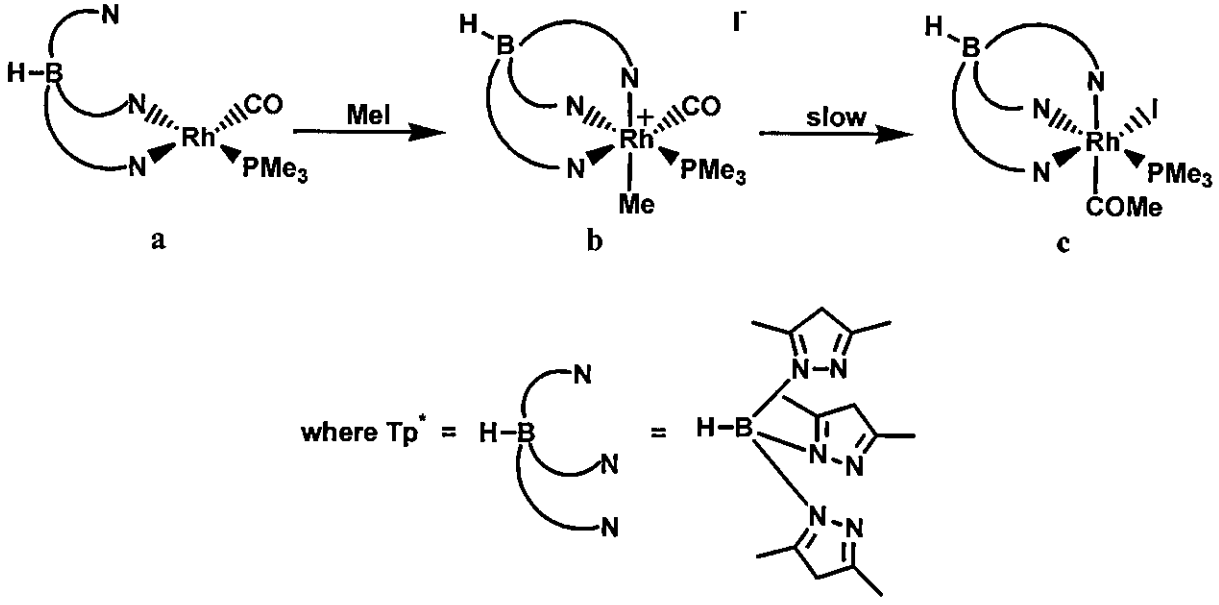

Scheme 2.27: Mechanism of MeI addition to [κ^2-Tp*Rh(CO)(PMe$_3$)] (where Tp* = HB(3,5-Me$_2$pz)$_3$).

The reaction of MeI with the square planar [κ^2-Tp*Rh(CO)(PMe$_3$)] (where Tp* = HB(3,5-Me$_2$pz)$_3$), as studied by Chauby *et al.*,[130] is illustrated in **Scheme 2.27**. The reaction products **b** and **c** have been fully characterized by spectroscopy and X-ray crystallography. The pseudooctahedral geometry of the cationic species **b** (**Scheme 2.27**), which contains a κ^3-coordinated Tp* ligand, indicates a reaction mechanism in which a nucleophilic attack of Rh on MeI is accompanied by coordination of the pendant pyrazolyl group. In solution, **b** transforms slowly into a neutral acetyl Rh complex [κ^3-Tp*Rh(PMe$_3$)(COMe)I] as illustrated by **c** (**Scheme 2.27**). Kinetic studies on the reactions of [κ^2-Tp*Rh(CO)(L)] (where L = PMe$_3$, PMe$_2$Ph, PMePh$_2$, PPh$_3$, CO) with MeI showed a second-order behaviour with large negative activation entropies (ΔS^*), which are consistent with an S_N2 mechanism. The second-order rate constants correlate well with phosphine basicity. For L = CO, the reaction with MeI gives an acetyl complex, [κ^3-Tp*Rh(CO)(COMe)I]. The bis(pyrazolyl)borate complexes [κ^2-Bp*Rh(CO)(L)] (where L = PPh$_3$, CO) (**Scheme 2.28**) are much less reactive toward MeI than

---

[130] V. Chauby, J. Daran, C.S. Berre, F. Malbosc, P. Kalck, O.D. Gonzalez, C.E. Haslam, A. Haynes, Inorg. Chem. 41 (2002) 3280.

the Tp^* analogues, indicating the importance of the third pyrazolyl group and the accessibility of a κ^3 coordination mode. The results strengthen the evidence in favour of an S_N2 mechanism for oxidative addition of MeI to square planar d^8 transition metal complexes.

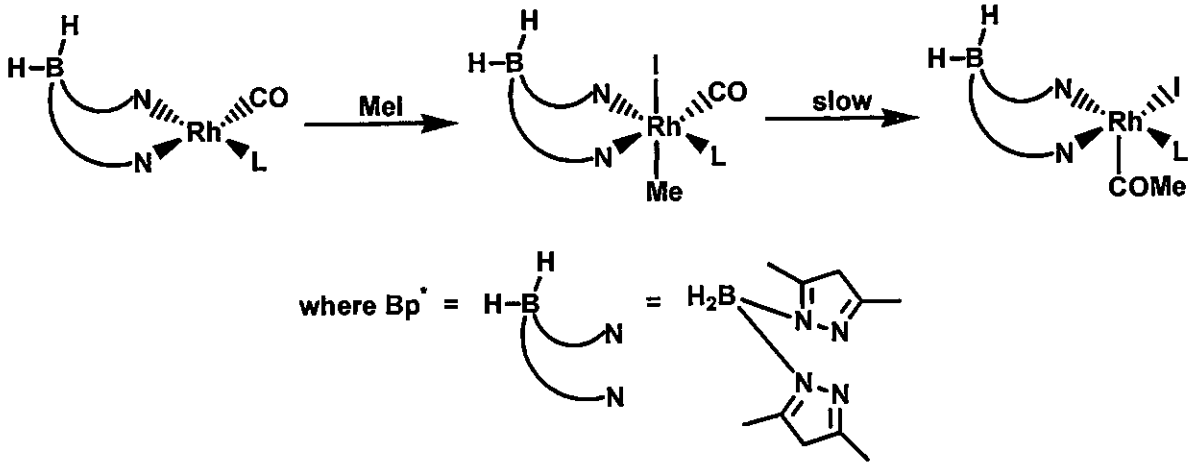

Scheme 2.28: Mechanism of MeI addition to [κ^2-Bp*Rh(CO)(L)] (where Bp* = bis(pyrazolyl)borate and L = PPh_3, CO).

2.4.3.2 Example 2:[131] [Rh^I(P-S-bidentate ligand)(CO)(I)].

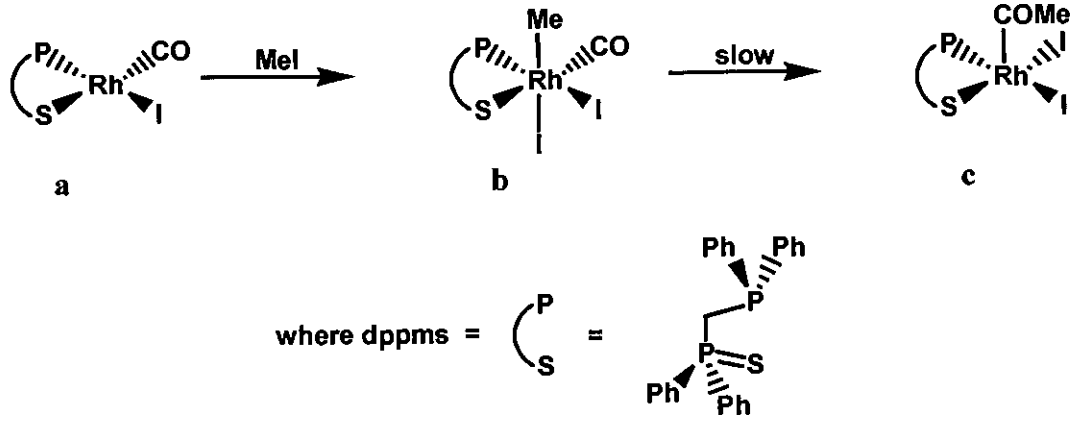

Scheme 2.29: Mechanism of MeI addition to [Rh(CO)I(dppms)].

The reaction of MeI with the square planar [Rh(CO)I(dppms)], as studied by Gonsalvi *et al.*,[131] is illustrated in **Scheme 2.29**. The stoichiometric reaction of **a** (**Scheme 2.29**) with MeI yields a stable acyl product **c** via a presumed alkyl intermediate **b**. The reaction, monitored by IR spectrophotometry (**Figure 2.22**), is first order in both **a** and MeI. The activation parameters are typical for MeI addition. The large negative activation entropies (ΔS^*) reflect a highly ordered S_N2 transition state. The Rh acetyl complex **c** was crystallographically characterized. The

[131] L. Gonsalvi, H. Adams, G.J. Sunley, E. Ditzel, A. Haynes, J. Am. Chem. Soc. 121 (1999) 11233.

electronic and steric effects of the groups on the ddpms ligand combine to give surprising and dramatic effects on the rates of the key steps in the reaction. The dppms ligand is able to promote both oxidative addition and migratory insertion steps, an unusual occurrence. The strong donor ligands (phosphines) accelerate the rate determining oxidative addition of MeI to Rh(I) and hence promote catalysis. The strong electron donation, would normally be expected to inhibit the CO insertion, but this is overcome by a steric effect of the dppms ligand.

The migratory insertion in the alkyl species **b** (**Scheme 2.29**) is so fast, that the intermediate was not previously detected.[132] Gonsalvi *et al.*[131] have obtained spectroscopic evidence for **b**. A series of IR spectra obtained during the reaction are shown in **Figure 2.22**. The strong carbonyl stretching frequencies (ν_{CO}) represent the appearance and disappearance of **c** and **a** respectively. A very weak absorption is observed at a higher frequency (2062 cm^{-1}) which is exactly in the region expected for **b**. This band decays in direct proportion to that of **a** as predicted by the steady-state approximation.

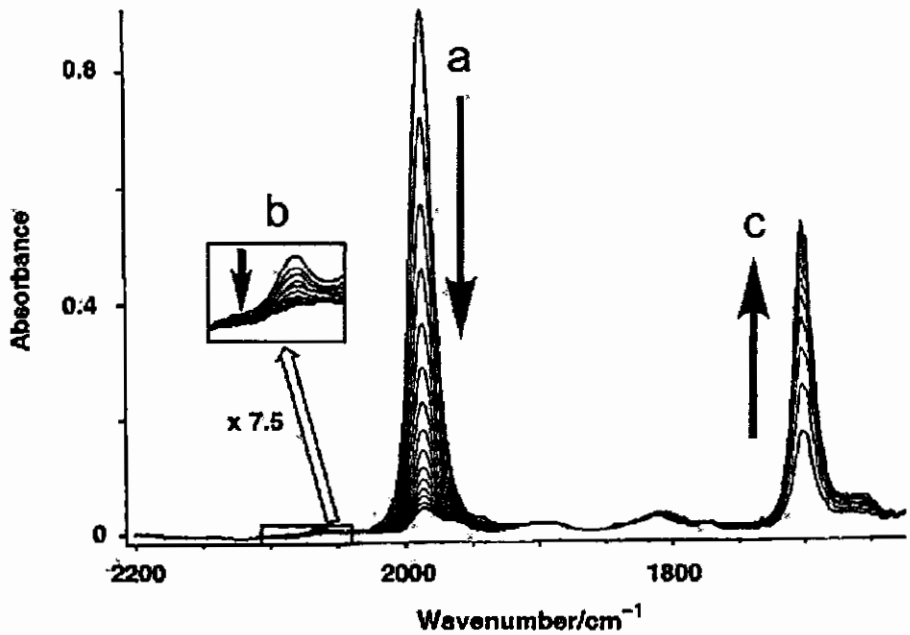

Figure 2.22: Series of IR spectra of the reaction of [Rh(CO)I(dppms)] with MeI of 8 M in CH_2Cl_2, 10 °C. (Figure is adopted from reference **131**.)

[132] M.J. Baker, M.F. Giles, A.G. Orpen, M.J. Watt, J. Chem. Soc., Chem. Commun. (1995) 197.

2.4.3.3 Example 3:[133] $[Rh^{I}(acac)(CO)(PX_3)]$.

$$[Rh(acac)(CO)(PX_3)] + CH_3I$$
a

$$k_{-1} \rightleftharpoons k_1$$
$$[Rh(acac)(CO)(PX_3)(CH_3)]^+I^-$$
b

$$k_{-2} \rightleftharpoons k_2$$
$$[Rh(acac)(COCH_3)(I)(PX_3)]$$
c

$$k_{-3} \rightleftharpoons k_3$$
$$[Rh(acac)(CO)(CH_3)(I)(PX_3)]$$
d

Rh(I) disappearance:
$k_{obs} = k_1 [MeI] + k_{-1}$

Rh(III) alkyl disappearance:
$k_{obs} = (k_2 K_1 [MeI]) / (1 + K_1 [MeI])$

Scheme 2.30: Proposed mechanism of MeI addition to $[Rh(acac)(CO)(PX_3)]$ (where PX_3 = *p*-PhCl, *p*-PhOMe, Ph).

The reaction of MeI with the square planar $[Rh(acac)(CO)(PX_3)]$ (where PX_3 = *p*-PhCl, *p*-PhOMe, Ph), as studied by Basson *et al.*,[133] is illustrated in **Scheme 2.30**. These reactions were followed on the IR and UV/vis spectrophotometry in 1,2-dichloroethane. The equilibrium and rate constants decrease with the phosphine basicity: $P(p\text{-}POMe)_3 > PPh_3 > P(p\text{-}PhCl)_3$. Repeated IR time scans showed that for the duration of the induction period, the first equilibrium involves a near complete disappearance of the Rh(I)-CO peak and the simultaneous appearance of a Rh(III)-CO peak ascribable to that of the ionic intermediate **b** (**Scheme 2.30**). The acyl peaks, ascribable to **c**, formed at nearly the same (for X = *p*-PhCl) or at progressively slower rates (for the more basic phosphines) compared to that of the corresponding Rh(III)-CO peaks of **b**. When **b** started to disappear, the acyl peaks of **c** were still increasing to a near maximum absorbance value. The time required for the latter process coincided with the absorbance increase immediately following the induction period of the visible spectra. The final and much slower disappearance of the acyl peak **c** led to the formation of a second Rh(III)-CO peak to the order of 12 cm^{-1} lower than **b**. This peak formation corresponds to the final oxidative addition product, **d**. The IR carbonyl wavenumbers and rate constants for the reaction are tabulated in **Table 2.11**.

[133]. S.S. Basson, J.G. Leipoldt, A. Roodt, J.A. Venter, T.J. van der Walt, Inorg. Chim. Acta 119 (1986) 35.

Table 2.11: IR carbonyl wavenumbers and rate constants for oxidative addition of 0.5 M MeI to [Rh(acac)(CO)(PX_3)] complexes in dichloromethane (standard deviations in parentheses).

X	CO wavenumbers			k_{obs} x 10^3 / s^{-1} (disappearance of a)	k_2 x 10^3 / s^{-1} (disappearance of b)	k_3 x 10^3 / s^{-1} (disappearance of c)
	complex a	complex b	complex d			
p-PhCl	1982	2076	2064	2.41(0.06)	2.4(0.2)	1.41(0.04)
Ph	1978	2072	2060	12(1)	6.3(0.5)	4.3(0.1)
p-PhOMe	1974	2068	2056	36(2)	9.2(1.7)	4.0(0.2)

2.4.3.4 Example 4:[134] [Rh^I(bidentate ligand)($P(OPh)_3)_2$].

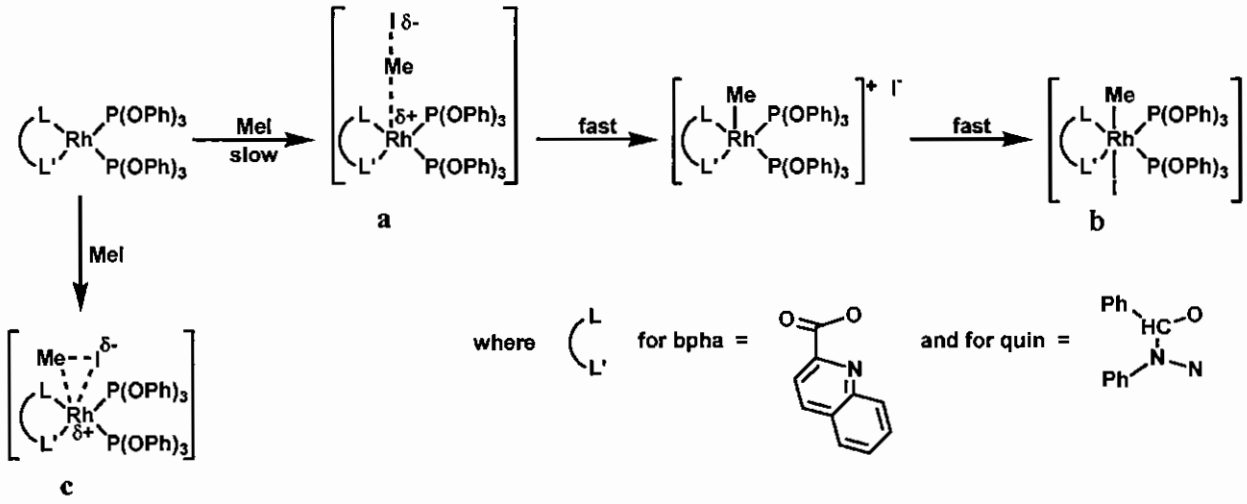

Scheme 2.31: Proposed mechanism of MeI addition to [Rh(bpha){$P(OPh)_3$}$_2$] and [Rh(quin){$P(OPh)_3$}$_2$].

The reaction of MeI with [Rh(bpha){$P(OPh)_3$}$_2$] and [Rh(quin){$P(OPh)_3$}$_2$] was studied by Lambrecht *et al.*[134]. The final oxidative addition product, [Rh(quin){$P(OPh)_3$}$_2$(CH_3)(I)] (**c**), was described with Me trans to the I.[135] Both oxidative addition reactions studied displayed simple kinetics and followed a well-defined second-order behaviour with large negative entropies (ΔS). Based on this study preformed by Lambrecht *et al.*[134] as well as other studies,[136,137,138,139] a mechanism for the reaction was proposed (**Scheme 2.31**). The proposed mechanism is a nucleophilic attack of the Rh(I) atom on the carbon atom of the MeI, where a polar linear transition state **a** is formed, which lead to *trans* addition as illustrated in **Scheme 2.31**. The polar

---

134 G.J. Lambrecht, J.H. Beetge, S. Afr. J. Chem. 40 (1987) 2.

135 G.J. van Zyl, Strukturele en Kinetiese Aspekte van die Oksidatiewe Addisie- en Substitusiereaksies van Rodium(I)-komplekse, Ph.D. Thesis, University of the Free State, South Africa., 1986, p. 74.

136 J.K. Stille, S.Y. Lau, Acc. Chem. Res. 10 (1977) 434.

137 W.H. Thomas, C.T. Sears, Inorg. Chem. 16 (1977) 769.

138 M. Kubota, D.M. Blake, S.A. Smith, Inorg. Chem. 10 (1971) 1430.

139 R. Ugo, A. Pasini. A. Fusie, S. Cenini, J. Am. Chem. Soc. 94 (1972) 7364.

transition state is stabilized by more polar solvents. The possibility of a polar three-centred transition state **c** cannot be ruled out. The latter transition state is however unlikely, since it normally leads to *cis* addition (**paragraph 2.4.1.2.b.i**) unless there is a fast consecutive isomerization process, and because the isomerization of *cis*-[Rh(β-diketonato){$P(OPh)_3$}$_2$(CH_3)(I)] to *trans*-[Rh(β-diketonato){$P(OPh)_3$}$_2$(CH_3) (I)] is a relatively slow reaction. They have also established that [Rh(quin){$P(OPh)_3$}(CO)] does not react with MeI.

2.4.3.5 Example 5:[140,141,142] [Rh^I(N,S-bidentate ligand)(CO)(PPh_3)].

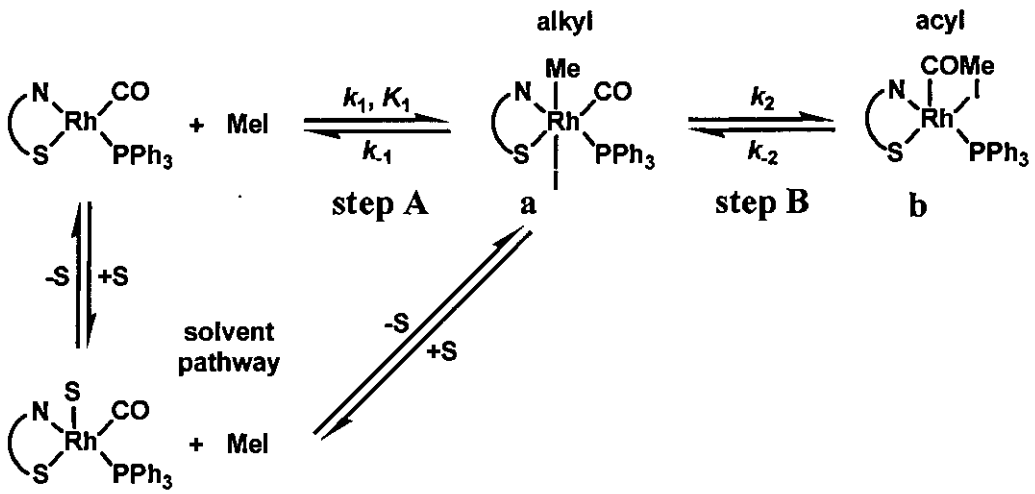

Scheme 2.32: Proposed mechanism of MeI addition to rhodium complexes of the type [Rh(N,S-BID)(CO)(PPh_3)].

Steyn *et al.*[140,141,142] have studied the oxidative addition reaction of MeI with rhodium complexes of the type [Rh(L,L'-BID)(CO)(PX_3)] (where L,L'-BID is a bidentate ligand). These papers focus on N,S-bidentate ligands and compare the results with precious studies that contain O,O; O,N or O,S L,L'-BID ligands. Examples of the N,S-types of complexes are macsm, hacsm, cacsm and stsc (**Figure 2. 23**).

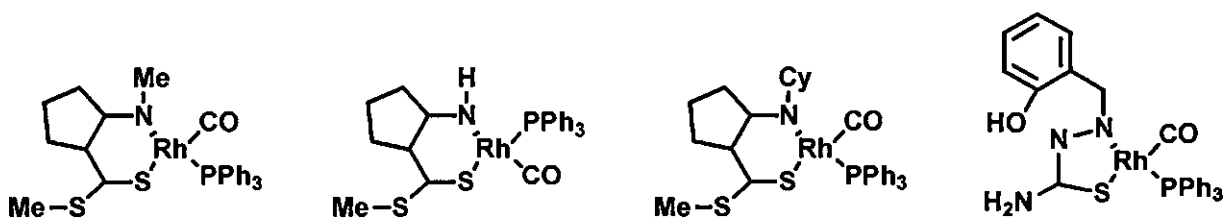

Figure 2. 23: Examples of N,S-bidentate ligands complexed to rhodium.

---

[140] A. Roodt, G.J.J. Steyn, Recent Res. Devel. Inorganic Chem. 2 (2000) 1.

[141] G.J.J. Steyn, A. Roodt, J.G. Leipoldt, Rhodium Express 1 (1993) 25.

[142] G.J.J. Steyn, A. Roodt, J.G. Leipoldt, Inorg. Chem. 31 (1992) 3477.

The general route for the oxidative addition of MeI to Rh(I) complexes of this type is presented in **Scheme 2.32**. In this reaction steps **A** and **B** are characterized firstly by the formation of an Rh(III) alkyl **a** as intermediate, followed by the disappearance thereof, coupled by the simultaneous formation of the Rh(III) acyl **b** species. These intermediate species have been characterized by IR[142] and X-ray crystallographic[143,144,145,146] investigations. The pseudo first-order rate constant for the formation of the intermediate alkyl species, which is dependent on the [MeI], is shown in **Equation 2.5**.

Equation 2.5: $k_{al} = k_1 [MeI] + k_{-1}$

Similarly, the pseudo first-order rate constant for the formation of the acyl species, which corresponds exactly to the disappearance of the alkyl species, is shown in **Equation 2.6**.

Equation 2.6: $k_{ac} = (k_2 K_1 [MeI]) / (1 + K_1 [MeI]) + k_{-2}$ with $K_1 = k_1 / k_{-1}$

No detectable solvent pathway or an equilibrium for the formation of the acyl species (negligible k_{-2} values) was observed for the complexes containing N,S-bidentate ligands.[140]

A important point worth noting is the fact that, under conditions where the Rh(III)-alkyl species are not present in significant amounts, first-order dependence on [MeI] will always be observed, with the second-order rate constant k_{ac}/[MeI] given by k_2K_1. This was observed in the oxidative addition[147,148] of iodomethane to [Rh(sacac)(CO)(PPh_3)] (sacac = thioacetylacetonato = $CH_3COCHCSCH_3$), but in this case it was assumed that the formation of the acyl species was rapid compared to that of the Rh(III)-alkyl species ($k_2 >> k_1$ in **Scheme 2.32**). However, the study in this example by Steyn *et al.*[142] suggests that the kinetics with the sacac system might be governed by small K_1 values, rather than k_2 being much larger than k_1.

To illustrate the first-order dependence on [MeI], a reaction of MeI with [Rh(macsm)(CO)(PPh_3)] in $CHCl_3$ at 25.0 °C was preformed with the MeI concentration

---

143 G.J.J. Steyn, A. Roodt, J.G. Leipoldt, Rhodium Express 0 (1993) 13.

144 K.G. van Aswegen, J.G. Leipoldt, I.M. Potgieter, G.J. Lambrecht, A. Roodt, G.J. van Zyl, Transition Met. Chem. 16 (1991) 369.

145 S.S. Basson, J.G. Leipoldt, A. Roodt, J.A. Venter, Inorg. Chim. Acta 128 (1987) 31.

146 C.H. Cheng, D.B. Spivack, R. Eisenberg, J. Am. Cem. Soc. 99 (1977) 3003.

147 J.G. Leipoldt, S.S. Basson, L.J. Botha, Inorg. Chim. Acta 168 (1990) 215.

148 J.A. Venter, J.G. Leipoldt, R. van Eldik, Inorg. Chem. 30 (1991) 2207.

respectively 1.0 M and 0.05 M. **Figure 2.24** illustrates the observed reaction progress in the 1650 – 2100 cm^{-1} range, as monitored by IR spectrophotometry. **Figure 2.24.a** shows that the disappearance of the Rh(I) complex (signal at 1965 cm^{-1}) in 1.0 M MeI basically corresponds to the formation of the alkyl species (rather strong peak at 2060 cm^{-1}) followed by the slow formation of the acyl species at 1715 cm^{-1} (which in turn corresponds to the disappearance of the 2060 cm^{-1} signal). On the other hand, **Figure 2.24.b** shows that at [MeI] = 0.05 M, the formation of the alkyl species is less pronounced and more slowly and the rate of disappearance of the Rh(I) complex in this case is the same as the formation rate of the acyl species. The observed rate of formation of the alkyl complex was, at higher MeI concentrations, generally found to be a little higher than the disappearance rate of the Rh(I) complex, since the formation of the acyl species (and subsequent disappearance of the alkyl complex) caused lower values of the absorbance at infinity (for alkyl formation). It is, however, clear that the disappearance of [Rh(macsm)(CO)(PPh_3)] is governed by the formation of the alkyl species and subsequently by that of the acyl complex and cannot be assigned to only one of the reactions over the concentration range 0.05 – 1.0 M MeI.

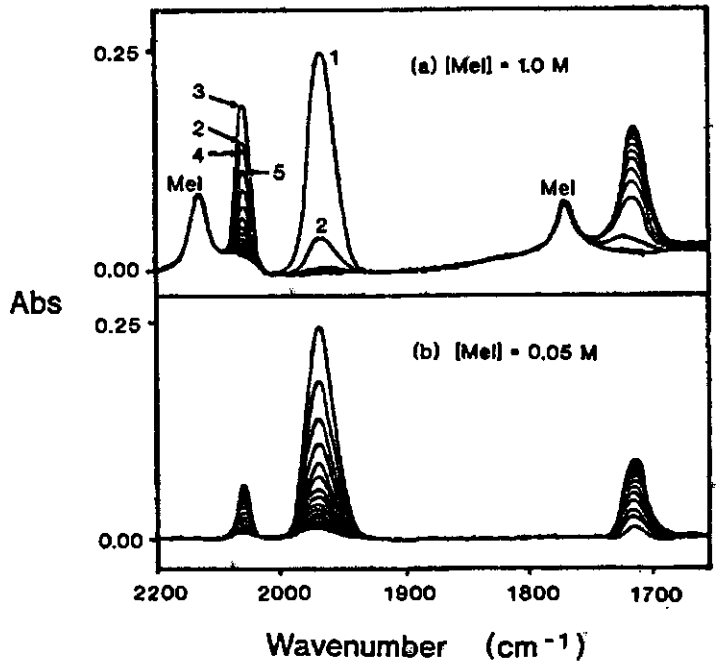

Figure 2.24: Repetitive IR scans (50 s intervals) for the oxidative addition reaction of MeI to [Rh(macsm)(CO)(PPh_3)] in $CHCl_3$ at 25.0 °C. $[Rh]_{tot.}$ = 7 x 10^{-3} M, for (a) [MeI] = 1.0 M and (b) [MeI] = 0.05 M. (Figure is adopted from reference **142**.)

The mechanism in **Scheme 2.32** is a general method for complexes of the kind [Rh(L,L'-BID)(CO)(PPh_3)] (where L,L'-BID is a bidentate ligand). This includes bidentate

ligands where L,L'-BID = β-diketonato. **Table 2.12** gives a summary of the rate and equilibrium data for the oxidative addition step in **Scheme 2.32** for selected complexes of the kind [Rh(L,L'-BID)(CO)(PPh_3)].

Table 2.12: Rate and equilibrium data of the oxidative addition steps in **Scheme 2.32** of MeI to [Rh(L,L'-BID)(CO)(PPh_3)] complexes in $CHCl_3$, 25 °C (see List of Abbreviations and **Figure 2. 23** for different bidentate ligands).

L,L'-BID	L	L'	$10^3 k_1$ / $M^{-1} s^{-1}$	$10^3 k_{-1}$ / s^{-1}	$10^3 k_2$ / s^{-1}
hfaa[149]	O	O	0.13(1)	0.05(1)	0.48(9)
cupf[133]	O	O	1.2(1)	<0.5	0.31(3)
acac[149]	O	O	24(4)	0.25(2)	6.5(5)
hacsm[141]	N	S	27(1)	~2	3(1)
ox[150] a	O	N	30(1)	0.5(1)	6(1)
sacac[147]	O	S	40(9)	9(3)	2.0(5)
anmeth[151]	O	S	24(3)	7.1(3)	9.7(2)
macsm[142]	N	S	34(1)	0.86(8)	7.6(4)
cacsm[140]	N	S	56(1)	1.9(6)	5(1)
dmavk[140]	O	N	114(2)	0.4(1)	2.0(1)
macsh[141]	N	S	380(10)	2.6(4)	7.2(2)

a In acetone

[149] S.S. Basson, J.G. Leipoldt, J.T. Nel, Inorg. Chim. Acta 84 (1984) 167.

[150] K.G. van Aswegen, Kinetiese en Strukturele Aspekte van die Oksidatiewe Addisiereaksies van Rhodium(I)-komplekse met Jodometaan, ,M.Sc. Thesis, University of the Free State, South Africa., 1990.

[151] H. Preston, Spesifieke Isomeervorming en Oksidatiewe Addisie Gedrag van Rodium(I)tiolato-komplekse, Ph.D. Thesis, University of the Free State, South Africa, 1993.

2.5 Computational chemistry.

Computational chemistry is a powerful tool in exploring and understanding experimental phenomena. Since this thesis is concerned with the oxidative addition of MeI to square planar Rh(I) complexes, representative examples exploring this topic, by means of computational chemistry, will be discussed in this paragraph.

2.5.1 Example 1: Theoretical and experimental evidence for S_N2 transition states (TS) in oxidative addition of iodomethane (MeI) to *cis*-$[M(CO)_2I_2]^-$ (where M = Rh, Ir).[152]

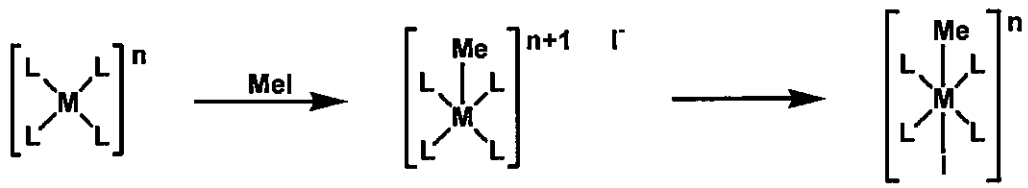

Scheme 2.33: Proposed stepwise mechanism for MeI addition to square planar complexes.

Griffin *et al.*[152] have studied the reaction of MeI with *cis*-$[M(CO)_2I_2]^-$ (where M = Rh, Ir) and presented new theoretical and experimental evidence for the nature of the transition state (TS). There has been considerable debate concerning the mechanism by which alkyl halides add to square planar complexes, namely a linear S_N2 mechanism or via a concerted *cis* addition.[153] The first step of the linear stepwise mechanism (see **Scheme 2.33**) is the nucleophilic replacement of the iodide with the metal complex, presumed to proceed with inversion of configuration at the carbon. Subsequent coordination of iodide completes the addition to give a six-coordinate alkyl complex. The concerted *cis* addition is expected to lead to the retention of the configuration at the carbon.[154]

---

[152] T.R. Griffin, D.B. Cook, A. Haynes, J.M. Pearson, D. Monti, G.E. Morris, J. Am. Chem. Soc. 118 (1996) 3029.

[153] S. Henderson, R.A. Henderson, Adv. Phys. Org. Chem. 23 (1987) 23.

[154] R.G. Pearson, W.R. Muir, J. Am. Chem. Soc. 92 (1970) 5519.

Optimized geometries, transition states and frequencies have been obtained at the restricted Hartree-Fock (RHF) level of theory using Gaussian 92.[155] The Los Alamos pesudopotentials and associated Gaussian bases[156] were used throughout with occasional enhancement.[157] The effect of the electron correlation on the reaction energetics was studied by performing single-point second-order Møller-Plesset (MP2) calculations on the RHF optimized structures. Computed kinetic isotope effects (KIEs)[158] (25 °C) correspond to the central barrier (i.e. transformation of the optimized reactant ion – dipole complex into the TS).

Griffin *et al.*[152] have located two different transition structures, each having a C_S symmetry, for a nucleophilic attack of *cis*-$[Rh(CO)_2I_2]^-$ on MeI. The first of these (**Figure 2.25.a**) is a "linear" TS, involving a classical backside attack by the transition metal nucleophile and leading to an inversion of the stereochemistry at the carbon. The second (**Figure 2.25.b**) is a considerably more "bent" TS which leads to a retention of the configuration at the carbon. The important geometrical parameters are tabulated in **Table 2.13**. Radical pathways were not considered, since experimental evidence indicated that single electron transfer processes are important only for higher alkyl substrates.[159,160]

---

[155] M.J. Frisch, G.W Trucks, H.B. Schlegel, P.M.W. Gill, B.G. Johnson, M.W. Wong, J.B. Foresman, M.A. Robb, M. Head-Gordon, E.S. Replogle, R. Gomperts, J.L. Andres, K. Raghavavhari, J.S. Binkley, C. Gonzalez, R.L. Martin, D.J. Fox, D.J. Defrees, J. Baker, J.J.P. Stewart, J.A. Pople, Gaussian 92/DFT, Gaussian Inc., Pitsburgh, PA, 1993.

[156] P.J. Hay, W.R. Wadt, J. Chem. Phys. 82 (1985) 270.

[157] T.R. Griffin, D.B. Cook, A. Haynes, J.M. Pearson, D. Monti, G.E. Morris, J. Am. Chem. Soc. 118 (1996) 3029, Supporting information.

[158] J. Bigeleisen, M.G. Mayer, J. Chem. Phys. 15 (1947) 261.

[159] J.A. Labinger, J.A. Osborn, Inorg. Chem 19 (1980) 3230.

[160] P.R. Ellis, J.M. Pearson, A. Haynes, H. Adams, N.A. Bailey, P.M. Maitlis, Organometallics 13 (1994) 3215.

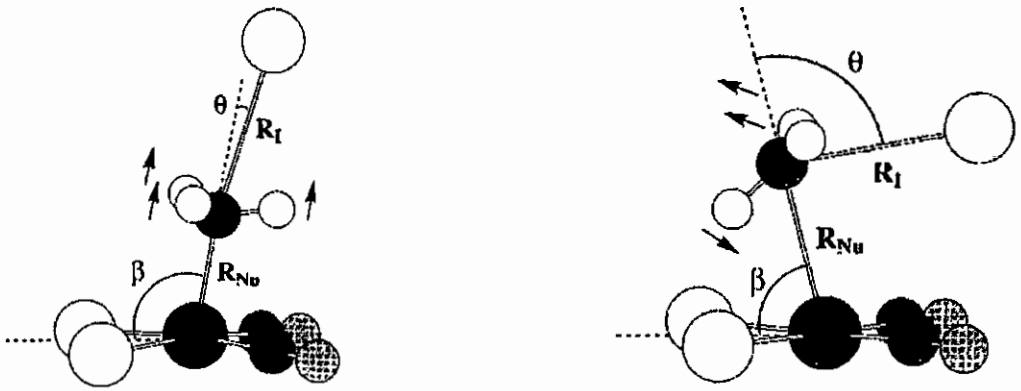

(a) "Linear" TS **(b)** "Bent" TS

Figure 2.25: Linear (**a**) and bent (**b**) transition states for a nucleophilic attack by *cis*-$[Rh(CO)_2I_2]^-$ on MeI. Geometrical parameters, R_{Nu}, R_I, θ, and β are listed in **Table 2.13**. The arrows indicate the C-H(D) bending modes of principal importance in determining the α-D KIEs. (Figure is adopted from reference **152**.)

Table 2.13: Optimized geometrical parameters for transition states (TS) in reactions of *cis*-$[M(CO)_2I_2]^-$ and I^- with MeI (where M = Rh, Ir).

nucleophile	R_{Nu} / Å	R_I / Å	θ / deg	β / deg
"Linear" TS				
$[Rh(CO)_2I_2]^-$	2.190	3.202	9.7	99.2
$[Ir(CO)_2I_2]^-$	2.430	2.939	2.6	94.3
I^-	2.788	2.788	0	
"Bent" TS				
$[Rh(CO)_2I_2]^-$	2.801	3.195	94.7	84.6

Theoretical results indicated that the linear TS for the nucleophilic attack by *cis*-$[M(CO)_2I_2]^-$ on MeI, with an inversion configuration at the carbon, is energetically preferred and gives computed kinetic isotope effects (KIEs) in excellent agreement with experimental data for both the Rh and Ir complexes.

Kinnunen[161,162,163] used a B3LYP DFT method and characterized the same S_N2-like TS found by Griffin. Feliz *et al.*[164] recently studied the oxidative addition of methyl iodide to Rh complexes, computationally by means of DFT calculations including solvent effects. Monsanto's catalyst *cis*-$[Rh(CO)_2I_2]^-$, Cole-Hamilton's *trans*-$[Rh(PEt_3)_2(CO)I]$, and Freixa's new diRh

[161] T. Kinnunen, K. Laasonen, J. Mol. Struct. (THEOCHEM) 540 (2001) 91.

[162] T. Kinnunen, K. Laasonen, J. Mol. Struct. (THEOCHEM) 542 (2001) 273.

[163] T. Kinnunen, K. Laasonen, J. Organomet. Chem. 628 (2001) 222.

[164] M. Feliz, Z. Freixa, P.W.N.M. van Leeuwen, C. Bo, Organometallics (24) 2005 5718.

$[Rh_2(\mu\text{-}Cl)_2(SPAN\text{-}PPh_2)(CO)_2]$[165] and related complexes were considered. Results led to the same conclusion as that of Griffin *et al.*[152], namely that the TS for the oxidative addition of MeI on square planar Rh complexes correspond to a linear S_N2 nucleophilic attack by the metal compound on MeI. The geometry of the TS structure showed a collinear I-C-Rh disposition. A concerted three-centre TS structure exists as well, although it lay at a higher energy. Activation enthalpies and activation entropies calculated in this study were in excellent agreement with experimental values. Calculations, in agreement with experimental observation, showed that the more nucleophilic the Rh centre (by introducing electron donor ligands such as phosphines) was, the lower the activation barrier.

2.5.2 Example 2: A theoretical study of steric and electronic effects in the Rh-catalyzed carbonylation reactions.[166]

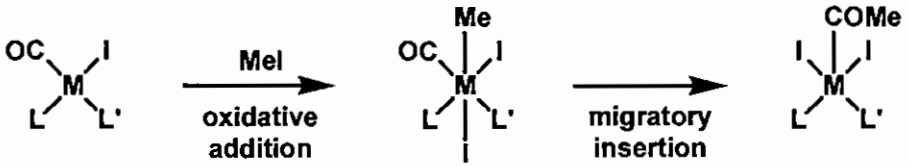

Scheme 2.34: The oxidative addition of MeI to a metal complex.

Cavallo *et al.*[166] have preformed a quantum mechanic (QM) and a quantum/molecular mechanic (QM/MM) study to determine the steric and electronic effects in the two main steps of Rh-catalyzed carbonylation reactions. In particular, they have investigated the energetics of the product of oxidative addition of MeI to several square-planar complexes and the detail in the subsequent CO insertion step (**Scheme 2.34**). The square-planar Rh complexes they have investigated are presented in **Figure 2.26**.

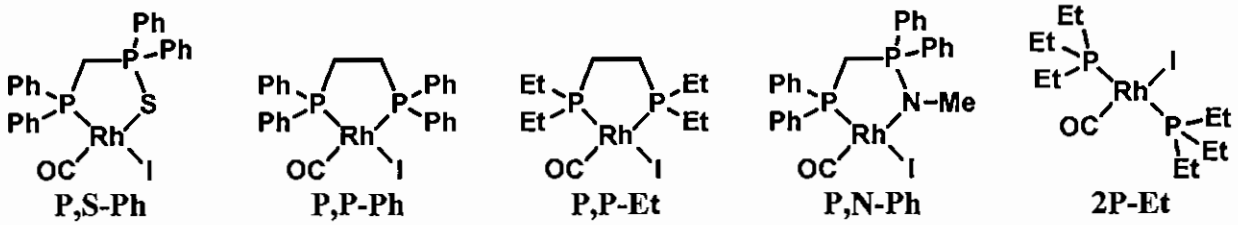

Figure 2.26: The square-planar Rh complexes investigated by Cavallo *et al.*[166]

---

[165] Z. Freixa, P.C.J. Kamer, M. Lutz, A.L. Spek, P.W.N.M. van Leeuwen, Angew. Chem., Int. Ed. Engl. (44) 2005 4385.

[166] L. Cavallo, M. Solà, J. Am. Chem. Soc. 123 (2001) 12294.

The QM approach they used is based on the density functional theory (DFT) and the function they used has previously been employed by Ziegler and co-workers[167] to successfully investigate the full cycle of the Monsanto process with the Monsanto catalyst, $[Rh(CO)_2I_2]^-$, and with the new catalysts developed at BP chemicals, $[Ir(CO)_2I_2]^-$, in which Ir replaces Rh (the Cativa process). Theoretical calculations were done utilizing the Amsterdam Density Functional (ADF) program system. The ADF program was modified to include standard molecular mechanics force fields.[161,168]

Carvallo *et al.*[166] concluded that all the systems considered (**Figure 2.26**) adopted a square-planar geometry prior to the MeI oxidative addition. In the **P,S** and **P,N** based systems, the isomer in which the CO group was *trans* to the S or N atom was clearly favoured relative to the geometry in which the CO group was *trans* to the P atom. In the unbridged **2P** based system, the favoured geometry presented the two P atoms *trans* to each other. For example, see **Figure 2.27.b** for the results for the P,S-Ph complex.

The oxidative addition of MeI to a square-planar complex results in an octahedral complex (**Scheme 2.34**). The Me-group was in the apical position for the minimum energy geometry of all the optimized octahedral complexes (for example, **Figure 2.27.c**). Simplified unsubstituted geometries, where the Ph and Et in the complexes were replaced with H, were also considered (for example, **Figure 2.27.a**). A comparison between the unsubstituted pure QM models and the real-size QM/MM models indicated that the energy gain due to MeI oxidative addition was reduced considerably by the steric pressure of the substituents on the ligand. Substantially similar results were obtained with the real size QM/MM and full QM models, indicating that electronic effects were not the only factor in determining the energy of oxidative addition. The steric effects were more relevant for the Ph-substituted ligands (the **P,P-Ph** system in particular) since in the latter system the four Ph substituents were quite a bit closer to the added Me and I ligands. Finally, regarding the P,P and P,S based systems, geometries in which the CO group was *trans* to the added Me group were of substantially higher energy relative to the isomer in which the CO group was in the mean plane of the P,P or P,S based ligand (for example, **Figure 2.27.c** and **Figure 2.27.d**). The only exception was the full QM **P,P-Ph** system, for

---

[167] M. Cheong, R. Schmid, T. Ziegler, Organometallics 19 (2000) 1973.

[168] T.K. Woo, L. Cavallo, T. Ziegler, Theor. Chem. Acc. 100 (1998) 307.

which the two isomers were isoenergetic. Solvent effects slightly stabilized the octahedral complexes relative to the separated square-planar complexes and free MeI.

A comparison between the unsubstituted pure QM models and the real-size QM/MM models indicated that the energy barrier of the CO insertion reaction (**Scheme 2.34**) was lowered in the presence of the Ph and Et substituents. This effect was related to a relief of the steric pressure on the complex, as the systems moved from a six-coordinated octahedral geometry toward a five-coordinate square-pyramidal geometry (for example **Figure 2.27.e**). As regarded to the electronic contributions, a comparison between the real-size QM/MM and full QM models indicated that the Ph and Et substituents had opposite effects. The Ph substituents lowered the CO insertion barrier, whereas the Et substituents increased it. The energy barrier calculated for the **P,S-Ph** system was in a rather good agreement with the experimental values, whereas that of the **P,P-Ph** system was somewhat underestimated. Inclusion of solvent effects with the continuum model led only to a slightly better agreement.

For all the systems considered, the thermodynamic product after CO migratory insertion, adopted a square-pyramidal geometry with the C(O)Me group in the apical position (for example, **Figure 2.27.f**). The release of steric pressure on the octahedral complexes was reflected in the more favoured thermodynamics of the reaction on going from the pure QM models to the real-size QM/MM models. However, electronic effects clearly dominated the thermodynamics of the reaction, which became endogenic for the full QM **P,N-Ph** system. Solvent effects stabilized the various systems differently. When these effects were considered all the 5-coordinated products resulted from lower energy with respect to the octahedral complexes, with the exception of the **P,N-Ph** system.

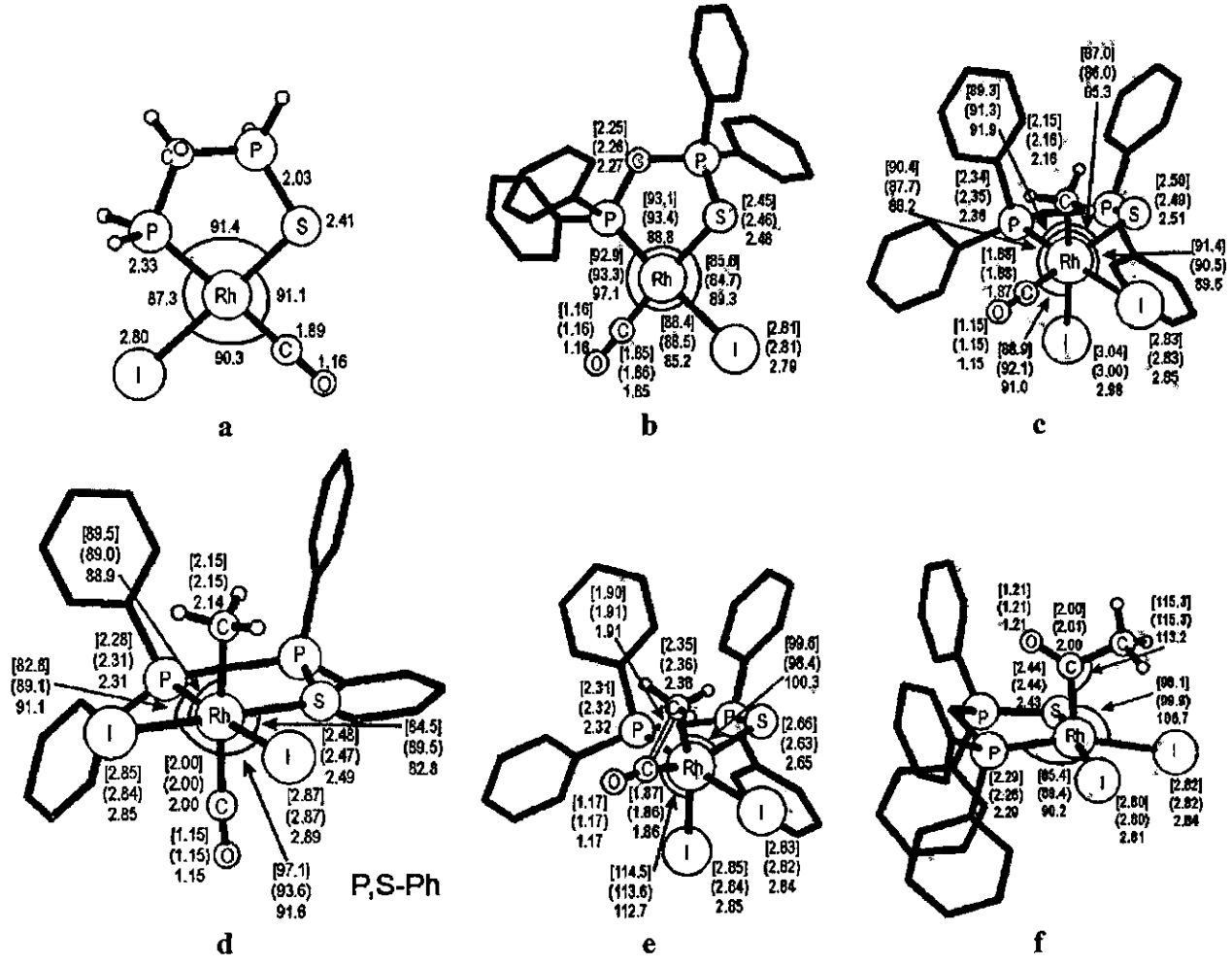

Figure 2.27: Summary of optimized results, for example the P,S-Ph system (first complex in **Figure 2.26**). Distances and angles are in Å and deg, respectively. The unbracketed values refer to the "real-size" full-QM geometry, while the round- and square-bracketed values refer to the "real-size" QM/MM and unsubstituted model-QM geometries, respectively. The other systems showed similar results. (Figures are adopted form reference **166.**)

a) Minimum energy geometries of the unsubstituted model-QM geometries of the square-planar complexes before CH_3I addition.
b) Minimum energy geometries of the square-planar complexes before CH_3I addition.
c) Minimum energy geometries of the octahedral complexes after CH_3I addition.
d) Minimum energy geometries of the octahedral complexes with the CO group trans to the CH_3 group.
e) Geometries of the transition states of the CO insertion reaction.
f) Minimum energy geometries of the square-pyramidal products after CO insertion.

3 Results and discussion

3.1 Introduction.

In this chapter, the synthesis and characterization of new and known thienyl (Th) containing β-diketones of the type $ThCOCH_2COR$, with R = Th, Ph (phenyl or C_6H_5), CF_3, are presented. A discussion of the synthesis and characterization of new and known [Rh^I(β-diketonato)$(CO)_2$], [Rh^I(β-diketonato)(CO)(PPh_3)] and [Rh^{III}(β-diketonato)(CO)(PPh_3)(Me)(I)] complexes are also described. Characterization of these β-diketones and rhodium complexes includes various techniques such as nuclear magnetic resonance (NMR) spectroscopy, infra red (IR) and ultra violet/visible (UV/vis) spectrophotometry and X-ray crystallography. A general mechanism for the oxidative addition of MeI to the [Rh(β-diketonato)(CO)(PPh_3)] complexes was determined by means of detailed kinetic studies utilising NMR techniques, IR and UV/vis spectrophotometry. Computational chemistry, by means of density functional theory (DFT), was used to obtain an insight into the possible reaction products of this oxidative addition reaction. Since the β-diketones and Rh^I(β-diketonato) complexes synthesized in this study all contain a Th group, a determination of the group electronegativity of the Th group is appropriate.

3.2 Group electronegativity (χ) determination of the thienyl (Th) group.

It has previously been shown that accurate apparent group electronegativities (χ_R) of R groups for esters, $RCOOCH_3$, can be obtained from a linear fit between χ_R and the carbonyl IR stretching frequencies (ν_{CO}).[1,2] In this study, the group electronegativity (χ_{Th}) of the Th group was determined by using the ν_{CO} of the ester, $ThCOOCH_3$. A calibration curve (**Figure 3.1**) of known χ_R values against ν_{CO} for esters, with R = CF_3, Cl, CCl_3, $CHCl_2$, CH_2Cl, CH_2Br, CH_3, Ph,

---

[1] W.C. du Plessis, J.J.C. Erasmus, G.J. Lamprecht, J. Conradie, T.S. Cameron, M.A.S. Aquino, J.C. Swarts, Can. J. Chem. 77 (1999) 378.

[2] W.C. du Plessis, T.G. Vosloo, J.C. Swarts, J. Chem. Soc., Dalton Trans. (1998) 2507.

H, Fc (ferrocenyl) was constructed using the data of **Table 3.1**. A linear fit gave the relationship $\nu_{CO} = 74.53\ \chi_R + 1561$. The experimentally determined ν_{CO} for R = Th was then fitted to this calibration curve giving $\chi_{Th} = 2.10$ on the Gordy scale. The χ_R values obtained from the carbonyl IR stretching frequencies of esters, describe the χ_R of the side groups of β-diketones and β-diketonato ligands in metal complexes very well.[2,3]

Table 3.1: IR stretching frequencies of esters of the type $RCOOCH_3$ and group electronegativities (χ_R) of each R group as indicated in the table.

R groups of esters of the type $RCOOCH_3$	ν_{CO} of R groups / cm^{-1}	χ_R
CF_3 [2]	1785	3.01
Cl [2]	1780	2.97
CCl_3 [2]	1768	2.76
$CHCl_2$ [2]	1755	2.62
CH_2Cl [4]	1748	2.48
CH_2Br [4]	1740	2.44
CH_3 [2]	1738	2.34
Ph [2]	1725	2.21
H [2]	1717	2.13
Th [a]	1717	2.10
Fc [2]	1700	1.87

a This study

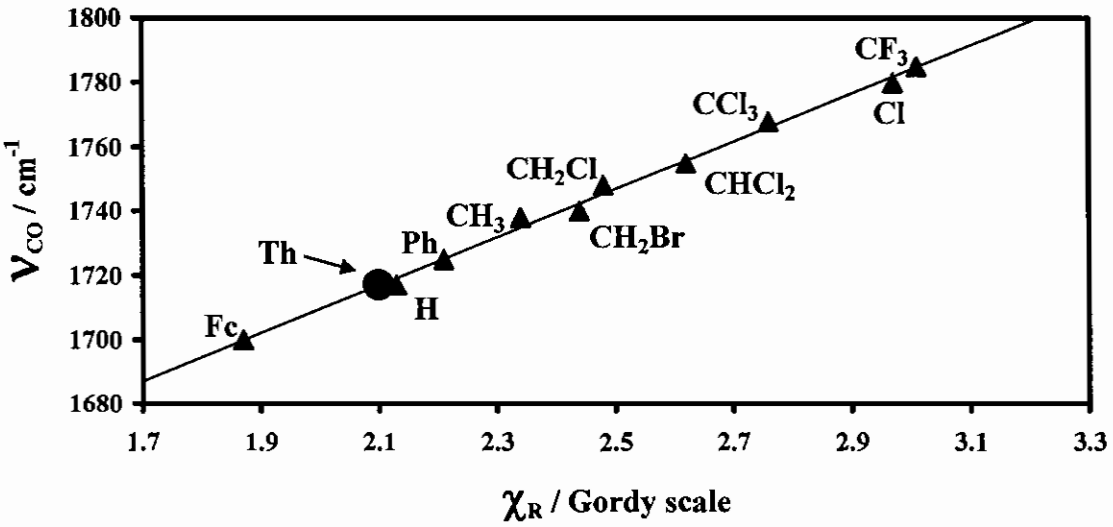

Figure 3.1: Linear relationship between the carbonyl stretching frequencies (ν_{CO}) and Gordy scale group electronegativities (χ_R) of the R groups of the esters of the type $RCOOCH_3$. Calibration data from references **2** and **4** allowed the determination of χ_{Th} from $\nu_{CO} = 1717\ cm^{-1}$ for $ThCOOCH_3$.

---

[3] J. Conradie, T.S. Cameron, M.A.S. Aquino, G.J. Lamprecht, J.C. Swarts, Inorg. Chim. Acta 358 (2005) 2530.

[4] R.E. Kagarise, J. Am. Chem. Soc. 77 (1955) 1377.

3.3 β-diketones.

3.3.1 Synthesis of β-diketones.

The β-diketones Hbth {1} (1-phenyl-3-(2-thenoyl)-1,3-propanedione) and Hdtm {2} (1,3-di(2-thenoyl)-1,3-propanedione) were prepared by Claisen condensation of the appropriate ketone with ethyl 2-thiophenecarboylate (an ester) in the presence of the base LDA. **Scheme 3.1** illustrates the synthetic route for the synthesis of thienyl containing β-diketones used in this study.

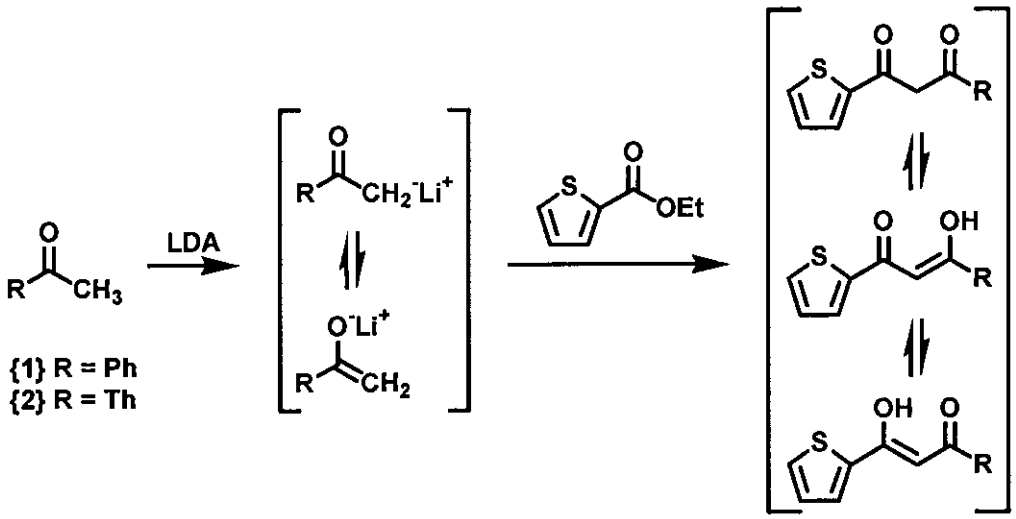

Scheme 3.1: Claisen condensation of the appropriate ketone with ethyl 2-thiophenecarboylate (an ester), in the presence of the base LDA) gives the β-diketones Hbth {1} and Hdtm {2}.

Rigorous Schlenk conditions were necessary for the reaction to proceed effectively. Adhering to these conditions results in the clean products of Hbth {1} (18.8% yield) and Hdtm {2} (18.5% yield). Hbth {1} was recrystallized with ether overnight. The β-diketone Htta (thenoyltrifluoroacetone or 4,4,4-trifluoro-1-(2-thenoyl)-1,3-propanedione) was bought from Aldrich for use in this study.

β-Diketones exist in solution and in the vapour phase[5] in equilibrium mixtures of enol and keto tautomers as illustrated in **Scheme 3.1**. This equilibrium was studied for β-diketones Hbth {1}, Hdtm {2} and Htta and will be discussed in **paragraph 3.3.2**.

---

[5] A.H. Lowrey, P.D. D'Antonio, J. Karle, J. Am. Chem. Soc. 93 (1971) 6399.

The properties and yields of the β-diketones are given in **Table 3.2**.

Table 3.2: Characteristic data and results of the thienyl containing β-diketones synthesis.

β-diketone	Yield	^{1}H NMR enol / ppm [a, b]				^{1}H NMR keto / ppm [a, b]				m.p. literature / °C	m.p. this study / °C
		CH	H^a	H^b	H^c	CH_2	H^a	H^b	H^c		
Hdtm {2}	18.5%	6.56	7.63	7.18	7.79	4.49	7.72	7.17	7.91	78-78.5 [6]	99.5-100.2
Hbth {1}	18.8%	6.71	7.66	7.19	8.83	4.57	7.71	7.17	8.86	99-100 [6]	80.3-81.3
Htta	-	6.47	7.78	7.23	7.86	4.95	7.82	7.22	7.84	42.5-43.2 [7]	42.1-43.0

a In $CDCl_3$

b H^a, H^b and H^c are the protons of the thienyl group with coupling constants H^a (^3J = 5 Hz, ^4J = 1 Hz), H^b (^3J = 5 Hz, ^3J = 4 Hz) and H^c (^3J = 4 Hz, ^4J = 1 Hz). See **paragraph 3.4.2** for a discussion on the coupling constants of the thienyl protons

Using the ^{1}H NMR data from **Table 3.2** and the group electronegativity from **Table 3.1**, a linear relationship between the methylene proton of the keto signal of the β-diketones and the group electronegativity of the R group was found as illustrated in **Figure 3.2**. The same trend was observed for the ^{1}H NMR signals of the protons on the thienyl group of the enol isomer. The protons H^b and H^c with a coupling of (^3J = 5 Hz, ^3J = 4 Hz) and (^3J = 5 Hz, ^4J = 1 Hz) exhibit a linear relationship, as illustrated in **Figure 3.3**. No relationship between the ^{1}H NMR enol signal of the methine proton of the thienyl containing β-diketones or the protons on the thienyl group of the keto isomer was found with the group electronegativity of the R group.

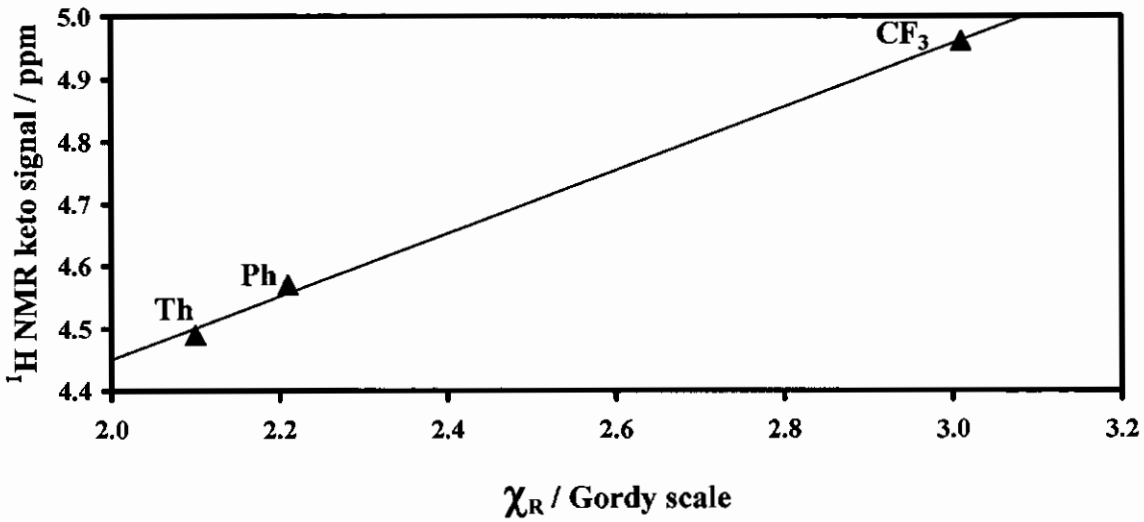

Figure 3.2: Linear relationship observed between group electronegativities (χ_R) and the ^{1}H NMR methylene signals of the keto isomer of the β-diketones of the type $ThCOCH_2COR$, with R = Th, Ph and CF_3.

[6] S.R. Harris, R. Levine, J. Am. Chem. Soc. 70 (1948) 3360.

[7] J.C. Reid, M. Calvin. J. Am. Chem. Soc. 72 (1950) 2948.

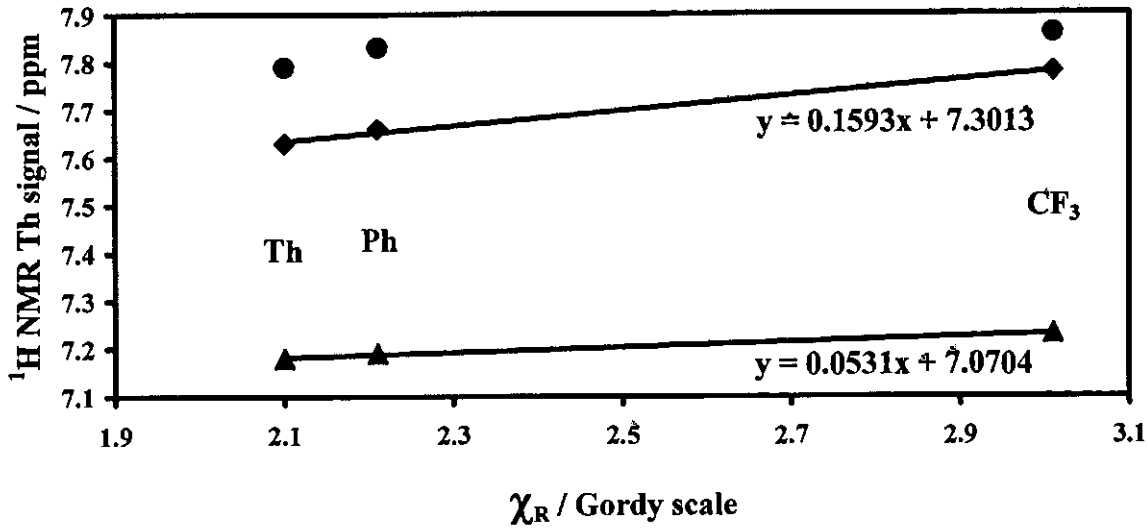

Figure 3.3: Trend observed between the group electronegativities (χ_R) of the R groups on enol β-diketones of the type ThCOCHC(OH)R and the thienyl proton signals of the enol β-diketones with R = Th, Ph and CF_3. At the top is the trend of thienyl proton H^c with coupling (^3J = 4 Hz, ^4J = 1 Hz). In the **middle** is the linear trend of the thienyl proton H^a with coupling (^3J = 5 Hz, ^4J = 1 Hz). At the **bottom** is the linear trend of thienyl proton H^b with coupling (^3J = 5 Hz, ^3J = 4 Hz).

It is expected that electron withdrawing groups, in other words groups with a higher group electronegativity ($\chi_{CF3} > \chi_{Ph} > \chi_{Th}$), will decrease the electron density around the nucleus of the methylene protons of the keto isomer. This results in deshielding to lower field (a higher chemical shift in ppm) as observed in **Figure 3.2.** In the enol isomer, conjugation exists in the O-C-C-C-O backbone of the β-diketone (**Figure 3.4**), but not in the keto isomer. Therefore, as noted from **Table 3.2**, the chemical shift in the ^{1}H NMR for the methane/methylene proton(s) will be in the aromatic region for the enol isomer and in the aliphatic region for the keto isomer.

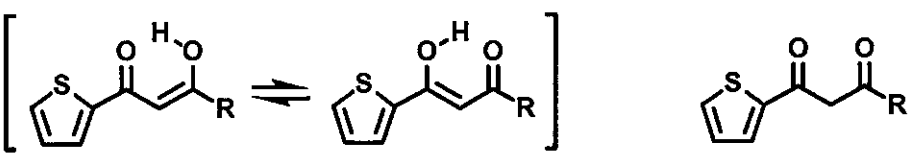

enol
pseudo aromatic character

keto
aliphatic character

Figure 3.4: The character of the O-C-C-C-O backbone of thienyl containing β-diketones.

Thus, in the enol isomer, the electron density will be distributed between the O-C-C-C-O backbone and the thienyl ring, resulting in the relationship shown in **Figure 3.3.** In the keto isomer, there is no conjugation thus no direct communication between the thienyl ring and the R

group and therefore no direct relationship could be detected. With the methylene/methine proton, the effect is the other way around. In the keto isomer, the methylene proton is not disturbed by the conjugation and thus has a direct relationship with the group electronegativity of the R group (**Figure 3.2**).

3.3.2 Keto-enol equilibrium in β-diketones.

β-Diketones generally exist as a mixture of keto and enol forms. The ^{1}H NMR spectrums of the β-diketones Hdtm **{2}**, Hbth **{1}** and Htta at 25 °C are given in **Figure 3.5** to illustrate the keto (CH_2) and the enol (CH) signals at equilibrium.

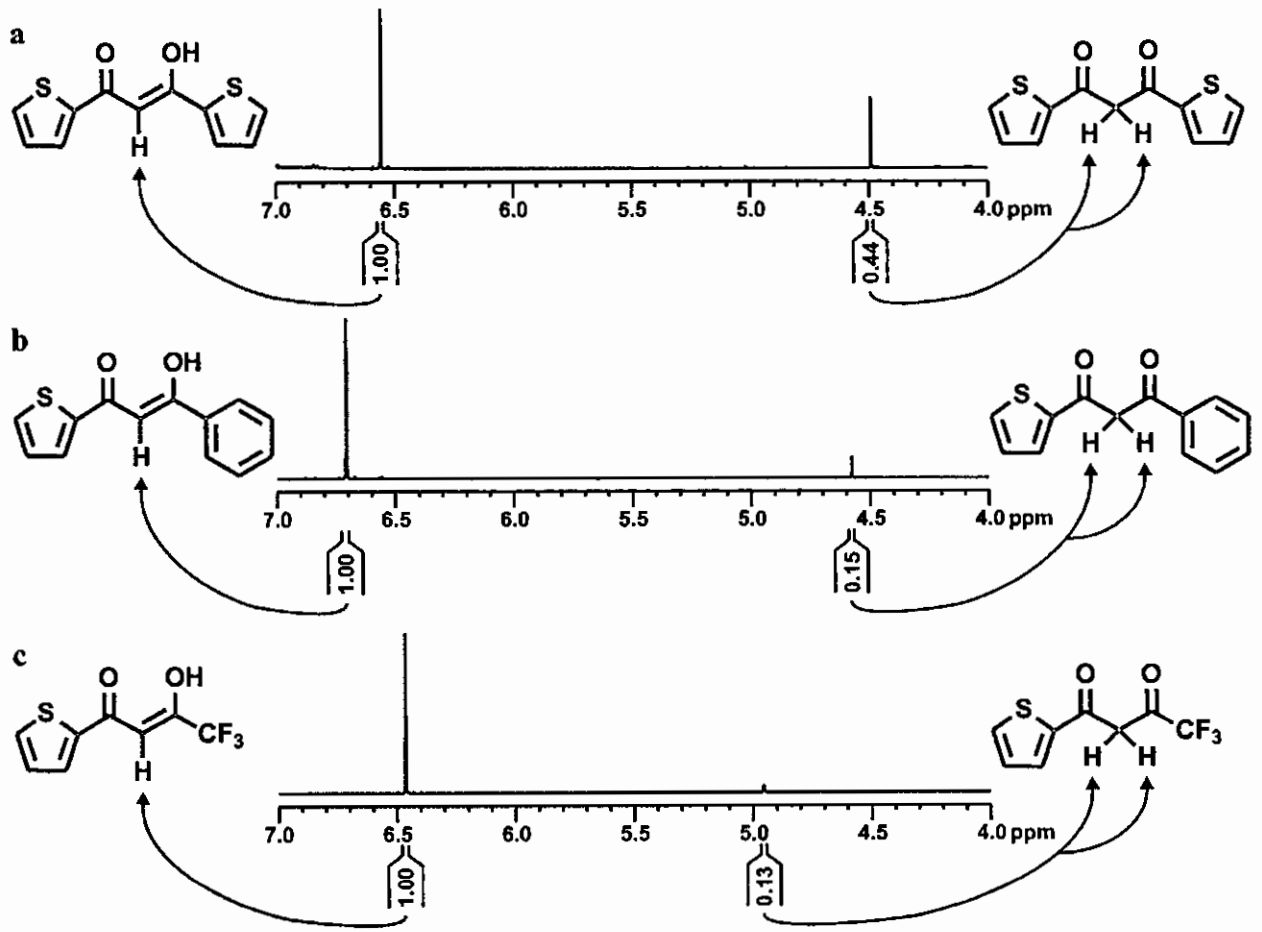

Figure 3.5: ^{1}H NMR spectrums in $CDCl_3$ of **a)** Hdtm **{2}**, **b)** Hbth **{1}** and **c)** Htta showing the keto (CH_2) and the enol (CH) signals at equilibrium. The keto signals are on the right and the enol signals are on the left.

3.3.2.1 Keto-enol equilibrium constant (K_c) at 25 °C.

The equilibrium between the keto and enol forms of the β-diketones can be expressed in terms of the equilibrium constant K_c (**Equation 4.3, Chapter 4**) as shown in **Scheme 3.2**.

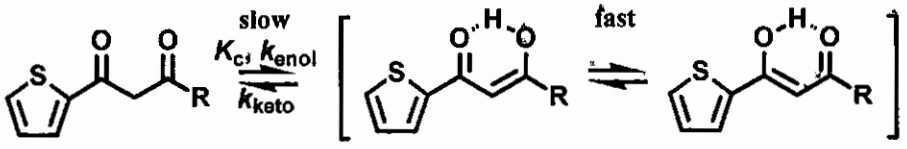

Keto form **Enol forms**

Scheme 3.2: Keto-enol equilibrium for thienyl containing β-diketones.

In this study, K_c values for thienyl containing β-diketones, in $CDCl_3$ solutions, were obtained from ^1H NMR spectroscopy at 25 °C using the method described in **Chapter 4, paragraph 4.4.1**. The Gibbs free energy (ΔG) for the equilibrium reaction can be calculated from the well known thermodynamic expression:[8]

Equation 3.1: $\Delta G = -RT \ln (K_c)$

where ΔG = Gibbs free energy, R = universal gas constant ≐ 8.314 J mol^{-1} K^{-1}, T = temperature and K_c = keto-enol equilibrium constant. Results are summarized in **Table 3.3**.

Table 3.3: Equilibrium constant (K_c) in $CDCl_3$ at 25 °C, the % keto isomer at equilibrium for the keto-enol equilibrium and the Gibb's free energy (ΔG) for the thienyl containing β-diketones.

β-diketone	[β-diketone] / mol dm^{-3}	K_c [a]	% keto	ΔG / kJ mol^{-1}
Hdtm {2}	0.013	4.5	18.0	-3.7
Hbth {1}	0.012	13.3	6.98	-6.4
Htta	0.014	15.4	6.10	-6.8

a In $CDCl_3$ at 25 °C

As ΔG becomes more negative, in other words the thermodynamic driving force associated with **Scheme 3.2** becomes more favourable, the keto content of the β-diketones becomes less. Results are consistent with the study of β-diketones preformed by du Plessis *et al.* with ΔG values ranging between -1.7 and -8.3 kJ mol^{-1} for a series of β-diketones containing a ferrocenyl group.[9] Another correlation observed is that the enol content of the β-diketones $ThCOCH_2COR$ increases as the group electronegativity of R group increases ($\chi_{Th} < \chi_{Ph} < \chi_{CF3}$).

---

[8] G.M. Barrow, Physical Chemistry, McGraw-Hill, New York International Student Edition, 1961, p. 155.

[9] W.C. Du Plessis, W.L. Davis, S.J. Cronje, J.C. Swart, Inorg. Chim. Acta. 314 (2001) 97.

3.3.2.2 Thermodynamic properties.

Although K_c is constant for a given β-diketone at a constant temperature, its magnitude can vary as the temperature is changed. The enol content generally decreases as the temperature increases, due to the disruption of hydrogen bonds (**Chapter 2, paragraph 2.2.2.2**). This study investigated the effect of temperature on the K_c values of the β-diketones Hdtm **{2}**, Hbth **{1}** and Htta. The results are tabulated in **Table 3.4**. By noting the % keto isomer at equilibrium at the different temperatures, it is obvious that temperature has only a limited effect on the equilibrium position of the thienyl containing β-diketones. The 50 °C increase of the temperature resulted in a slight decrease in the equilibrium constant, K_c, for the equilibrium in **Scheme 3.2**.

Table 3.4: The equilibrium constant (K_c) in $CDCl_3$ at different temperatures for the equilibrium shown in **Scheme 3.2** experimentally obtained with ^1H NMR spectroscopy.

Temperature / °C	integral value of ^1H NMR enol (1H of CH)	integral value of ^1H NMR keto (1H of CH_2)	K_c	% keto
***Hdtm* {2} (0.013 mol dm^{-3})**				
0	1	0.174	5.8	14.8
23	1	0.220	4.5	18.0
50	1	0.280	3.6	21.9
***Hbth* {1} (0.012 mol dm^{-3})**				
0	1	0.056	17.7	5.3
25	1	0.075	13.3	7.0
50	1	0.105	9.5	9.5
***Htta* (0.014 mol dm^{-3})**				
-1	1	0.044	22.8	4.2
25	1	0.059	16.9	5.6
44	1	0.073	13.8	6.8
52	1	0.077	13.0	7.2
60	1	0.084	11.9	7.8

The numeric values for the thermodynamic quantities Gibbs free energy (ΔG), enthalpy (ΔH) and entropy (ΔS) for the equilibrium reaction written as in **Scheme 3.2**, can be calculated from **Equation 3.1**, **Equation 3.2** and **Equation 3.3**.[9]

Equation 3.2: $$\ln K_c = \frac{-\Delta H}{RT} + \text{constant}$$

where K_c = keto-enol equilibrium constant, ΔH = enthalpy, R = universal gas constant = 8.314 J mol^{-1} K^{-1} and T = temperature.

From **Equation 3.2** it follows that a graph of ln K_c *versus* 1/T should give a straight line with a slope equal to -ΔH/R (**Figure 3.6**). ΔH can thus be obtained from the slope. At a specific temperature, ΔG and ΔS can be calculated from **Equation 3.1** and **Equation 3.3** respectively.

Equation 3.3: $\Delta G = \Delta H - T\Delta S$

where ΔG = Gibbs free energy, ΔH = enthalpy, T = temperature and ΔS = entropy.

The thermodynamic quantities of Hdtm {2}, Hbth {1} and Htta are summarized in **Table 3.5**. In calculating the thermodynamic quantities, it was assumed that activities may be replaced with concentration. This is a perfect valid assumption under the experimental conditions, since it is known that ionic solutions of low concentrations approach ideal behaviour, implying that under these experimental conditions, concentration and activity are equal.[10]

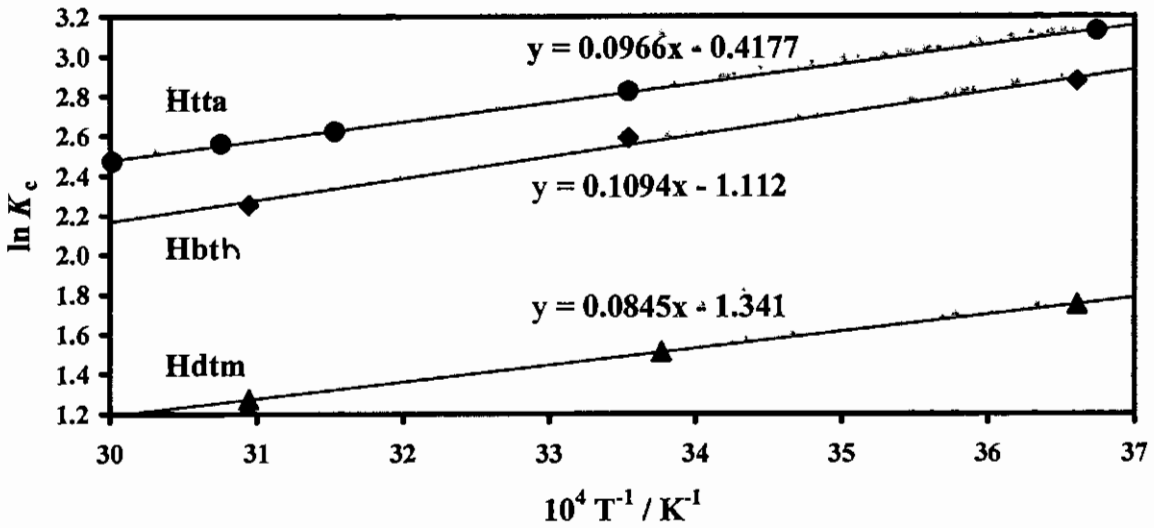

Figure 3.6: Temperature (T) dependence of K_c for the equilibrium position between the keto and enol isomers of the β-diketones Hbth {1} Hdtm {2} and Htta. Slope of graph = $-\Delta H/R$.

Table 3.5: The average equilibrium constant (K_c) at 25 °C for the equilibrium shown in **Scheme 3.2** and the thermodynamic quantities relevant to this equilibrium.

β-diketone	average K_c [a, b]	ΔH / kJ mol^{-1}	ΔG [a] / kJ mol^{-1}	ΔS [a] / J mol^{-1} K^{-1}
Hdtm {2}	4.5	-7.0	-3.7	-11
Hbth {1}	12.9	-9.1	-6.3	-9
Htta	16.8	-8.0	-7.0	-3

a In $CDCl_3$ at 25 °C

b Calculated from the straight line fittings in **Figure 3.6** at 25 °C

The data in **Table 3.5** are consistent with the data in **Table 3.3**. The data differ slightly, since the data in **Table 3.5** were obtained from different temperatures and therefore calculated as an average from a linear fit. The small negative ΔS value for the conversion from keto to enol

[10] P.W. Atkins, Physical Chemistry, Fifth edition, Oxford University Press, Oxford, 1994, p. 319.

structures, according to **Scheme 3.2**, implies a lowering in the degree of disorder of the β-diketone molecules in changing from keto to enol.

3.3.2.3 Kinetics of ketonization.

The above K_c values were determined after the keto-enol equilibrium of the β-diketone in a $CDCl_3$ solution was reached. However, in the solid state, conversion from keto to enol slowly takes place until the equilibrium in the solid state is reached. Solid state samples of β-diketones that are older than 4 months are thus enol enriched. Therefore, upon dissolving an old β-diketone sample, conversion from enol to keto takes place until equilibrium in solution sets in.[9]

From a kinetic point of view, the equilibrium constant (K_c) can also be expressed in terms of the quotient of the rate of conversion of keto to enol isomers and the rate of conversion of enol to keto isomers, as given by **Scheme 3.2.**

In particular, $K_c = k_{enol} / k_{keto}$, with k_{enol} = rate constant for the conversion of keto to enol isomer and k_{keto} = rate constant for the conversion of enol to keto isomer. The conversion of the enol isomer to the keto isomer was monitored by recording ^{1}H NMR spectra at specific time intervals until the % keto isomer remained constant (or until equilibrium is reached). Enol enriched ^{1}H NMR's for Hdtm **{2}** and Hbth **{1}** are given in **Figure 3.7 (top)** and **Figure 3.8 (top)** and the ^{1}H NMR's at equilibrium for Hdtm **{2}** and Hbth **{1}** are given in **Figure 3.7 (bottom)** and **Figure 3.8 (bottom)**.

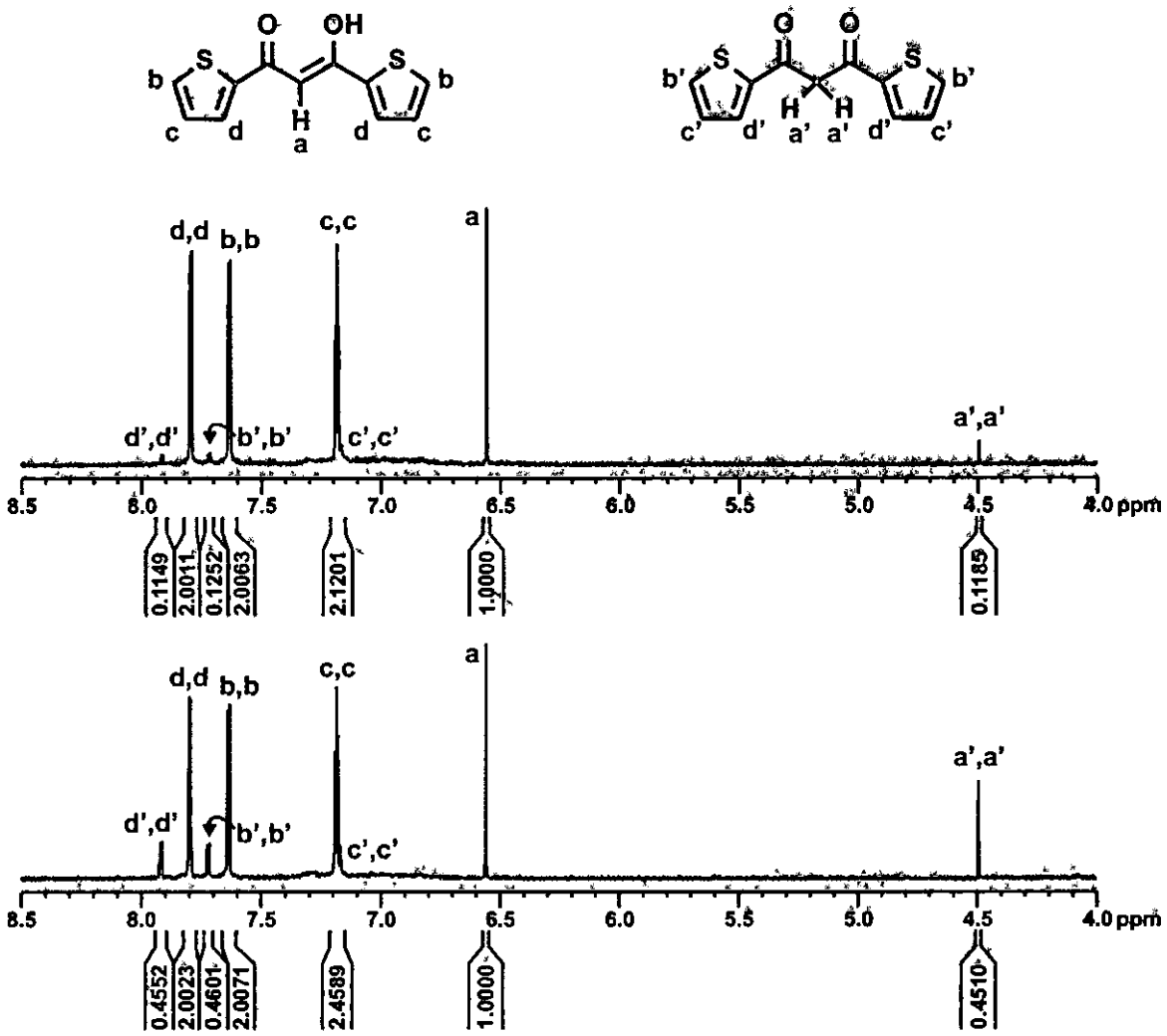

Figure 3.7: At the **top** is the ^{1}H NMR spectrum of an aged sample of Hdtm {2} containing mostly the enol isomer. At the **bottom** is the ^{1}H NMR spectrum of Hdtm {2} at equilibrium. All spectra were recorded in $CDCl_3$ at 25 °C. The labelling of the peaks is as indicated at the top structures. $CDCl_3$ peak is suppressed for clarity.

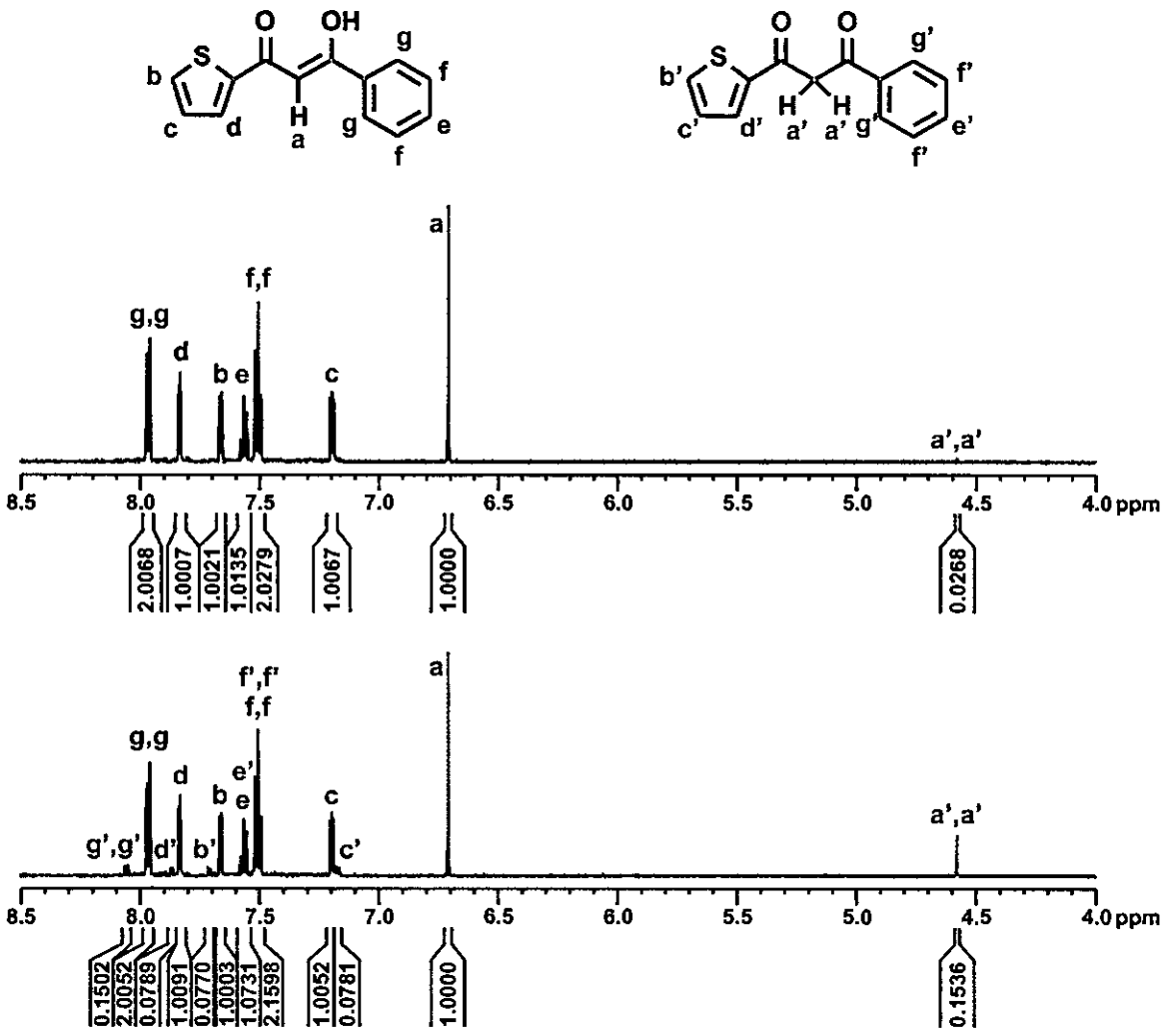

Figure 3.8: At the **top** is the ^{1}H NMR spectrum of an aged sample of Hbth {**1**} containing mostly the enol isomer. At the **bottom** is the ^{1}H NMR spectrum of Hbth {**1**} at equilibrium. All spectra were recorded in $CDCl_3$ at 25 °C. The labelling of the peaks is as indicated at the top structures. $CDCl_3$ peak is suppressed for clarity.

For each time interval, the % keto isomer was determined and the observed first-order rate constant, k_{obs}, was obtained from **Equation 3.4**,[11] utilising the fitting program MINSQ.[12]

Equation 3.4: $[A]_t = [A]_i + ([A]_0 - [A]_i)\exp^{(-kobs)t}$

with $[A]_t$ = % keto isomer at time t, $[A]_i$ = % keto isomer at infinite time, $[A]_0$ = initial % keto isomer, $k_{obs} = k_{keto} + k_{enol}$. The individual rate constant k_{keto} and k_{enol} were obtained by simultaneously solving the equations $k_{obs} = k_{keto} + k_{enol}$ and $K_c = k_{enol} / k_{keto}$.

[11] J.H. Espenson, Chemical Kinetics and Reaction Mechanisms, Second edition, McGraw-Hill International Editions, 1995, p. 46.

[12] MINSQ, Least squares parameter Estimation, Version 3.12, MicroMath, 1990.

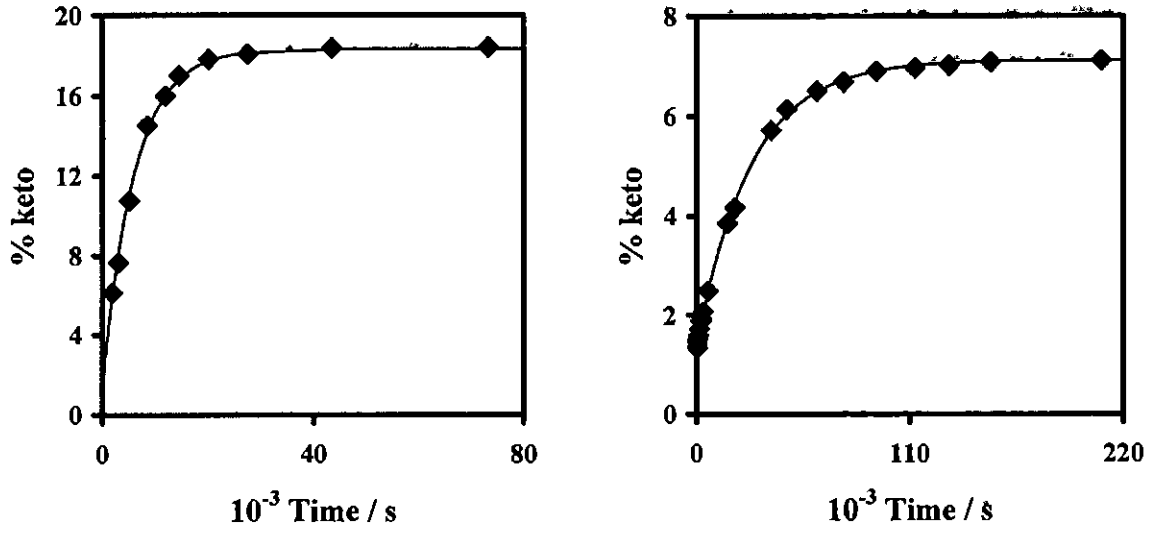

Figure 3.9: Time traces showing the conversion from the enol to the keto isomers of **a)** Hdtm {2} and **b)** Hbth {1} at 25 °C in $CDCl_3$.

From the kinetic conversion of the β-diketones from the enol isomer to the keto isomer (**Figure 3.9**), the first order rate constant (k_{obs}) was found to be 0.00017(2) s^{-1} for Hdtm {2} and 0.000036(2) s^{-1} for Hbth {1}. The first order rate constant (k_{obs}) for Htta was found to be too fast to measure, which is consistent with the finding of Iglesias.[13] From this data, the rate constants for the forward reaction (k_{enol}) and the reverse reaction (k_{keto}) in **Scheme 3.2** were calculated and are given in **Table 3.6.**

Table 3.6: Rate constants for the conversion of keto to enol isomer (k_{enol}) and for the conversion of enol to keto isomer (k_{keto}) for the β-diketones as indicated. Also listed are the half lives for observed rate constants (k_{obs}). Values at 25 °C in $CDCl_3$.

β-diketone	[β-diketone] / mol dm^{-3}	k_{enol} / s^{-1}	k_{keto} / s^{-1}	$t_{1/2}$ / min
Hdtm {2}	0.0012	1.4×10^{-4}	3.1×10^{-5}	70
Hbth {1}	0.0012	3.3×10^{-5}	2.6×10^{-6}	320

From **Table 3.6** it follows that larger rate constants for the conversion of keto to enol isomers (k_{enol}) were observed as compared to the conversion of enol to keto isomers (k_{keto}) for both β-diketones in this study. This implies that the enol isomer is the favoured stable isomer in which Hdtm {2}, Hbth {1} and Htta exist in $CDCl_3$ solutions. For Htta the equilibrium in $CHCl_3$ sets in within seconds, whereas for Hdtm {2} the equilibrium was reached after 15 hours and Hbth {1} after 62 hours. Compared to the β-diketones listed in **Table 2.2 (Chapter 2)**, the thienyl

[13] E. Iglesias, J. Org. Chem. 68 (2003) 2680.

containing β-diketones Hdtm {2} and Hbth {1} have a relatively slow equilibrium, with k_{enol} ten to hundred times faster than the ferrocene containing β-diketones Hfctfa, Hfca and Hdfcm with k_{enol} (k_{keto}) values of 64 x 10^{-6} (2 x 10^{-6}), 44 x 10^{-6} (13 x 10^{-6}) and 20 x 10^{-6} (10 x 10^{-6}) s^{-1} respectively.

3.3.3 Acid dissociation constant (K_a) determinations of β-diketones.

The pK_a' values for the thienyl containing β-diketones refer to the reaction in **Scheme 3.3**.

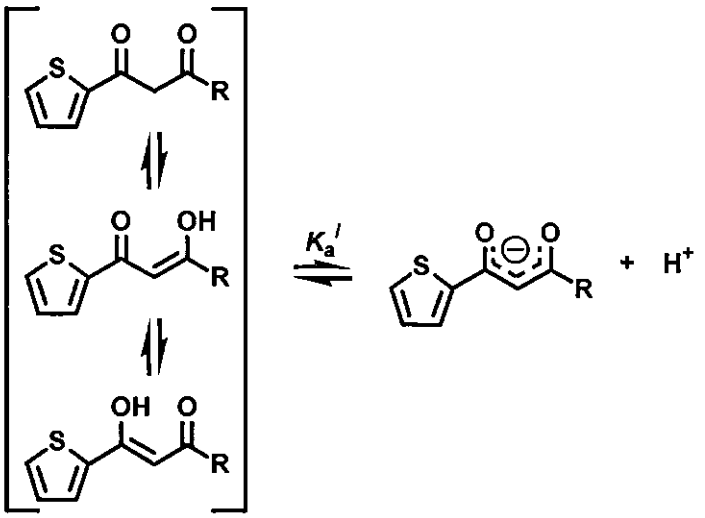

Scheme 3.3: The reaction that occurs during the determination of pK_a' values. The three ligands on the left represent the acid form and the ligand on the right represents the base form of the β-diketone, with R = Ph, Th and CF_3.

Since the thienyl containing β-diketones Hbth **{1}** and Hdtm **{2}** were not well soluble in pure or basic water, water-acetonitrile mixtures were used as solvent. The effect of 10% acetonitrile in the solvent medium was tested using Hacac as reference. For Hacac a pK_a' value of 8.95(8) was obtained. This was within experimental error the same as the best available published pK_a for acetylacetone in water (8.878(5) when μ = 1 mol dm^{-3} and 8.98 when μ = 0.0172 mol dm^{-3}).[14] It was therefore concluded that the electrode was calibrated to measure hydrogen ion activity under the conditions used. It is not expected that the electrode would behave differently for any of the other pK_a determinations because only pK_a values of a series of β-diketones were determined.

[14] A.E. Martell, Stability Constants of Metal-Ion Complexes, The Chemical Society, Third edition, London, Special Publication No. 25, part II, 1971, p. 365.

The apparent pK_a values of Hdtm {2}, Hbth {1} and Htta were determined by measuring the UV/vis absorbance/pH data with titration from high to low as well as from low to high pH and a least squares fit, utilizing the fitting program MINSQ,[12] of the absorbance/pH data using **Equation 3.5**.

Equation 3.5: $$A_T = \frac{A_{HA}10^{-pH} + A_A 10^{-pK_a}}{10^{-pH} + 10^{-pK_a}}$$

with A_T = total absorbance, A_{HA} the absorbance of the β-diketone in the protonated form and A_A the absorbance of the β-diketone in the deprotonated (basic) form.

The UV/vis spectra of the protonated (acidic) and deprotonated (basic) forms of the β-diketones Hdtm {2}, Hbth {1} and Htta are given in **Figure 3.10** with the peak extinction coefficient in **Table 3.7**. Also tabulated are the concentrations of the β-diketone during the pK_a determination as well as the pK_a' values as determined from the experimental absorbance - pH data in **Figure 3.11**.

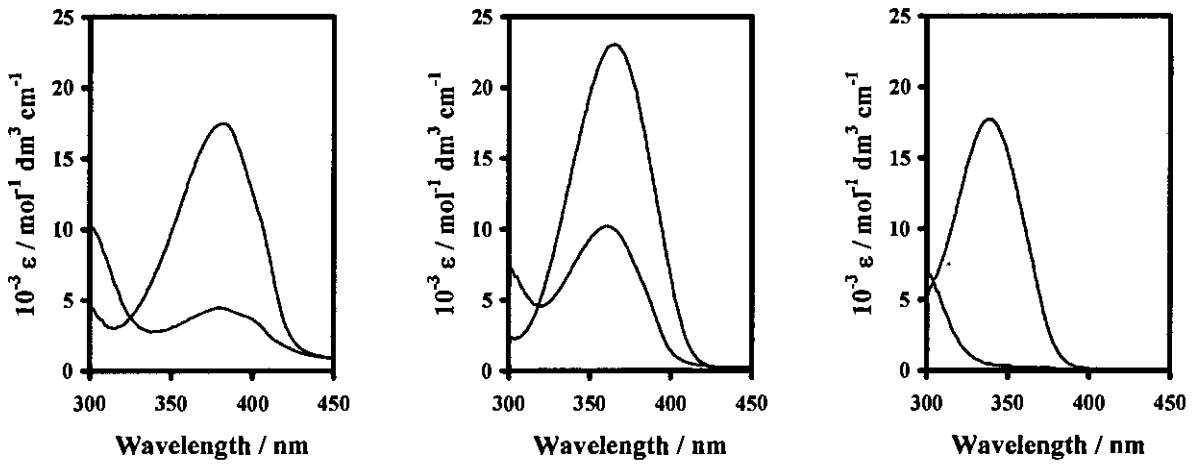

Figure 3.10: UV/vis spectra of the protonated (line below) and deprotonated (line above) β-diketone **a)** Hdtm {2}, **b)** Hbth {1} and **c)** Htta in a 10% acetonitrile/water mixture, μ = 0.100 mol dm^{-3} ($NaClO_4$) at 25.0(5) °C.

Table 3.7: pK_a' values and molar extinction coefficients (ε) at λ_{max} of the β-diketones Hdtm {2}, Hbth {1} and Htta in a 10% acetonitrile/water mixture.

β-diketone	c / mmol dm^{-3}	λ_{max} (deprotonated) / nm [ε / mol^{-1} dm^3 cm^{-1}]	λ_{exp} / nm [ε / mol^{-1} dm^3 cm^{-1}]	pK_a'
Hdtm {2}	0.07	382 [17498]	365 [14744]	8.893(3)
Hbth {1}	0.07	365 [23039]	380 [18906]	9.006(8)
Htta	0.07	340 [17720]	337 [17649]	6.491(8)

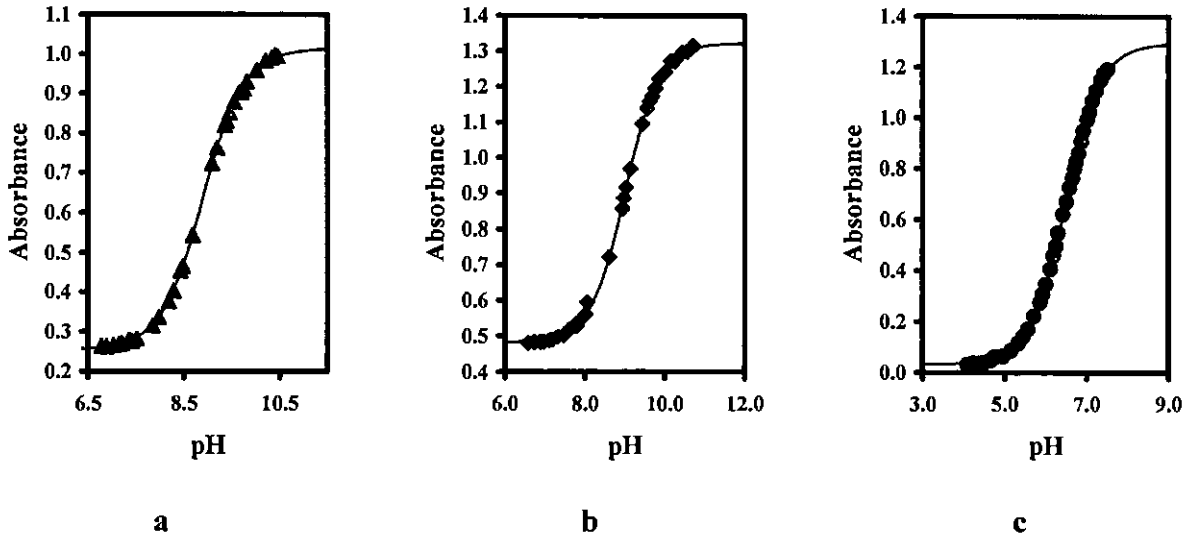

Figure 3.11: Effect of pH on absorbance for **a)** Hdtm {**2**} at 365 nm, **b)** Hbth {**1**} at 380 nm and **c)** Htta at 337 nm in a 10% acetonitrile/water mixture, μ = 0.100 mol dm^{-3} ($NaClO_4$) at 25.0(5) °C. The solid line represents the least square fit of **Equation 3.5**.

The pK_a' of Htta determined as 6.491(8) in this study is in 1-4% of the published pK_a' values of 6.23 in 1950[7,15] (determined by a direct titration with sodium hydroxide of an aqueous ketone solution at room temperature), 6.38 in 1952[15,16] and 6.53 in 1962.[15,17] The newly determined pK_a values fit in the series of increasing pK_a values of β-diketones[2,18,19,20] as follows (pK_a values in brackets after each β-diketone):

(*strongest acid*) Hhfaa (4.71) < Htfba (6.3) = Htfaa (6.3) < **Htta (6.49)** < Hfctfa (6.56) < Htfhd (6.64) < Htfdma (6.80) < Hfch (7.04) < Hfctca (7.13) = Htftma (7.13) < Hba (8.70) < **Hdtm (8.89)** < Hacac (8.95) < **Hbth (9.01)** < Hdbm (9.35) < Hfca (10.01) < Hbfcm (10.41) < Hdfcm (13.1) (*strongest base*)

Groups on the β-diketone backbone with a high group electronegativity (highly electron withdrawing) make the β-diketone more acidic, which results in a decrease in the pK_a value of

---

[15] J. Starý, The Solvent Extraction of Metal Chelates, MacMillan Company, New York, 1964, Appendix.

[16] E.H. Cook, R.W. Taft, J. Am. Chem. Soc. 74 (1952) 6103.

[17] V.M. Peshkova, Pen-An, Zh. Neorg. Khim. 7 (1962) 1484.

[18] J. Starý, The Solvent Extraction of Metal Chelates, MacMillan Company, New York, 1964, pp. 196-202.

[19] M. Ellinger, H. Duschner, K. Starke, J. Inorg. Nucl. Chem. 40 (1978) 1063.

[20] S.S. Basson, J.G. Leipoldt, J.T. Nel, Inorg. Chim. Acta 84 (1984) 167.

the β-diketone. For example, Hhfaa, which contains two CF_3 groups ($\chi_{CF_3} \triangleq 3.01$), is the most acidic β-diketone with a pK_a of 4.71. On the other side of the scale lies Hdfcm, which contains two Fc groups ($\chi_{Fc} = 1.87$), with a pK_a of 13.1. The effect of the electronegativity of each group is additive (although not linear) in determining the acidity (or basicity) of the β-diketone. **Figure 3.12** illustrates the relationship between the pK_a value of β-diketone $R^1COCH_2COR^2$ and the sum of the group electronegativities ($\chi_{R1} + \chi_{R2}$) of the groups R^1 and R^2 on the β-diketone.

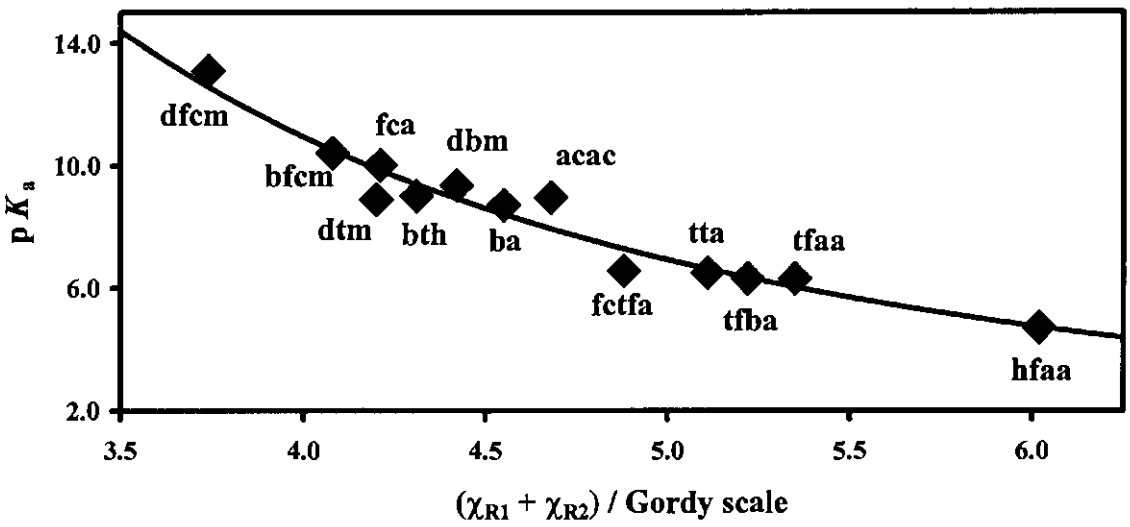

Figure 3.12: Relationship between the pK_a value and the sum of the group electronegativities ($\chi_{R1} + \chi_{R2}$) of the groups R^1 and R^2 on the β-diketone $R^1COCH_2COR^2$. The β-diketones are as indicated, group electronegativities from **Table 3.1**

3.3.4 Crystal structure data of Hbth {1}.

To further the characterisation of the thienyl containing β-diketones, results of a single crystal structure determination for 1-phenyl-3-(2-thenoyl)-1,3-propanedione (Hbth) is presented. The author acknowledges Dr. A.J. (Fanie) Muller of the Department of Chemistry, University of the Free State, for the data collection, refinement and useful discussions of the crystal structures.

A molecular diagram of Hbth, showing atom labelling, is presented in **Figure 3.13**. Crystal data for the structure of Hbth are summarized in **Table 3.8**, selected bond lengths, angles and torsion angles can be found in **Table 3.9**. The complete table of bond lengths and angles and the crystallographic data for the structural analysis are given in **Appendix B**. Selected comparative

geometrical data of the thienyl containing β-diketones Hdtm, Hbth and Htta are given in **Table 3.10**.

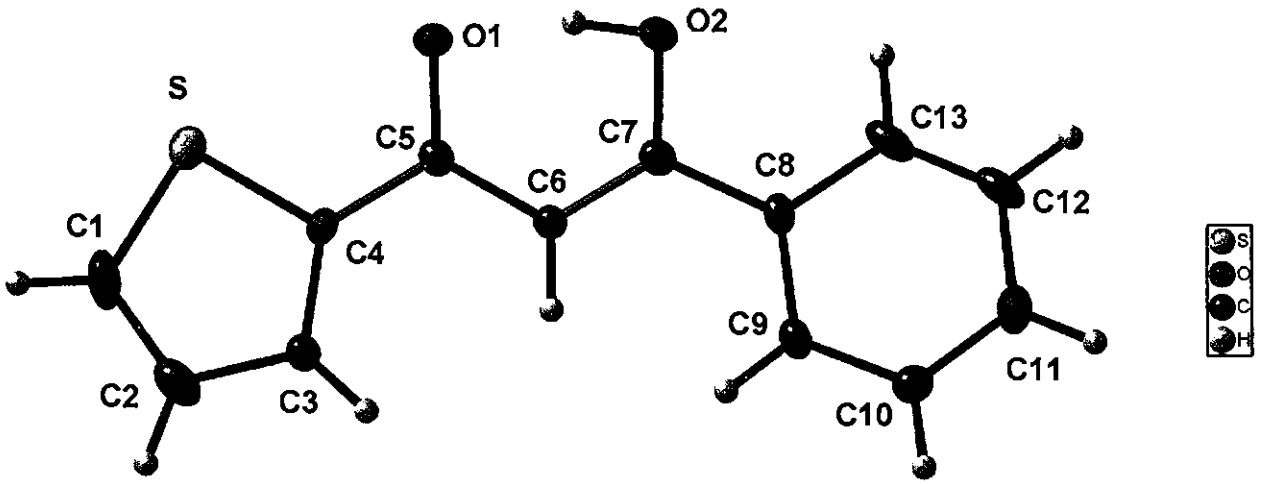

Figure 3.13: Molecular diagram of 1-phenyl-3-(2-thenoyl)-1,3-propanedione (Hbth) showing atom numbering and displacement ellipsoids of 50% probability.

Table 3.8: Crystal data and structure refinement for Hbth.

Empirical formula	$C_{13}H_{10}O_2S$	**Theta range for data collection**	2.95 to 28.32°
Formula weight	230.27 g mol^{-1}	**Limiting indices**	-11 <= h <= 11 -14 <= k <= 14 -31 <= l <= 31
Temperature	100(2) K	**Reflections collected**	21300
Wavelength	0.71073 Å	**Unique reflections**	2695 [R(int) = 0.0290]
Crystal system	Orthorhombic	**Completeness to theta = 28.32**	99.7%
Space group	*Pbac*	**Absorption correction**	Semi-empirical from equivalents
Unit cell dimensions	a = 8.4329(2) Å b = 10.6891(2) Å c = 24.0104(5) Å α = 90° β = 90° γ = 90°	**Max. and min. transmission**	0.9674 and 0.9089
Volume	2164.30(8) $Å^3$	**Refinement method**	Full-matrix least-squares on F^2
Z	8	**Data / restraints / parameters**	2695 / 0 / 143
Density (calculated)	1.413 g cm^{-3}	**Goodness-of-fit on F^2**	1.063
Absorption coefficient (μ)	0.278 mm^{-1}	**Final R indices [I>2sigma(I)]**	R1 = 0.0634 wR2 = 0.1705
F(000)	960	**R indices (all data)**	R1 = 0.0698 wR2 = 0.1768
Crystal size	0.35 x 0.24 x 0.12 mm^3	**Largest diff. peak and hole**	1.351 and -0.822 e.$Å^{-3}$

Table 3.9: Selected bond lengths (Å), bond angles (degree) and torsion angles (degree) for Hbth.

Bond lengths / Å					
S-C4	1.721(2)	O2-H14	0.94(4)	C5-C6	1.435(3)
O1-C5	1.268(3)	C1-C2	1.390(4)	C6-C7	1.371(3)
O2-C7	1.330(3)	C4-C5	1.457(3)	C7-C8	1.469(3)
Bond angles / degree					
C1-S-C4	91.85(12)	O1-C5-C4	118.9(2)	O2-C7-C8	114.47(19)
C7-O2-H14	97(3)	C6-C5-C4	119.9(2)	C6-C7-C8	124.6(2)
C3-C4-C5	128.6(2)	C7-C6-C5	119.9(2)	C9-C8-C7	122.7(2)
O1-C5-C6	121.2(2)	O2-C7-C6	120.9(2)	-	-
Torsion angles / degree					
C1-S-C4-C5	-177.20(19)	O1-C5-C6-C7	1.6(3)	O2-C7-C8-C9	166.2(2)
C3-C4-C5-O1	-173.9(2)	C4-C5-C6-C7	-178.7(2)	C6-C7-C8-C9	-14.7(4)
S-C4-C5-O1	3.3(3)	C5-C6-C7-O2	-0.5(3)	O2-C7-C8-C13	-12.5(3)
C3-C4-C5-C6	6.4(4)	C5-C6-C7-C8	-179.5(2)	C6-C7-C8-C13	166.5(2)

The β-diketone Hbth packs in the *Pbca* space group with Z = 8, resulting in the molecules lying on general positions of the unit cell. All bond lengths and angles are in the typical range for these types of compounds[21, 22] and will be discussed in more detail later in this paragraph.

The molecule as a whole is non-planar (**Figure 3.14**), possibly due to crystal packing as several close contacts are observed in Mercury[23]. The plane of the phenyl ring and the thienyl ring makes an angle of 13.65 and 5.88° respectively with the plane of the enol ring. When comparing the geometrical data of the three thienyl containing β-diketones of this study, the striking difference is that Hbth is non-planar, while both Htta and Hdtm can be considered as planar, since the angle between the plane of the thienyl ring(s) and the plane of the enol ring is 0.83 - 1.67° for Htta and 0.85 - 4.92° for Hdtm, see **Table 3.8**. The bond lengths and bond angles in the backbone of the β-diketone are all similar for Hdtm, Hbth and Htta as can be seen from the tabulated bond lengths and angles in **Table 3.10** and the superimposed view of Hdtm, Hbth and Htta in **Figure 3.17**

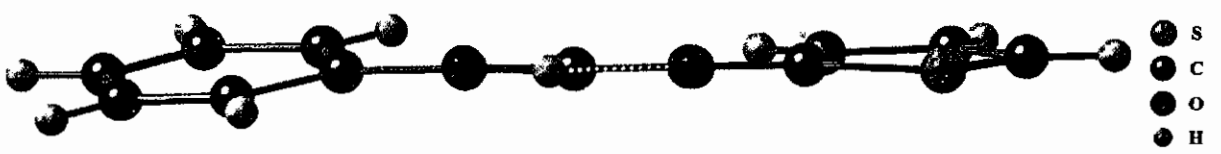

Figure 3.14: View of Hbth with the plane of the enol ring perpendicular to the page, showing the non-planar arrangement.

21 Cambridge Structural Database (CSD), Version 5.27, August 2006 update

22 Allen, F. H. (2002). Acta Cryst. B58, 380–388.

23 Mercury 1.5, The Cambridge Crystallographic Data Centre, Cambridge, UK.

Figure 3.15 shows the packing of the molecules in the unit cell having a "herring bone" arrangement. The molecules are stacked with the propanedione moieties in opposing directions, *i.e.* in a "tail to tail" fashion (**Figure 3.16**). Pi-stacking arrangements with inter planar distances of *ca* 4.038 Å are observed between opposing phenyl and thienyl substituents. The "herring bone" arrangement was also observed for Hdtm.

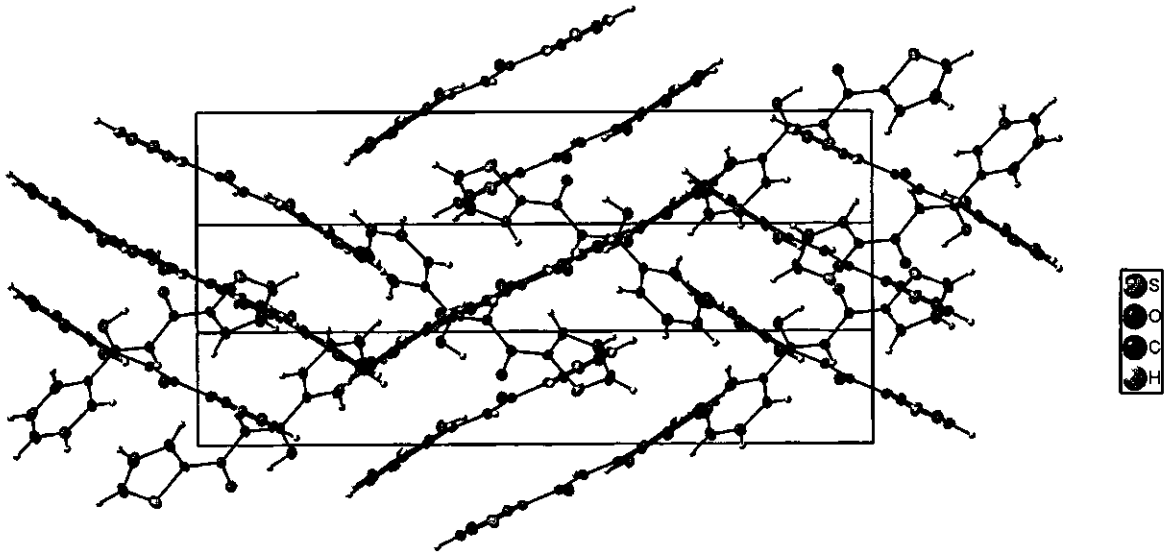

Figure 3.15: Packing diagram of Hbth molecules in unit cell.

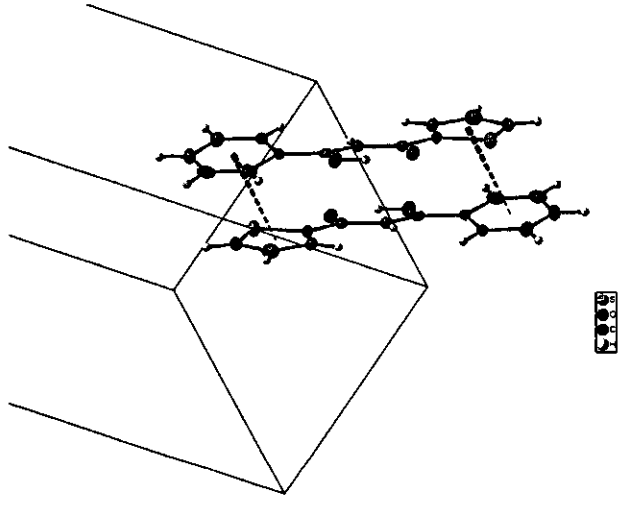

Figure 3.16: Pi-stacking of Hbth molecules in unit cell.

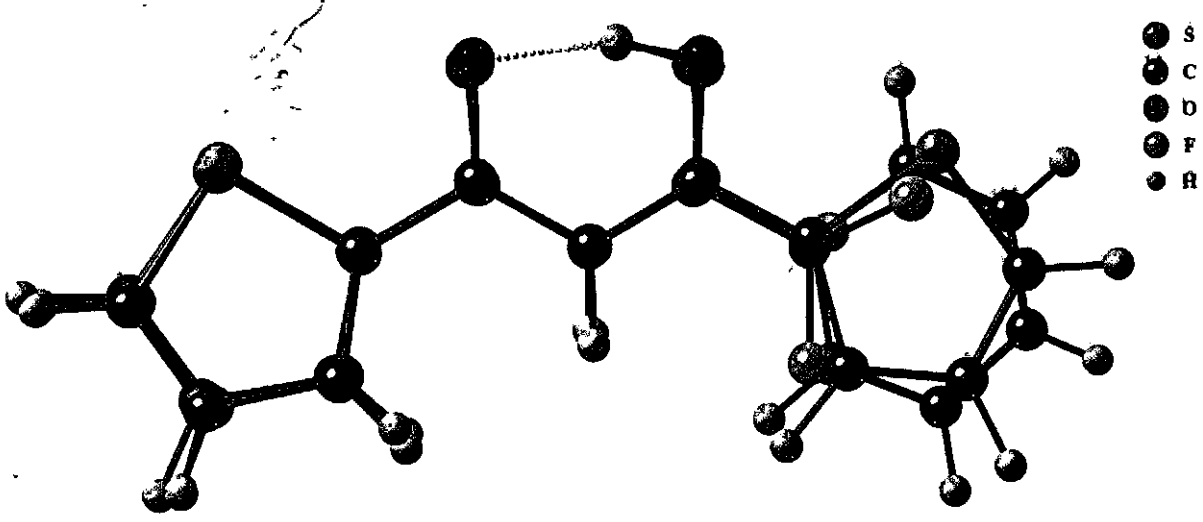

Figure 3.17: Superimposed view of the three thienyl containing β-diketones Hbth, Htta and Hdtm.

In the structural analysis, the bond lengths indicate that a dominant enol tautomer is formed and that a tautomeric equilibrium between the two enol forms in the solid state is not predominant: C7-O2 is longer than C5=O1 and C6=C7 is shorter than C5-C6 (**Table 3.10**). In all the molecules, the thienyl S atom(s) is *cis* to the O atoms of the central enol moiety, possibly due to the S···O interactions between neighbouring molecules, also observed from a Mercury packing diagram.

The electronegativity (χ_R) (**paragraph 3.2**) of a Ph is slightly larger than that of a Th moiety (2.21 and 2.10 respectively). According to the electronic driving force, the hydroxyl proton should thus be located on the side of the Th group (**paragraph 2.2.2.2, Chapter 2**). However, the hydroxyl proton is located on the opposite side. A possible reason for this could be that although both the Ph and the Th groups are aromatic, a larger angle is observed between the Ph- and enol-planes than that of angle between the planes of the Th and enol moieties, implying that the conjugation between the pseudo aromatic enol ring and the thienyl ring is stronger. Thus, the resonance driving force between the enol and the thienyl ring dominate over the electronic driving force, resulting in the hydroxyl proton being located on the side of the Ph group – as was found in the crystal structure of Hbth. Similarly, in the crystal structure of Htta, the hydroxyl proton was also located on the side of the Th group as a result of the resonance driving force rather than the inductive electronic effect of the CF_3 group.

Table 3.10: Selected geometrical data of the thienyl containing β-diketones Hdtm, Hbth and Htta.

β-diketone	enol type	C=O bond length / Å	C-O (enol) bond length / Å	C=C bond length between carbonyl groups / Å	C-C bond length between carbonyl groups / Å	angle between carbonyl (C5-C6-C7) groups / °	O····O distance / Å	Space group	angle between planes through thienyl group and enol group
Hdtm[24] [a]	asym enol	1.286(2)	1.308(2)	1.38(6)	1.41(3)	118.3(2)	2.514	*Cc*	0.85, 3.59
	sym enol	1.278(2)	1.283(2)	1.40(3)	1.41(3)	120.0(2)	2.517		0.85, 4.92
Hbth	asym enol	1.268(3)	1.330(3)	1.371(3)	1.435(3)	119.9(2)	2.477	*Pbca*	5.88
Htta[25] [a]	asym enol	1.269(4)	1.306(4)	1.343(4)	1.432(5)	120.4(3)	2.522	$P2_1/n$	0.83
	asym enol	1.272(4)	1.310(4)	1.353(5)	1.417(4)	120.8(3)	2.511		1.67

a Two molecules in the same asymmetric unit

A theoretical bond angle value of 120° is expected for carbon sp^2 hybridization. The angle C5-C6-C7 (119.9(2)°) is within experimental error as expected. The β-diketone Hbth can thus be classified as an asymmetrical enol. Unlike in the solid state, it was established by ^{1}H NMR that both the enol and the keto form of Hbth exists in a $CDCl_3$ solution with the equilibrium mainly on the enol side (7 % keto at 25 °C, **paragraph 3.3.2**).

The typical bond lengths (**Table 2.5**, **Chapter 2**) in an enolized β-diketone are 1.269 – 1.283 Å for a C=O bond and 1.306 – 1.337 Å for a C-O bond.[26] The bonds C5=O1 (**Figure 3.13**) and C7-O2 are 1.268(3) Å and 1.330(3) Å respectively and are in agreement with these typical bond lengths. The C5=O1 bond therefore displays double bond character and the C7-O2 bond displays single bond character. Normal C=C double bond lengths are typically 1.337 Å, while typical single C-C bonds have a length of 1.54 Å.[27] In β-diketones, however, these bonds are 1.343 – 1.392 Å and 1.403 – 1.432 Å respectively.[26] These bonds are represented by C6-C7 (1.371(3) Å) and by C5-C6 (1.435(3) Å), which are in agreement with these typical bond lengths. The O····O distance for an enolized β-diketone varies between 2.40 – 2.54 Å (**Table 2.5**,

---

[24] L.A.M. Baxter, A.J. Blake, G.A. Heath, T.A. Stephenson, Acta Crystallogr., Sect. C: Cryst. Struct. Commun. 46 (1990) 508.

[25] R.D.G. Jones, Acta Crystallogr., Sect. B: Struct. Crystallogr. Cryst. Chem. 32 (1976) 1224.

[26] W. Bell, J. A Crayston, C. Glidewell, M.A. Mazid, M.B. Hursthouse, J. Organomet. Chem. 434 (1992) 115.

[27] R.C. Weast, Handbook of Chemistry and Physics, Sixty-third edition, The Chemical Rubber Co., Ohio, pp. F180-181.

paragraph 2.2.4, Chapter 2). The O1···O2 distance of 2.477 Å falls within this range. β-diketones in the keto form typically have O···O distances larger than 2.767 Å[28] up to 3.3 Å (**Table 2.5, paragraph 2.2.4, Chapter 2**). From a difference map, the hydroxyl H is shown to be approximately 0.615 Å further away from O1 than from O2 with O2-H *ca* 0.942 Å.

3.4 Rh(I) and Rh(III) complexes.

3.4.1 Synthesis of thienyl-containing β-diketonato Rh complexes.

3.4.1.1 Introduction

The Rh(I) and Rh(III) complexes synthesized in this study are of the form [Rh^{I}(β-diketonato)$(CO)_2$], [Rh^{I}(β-diketonato)(CO)(PPh_3)] and [Rh^{III}(β-diketonato)(CO)(PPh_3)(Me)(I)]. The β-diketonato ligands used are of the form $ThCOCH_2COR$ with R = Th, Ph and CF_3. The general synthetic route for these thienyl-containing β-diketonato Rh complexes (complexes **{3}**, **{5}**, **{6}** and **{8}** new, **{4}** and {7}[29,30,31,32] known) is given in **Scheme 3.4**.

---

[28] S. Yamabe, N. Tsuchida, K. Kiyajima, J. Phys. Chem. A 108 (2004) 2750.

[29] Y.S. Varshavsky, I.A. Poletaeva, T.G. Cherkasova, L.S. Podkorytov, Rhodium Express 14 (1995) 10.

[30] A.M. Trzeciak, J.J. Ziółkowski, Inorg. Chim. Acta 96 (1985) 15.

[31] I.A. Poletaeva, T.G. Cherkasova, L.V. Osetrova, Y.S. Varshavsky, A. Roodt and J.G. Leipoldt, Rhodium Express 3 (1994) 21.

[32] J.G. Leipoldt, L.D.C. Bok, J.S. van Vollenhoven, A.I. Pieterse, J. Inorg. Nucl. Chem. 40 (1978) 61.

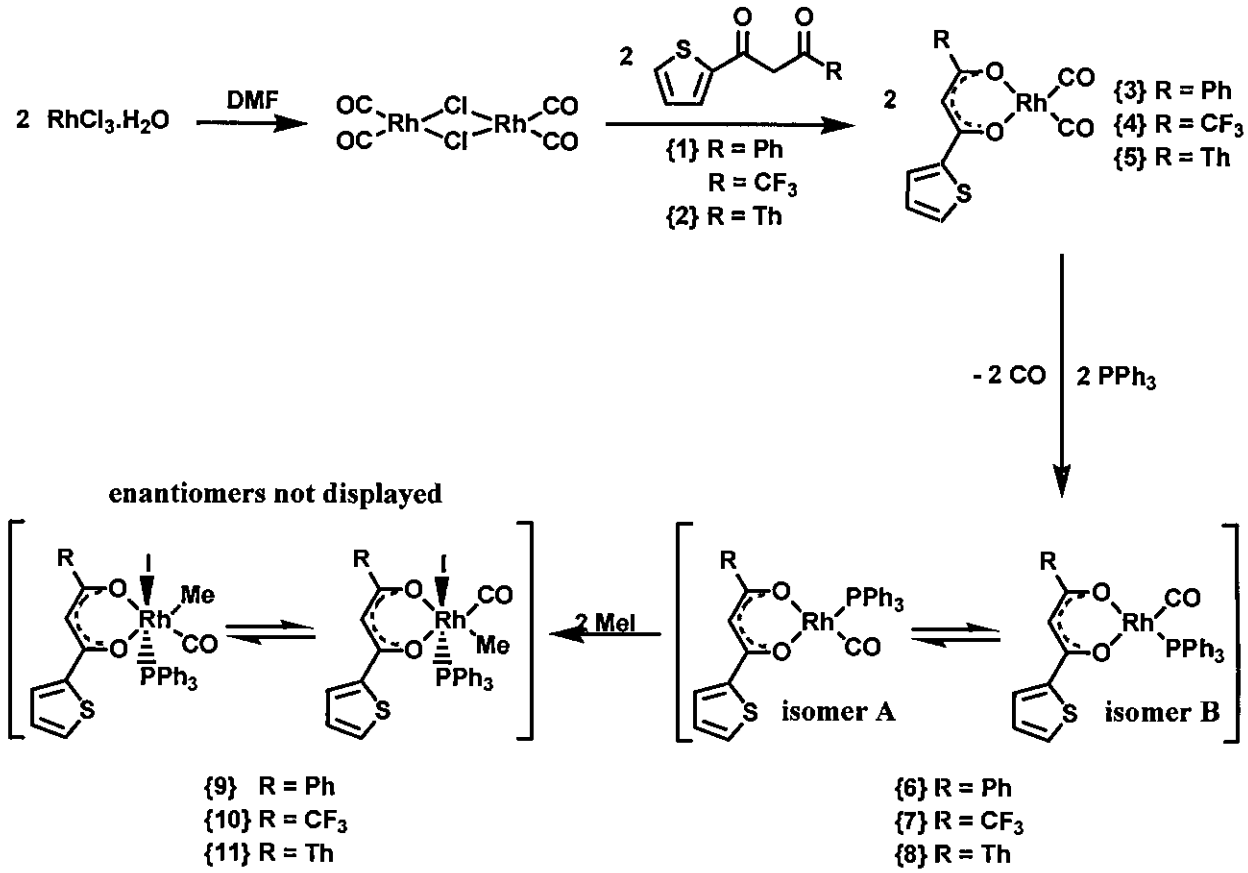

Scheme 3.4: Synthetic route for the synthesis of [Rh^{I}(β-diketonato)$(CO)_2$], [Rh^{I}(β-diketonato)$(CO)(PPh_3)$] and [Rh^{III}(β-diketonato)$(CO)(PPh_3)(Me)(I)$] from $RhCl_3.H_2O$.

3.4.1.2 Synthesis of Rh(I) complexes.

Rhodium(III) chloride trihydrate ($RhCl_3.3H_2O$) was dissolved in a few drops of water, due to the weak solubility in the reaction solvent and reduction agent, N,N-Dimethylformamide (DMF). Distilled DMF was added to the $RhCl_3.3H_2O$ solution and refluxed for *ca* 30 minutes until the reaction mixture colour changed from dark red to light yellow.[33] The light yellow colour[34] was due to the formation of the Rh(I) dimer, as illustrated in **Scheme 3.4**. The reaction solvent and reduction agent DMF can be used as a source of CO, since DMF decomposes into $HN(CH_3)_2$ and CO upon thermolysis, as illustrated in **Scheme 3.5**.[35]

---

[33] J.G. Leipoldt, S.S. Basson, L.D.C. Bok, T.I.A. Gerber, Inorg. Chim. Acta, 26 (1978) L35.

[34] J.S. McCleverty, G. Wilkonson, Inorg. Synth. 211 (1966).

[35] J.A. Davies, C.M. Hockensmith, V.Y. Kykyshkin, Y.N. Kukushkin, Synthetic Coordination Chemistry, Principles and Practive, Singapore, 1996, Chapter 9.

Scheme 3.5: Decomposition of DMF into $HN(CH_3)_2$ and CO.

The respective β-diketones (Hbth **{1}**, Hdtm **{2}** and Htta) were added to the Rh(I) dimer solution in a 2:1 mole ratio and stirred for 30 minutes. The Rh(I) carbonyl complexes bth **{3}**, tta **{4}** and dtm **{5}** (**Scheme 3.4**) were precipitated by the addition of ice cold water. The precipitate was washed with water and dried. Red crystals of bth **{3}** and tta **{4}** were recrystallized from hexane and blue-purple crystals of dtm **{5}** were recrystallized from chloroform. The crystals were characterized by means of IR and ^{1}H NMR. The crystal structure of $[Rh^I(dtm)(CO)_2]$ **{5}**, as representative example of the thienyl-containing β-diketonato Rh(I) dicarbonyl complexes in this study, was solved and will be discussed in **paragraph 3.4.4.** The properties and yields of the $[Rh^I(\beta\text{-diketonato})(CO)_2]$ complexes are given in **Table 3.11.**

The $[Rh^I(\beta\text{-diketonato})(CO)_2]$ complexes were dissolved in a minimal quantity of warm hexane in the case of bth **{3}** and tta **{4}** and in chloroform in the case of dtm **{5}**. Triphenyl phosphine (PPh_3), dissolved in the reaction solvent, was added to the reaction mixture in a 1:1 mole ratio. The Rh(I) carbonyl phosphine complexes bth **{6}** and tta **{7}** (**Scheme 3.4**) precipitated out of the solution and the remaining reaction solvent was removed by decantation. In the case of dtm **{8}**, the product stayed in solution and the reaction solvent was removed by evaporation. The formation of CO gas during the reaction can be used as a way to monitor the reaction progress. The yellow products were characterized by means of IR and NMR. Both isomers A and B (as defined in **Scheme 3.4**) of the complex $[Rh^I(\beta\text{-diketonato})(CO)(PPh_3)]$ exist in solution and each gives rise to a singlet methine peak on the ^{1}H NMR, except for dtm **{8}**, which is symmetrical and therefore only has one isomer. The methine signals of $[Rh^I(\beta\text{-diketonato})(CO)(PPh_3)]$ complexes are in the aromatic region above 6.4 ppm. This is due to the pseudo aromatic metallocyclic ring to which it is bound. The properties and yields of the $[Rh^I(\beta\text{-diketonato})(CO)(PPh_3)]$ complexes are given in **Table 3.11** and **Table 3.12.**

Table 3.11: Characteristic data and results of the [Rh^{I}(β-diketonato)(CO)$_2$] and [Rh^{I}(β-diketonato)(CO)(PPh$_3$)] synthesis.

[Rh^{I}(β-diketonato)(CO)$_2$]	Yield	^{1}H NMR methine (CH) / ppm [a]	ν_{CO} / cm^{-1}	m.p.
dtm {5}	89.6%	6.75	1992, 2057	149.2-149.9
bth {3}	80.5%	6.85	1996, 2058	147.2-148.8
tta {4}	57.3%	6.58	2008, 2026, 2033, 2078, 2098	134.3-134.7
[Rh^{I}(β-diketonato)(CO)(PPh$_3$)]	Yield	^{1}H NMR methine (CH) / ppm [a, b]	ν_{CO} / cm^{-1}	m.p.
dtm {8}	71.3%	6.65	1971	180.0-181.5
bth {6}	66.7%	6.75, 6.75	1970, 1980	189.1-189.5
tta {7}	40.1%	6.42, 6.43	1981	181.9-182.4

a In $CDCl_3$

b Two isomers each, except for complex {8} which is symmetrical

Table 3.12: Chemical shift δ (ppm) and coupling constants, *J*(Rh-P), in ^{31}P NMR spectra of synthesized [Rh^{I}(β-diketonato)(CO)(PPh$_3$)] complexes in $CDCl_3$. Also given is the chemical shift δ (ppm) of the CF_3 group in the ^{19}F NMR spectrum for [Rh^{I}(tta)(CO)(PPh$_3$)] {7} in $CDCl_3$.

[Rh^{I}(β-diketonato)(CO)(PPh$_3$)]	^{31}P NMR / ppm [a]	*J*(Rh-P) / Hz	^{19}F NMR / ppm [a]
dtm {8}	47.61	176	
bth {6}	47.41, 49.21	176, 177	
tta {7}	47.61, 47.66	177, 177	-74.48, -74.12

a In $CDCl_3$

Using the yields in **Table 3.11** and the group electronegativity from **Table 3.1**, a linear relationship between the yield of the Rh(I) complexes and the group electronegativity of the R group was found as illustrated in **Figure 3.18**.

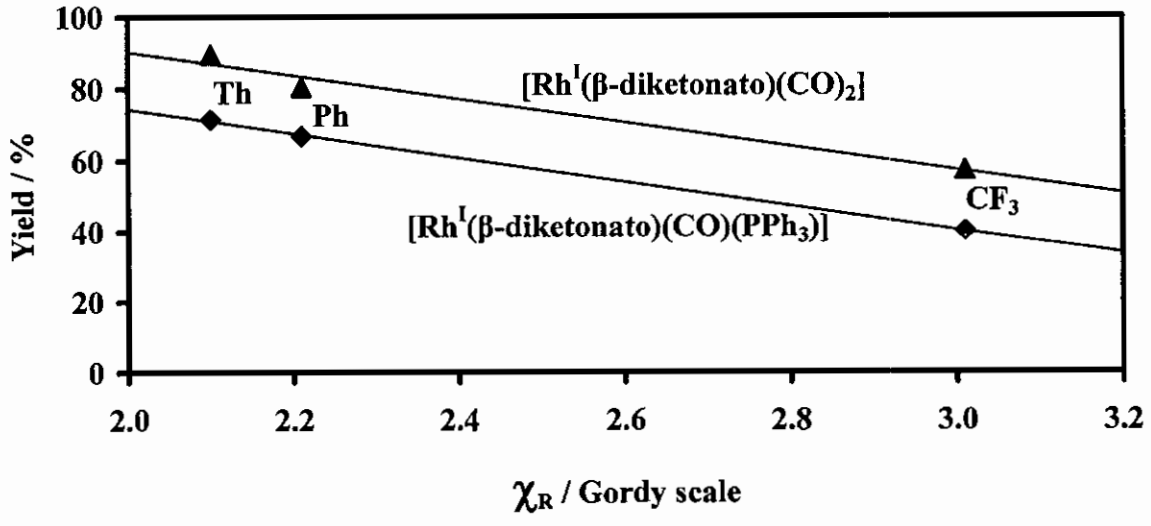

Figure 3.18: Linear relationship observed between group electronegativities (χ_R) and the yield the [Rh^{I}(β-diketonato)(CO)$_2$] complexes.

Another relationship that can be observed in **Table 3.11** is that between the electronegativity of the R groups in β-diketonato ligand and the IR stretching frequency (ν_{CO}) of the carbonyl groups bonded to the Rh. An increase in electronegativity of R, as moving from top to bottom in **Table 3.11**, causes the Rh-C bond to weaken and the C-O bond to strengthen, resulting in the shift of the ν_{CO} band to a higher frequency. This tendency was the strongest in the dicarbonyl [Rh^{I}(β-diketonato)$(CO)_2$] complexes. The dicarbonyl complexes give an IR spectrum with two distinctive singlet ν_{CO} peaks, one for the symmetrical and one for the asymmetrical carbonyl stretching. The five peaks in [Rh^{I}(tta)$(CO)_2$] have also been observed by Trzeciak *et al.*[30] The origin of these five peaks is unfortunately unknown. Replacement of one of these CO groups with PPh_3 results in a carbonyl phosphine [Rh^{I}(β-diketonato)$(CO)(PPh_3)$] complex. Subsequently only one ν_{CO} peak is observed, represented by the one CO group. Once again, the origin of the extra peak in [Rh^{I}(bth)$(CO)(PPh_3)$] is unknown.

The ^{31}P NMR spectra of the [Rh^{I}(β-diketonato)$(CO)(PPh_3)$] complexes in **Table 3.12** are a rich source of information about the phosphorous ligand coordinated in the complexes. The chemical shifts[36] and especially the coupling constants, J(Rh-P), are very sensitive to electron density variations on rhodium ions. This information is especially of aid when following the oxidative addition of MeI, as discussed in **paragraph 3.5**. The data in **Table 3.12** indicate that the change of the β-diketone in the [Rh^{I}(β-diketonato)$(CO)(PPh_3)$] complex has very little effect on the chemical shift and, within experimental error, none on the coupling constant values. The spectra exhibit two doublets (due to Rh-P coupling) for bth **{6}** and tta **{7}** - one for each isomer. In the case of dtm **{8}** which only has one isomer (as mentioned before), there is only one doublet. The chemical shift varied between 47 and 50 ppm and the coupling constant was either 176 or 177 Hz. ^{31}P and J(Rh-P) values (47.61, 47.66 ppm and 177, 177 Hz in $CDCl_3$) obtained for tta **{7}** in this study are consistent with results of Trzeciak *et al.*[30] (47.1, 47.6 ppm and 179.7, 175.8 Hz in C_6D_6) and Poletaeva *et al.*[31] (47.84, 47.78 ppm and 177.7, 176.7 Hz in $CDCl_3$). The ^{19}F NMR spectrum of tta **{7}** exhibits two singlets – one for each isomer's CF_3 group.

---

[36] P. Diehl, E. Pluck, R. Kosfeld, Basic Principles and Progress, Springer Verlag, Berlin-Heidelberg-New York, 1979.

3.4.1.3 Synthesis of Rh(III) complexes.

Upon the addition of MeI to a [Rh^{I}(β-diketonato)(CO)(PPh_3)] complex, various Rh(III) products are formed, differing in their spatial arrangements. The complete mechanism and kinetics of the reactions are discussed in **paragraph 3.5**. The main product that eventually forms is an octahedral alkyl species [Rh^{III}(β-diketonato)(CO)(PPh_3)(Me)(I)]. This product was characterized by 1D and 2D NMR experiments. As a representative example, [Rh^{III}(tta)(CO)(PPh_3)(Me)(I)] **{10}** will be discussed in detail.

The ^{1}H NMR spectra of [Rh^{III}(tta)(CO)(PPh_3)(Me)(I)] **{10}** in $CDCl_3$ and in acetone-d_6 are given in **Figure 3.19** and **Figure 3.20**, respectively. Two isomers were observed in a ratio of 1:1 in both solvents. The equilibrium showed no dynamic character at the investigated temperatures (-10 to 55 °C) and solvents ($CDCl_3$ and acetone-d_6).

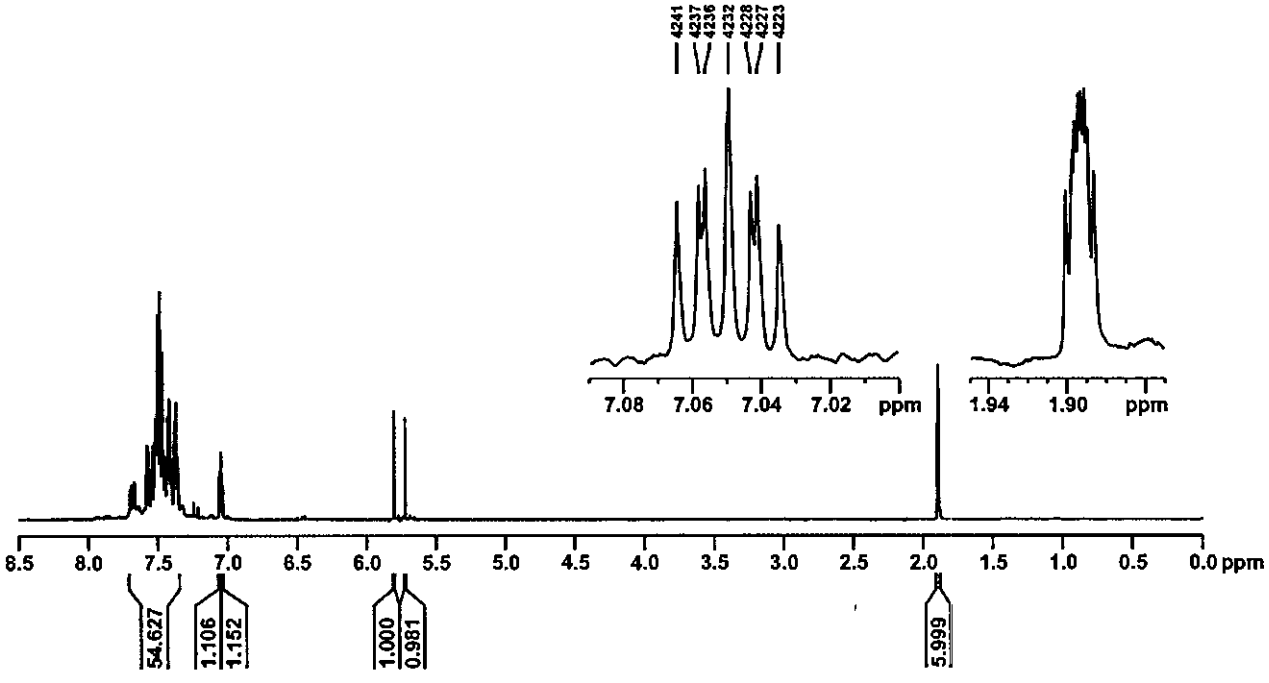

Figure 3.19: ^{1}H NMR of [Rh^{III}(tta)(CO)(PPh_3)(Me)(I)] in $CDCl_3$ at 25 °C. $CDCl_3$ peak is suppressed for clarity.

In $CDCl_3$ at 25 °C, the signal of the methine proton of the β-diketonato ligand in [Rh^{III}(tta)(CO)(PPh_3)(Me)(I)] **{10}** is presented as singlets at 5.72 and 5.80 ppm (one for each isomer). The corresponding signals of [Rh^{I}(tta)(CO)(PPh_3)] **{7}** are at 6.42 and 6.43 ppm. A chemical shift of 6.4 ppm resonates in the aromatic region, implying that the O-C-C-C-O backbone of the β-diketonato ligand in [Rh^{I}(tta)(CO)(PPh_3)] has a pseudo aromatic character (as discussed in **paragraph 3.3.1**). The pseudo aromatic character of the core of the β-diketonato

ligand is also clear from the crystal structure of [Rh^{I}(tta)(CO)(PPh_3)] {7}[32], showing a C=C bond of 1.345 Å (more double bond character) and a C-C bond of 1.432 Å (more single bond character) next to the methine proton. The chemical shift of the methine protons in [Rh^{III}(tta)(CO)(PPh_3)(Me)(I)] **{10}** at 5.72 and 5.80 ppm (one for each isomer), however, lies in the aliphatic region, implying that the aromaticity of the pseudo aromatic core of the β-diketonato ligand is destroyed while changing from [Rh^{I}(tta)(CO)(PPh_3)] {7} to [Rh^{III}(tta)(CO)(PPh_3)(Me)(I)] **{10}**. A possible explanation for this change in aromaticity, which results in a change of almost 0.7 ppm in the chemical shift, will be given at the end of this section after the discussion on the NOESY spectra of [Rh^{III}(tta)(CO)(PPh_3)(Me)(I)] **{10}**.

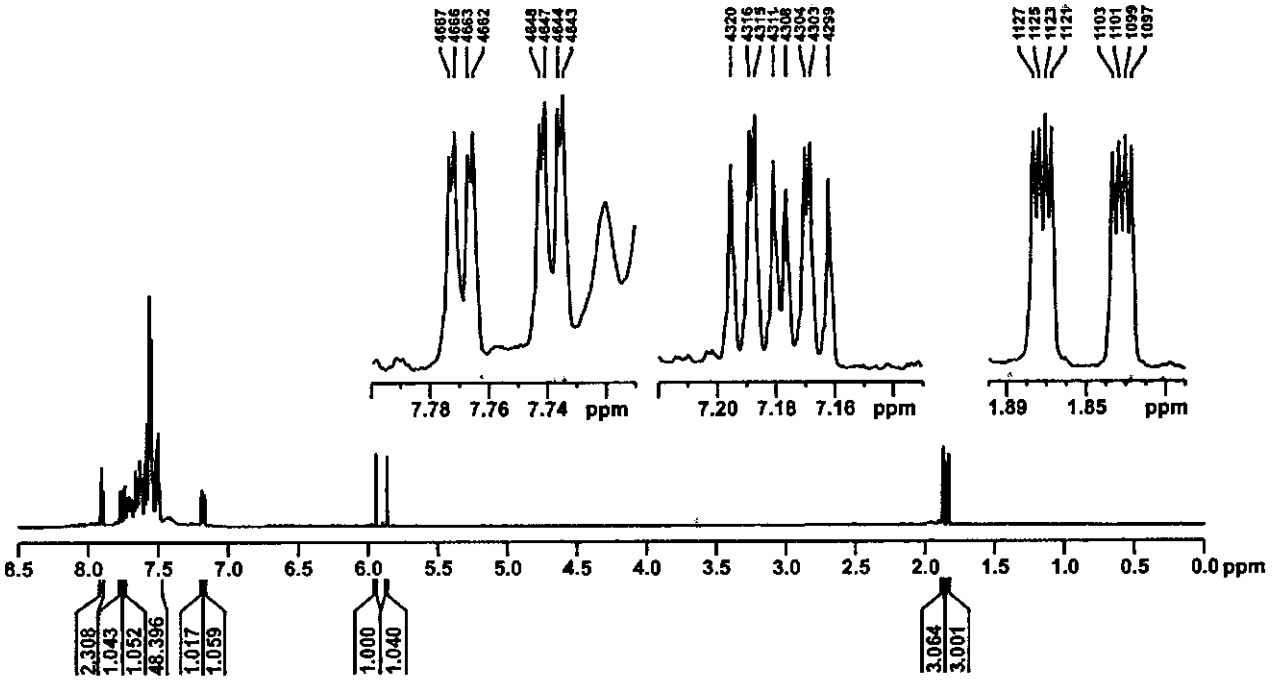

Figure 3.20: ^{1}H NMR of [Rh^{III}(tta)(CO)(PPh_3)(Me)(I)] in acetone-d_6 at 25 °C. Acetone-d_6 peak is suppressed for clarity.

In acetone-d_6 at 25 °C, the quartets of each of the methyl groups of the two isomers of [Rh^{III}(tta)(CO)(PPh_3)(Me)(I)] **{10}** can clearly be distinguished at 1.83 and 1.87 ppm (**Figure 3.20**), but they overlap in $CDCl_3$ at 1.89 ppm (**Figure 3.19**). The multiplet for the methyl group is due to the Rh-H and P-H coupling.[37] The signal of one set of the thienyl protons (one for each isomer) with a coupling of (^3J = 5 Hz, ^3J = 4 Hz) can be observed at 7.04 and 7.06 ppm (in $CDCl_3$) and at 7.17 and 7.19 ppm (in acetone-d_6) as a doublet of doublets (see **paragraph 3.4.2** for a discussion on the chemical shifts of the thienyl protons in $CDCl_3$). The

[37] C.A. Reilly, H. Thyret, J. Am. Chem. Soc., 89 (1967) 5144.

other thienyl protons overlap in $CDCl_3$ with the aromatic phenyl protons at 7.3 – 7.7 ppm. In acetone-d_6 another set of thienyl protons with a coupling of (^3J = 4 Hz, ^4J = 1 Hz) can be observed at 7.74 and 7.77 ppm. **Figure 3.21** shows a section of the 2D ^{1}H TOCSY of [Rh^{III}(tta)(CO)(PPh_3)(Me)(I)] **{10}** in $CDCl_3$. From the scalar coupling through the bonds of the thienyl protons at 7.04 and 7.06 ppm, it follows that the signals at 7.45 and 7.46 ppm and 7.57 and 7.58 ppm represent the other two sets of thienyl protons.

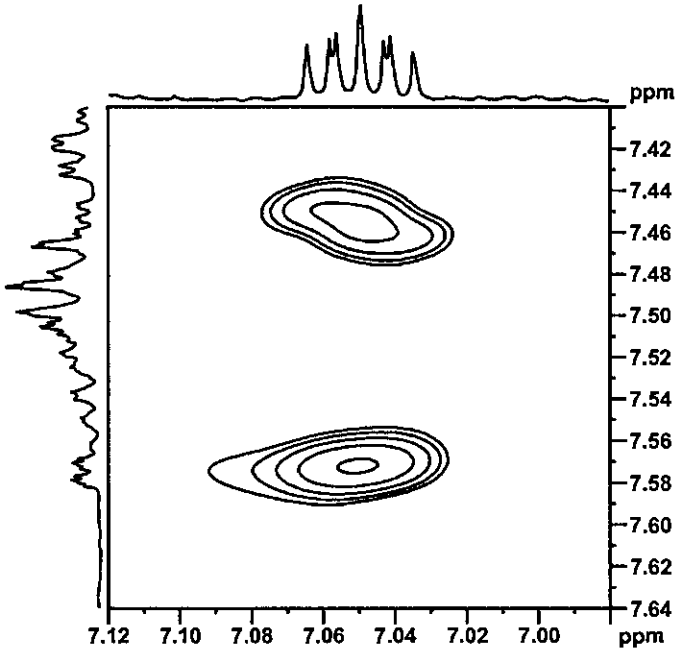

Figure 3.21: A section of the 2D ^{1}H TOCSY spectrum of [Rh^{III}(tta)(CO)(PPh_3)(Me)(I)] **{10}** in $CDCl_3$ at 25 °C. Scalar coupling between thienyl protons can be observed.

1D ^{1}H NOESY's were recorded to establish the relative dispositions of the ligands in [Rh^{III}(tta)(CO)(PPh_3)(Me)(I)] **{10}** and are given in **Figure 3.22** and **Figure 3.23**.

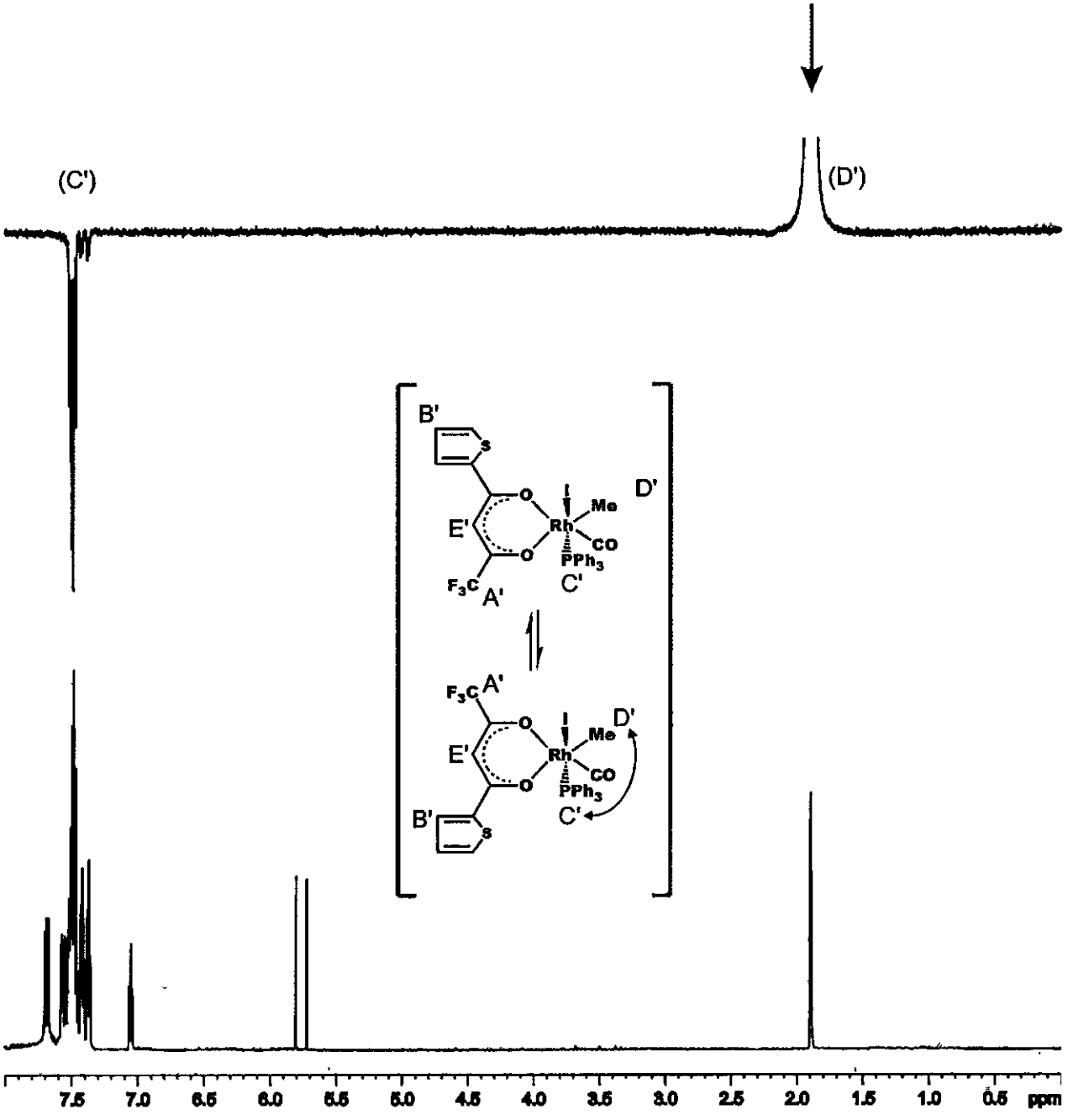

Figure 3.22: 1D ^{1}H NOESY (top) of [Rh^{III} (tta)(CO)(PPh_3)(Me)(I)], pulsing on the methyl group as indicated by the blue arrow. ^{1}H NMR spectrum (bottom) of [Rh^{III} (tta)(CO)(PPh_3)(Me)(I)]. Peaks are as indicated, PPh_3 and I groups can be switched around as well as the I and the CO group. $CDCl_3$ peak is suppressed for clarity.

Theoretically calculated (**Figure 3.102, paragraph 3.6.4**), 12 alkyl isomers (excluding enantiomers) are possible. When pulsing on the methyl group of [Rh^{III}(tta)(CO)(PPh_3)(Me)(I)] **{10}**, as illustrated in **Figure 3.22**, a strong coupling with the PPh_3 protons is observed. This 1D ^{1}H NOESY result is only possible if the Me group is adjacent to the PPh_3 group. This rules out the possiblitity that both the Me and PPh_3 groups are above and below the plane and leaves one with only 10 of the 12 possible alkyl isomers (excluding enantiomers).

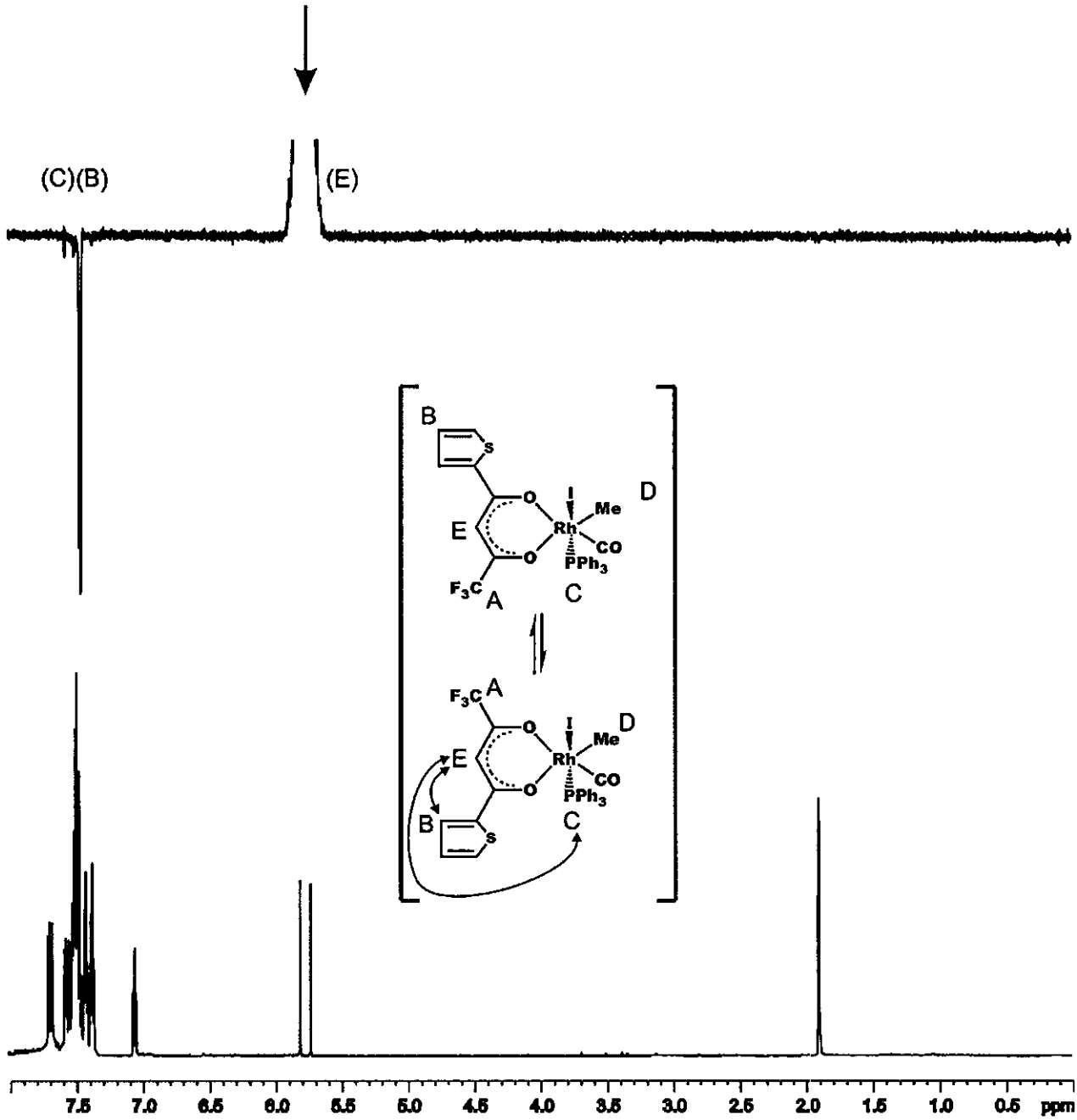

Figure 3.23: 1D ^{1}H NOESY (**top**) of [Rh^{III}(tta)(CO)(PPh$_3$)(Me)(I)] **{10}**, pulsing on the methine proton as indicated by the blue arrow. ^{1}H NMR spectrum (**bottom**) of [Rh^{III} (tta)(CO)(PPh$_3$)(Me)(I)] **{10}**. Peaks are as indicated, PPh$_3$ and I groups can be switched around as well as the I and the CO groups. CDCl$_3$ peak is suppressed for clarity.

When pulsing on the methine proton of [Rh^{III}(tta)(CO)(PPh$_3$)(Me)(I)] **{10}**, as illustrated in **Figure 3.23**, a strong coupling with one of the thienyl protons and a weak coupling with some of the PPh$_3$ protons are observed. This 1D ^{1}H NOESY result is only possible if the PPh$_3$ group is below (or above) the plane. Taking into account the result of the previous 1D ^{1}H NOESY (**Figure 3.22**), the Me group must therefore be in the plane.

From the 1D ^{1}H NOESY spectra it is not possible to establish whether the CO group or the I is adjacent to the PPh_3 group, since these groups do not contain any protons. It is thus clear that the octahedral alkyl species [Rh^{III}(tta)(CO)(PPh_3)(Me)(I)] **{10}** exists with the I and PPh_3 group above and below the plane or with the CO and PPh_3 groups above and below the plane. This results in 4 possible alkyl isomers (plus four enantiomers) as illustrated in **Figure 3.24**. The data in the top row are consistent with the type II crystal structures discussed in **paragraph 2.3.7.3, Chapter 2**.

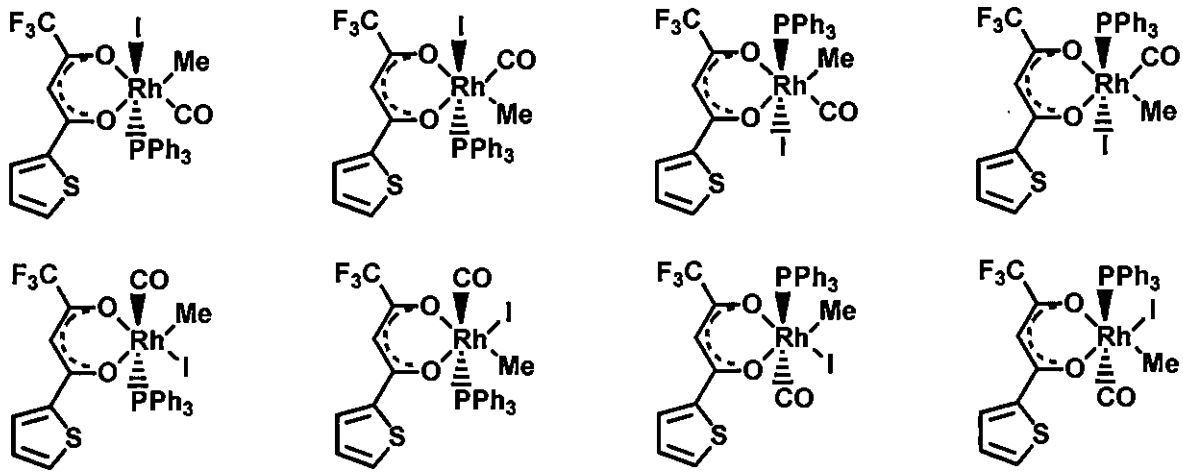

Figure 3.24: Possible structures of [Rh^{III} (tta)(CO)(PPh_3)(Me)(I)] **{10}**. The four complexes on the right are the enantiomers of the four complexes on the left. The top row is consistent with the crystal structures of the alkyl type 2 complexes in **Chapter 2**.

The positioning of the PPh_3 group above or below the plane, implies that as the PPh_3 group rotates, a Ph group will be coplanar to the O-C-C-C-O backbone of the β-diketonato ligand (see **Figure 2.19, paragraph 2.3.7.3, Chapter 2** for similar crystal structures). The coplanar Ph group may interfere with the electron density on the O-C-C-C-O backbone, destroying the aromaticity of the pseudo aromatic core of the β-diketonato ligand. Thus, the aromatic character of the O-C-C-C-O backbone of the β-diketonato ligand in [Rh^{III}(tta)(CO)(PPh_3)(Me)(I)] **{10}** may be due to the positioning of the PPh_3 group with a Ph group coplanar to the O-C-C-C-O backbone. If the PPh_3 group was in the plane, the disruption of electron density by the Ph group would not have been possible. Thus, the observed shift of the methine proton of the β-diketonato ligand from the aromatic region (~6.4 ppm) to the aliphatic region (~5.7 ppm) is consistent with PPh_3 being positioned above or below the plane.

For example, the similar C-C bond lengths of 1.38 and 1.40 Å in the O-C-C-C-O backbone of the β-diketonato ligand of the Rh(III)-alkyl complex, $[Rh^{III}(fctfa)(CO)(PPh_3)(Me)(I)]$[38] with PPh_3 above the plane (**Figure 2.19, paragraph 2.3.7.3, Chapter 2**) are thus consistent with the observed lack of aromaticity and shift of this complex's methine proton's signal to 5.31 ppm which lie in the aliphatic region.

The ^1H and ^{31}P NMR data and carbonyl stretching frequencies of the $[Rh^{III}(\beta\text{-diketonato})(CO)(PPh_3)(Me)(I)]$ complexes are given in **Table 3.13**. The IR spectrum of $[Rh^{III}(tta)(CO)(PPh_3)(Me)(I)]$ **{10}** shows a carbonyl absorption band (ν_{CO}) at 2064 cm^{-1} in solution. This is 73 cm^{-1} higher than ν_{CO} = 1991 cm^{-1} for $[Rh^{I}(tta)(CO)(PPh_3)]$ **{7}** in solution. The shift to a higher ν_{CO} is characteristic of the transformation of a square planar Rh(I) complex to an octahedral Rh(III) species as a result of the weaker π backbonding in Rh(III) complexes compared to Rh(I) complexes, as discussed in **paragraph 2.3.4.**[39]

Table 3.13: Chemical shift δ (ppm) of methine protons in the ^1H and ^{31}P NMR spectra of the $[Rh^{III}(\beta\text{-diketonato})(CO)(PPh_3)(Me)(I)]$ alkyl type 2 complexes.

$[Rh^{III}(\beta\text{-diketonato})(CO)(PPh_3)(Me)(I)]$	^1H NMR methine (CH) / ppm [a]	^{31}P NMR / ppm [a]	ν_{CO} / cm^{-1} [b]
dtm **{11}**	6.03	28.93	2056
bth **{9}**	6.09, 6.10	28.62, 29.21	2056
tta **{10}**	5.73, 5.80	27.07, 28.74	2064

a In $CDCl_3$
b In $CHCl_3$

3.4.2 ^1H NMR study of thienyl group.

When looking at the ^1H NMR spectra of the thienyl-containing β-diketones and Rh(I) complexes, a very distinct pattern concerning the thienyl protons can be observed. The thienyl group contains three protons, as illustrated in **Figure 3.25**. For the independent verification of the assignment of the H^a and H^c resonances in the spectrum, a ^1H NOESY experiment was preformed. A simultaneous saturation of the methine protons of both isomer A and B of $[Rh^{I}(tta)(CO)(PPh_3)]$ **{7}** at 6.42 – 6.43 ppm gave a signal for the doublet of doublets centred at 7.18 ppm (isomer B) and 7.75 ppm (isomer A) and no signals for the rest of the thienyl protons.

---

[38] G.J. Lamprecht, J.C. Swarts, J. Conradie, J.G. Leipoldt, Acta Crystallogr., Sect. C: Cryst. Struct. Commun. 49 (1993) 82.

[39] J.A. Gaunt, V.C. Gibson, A. Haynes, S.K. Spitzmesser, A.J.P. White, D.J. Williams, Organometallics, 23 (2004) 1015.

Therefore, the H^c proton is most likely to be spaced closest to the methine proton, which is consistent with the findings of Varshavsky *et al.*[29]

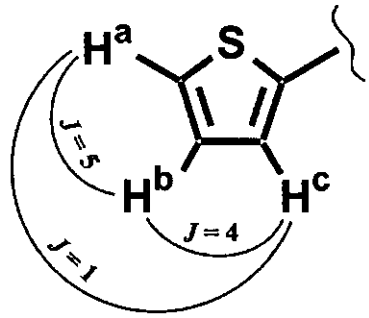

Figure 3.25: Protons in the thienyl group, with coupling constant *J*.

Since the protons are within four bond lengths from one another, each proton's ^1H NMR signal will be split into a doublet of doublets. The coupling constants are as follow: H^a (^3J = 5 Hz, ^4J = 1 Hz), H^b (^3J = 5 Hz, ^3J = 4 Hz) and H^c (^3J = 4 Hz, ^4J = 1 Hz). This information is very useful in solving ^1H NMR spectra of thienyl-containing complexes. To distinguish between the thienyl peaks of the different isomers A and B of the [Rh^I(β-diketonato)(CO)(PPh_3)] complex, 2D ^1H NOESY's were preformed (not illustrated). ^1H NMR spectra of the thienyl-containing ligands and complexes of this study are given in **Figure 3.26**, **Figure 3.28** and **Figure 3.30**. Data are summarized in **Table 3.14**.

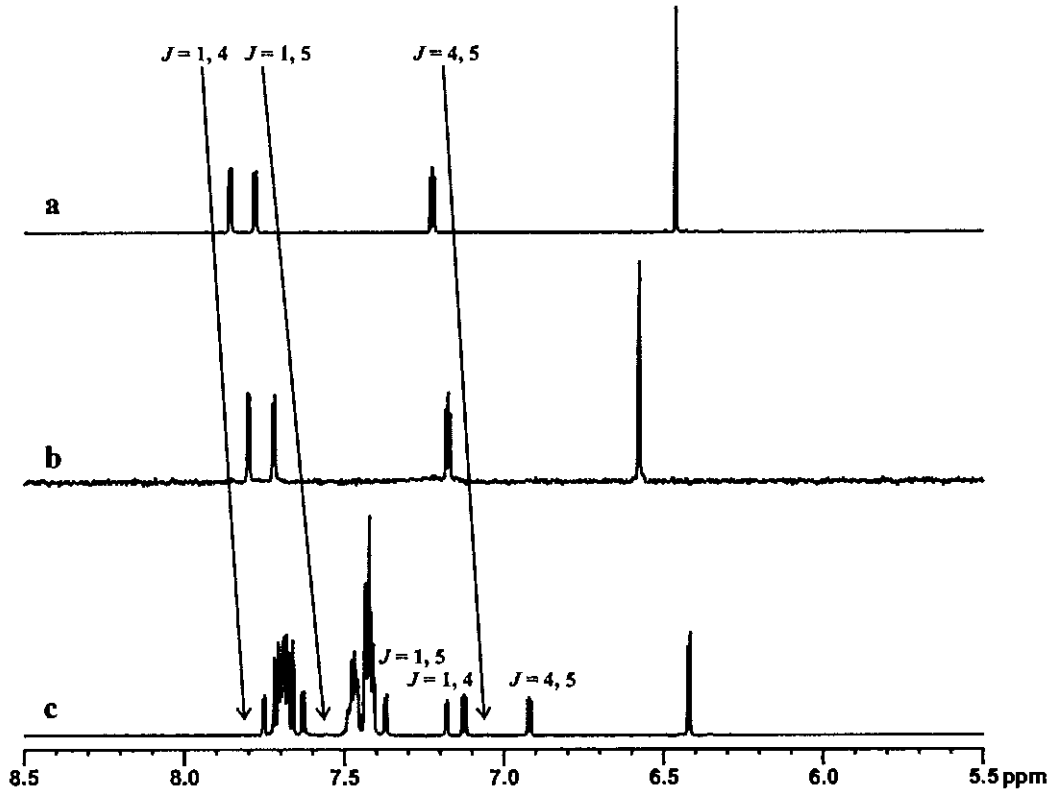

Figure 3.26: ^1H NMR spectra of tta series in $CDCl_3$. **a)** β-diketone, **b)** [Rh^I(β-diketonato)$(CO)_2$] and **c)** [Rh^I(β-diketonato)(CO)(PPh_3)]. Thienyl signals are colour coded. $CDCl_3$ peak is suppressed for clarity.

It is easiest to consider the ^{1}H NMR spectra of tta series first, since all the thienyl peaks are separated from the PPh_3 signals in the [Rh^I(tta)(CO)(PPh_3)] spectrum. Proton H^b lies more high field (to the right of the spectrum), proton H^a lies in the middle more low field and proton H^c lies most low field (to the left of the spectrum) as indicated by the red peaks in **Figure 3.26.** The sulphur atom has a strong deshielding effect, which will result in a chemical shift more low field. One would therefore expect that the H^a proton, which lies next to the sulphur atom, would lie more low field than the H^c proton. This is not the case in these spectra. Although, when the sulphur atom is in a five-membered unsaturated heterocycle, its chemical properties are not consistent with other sulphur-containing systems. Unlike most sulphur-containing systems, thiophene is not basic.[40] It is thus possible that the H^c proton lies more low field than the H^a proton. In **Figure 3.26.c** an extra set of green peaks exits. The two sets of peaks belong to the two isomers (A and B) of [Rh^I(tta)(CO)(PPh_3)]. The PPh_3 group of the one isomer shields the thienyl protons through space, causing the protons to move more high field. Therefore, the green set of peaks belongs to isomer B and the red set of peaks belongs to isomer A, as indicated in **Figure 3.27.**

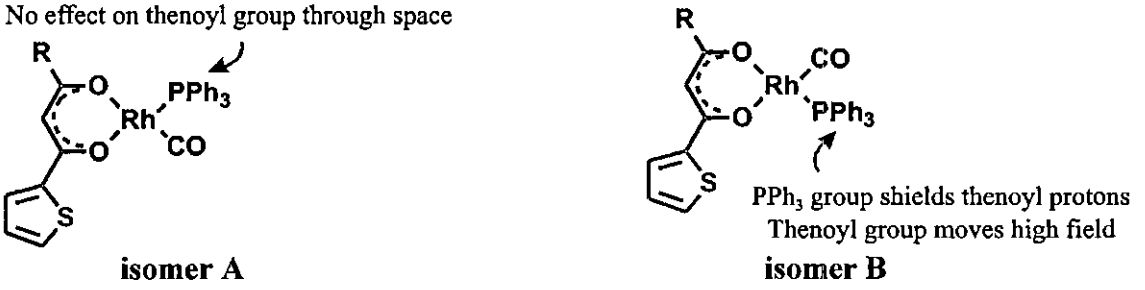

Figure 3.27: PPh_3 influence on the thienyl groups of the isomers of [Rh^I(β-diketonato)(CO)(PPh_3)].

[40] J. McMurry, Organic Chemistry, Sixth edition, Brooks/Cole-Thomson Learning, Belmont, 2004, p. 899, 1061.

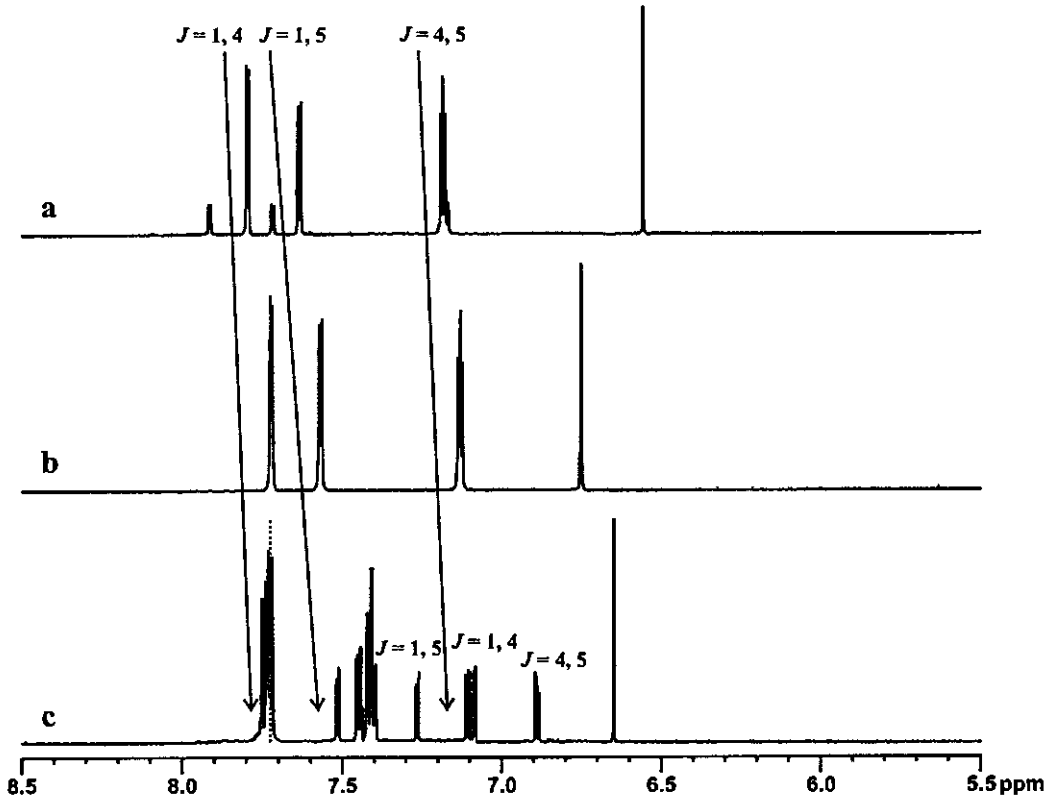

Figure 3.28: ^{1}H NMR spectra of dtm series in $CDCl_3$. **a)** β-diketone, **b)** [Rh^I(β-diketonato)$(CO)_2$] and **c)** [Rh^I(β-diketonato)$(CO)(PPh_3)$]. Thienyl signals are colour coded. $CDCl_3$ peak is suppressed for clarity.

The dtm ^{1}H NMR series (**Figure 3.28**) shows the same tendency as the tta series (**Figure 3.26**), with the difference that one of the thienyl peaks (H^c) in **Figure 3.28.c** overlaps with the PPh_3 signal at 7.74. By looking at the tendency and by performing a *J* resolved experiment, the position of the H^c thienyl proton was determined and is indicated by the dotted red line. The small black peaks in **Figure 3.28.a** belong to the keto isomer of the β-diketone, as discussed in **paragraph 3.3.2**. Since [Rh^I(dtm)$(CO)(PPh_3)$] has only one isomer, the green set of peaks belongs to the thienyl group opposite to the PPh_3 group, as illustrated in **Figure 3.29**.

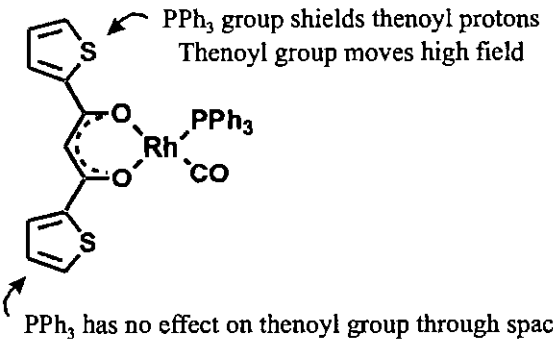

Figure 3.29: PPh_3 influence on the thienyl group of [Rh^I(dtm)$(CO)(PPh_3)$].

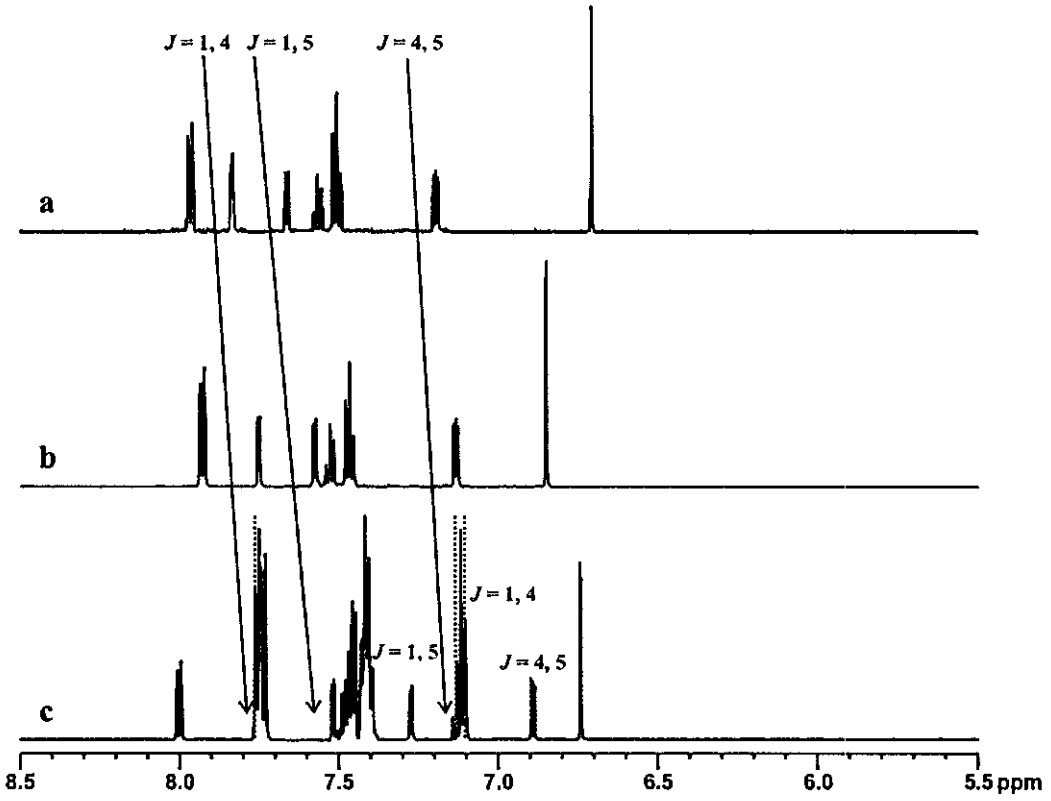

Figure 3.30: ^{1}H NMR spectra of bth series in $CDCl_3$. a) β-diketone, b) [Rh^I(β-diketonato)$(CO)_2$] and c) [Rh^I(β-diketonato)(CO)(PPh_3)]. Thienyl signals are colour coded. $CDCl_3$ peak is suppressed for clarity.

Once again the same tendency in the bth series (**Figure 3.30**) is observed, but three of the thienyl peaks overlap with the other peaks in **Figure 3.30.c**. Once again, the dotted lines show the position of the thienyl protons of the [Rh^I(bth)(CO)(PPh_3)] complex as determined by a *J* resolved experiment. The extra set of green peaks belongs to isomer B (**Figure 3.27**).

The data of the above spectra are summarized in **Table 3.14.**

Table 3.14: Summary of the spectra series in **Figure 3.26** (tta), **Figure 3.28** (dtm) and **Figure 3.30** (bth). Values determined by a *J* resolved experiment are placed in square brackets.

		β-diketone	[Rh^I(β-diketonato)$(CO)_2$]	[Rh^I(β-diketonato)(CO)(PPh_3)]	
				red [a]	green [a]
tta	H^b	7.23	7.18	7.13	6.92
	H^a	7.78	7.72	7.63	7.37
	H^c	7.86	7.80	7.76	7.18
dtm	H^b	7.18	7.13	7.11	6.89
	H^a	7.63	7.56	7.52	7.27
	H^c	7.79	7.72	[7.71]	7.08
bth	H^b	7.19	7.13	[7.11]	6.89
	H^a	7.66	7.58	7.52	7.27
	H^c	7.83	7.75	[7.76]	[7.10]

a As illustrated in **Figure 3.27** and **Figure 3.29**

3.4.3 Isomer equilibrium constant in Rh^{I} and Rh^{III} complexes.

The two isomers observed for each of the [Rh^{I}(β-diketonato)(CO)(PPh_3)] and [Rh^{III}(β-diketonato)(CO)(PPh_3)(Me)(I)] complexes, exist in a equilibrium with each other. This equilibrium is illustrated in **Figure 3.31**. Solvent and the temperature effects on these equilibriums were investigated for both the bth and tta complexes by means of ^{1}H NMR spectroscopy. The dtm complexes could not be subjected to this treatment, since they have only one isomer for each of the Rh(I) and Rh(III) alkyl complexes, due to the symmetrical β-diketonato ligand.

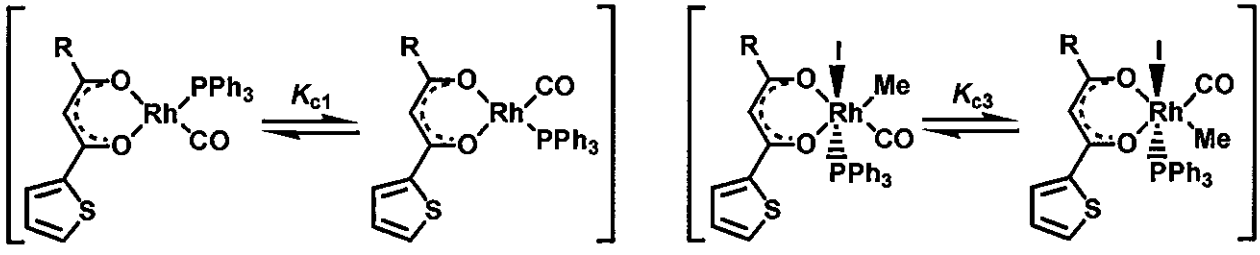

a) [Rh^{I}(β-diketonato)(CO)(PPh_3)] **b)** [Rh^{III}(β-diketonato)(CO)(PPh_3)(Me)(I)]

Figure 3.31: Equilibrium between isomers for thienyl-containing complexes.

The equilibrium constant (K_c) can be calculated according to **Equation 3.6**.

Equation 3.6: K_c = (% isomer B)/(% isomer A) = (100 - % isomer A)/(% isomer A)

The variation of the K_c value with temperature for the equilibrium shown in **Figure 3.31** can be mathematically quantified by

Equation 3.7: $$\ln K_{c(ii)} = \ln K_{c(i)} - \frac{\Delta_r H}{R}\left(\frac{1}{T_{(ii)}} - \frac{1}{T_{(i)}}\right)$$

where ln $K_{c(ii)}$ and ln $K_{c(i)}$ are the equilibrium constants at temperatures T_{ii} and T_i, R = 8.314 J K^{-1} mol^{-1} and $\Delta_r H$ the reaction enthalpy as defined elsewhere.[41,42] The thermodynamic quantity "Gibbs free energy", $\Delta_r G$, and reaction entropy, $\Delta_r S$, may be calculated from the equations $\Delta_r G = - R T \ln K_c$ and $\Delta_r G = \Delta_r H - T \Delta_r S$.[43] **Equation 3.7** aslo implies that

---

[41] S.H. Maron, J.B. Lando, Fundamentals of Physical Chemistry, Macmillan Publishing Co. Inc., New York, 1974, pp. 376-383.

[42] P.W. Atkins, Physical Chemistry, Fifth edition, Oxford University Press, Oxford, 1994, pp. 141-154, 288.

[43] P.W. Atkins, Physical Chemistry, Fifth edition, Oxford University Press, Oxford, 1994, pp. 141, 154, 276, 289.

a graph of ln K_c versus 1/T should be linear[42] with a slope equal to $-\Delta_r H$ / R. **Figure 3.32** illustrates this linearity for [Rh^I(tta)(CO)(PPh_3)] in $CDCl_3$. Changes in the temperature (-30 to 55 °C in $CDCl_3$) have little influence on the K_c value of [Rh^I(bth)(CO)(PPh_3)] and the [Rh^{III}(β-diketonato)(CO)(PPh_3)(Me)(I)] complexes of tta and bth. The observed equilibrium constants were concentration independent over a concentration range of ~ 0.05 - 3 mmol dm^{-3}. Results are summarized in **Table 3.15**.

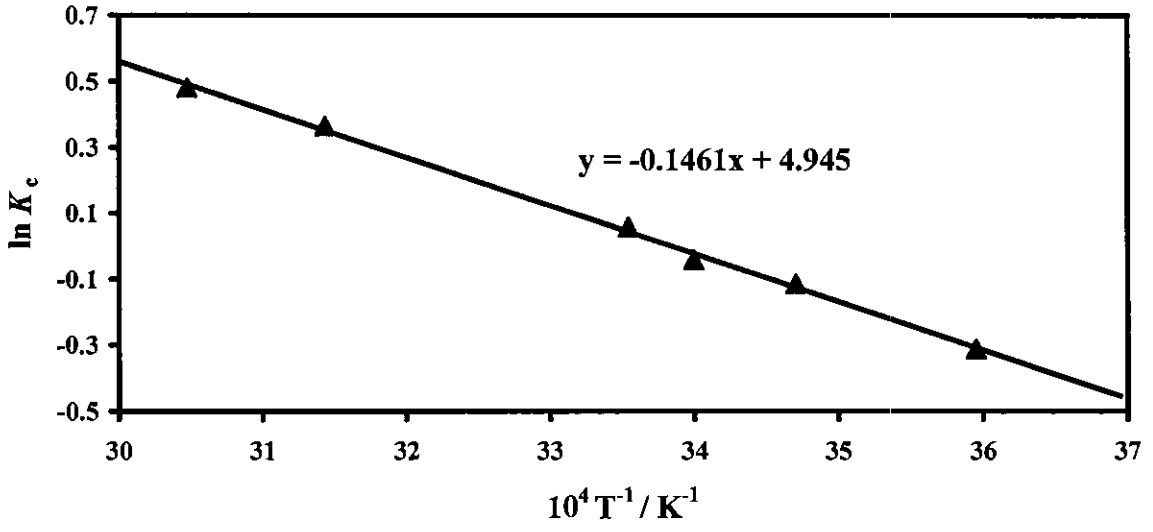

Figure 3.32: Temperature dependence of K_c for the equilibrium position between the two isomers of the [Rh(tta)(CO)(PPh_3)] complex. Slope of graph = -ΔrH / R.

Table 3.15: Equilibrium constants at various temperatures in different solvents for thienyl-containing [Rh^I(β-diketonato)(CO)(PPh_3)] and [Rh^{III}(β-diketonato)(CO)(PPh_3)(Me)(I)] complexes.

	[Rh^I(β-diketonato)(CO)(PPh_3)]		[Rh^{III}(β-diketonato)(CO)(PPh_3)(Me)(I)]	
	K_{c1} (tta)	K_{c1} (bth)	K_{c3} (tta)	K_{c3} (bth)
$CDCl_3$ [a]	1.05 [c, d]	1.0	1.0	1.4
Acetone [b]	1.5	0.8	1.0	1.3

a Temperatures between -30 and 55 °C
b Temperatures between -70 and 45 °C
c K_{c1} at 25 °C
d $\Delta_r H$ = 12.1 kJ mol^{-1}, $\Delta_r G$ = -111.2 J mol^{-1}, $\Delta_r S$ = 41.1 J mol^{-1} K^{-1}

3.4.4 Crystal structure data of [Rh(dtm)(CO)$_2$] {5}.

To further characterise the thienyl-containing β-diketonato-rhodium(I) complexes, results of a single crystal structure determination for [Rh(dtm)(CO)$_2$] (dicarbonyl(1,3-di(2-thenoyl)-1,3-propanedionato-κ^2O,O')rhodium(I)) are presented. The author acknowledges Dr. A.J. (Fanie) Muller of the Department of Chemistry, University of the Free State, for the data collection and refinement of the crystal structure.

The molecular diagram of [Rh(dtm)(CO)$_2$], showing atom labelling, is presented in **Figure 3.33**. The refinement of the data did not give satisfactory results, but for the purpose of this study the obtained data were regarded as sufficient. Crystal data for the structure of [Rh(dtm)(CO)$_2$] are summarized in **Table 3.16**, selected bond lengths, angles and torsion angles can be found in **Table 3.17**. The complete table of bond lengths and angles and the crystallographic data for the structural analysis are given in **Appendix B**. Selected comparative geometric data for square planar complexes of the type [Rh^I(R^1-CO-CH-CO'-R^2)(CO)$_2$], with R^1 and R^2 groups as indicated, are given in **Table 3.18.**

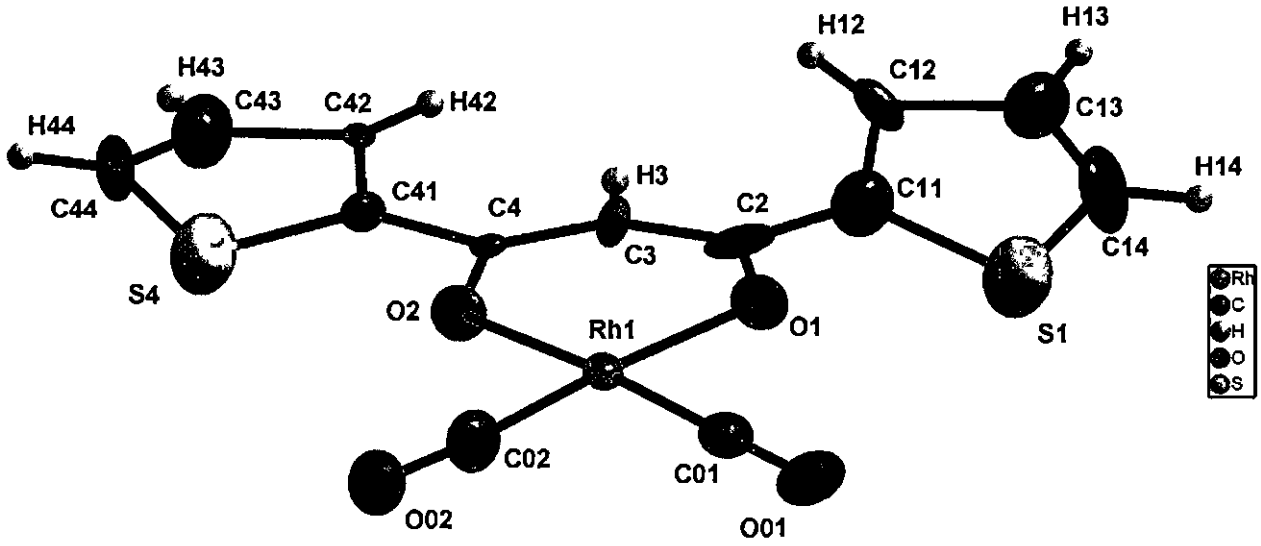

Figure 3.33: Molecular diagram of dicarbonyl(1,3-di(2-thenoyl)-1,3-propanedionato-κ^2O,O')rhodium(I) ([Rh(dtm)(CO)$_2$]) showing atom numbering and displacement ellipsoids of 50% probability.

Table 3.16: Crystal data and structure refinement for $[Rh(dtm)(CO)_2]$.

Empirical formula	$C_{13}H_7O_4RhS_2$	**Theta range for data collection**	10.27 to 26.36°
Formula weight	394.22 g mol^{-1}	**Index ranges**	-14<=h<=14 -7<=k<=6 -23<=l<=23
Temperature	100(2) K	**Reflections collected**	10495
Wavelength	0.71073 Å	**Independent reflections**	2636 [R(int) = 0.0447]
Crystal system	Orthorhombic	**Completeness to theta = 26.36°**	93.0 %
Space group	*P2na*	**Absorption correction**	Semi-empirical from equivalents
Unit cell dimensions	a = 11.409(5) Å b = 6.382(5) Å c = 19.101(5) Å α = 90° β = 90° γ = 90°	**Max. and min. transmission**	0.9272 and 0.5858
Volume	1390.8(13) $Å^3$	**Refinement method**	Full-matrix least-squares on F2
Z	4	**Data / restraints / parameters**	2636 / 133 / 181
Density (calculated)	1.883 Mg m^{-3}	**Goodness-of-fit on F^2**	1.144
Absorption coefficient (μ)	1.535 mm^{-1}	**Final R indices [I>2sigma(I)]**	R1 = 0.0868 wR2 = 0.2236
F(000)	776	**R indices (all data)**	R1 = 0.1167 wR2 = 0.2577
Crystal size	0.39 x 0.11 x 0.05 mm^3	**Largest diff. peak and hole**	4.402 and -1.576 e.$Å^{-3}$
-	-	**Absolute structure parameter**	0.38(16)

Table 3.17: Selected bond lengths (Å), bond angles (degree) and torsion angles (degree) for $[Rh(dtm)(CO)_2]$. Geometric parameters involving hydrogen atoms are omitted from this table.

Bond lengths / Å [a]					
Rh1-C02	1.78(2)	C41-C4	1.52(2)	O02-C02	1.28(2)
Rh1-C01	1.883(19)	O2-C4	1.273(19)	C3-C4	1.31(3)
Rh1-O2	2.006(11)	C2-O1	1.29(2)	C14-S1	1.62(2)
Rh1-O1	2.035(10)	C2-C3	1.34(3)	S1-C11	1.74(2)
Rh1-Rh1#1	3.177(3)	C2-C11	1.40(3)	C01-O01	1.26(3)
Bond angles / degree [a]					
C02-Rh1-C01	84.5(8)	C02-Rh1-Rh1#1	98.4(6)	C3-C2-C11	124.7(18)
C02-Rh1-O2	90.0(7)	C01-Rh1-Rh1#1	87.6(4)	C2-O1-Rh1	123.0(12)
C01-Rh1-O2	174.4(6)	O2-Rh1-Rh1#1	94.3(3)	C4-C3-C2	134.9(19)
C02-Rh1-O1	176.1(7)	O1-Rh1-Rh1#1	83.6(3)	C3-C4-C41	121.8(15)
C01-Rh1-O1	92.3(6)	C4-O2-Rh1	121.7(10)	O02-C02-Rh1	175.9(15)
O2-Rh1-O1	93.1(5)	O1-C2-C3	121.7(18)	O01-C01-Rh1	177.4(16)
Torsion angles / degree [a]					
Rh1#1-Rh1-O2-C4	77.8(9)	Rh1#1-Rh1-C01-O01	-104(28)	O1-C2-C11-S1	17.0(12)
Rh1#1-Rh1-O1-C2	-91.8(11)	Rh1#1-Rh1-C02-O02	48(22)	O2-Rh1-C01-O01	146(26)
Rh1-O2-C4-C3	9.5(16)	S4-C41-C4-O2	6.3(10)	O1-Rh1-C01-O01	-21(28)

a Symmetry transformations used to generate equivalent atoms: #1 x,-y+1,-z+1

The $[Rh(dtm)(CO)_2]$ complex packs in the *P2na* space group with Z = 4, resulting in the molecules lying in the general positions in the unit cell. All bond lengths and angles are in the typical range for these types of compounds[44,45] and will be discussed in more detail later in this paragraph. The packing diagrams of the $[Rh(dtm)(CO)_2]$ molecules in a unit cell are given in **Figure 3.34**.

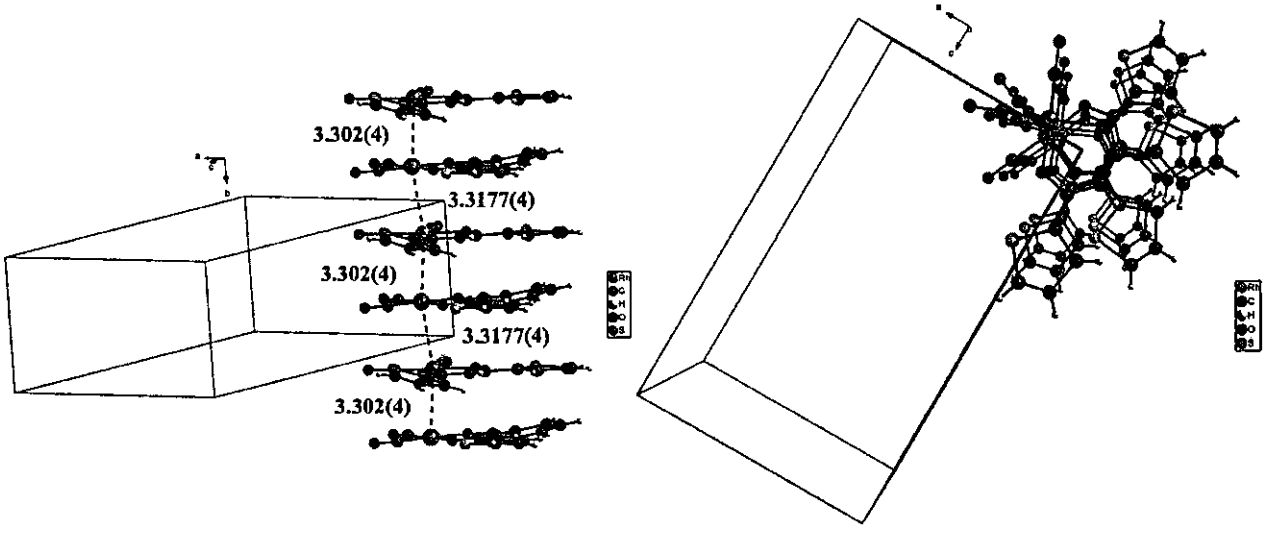

Figure 3.34: Packing diagrams of $[Rh(dtm)(CO)_2]$ molecules viewed from different observation points. Molecules stack in infinite arrays around each corner (and the center) of the unit cell along the b-axis (left). A perspective view (right) along the b-axis shows the channels formed by the infinite stack of molecules.

The $[Rh(dtm)(CO)_2]$ molecules form pairs of two molecules with a Rh···Rh distance of 3.177 Å (see **Figure 3.34**). These pairs stack as an infinite chain around each corner (and the center) of the unit cell along the b-axis. The distance between the pairs is 3.302(4) Å. Almost similar packing was observed for $[Rh(acac)(CO)_2]$ (no infinite chain in the center of the unit cell) with a Rh···Rh distance of 3.253 Å between the molecules and 3.271 Å between adjacent pairs of molecules.[46] When viewed from the top, the pair of $[Rh(dtm)(CO)_2]$ molecules are orientated with an angle of *ca* 35° between them (**Figure 3.34** right), while in $[Rh(acac)(CO)_2]$ the pair of molecules are orientated with an angle of 180° in opposite direction due to an inversion symmetry operation. In the pair of $[Rh(dtm)(CO)_2]$ molecules, the one molecule was also flipped as can be seen from the thienyl ring that does not lie in the square planar plane. $[Rh(PhCOCHCOCH_2CH_3)(CO)_2]$ and $[Rh(PhCOCHCOCH_2CH_2CH_3)(CO)_2]$, two dicarbonyl

44 Cambridge Structural Database (CSD), Version 5.27, August 2006 update

45 Allen, F. H. (2002). Acta Cryst. B58, 380–388.

46 F. Huq, A.C. Skapski, J. Cryst. Mol. Struct. 4 (1974) 411.

rhodium(I) complexes recently solved in this laboratory,[47] also packs in pairs with Rh···Rh distances of 3.175 and 3.179 Å respectively. The pairs of these molecules do not form a chain and are orientated with an angle of 180° between them due to an inversion symmetry operation.

The packing of the dicarbonyl complexes with an unsymmetrical β-diketonato ligand, fctfa[48] and tfba[49] are illustrated in **Figure 3.35**. The [Rh(tfba)(CO)$_2$] molecules stack in infinite arrays along the c-axis. The [Rh(fctfa)(CO)$_2$] molecules stacks in pairs with a Rh···Rh distances of 3.346. The packing of [Rh(fctfa)(CO)$_2$] further revealed that one molecule of such a pair was flipped and then rotated by an angle of *ca* 96°.

Table 3.18: Selected geometric and crystallographic data for square planar complexes [Rh(R^1-CO-CH-CO'-R^2)(CO)$_2$] with R^1 and R^2 groups as indicated (see List of Abbreviations for different bidentate ligands).

L,L'-BID	R^1	R^2	Rh-O distance / Å	Rh-O' distance / Å	Rh-C distance *trans* to R^2-CO' / Å	Rh-C' distance *trans* to R^1-CO / Å	O-Rh-O' angle / °	C-Rh-C' angle / °	Space group
acac[46]	CH_3	CH_3	2.040(4)	2.044(4)	1.831(7)	1.831(7)	90.8(2)	88.9(3)	$P\bar{1}$
tfba[49]	CF_3	Ph	2.02(2)	2.02(2)	1.79(3)	1.82(3)	89.8(7)	87(1)	*Pbca*
fctfa[48]	CF_3	Fc	2.016(9)	2.049(8)	1.84(1)	1.83(2)	90.2(3)	89.1(6)	*C2/c*
dtm [a]	Th	Th	2.01(1)	2.04(1)	1.78(2)	1.88(2)	93.1(5)	84.5(8)	*P2na*

a Two molecules in the same asymmetric unit with similar molecular dimensions

The Rh(I) atom has a square planar coordination sphere. The rhodium atom is displaced by 0.027 Å from this coordination plane. The [Rh(dtm)(CO)$_2$] molecule as a whole is non-planar. The planes of the S4 thienyl ring and the S1 thienyl ring make angles of 2.29 and 15.96° respectively with the plane of the enol ring. This might possibly be due to packing effects (**Figure 3.34**) as different interactions for the two Th groups are observed with neighbouring molecules in Mercury. Although both thienyl groups are aromatic, the larger angle between the S1 Th-plane and the enol-plane than the angle between the S4 Th-plane and the enol-plane, implies that the conjugation between the pseudo aromatic enol ring and the S4 Th-ring is stronger. Therefore the S4 thienyl ring will have a larger trans-influence (**paragraph 2.3.6,**

[47] M.F. Stuurman, Synthesis, chemical kinetics, thermodynamic and structural properties of phenyl-containing beta-diketonato complexes of rhodium(I), M. Sc. Thesis, University of the Free State, South Africa, 2007.

[48] J. Conradie, T.S. Cameron, M.A.S. Aquino, G.J. Lambrecht, J.C. Swarts, Inorg. Chim. Acta 358 (2005) 2530.

[49] J.G. Leipoldt, L.D.C. Bok, S.S. Basson, J.S. van Vollenhoven, T.I.A. Gerber, Inorg. Chim. Acta 25 (1977) L63.

Chapter 2) resulting in the elongation of the Rh-C1 bond. The Rh-C1 bond was found to be *ca* 0.1 Å longer than the Rh-C2 bond (**Table 3.18**). The bonds around the Rh atom of the $[Rh(dtm)(CO)_2]$ molecule were in the same range as the other $[Rh^I(R^1\text{-}CO\text{-}CH\text{-}CO'\text{-}R^2)(CO)_2]$ molecules reported above. Unlike the other molecules, the angles around the Rh atom of the $[Rh(dtm)(CO)_2]$ molecule deviate from the ideal 90° geometry as expected for a dsp^2 hybridization. The C2-C3-C4 angle, 135(5)°, also deviates from the expected 120° for sp^2 hybridized C atoms.

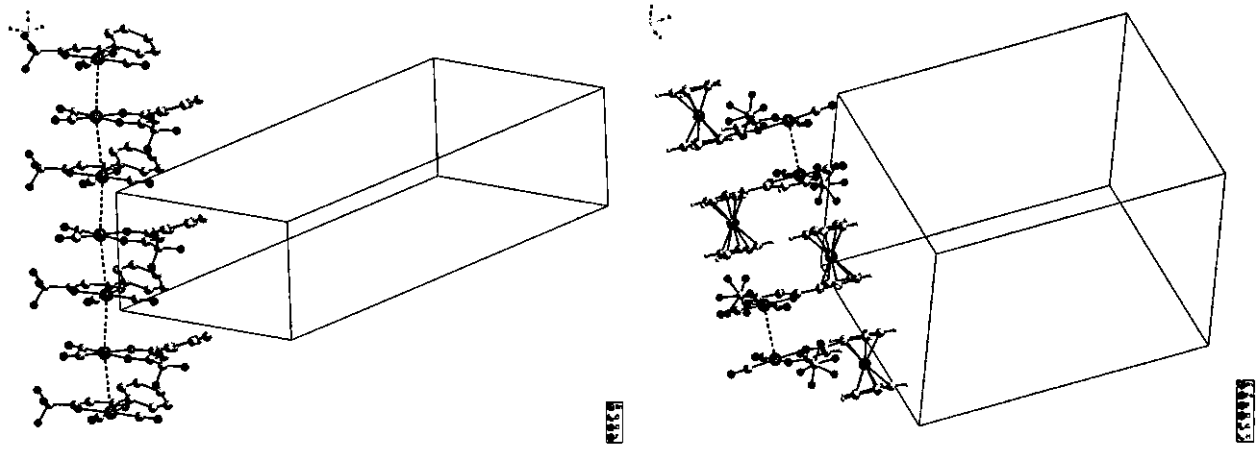

Figure 3.35: Packing diagrams of $[Rh(tfba)(CO)_2]$ molecules (left) and $[Rh(fctfa)(CO)_2]$ (right). The $[Rh(tfba)(CO)_2]$ molecules stack in infinite arrays along the c-axis. The $[Rh(fctfa)(CO)_2]$ molecules stack in pairs.

3.5 Oxidative addition and insertion (migration) reactions.

3.5.1 Introduction.

A kinetic study is required to determine the mechanism of the oxidative addition reaction of an alkyl halide to $[Rh^I(\beta\text{-diketonato})(CO)(PPh_3)]$ complexes. The reaction rate of any chemical change depends primarily on the properties of the reacting molecule. The most important factor that determines the reaction rate is the concentration. The rate law, the relationship between the reaction rate and concentration, is the cornerstone of the reaction mechanisms and alone allows much insight into the mechanism. However, by carrying out measurements at a number of temperatures and pressures, or even in different mediums, more useful information about the reaction mechanism can be obtained, even though the form of the rate law itself rarely changes.

In previous studies of oxidative addition of MeI to [Rh^{I}(β-diketonato)(CO)(PPh$_3$)] complexes, a variety of mechanisms was proposed, depending on the type of rhodium complex studied. The examples discussed in **paragraph 2.4.3, Chapter 2** include the following mechanisms:

(a) Rh(I) + MeI ⇌ Rh(III)-alkyl1 ⇌ Rh(III)-acyl1 Steyn *et al.*[47,48]

(b) Rh(I) + MeI ⇌ Rh(III)-alkyl1 ⇌ Rh(III)-acyl1 ⇌ Rh(III)-alkyl2 Basson *et al.*[49]

All reported studies to date showed that initial oxidative addition is followed by CO insertion. It is unlikely that a [Rh^{I}(β-diketonato)(CO)(PPh$_3$)] complex will be found that can undergo oxidative addition, but not carbonyl insertion, because if a ligand is tailored to be so bulky that it sterically prevents CO insertion, it will probably also not allow oxidative addition to take place.

In this study, UV/vis and IR spectrophotometry and NMR spectroscopy were used to study the reaction rates and the intermediate products of the oxidative addition of MeI to [Rh^{I}(β-diketonato)(CO)(PPh$_3$)] complexes, with the thienyl-containing β-diketonato ligands bth, tta and dtm. For the oxidative addition reaction between MeI and [Rh(tta)(CO)(PPh$_3$)], the same reaction mechanism was observed as was found by Basson *et al.*[49] The reaction mechanism for [Rh(tta)(CO)(PPh$_3$)] can be divided in two sets of reaction as illustrated in **Scheme 3.6**.

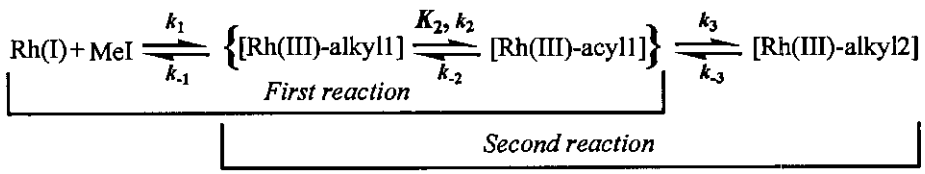

Scheme 3.6: Reaction mechanism for [Rh(tta)(CO)(PPh$_3$)].

However, for [Rh(bth)(CO)(PPh$_3$)] and [Rh(dtm)(CO)(PPh$_3$)], a further reaction was observed. This additional reaction involves another carbonyl insertion reaction to form a new Rh(III)-acyl species. This full reaction mechanism[50] is given in **Scheme 3.7**.

---

[47] G.J.J. Steyn, A. Roodt, J.G. Leipoldt, Rhodium Express 1 (1993) 25.

[48] G.J.J. Steyn, A. Roodt, J.G. Leipoldt, Inorg. Chem. 31 (1992) 3477.

[49] S.S. Basson, J.G. Leipoldt, A. Roodt, J.A. Venter, T.J. van der Walt, Inorg. Chim. Acta 119 (1986) 35.

[50] J. Conradie, Chemical Kinetics, Electrochemistry and Structural Aspects of Ferrocene-containing β-diketonato Complexes of Rhodium(I) and Iridium(I), Ph. D. Thesis, University of the Orange Free State, R.S.A., 2000.

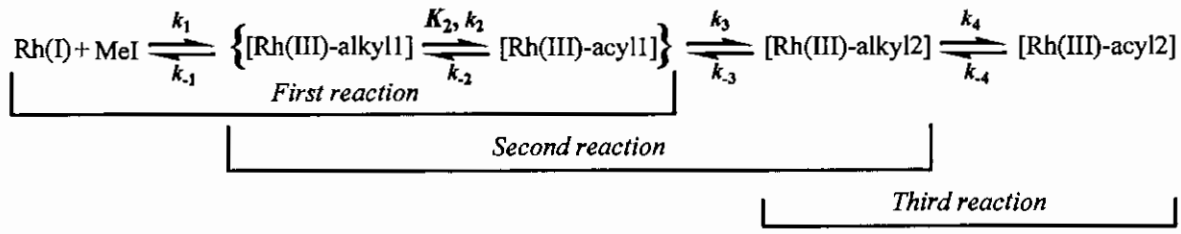

Scheme 3.7: Reaction mechanism for [Rh(bth)(CO)(PPh_3)] and [Rh(dtm)(CO)(PPh_3)].

Close inspection of reaction mechanisms reported by Steyn *et al.*[47,48] and Basson *et al.*[49] reveals that they are all only special cases of the general mechanism given above. Mechanism (a) is obtained if $k_3 = k_4 = 0$ and mechanism (b) is obtained if $k_4 = 0$. The equilibrium [Rh(III)-alkyl1 ⇌ Rh(III)-acyl1] has been suggested by Basson *et al.*[49], but the value of k_{-2} was small and it was a slow equilibrium. The k_4 step was previously observed by Smith,[51] but no attempt was made to characterize it. This study presents a opportunity to determine the rate constants for this step even though the actual structure of the Rh(III) complexes remains uncertain to date.

In the following paragraphs, the experimental results that implied the above reaction mechanism are systematically presented.

3.5.2 The Beer Lambert Law.

A linear relationship (not shown) between the UV/vis absorbance (A) and the concentration (c), for the complexes [Rh(β-diketonato)(CO)(PPh_3)] with the thienyl-containing β-diketonato ligands bth, tta and dtm, confirms the validity of the Beer Lambert law ($A = \varepsilon cl$ with l = path length = 1 cm) for each one of these complexes. The extinction coefficient (ε) for each complex is given in **Table 3.19**. The error of all the data is presented according to crystallographic conventions. For example k_{obs} = 0.0123(4) s^{-1} implies k_{obs} = (0.0123 ± 0.0004) s^{-1}. All the [Rh(β-diketonato)(CO)(PPh_3)] complexes were tested for stability in chloroform by means of overlay UV/vis and IR spectra for at least 24 hours. Also no decomposition of the [Rh(β-diketonato)(CO)(PPh_3)] complexes is detected after 24 hours in solution of $CDCl_3$ on ^{1}H NMR.

---

[51] D.M.C. Smit, Synthesis and Kinetic Study of Rhodium(I) Complexes Containing Organic Tripod Ligands (in Afrikaans), Ph. D. Thesis, University of the Free State, R.S.A., 1995.

Table 3.19: Molar extinction coefficients (ε) at the indicated wavelengths (λ) for the complexes [Rh(β-diketonato)(CO)(PPh_3)] with the thienyl-containing β-diketonato ligands bth, tta and dtm. Values in round brackets represent the error in the last digits.

Complex	ε / mol^{-1} dm^3 cm^{-1}	λ / nm
[Rh(bth)(CO)(PPh_3)] {6}	97(1)	375
[Rh(tta)(CO)(PPh_3)] {7}	32(1)	375
[Rh(dtm)(CO)(PPh_3)] {8}	10(1)	390

3.5.3 The oxidative addition between MeI and [Rh(tta)(CO)(PPh_3)] {7}.

The kinetic rate constants for the oxidative addition reaction between iodomethane (MeI) and [Rh(tta)(CO)(PPh_3)] were determined by UV/vis and IR spectrophotometry and NMR spectroscopy under pseudo first-order conditions. Rate constants, obtained by each of these techniques, were consistent and are summarized in **Table 3.20** (page 121) and **Table 3.21** (page 135). Rate constants were calculated utilizing a suitable fitting program[52] which fitted kinetic data to the first-order equation[53] $[A]_t = [A]_0 e^{(-kobs\ t)}$ ($[A]_t$ = absorbance of selected species at time t).

3.5.3.1 The UV/vis monitored reaction between MeI and [Rh(tta)(CO)(PPh_3)] {7}.

The UV/vis spectral region was chosen, since transition metal complex reactions are accompanied by spectral absorption changes in this region. The MeI, as well as the solvent used (chloroform), is transparent in this region. The scans were recorded from 350 nm to 550 nm in chloroform. An overlay spectrum is given in **Figure 3.36**.

[52] MINSQ, Least squares parameter Estimation, Version 3.12, MicroMath, 1990.

[53] J.H. Espenson, Chemical Kinetics and Reaction Mechanisms, Second edition, McGraw-Hill, New York, 1995, pp. 15, 49.

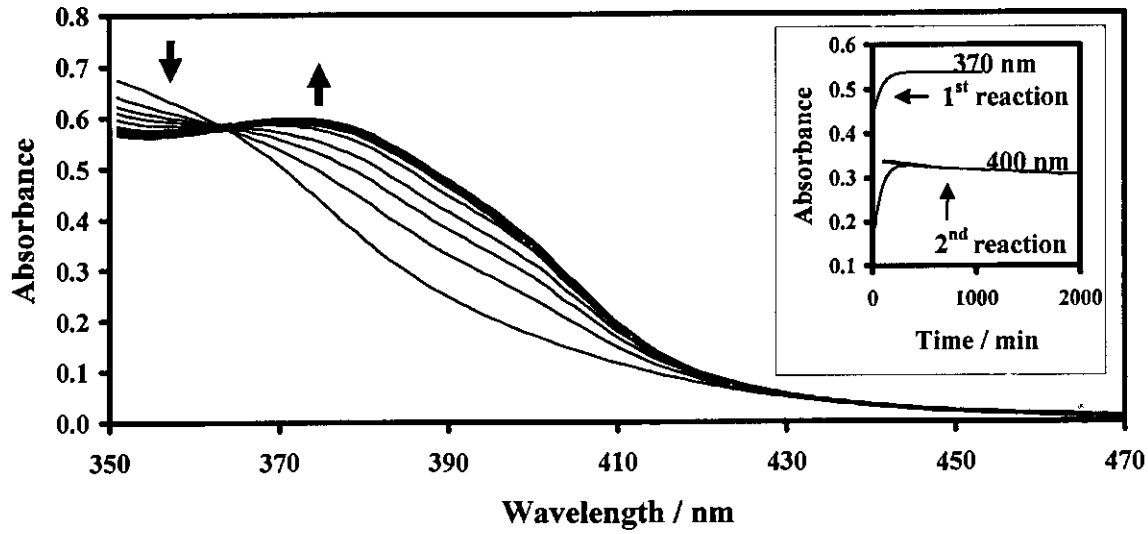

Figure 3.36: Spectrum of the oxidative addition reaction between MeI and [Rh(tta)(CO)(PPh_3)], as monitored on the UV/vis spectrophotometer between 350 – 550 nm in chloroform at 25 °C; [Rh(tta)(CO)(PPh_3)] = 0.00006 mol dm^{-3}, [MeI] = 0.154 mol dm^{-3}. **The insert:** Absorbance *vs* time data for the UV/vis monitored oxidative addition reaction of MeI to [Rh(tta)(CO)(PPh_3)] in chloroform at 370 nm and 400 nm.

From the above figure, it is clear that there are two different reactions. The *first reaction* is best followed at 370 nm and the *second reaction* at 400 nm. The insert in **Figure 3.36** illustrates the absorbance *vs* time data for the two reactions at selected wavelengths. The rate constants for the two reactions are summarized in **Table 3.20** (page 121).

The temperature and [MeI] dependence of the *first reaction* of the oxidative addition reaction between MeI and [Rh(tta)(CO)(PPh_3)], as monitored on the UV/vis spectrophotometry at 370 nm in chloroform, are demonstrated by **Figure 3.37**. The *second reaction* is [MeI] independent and gave a constant rate constant at different concentrations. Data are summarized in **Table 3.20** (page 121).

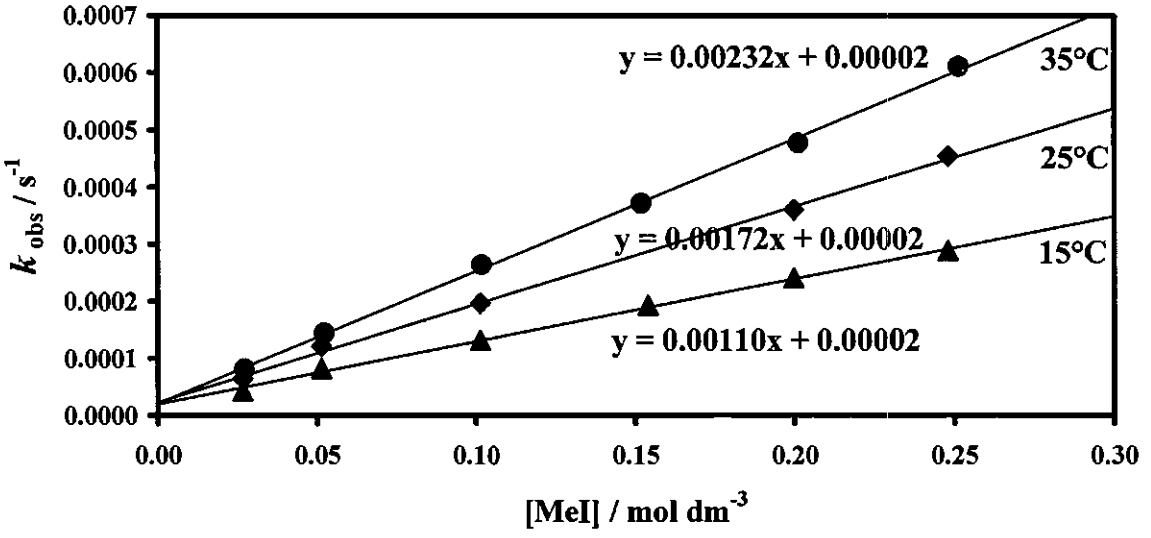

Figure 3.37: Temperature and MeI concentration dependence of the oxidative addition of MeI to [Rh(tta)(CO)(PPh_3)], as monitored on the UV/vis spectrophotometer at 370 nm in chloroform, for the *first reaction* { Rh(I) + MeI ⇌ [Rh(III)-alkyl1 ⇌ Rh(III)-acyl1] }.

The activation parameters ΔH^* (activation enthalpy) and ΔS^* (activation entropy), for the *first reaction* were determined from least-squares[52] fits of the reaction rate constants vs temperature data according to the Eyring relationship[54], **Equation 3.8**, or rewritten in the linear form as **Equation 3.9**. The activation free energy $\Delta G^* = \Delta H^* - T\Delta S^*$.[55]

Equation 3.8: $$k = \frac{k_B T}{h} e^{\frac{-\Delta H^*}{RT}} e^{\frac{\Delta S^*}{R}}$$

Equation 3.9: $$\ln k/T = -\frac{\Delta H^*}{RT} + \frac{\Delta S^*}{R} + \ln\frac{k_B}{h}$$

with k = rate constant, k_B = Boltzmann's constant = 1.3806 x 10^{-23} J K^{-1}, T = temperature, h = Planck's constant = 6.625 x 10^{-34} J s, and R = universal gas constant = 8.314 J mol^{-1} K^{-1}. A plot of $\ln(k/T)$ *vs* T^{-1} is linear with a slope of $-\Delta H^*/R$ and an intercept of { $\Delta S^*/R + \ln(k_B/h)$ } = { $\Delta S^*/R$ + 23.760 }. This linear relationship is illustrated in **Figure 3.38**. The activation parameters at 25 °C are summarized in **Table 3.20** (page 121).

---

[54] .H. Espenson, Chemical Kinetics and Reaction Mechanisms, Second edition, McGraw-Hill, New York, 1995, p. 156.

[55] P.W. Atkins, Physical Chemistry, Fifth edition, Oxford University Press, Oxford, 1994, pp. 939–950.

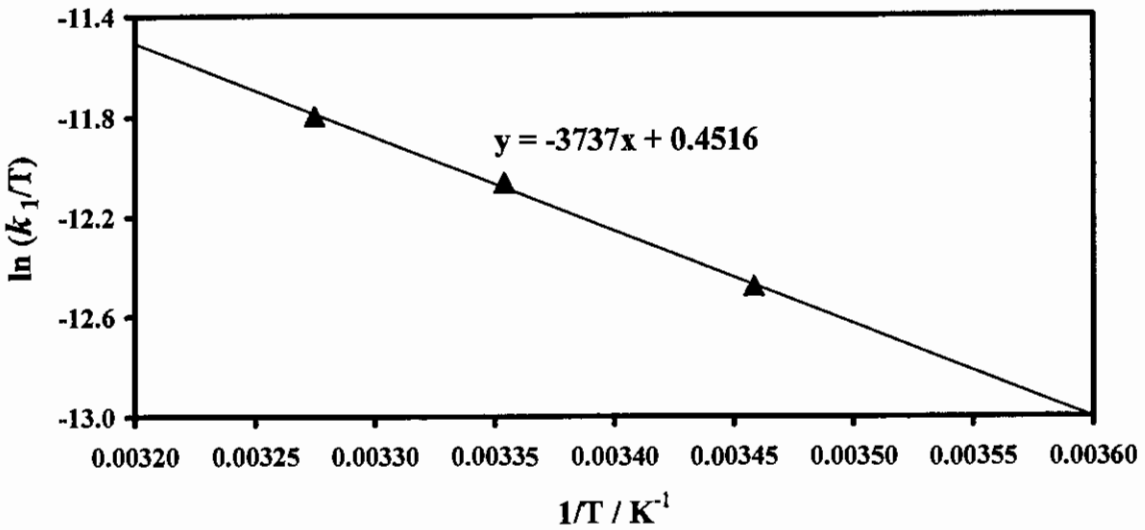

Figure 3.38: The Eyring curve of $\ln(k_1/T)$ *vs* 1/T for the *first reaction* { Rh(I) + MeI ⇌ [Rh(III)-alkyl] ⇌ Rh(III)-acyl] } of the oxidative addition reaction between MeI and [Rh(tta)(CO)(PPh_3)], as monitored on the UV/vis spectrophotometer in chloroform.

Table 3.20: Temperature dependent kinetic rate constants and activation parameters for the oxidative addition between MeI and [Rh(tta)(CO)(PPh_3)], as monitored on the UV/vis spectrophotometer in chloroform. k_1 and k_3 are the rate constants associated with the *first* and the *second reactions* of this oxidative addition reaction.

T / °C	1st reaction				
	k_1 / dm^3 mol^{-1} s^{-1}	k_{-1} / s^{-1}	ΔH^* / kJ mol^{-1}	ΔS^* / J mol^{-1} K^{-1}	ΔG^* / kJ mol^{-1} [a]
16.0	0.00111(2)	0.000017(4)	31.1(5)	-194(2)	89(1)
25.0	0.00171(4)	0.000023(6)			
32.2	0.00234(3)	0.000018(4)			
T / °C	**2nd reaction**				
	k_3 / s^{-1}		ΔH^* / kJ mol^{-1}	ΔS^* / J mol^{-1} K^{-1}	ΔG^* / kJ mol^{-1}
25.0	0.0008(3)		-	-	-

a At 25 °C

Results of the UV/vis study of the reaction between MeI and [Rh(tta)(CO)(PPh_3)] are interpreted to imply that the *first reaction* represents an oxidative addition whereby the Rh(I) nucleus converts to a Rh(III) nucleus. The product of this oxidative addition step may be either a Rh(III)-alkyl or Rh(III)-acyl species, [Rh(tta)(CH_3)(CO)(PPh_3)(I)] or [Rh(tta)($COCH_3$)(PPh_3)(I)] (or both), but in the absence of further experimental evidence, the nature of the oxidative addition product can only be speculated on. Since the *second reaction* is independent of [MeI] one may deduce that this reaction either involves solvent exchange with any of the ligands of the newly formed Rh(III) complex or it may be isomerization from a Rh(III)-alkyl to a Rh(III)-acyl

product (or *vice versa*). Based on the UV/vis study alone one may write a preliminary reaction sequence:

$$[Rh^{I}(tta)(CO)(PPh_3)] + MeI$$

$$k_{-1} \Updownarrow k_1$$

[Rh(III)-oxidative addition product X]

$$\Updownarrow \text{ (isomerization or solvent exchange)}$$

[different Rh(III)-product Y]

To obtain more insight into the nature of the Rh(III)-products X and Y, an infrared-based study of the reaction was conducted as this technique is ideal to distinguish between metal-CO bonds that absorb at ~1900 – 2100 cm^{-1}, and metal-$COCH_3$ that absorbs at ~ 1600 – 1800 cm^{-1}.

3.5.3.2 The IR monitored reaction between MeI and [Rh(tta)(CO)(PPh$_3$)] {7}.

IR spectrophotometry provides structural information that cannot be obtained from UV/vis spectrophotometry. The carbonyl stretching frequencies (ν_{CO}) are very sensitive to the metal environment and substitution reactions, as described in **paragraph 2.3.4, Chapter 2.** An illustration of the oxidative addition reaction between MeI and [Rh(tta)(CO)(PPh$_3$)], as monitored on the IR spectrophotometer between 1600 – 2200 cm^{-1} in chloroform at 25 °C, is given in **Figure 3.39. Figure 3.40, Figure 3.41** and **Figure 3.42** give the absorbance *vs* time data of the indicated species. Rate constants are summarized in **Table 3.21** (page 135).

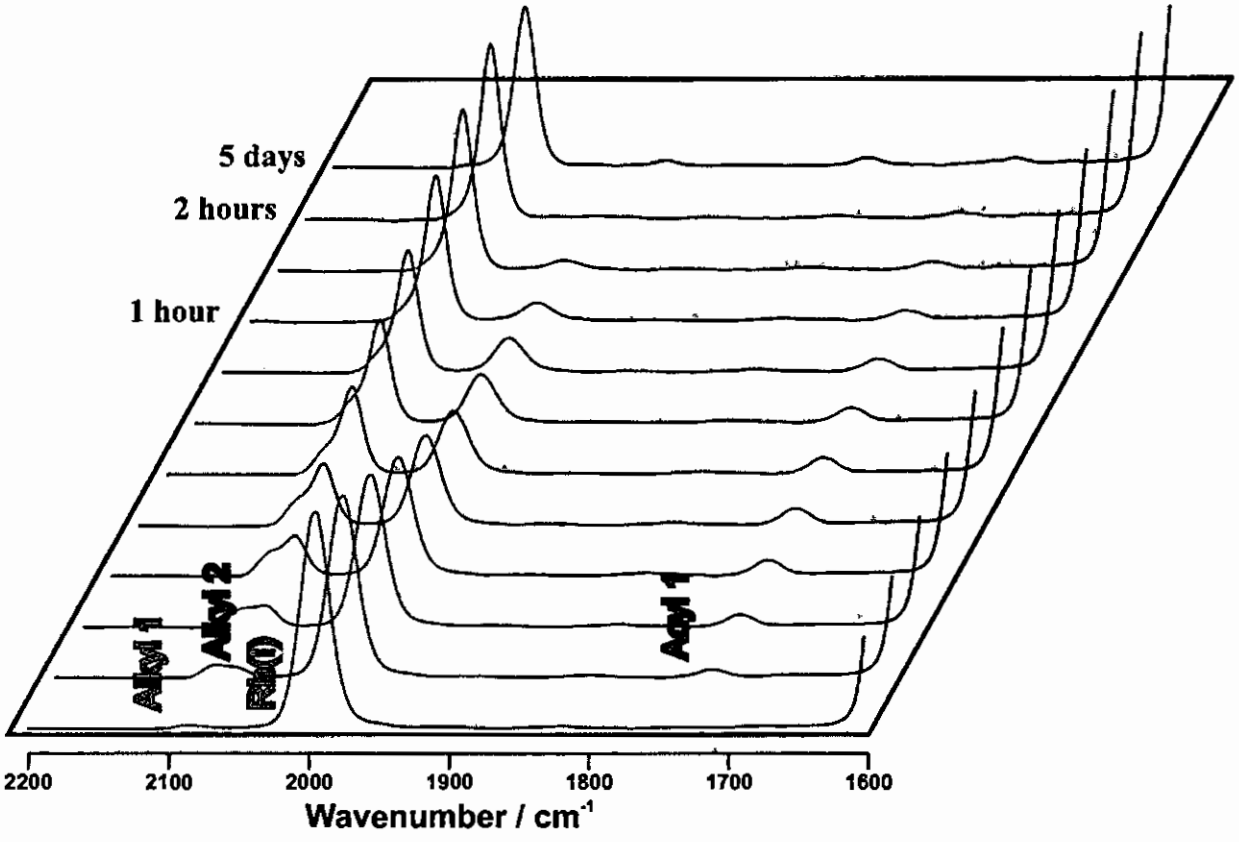

Figure 3.39: Illustration of the oxidative addition reaction between MeI and [Rh(tta)(CO)(PPh_3)], as monitored on the IR spectrophotometer between 1600 – 2200 cm^{-1} in chloroform at 25 °C; [Rh(tta)(CO)(PPh_3)] = 0.0081 mol dm^{-3}, [MeI] = 1.000 mol dm^{-3}. The *first reaction* is indicated by the disappearance of Rh(I) at 1991 cm^{-1} (**pink**) and the simultaneous appearance of Rh(III)-alkyl1 at 2079 cm^{-1} (**yellow**) and Rh(III)-acyl1 at 1728 cm^{-1} (**blue**). The *second reaction* is indicated by the simultaneous disappearance of Rh(III)-alkyl1 and Rh(III)-acyl1 and the formation of a Rh(III)-alkyl2 species at 2064 cm^{-1} (**green**). The first spectrum was recorded 120 s after mixing and the rest of the illustrated spectra were recorded at the indicated time intervals. The signals are colour coded for better clarity.

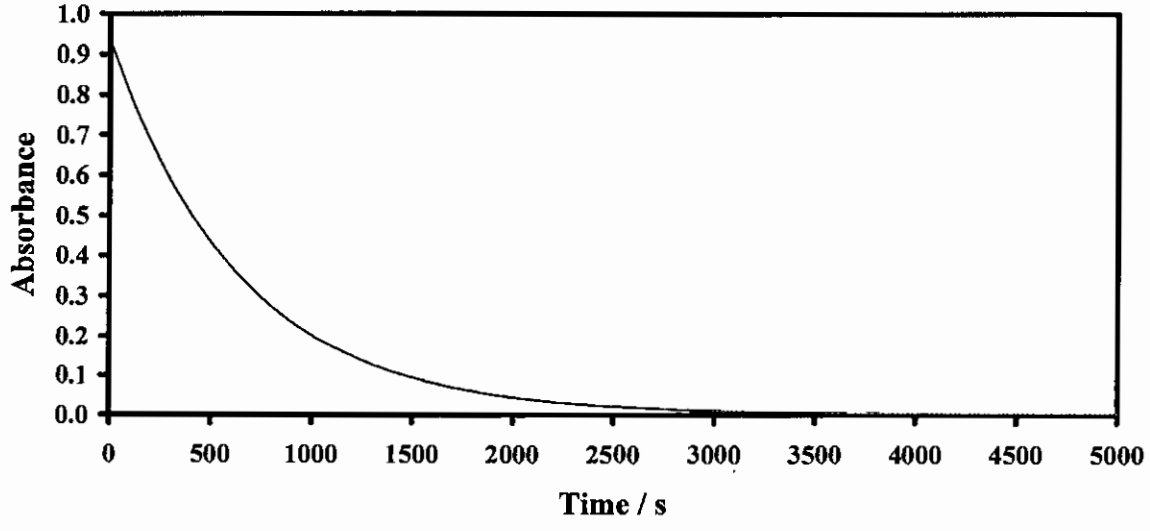

Figure 3.40: Absorbance *vs* time data of the oxidative addition reaction between MeI and [Rh(tta)(CO)(PPh_3)], as monitored on the IR spectrophotometer at 1991 cm^{-1} in chloroform at 25 °C; [Rh(tta)(CO)(PPh_3)] = 0.0081 mol dm^{-3}, [MeI] = 1.000 mol dm^{-3}. Indicated is the disappearance of Rh(I) (**pink**, k_{obs} = 0.00153(1) s^{-1}).

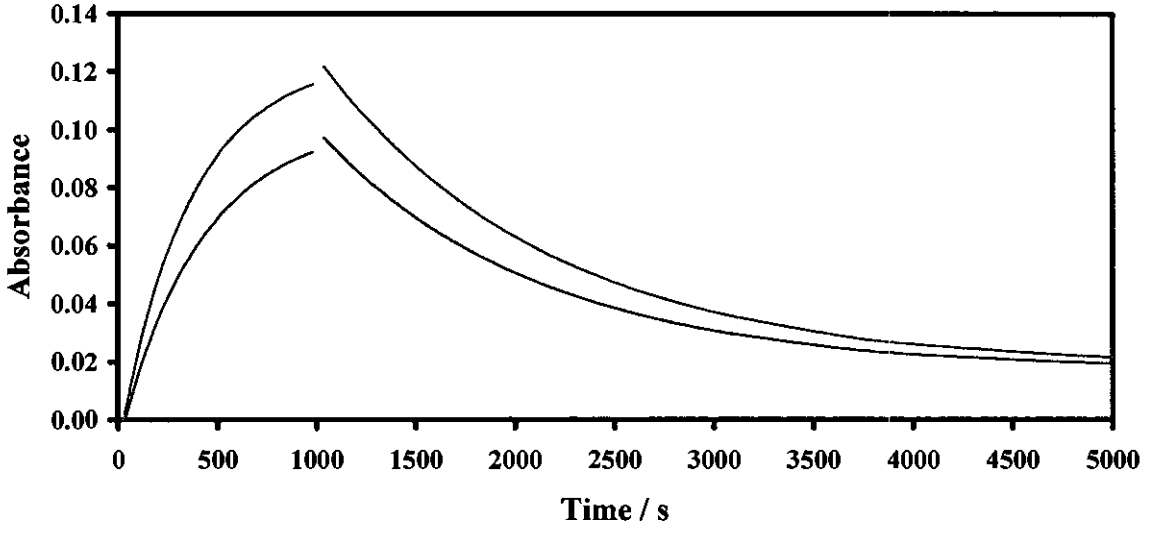

Figure 3.41: Absorbance *vs* time data of the oxidative addition reaction between MeI and [Rh(tta)(CO)(PPh_3)], as monitored on the IR spectrophotometer at 2079 and 1728 cm^{-1} in chloroform at 25 °C; [Rh(tta)(CO)(PPh_3)] = 0.0081 mol dm^{-3}, [MeI] = 1.000 mol dm^{-3}. Indicated is the appearance of Rh(III)-alkyl1 (**yellow**, k_{obs} = 0.0027(2) s^{-1}) and Rh(III)-acyl1 (**blue**, k_{obs} = 0.0024(2) s^{-1}), during the *first reaction* { Rh(I) + MeI ⇌ [Rh(III)-alkyl1 ⇌ Rh(III)-acyl1] }, followed by the disappearance of Rh(III)-alkyl1 (**yellow**, k_{obs} = 0.00087(2) s^{-1}) and Rh(III)-acyl1 (**blue**, k_{obs} = 0.00090(2) s^{-1}), during the *second reaction* { [Rh(III)-alkyl1 ⇌ Rh(III)-acyl1] → Rh(III)-alkyl2 }.

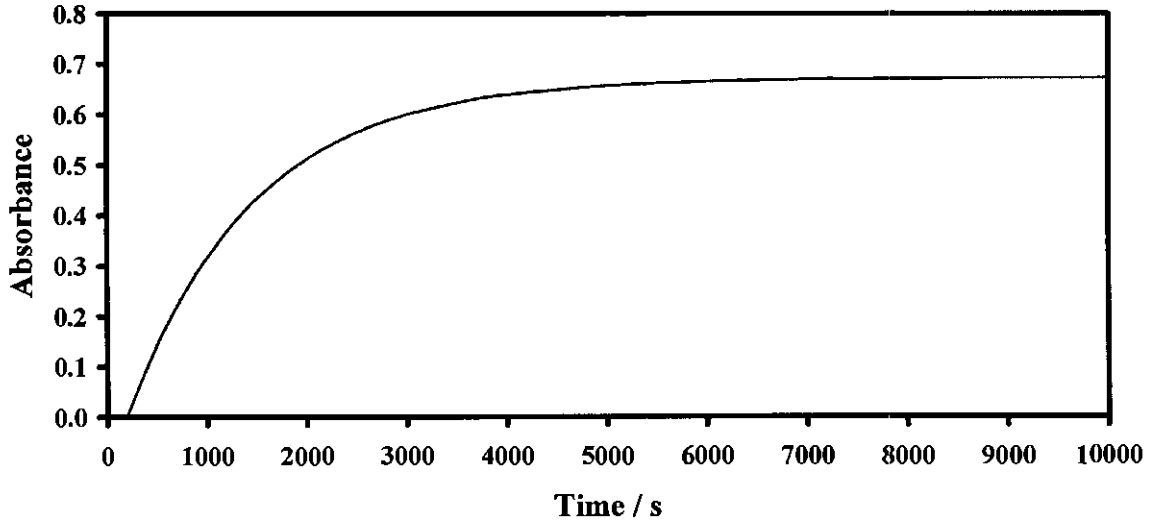

Figure 3.42: Absorbance *vs* time data of the oxidative addition reaction between MeI and [Rh(tta)(CO)(PPh_3)], as monitored on the IR spectrophotometer at 2064 cm^{-1} in chloroform at 25 °C; [Rh(tta)(CO)(PPh_3)] = 0.0081 mol dm^{-3}, [MeI] = 1.000 mol dm^{-3}. Indicated is the appearance of Rh(III)-alkyl2 (**green**, k_{obs} = 0.00080(2) s^{-1}), during the *second reaction* { [Rh(III)-alkyl1 ⇌ Rh(III)-acyl1] → Rh(III)-alkyl2 }.

In the *first reaction*, the rate of disappearance of the Rh(I) species [Rh^{I}(tta)(CO)(PPh_3)] (0.00153(1) s^{-1}) in chloroform at 25 °C, as monitored by the disappearance of the CO peak at 1991 cm^{-1} (pink), corresponds with the rate of formation of both a Rh(III)-alkyl1 species [Rh^{III}(tta)(CH_3)(CO)(PPh_3)(I)] (0.0027(2) s^{-1}), monitored by the appearance of the CO-peak at 2079 cm^{-1} (yellow), and a Rh(III)-acyl1 species [Rh^{III}(tta)($COCH_3$)(PPh_3)(I)] (0.0024(2) s^{-1}), monitored at 1728 cm^{-1} (blue). The observed rate of appearance of the Rh(III)-alkyl1 species was found to be a little higher than the disappearance rate of the Rh(I) species, since the formation of the Rh(III)-acyl1 species (and subsequently the disappearance of the Rh(III)-alkyl1 species) caused lower values for the absorbance at infinity for the Rh(III)-alkyl1 formation. This was also found by Steyn *et al.*[48] for reactions at high [MeI]. The half-life of the first reaction step with [MeI] = 1.000 mol dm^{-3} is 450 s. Since it is highly unlikely that the Rh(III)-acyl1 species can be formed from an undetected Rh(III)-alkyl1 species with a total different ligand coordination pattern than the detected Rh(III)-alkyl1 species at the same rate as the detected Rh(III)-alkyl1 species, this result is considered to imply that an equilibrium exists between the Rh(III)-alkyl1 and Rh(III)-acyl1 species that is fast enough to be maintained on the timescale of the [Rh^{I}(tta)(CO)(PPh_3)] disappearance. The same conclusion could be drawn using ^{1}H NMR data and will be discussed in **paragraph 3.5.3.3**. The structure of [Rh(tta)(CO)(PPh_3)] is reported elsewhere[56], but the structures of the Rh(III)-alkyl1 and the Rh(III)-acyl1 species are unknown. It is presumed, though, that the Rh(III)-alkyl1 species have the CH_3 and CO ligands in a *cis* configuration to allow carbonyl insertion during the generation of the Rh(III)-acyl1 species.

This *first reaction* may be presented by the reaction sequence:

$$\text{Rh(I)} + \text{MeI} \underset{k_{-1}}{\overset{k_1}{\rightleftharpoons}} \left\{\text{[Rh(III)-alkyl1]} \underset{k_{-2}}{\overset{K_2, k_2}{\rightleftharpoons}} \text{[Rh(III)-acyl1]}\right\}$$

where k_i represents the forward rate constants and k_{-i} the reverse rate constants, i = 1 or 2 .

The concentration dependence of the *first reaction* of the oxidative addition reaction between MeI and [Rh(tta)(CO)(PPh_3)], as monitored on the IR spectrophotometry at 1991 cm^{-1} in chloroform, is illustrated in **Figure 3.43**.

---

[56] J.G. Leipoldt, L.D.C. Bok, J.S. van Vollenhoven, A.I. Pieterse, J. Inorg. Nucl. Chem. 40 (1978) 61.

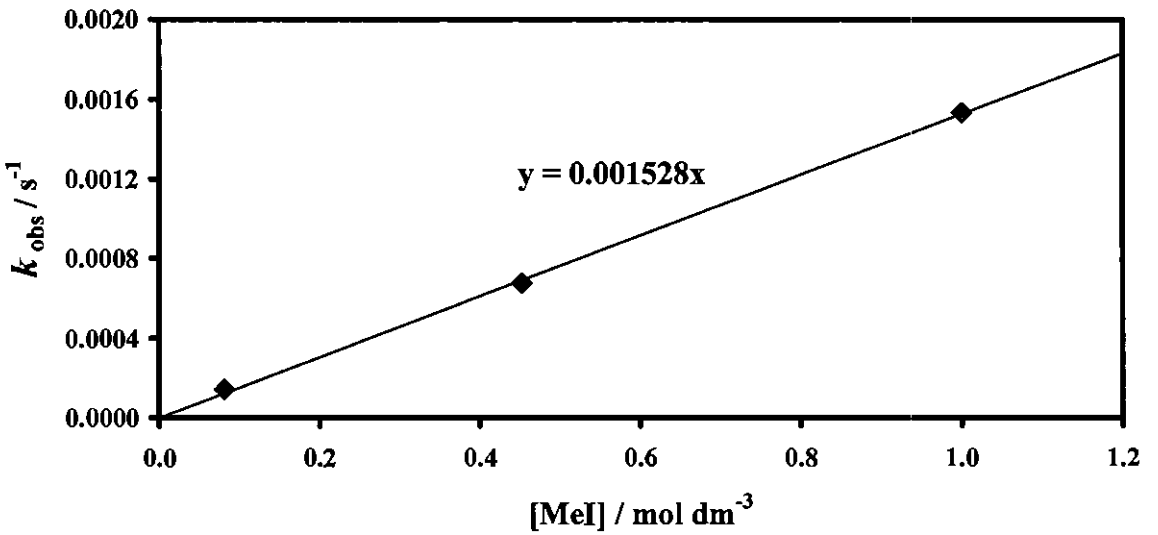

Figure 3.43: MeI concentration dependence of the oxidative addition of MeI to [Rh(tta)(CO)(PPh_3)], as monitored on IR spectrophotometer at 1991 cm^{-1} in chloroform, for the *first reaction* { Rh(I) + MeI ⇌ [Rh(III)-alkyl1 ⇌ Rh(III)-acyl1] }.

A slower *second reaction* ($t_{1/2}$ ≈ 15 min), that is MeI independent, is illustrated by the disappearance of the Rh(III)-alkyl1 species at 2079 cm^{-1} (yellow) and the Rh(III)-acyl1 species at 1728 cm^{-1} (blue) (**Figure 3.39**). The Rh(III)-alkyl1 species and the Rh(III)-acyl1 species both disappear at the same rate (0.00087(2) s^{-1} and 0.00090(2) s^{-1}) as the formation of the Rh(III)-alkyl2 species (0.00080(2) s^{-1}) at 2064 cm^{-1} (green). Again, this is regarded as proof that the equilibrium between these two species is fast. The [MeI]-independent *second reaction* is 0.0015/0.00080 ≈ 2 times slower than the [MeI]-dependent *first reaction* with [MeI] = 1.000 mol dm^{-3}. The kinetic data of the *second reaction* are consistent with an $A \underset{k_{-3}}{\overset{k_3}{\rightleftharpoons}} B$ type of reaction with $k_{-3} <<< k_3$ as shown in:

$$\left\{[\text{Rh(III)-alkyl1}] \underset{k_{-2}}{\overset{K_2, k_2}{\rightleftharpoons}} [\text{Rh(III)-acyl1}]\right\} \underset{k_{-3}}{\overset{k_3}{\rightleftharpoons}} [\text{Rh(III)-alkyl2}]$$

As was the case with the *first reaction*, k_3 obtained by the IR spectrophotometry is consistent with the results from the UV/vis spectrophotometry. The Rh(III)-alkyl2 complex was isolated. The stereochemistry of this [Rh^{III}(tta)(CO)(PPh_3)(Me)(I)-alkyl2 complex is discussed in **paragraph 3.4.1.3**. The structure of the other Rh(III) compounds, as yet unknown, will be explored by NMR and computational chemistry methods - see **paragraph 3.5.4.5** and **paragraph 3.6.4**.

The overall reaction sequence for this oxidative addition reaction can therefore be represented as:

$$\text{Rh(I)} + \text{MeI} \underset{k_{-1}}{\overset{k_1}{\rightleftharpoons}} \{\text{[Rh(III)-alkyl1]} \underset{k_{-2}}{\overset{K_2, k_2}{\rightleftharpoons}} \text{[Rh(III)-acyl1]}\} \underset{k_{-3}}{\overset{k_3}{\rightleftharpoons}} \text{[Rh(III)-alkyl2]}$$

3.5.3.3 The ^{1}H, ^{31}P and ^{19}F NMR monitored reaction between MeI and [Rh(tta)(CO)(PPh_3)] {7}.

NMR spectroscopy can be used as an analytical tool in which the strength of the signal is a measurement of the concentration of a particular complex. The advantage of NMR spectroscopy is that the different isomers in reaction can be monitored separately. One disadvantage of NMR spectroscopy is the relatively high concentrations of solute required for a spectrum.

When following an oxidative addition reaction on the ^{1}H NMR, it is best to look at either the methine or the methyl signals of the Rh(I), Rh(III)-alkyl and Rh(III)-acyl species. These signals are easy to identify and usually do not overlap with the other signals. On the ^{31}P NMR, each isomer is presented as a doublet and on the ^{19}F NMR as a singlet. By carefully comparing the positions and integrals of the different signals, the spectral parameters of the different isomers could be identified. An illustration of the oxidative addition reaction between MeI and [Rh(tta)(CO)(PPh_3)], as monitored by ^{1}H NMR spectroscopy in $CDCl_3$ at 25 °C, is given in **Figure 3.44**. An illustration of the reaction monitored by ^{31}P NMR spectroscopy in $CDCl_3$ at 25 °C, is given in **Figure 3.48**. An illustration of the reaction monitored by ^{19}F NMR spectroscopy in $CDCl_3$ at 25 °C, is given in **Figure 3.52**. All illustrations are followed by the graphs of the relative intensity *vs* time data of the relative experiment and species. Rate constants are summarized in **Table 3.21** (page 135).

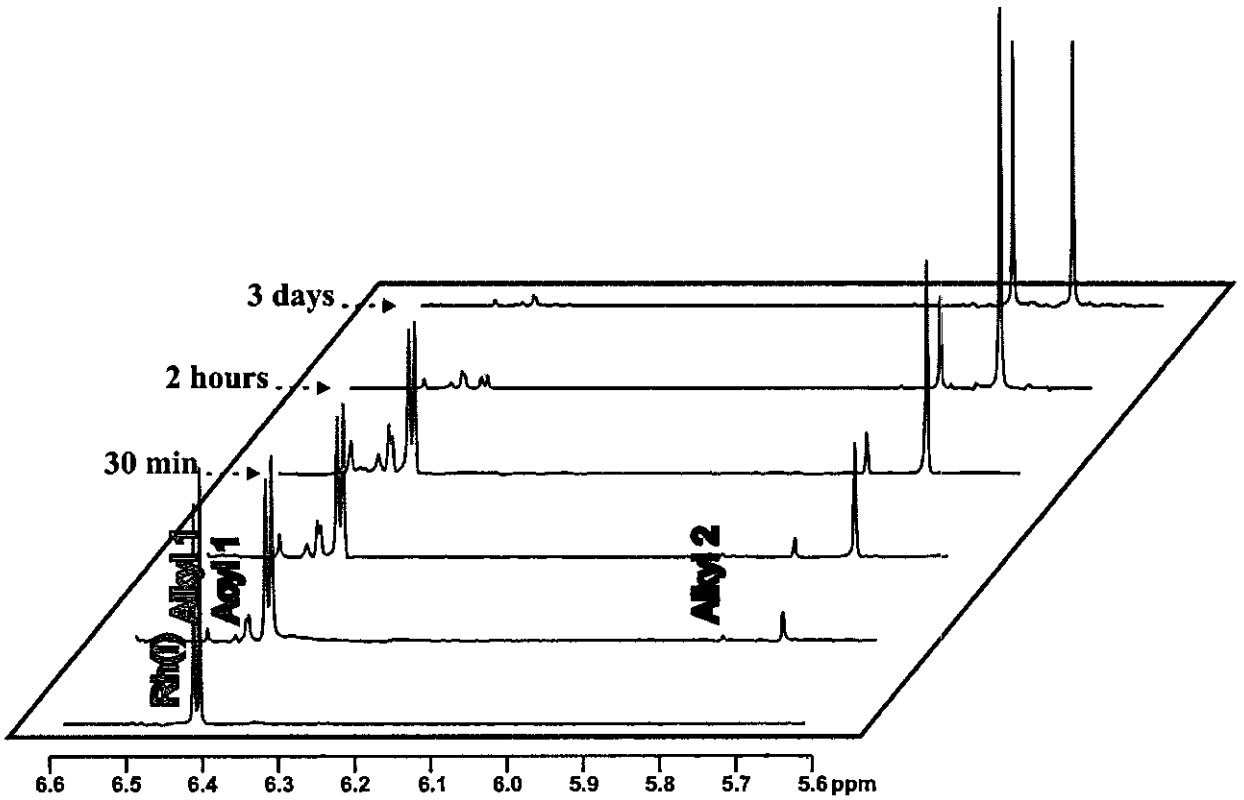

Figure 3.44: A fragment of the ^{1}H NMR spectra of the oxidative addition reaction between MeI and [Rh(tta)(CO)(PPh$_3$)], as monitored by ^{1}H NMR spectroscopy in $CDCl_3$ at 25 °C; [Rh(tta)(CO)(PPh$_3$)] = 0.0271mol dm^{-3}, [MeI] = 0.267 mol dm^{-3}. Two isomers for each species can be observed. The *first reaction* is indicated by the disappearance of Rh(I) at 6.42 and 6.43 ppm (**pink**) and the simultaneous appearance of Rh(III)-alkyl1 at 6.44 and 6.49 ppm (**yellow**) and Rh(III)-acyl1 at 6.43 and 6.45 ppm (**blue**). The *second reaction* is indicated by the simultaneous disappearance of Rh(III)-alkyl1 and Rh(III)-acyl1 and the formation of a Rh(III)-alkyl2 species at 5.72 and 5.80 ppm (**green**). The first spectrum was recorded before mixing and the rest of the illustrated spectra were recorded after mixing at the indicated time intervals. The signals are colour coded for better clarity.

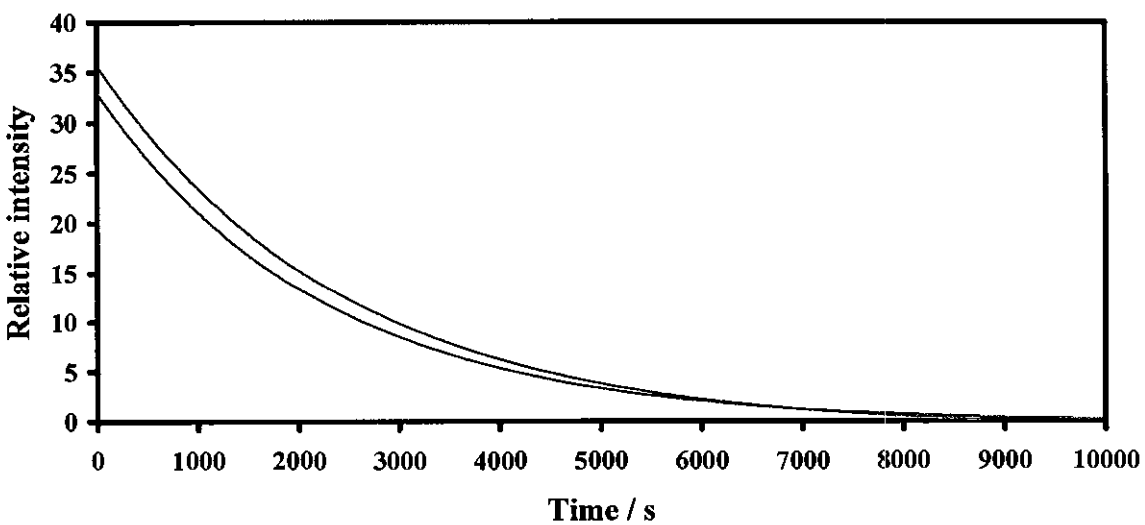

Figure 3.45: Relative intensity *vs* time data of the oxidative addition reaction between MeI and [Rh(tta)(CO)(PPh$_3$)], as monitored by ^{1}H NMR spectroscopy at 6.42 and 6.43 ppm in $CDCl_3$ at 25 °C; [Rh(tta)(CO)(PPh$_3$)] = 0.0271 mol dm^{-3}, [MeI] = 0.267 mol dm^{-3}. Indicated is the disappearance of both Rh(I) isomers A and B (pink, k_{obs} = 0.00041(8) s^{-1} and 0.00044(6) s^{-1}).

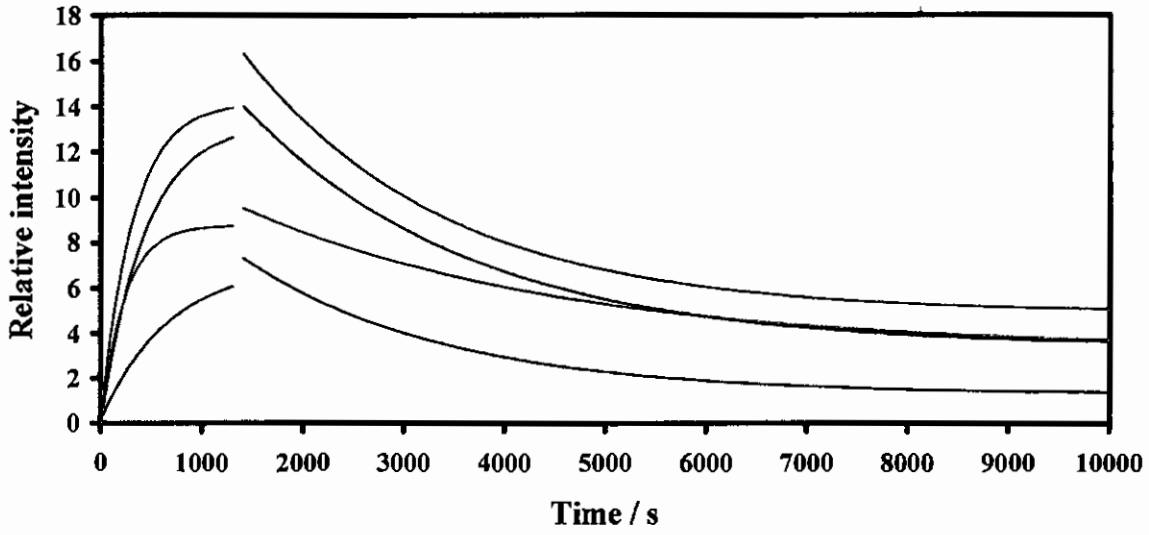

Figure 3.46: Relative intensity *vs* time data of the oxidative addition reaction between MeI and [Rh(tta)(CO)(PPh_3)], as monitored by ^1H NMR spectroscopy at 6.43, 6.44, 6.45 and 6.49 ppm in $CDCl_3$ at 25 °C; [Rh(tta)(CO)(PPh_3)] = 0.0271 mol dm^{-3}, [MeI] = 0.267 mol dm^{-3}. Indicated is the appearance of two Rh(III)-alkyl1 isomers (**yellow**, k_{obs} = 0.003(1) and 0.004(5) s^{-1}) and two Rh(III)-acyl1 isomers (**blue**, k_{obs} = 0.0015(2) and 0.0024(2) s^{-1}), during the *first reaction* { Rh(I) + MeI ⇌ [Rh(III)-alkyl1 ⇌ Rh(III)-acyl1] }, followed by the disappearance of the two Rh(III)-alkyl1 isomers (yellow, k_{obs} = 0.0007(2) and 0.0003(1) s^{-1}) and the two Rh(III)-acyl1 isomers (**blue**, k_{obs} = 0.00050(4) and 0.00044(2) s^{-1}), during the *second reaction* { [Rh(III)-alkyl1 ⇌ Rh(III)-acyl1] → Rh(III)-alkyl2 }.

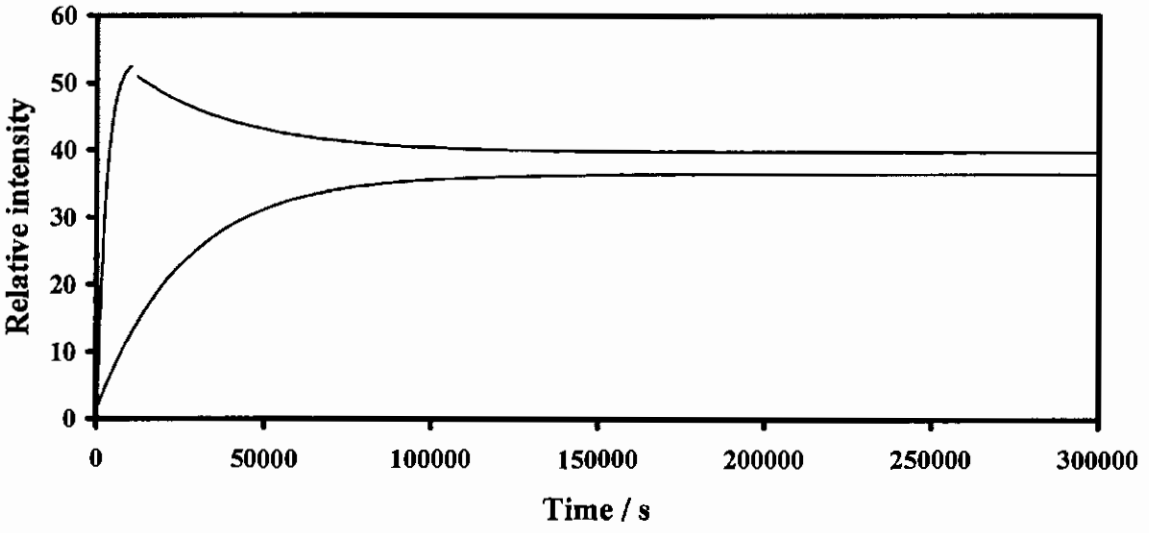

Figure 3.47: Relative intensity *vs* time data of the oxidative addition reaction between MeI and [Rh(tta)(CO)(PPh_3)], as monitored by ^1H NMR spectroscopy at 5.72 and 5.80 ppm in $CDCl_3$ at 25 °C; [Rh(tta)(CO)(PPh_3)] = 0.0271 mol dm^{-3}, [MeI] = 0.267 mol dm^{-3}. Indicated is the appearance of two Rh(III)-alkyl2 isomers (**green**), during the *second reaction* { [Rh(III)-alkyl1 ⇌ Rh(III)-acyl1] → Rh(III)-alkyl2 }. Note that the one isomer increases to a maximum (k_{obs} = 0.00039(6) s^{-1}) and then decreases to an equilibrium position with k_{obs} = 0.000031(4) s^{-1}. For the other isomer, k_{obs} = 0.00038(7) s^{-1}.

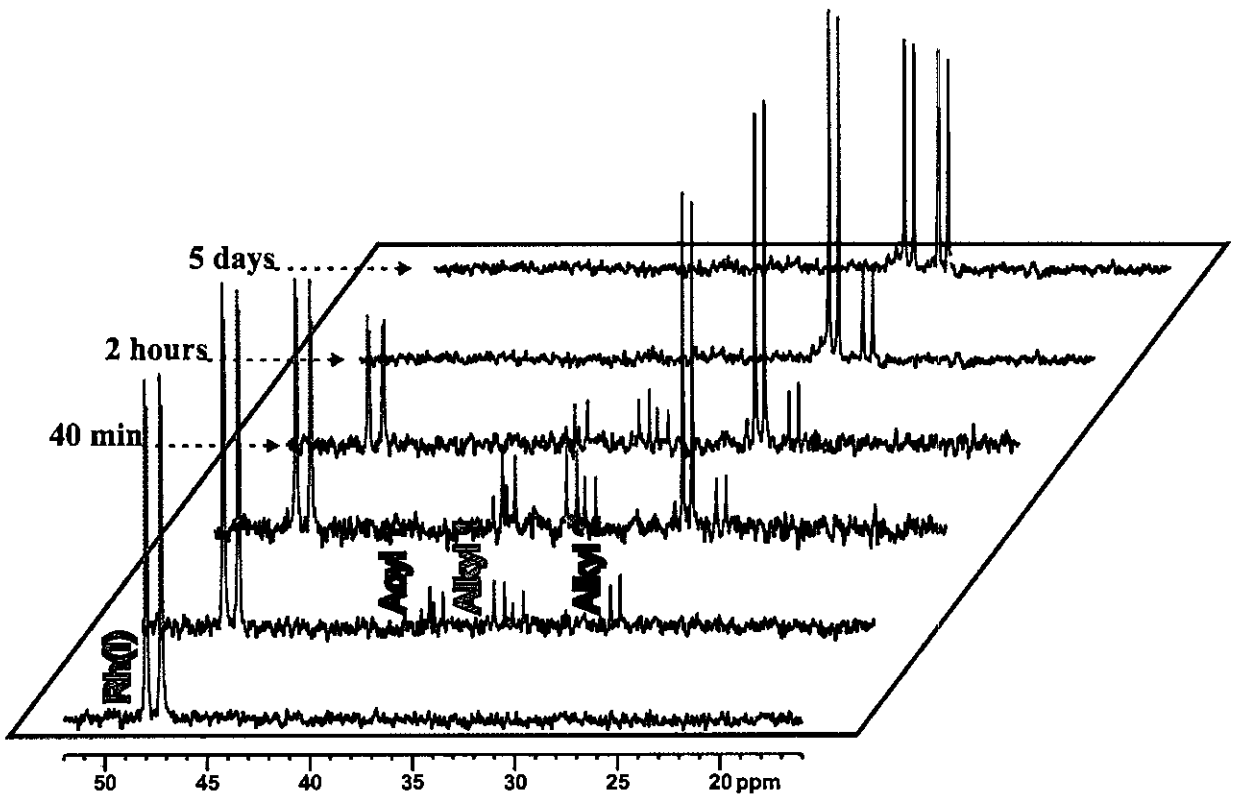

Figure 3.48: Illustration of the oxidative addition reaction between MeI and [Rh(tta)(CO)(PPh_3)], as monitored by ^{31}P NMR spectroscopy in $CDCl_3$ at 25 °C; [Rh(tta)(CO)(PPh_3)] = 0.0271 mol dm^{-3}, [MeI] = 0.267 mol dm^{-3}. The phosphorus atom on the PPh_3 group gives rise to a doublet for each isomer (due to Rh-P coupling). Two isomers for each species can be observed. The *first reaction* is indicated by the disappearance of Rh(I) at 47.61 and 47.66 ppm (**pink**) and the simultaneous appearance of Rh(III)-alkyl1 at 33.50 and 34.42 ppm (**yellow**) and Rh(III)-acyl1 at 37.51 and 37.93 ppm (**blue**). The *second reaction* is indicated by the simultaneous disappearance of Rh(III)-alkyl1 and Rh(III)-acyl1 and the formation of a Rh(III)-alkyl2 species at 27.07 and 28.74 ppm (**green**). The first spectrum was recorded before mixing and the rest of the illustrated spectra were recorded after mixing at the indicated time intervals. The signals are colour coded for better clarity.

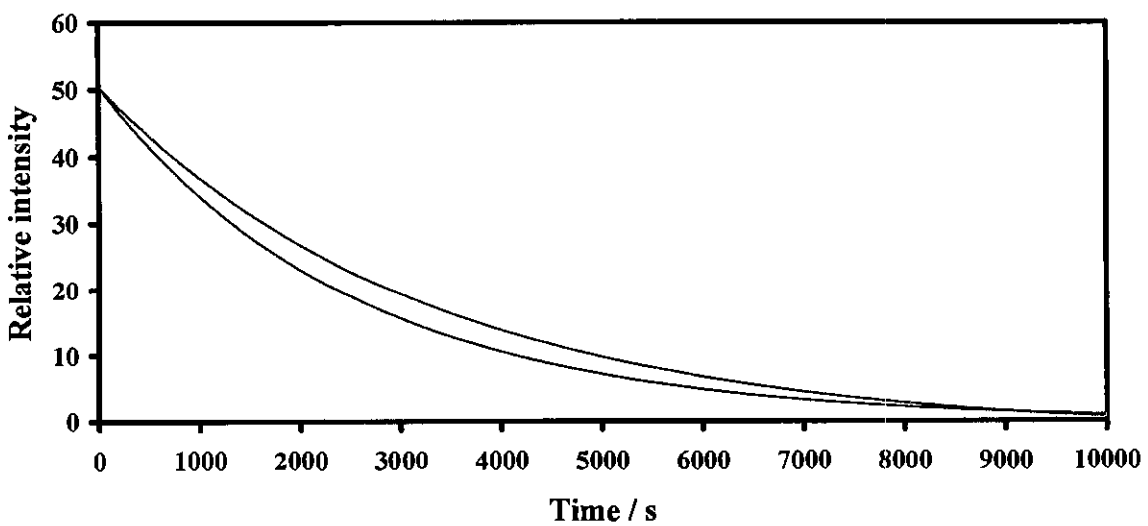

Figure 3.49: Relative intensity *vs* time data of the oxidative addition reaction between MeI and [Rh(tta)(CO)(PPh_3)], as monitored by ^{31}P NMR spectroscopy at 47.61 and 47.66 ppm in $CDCl_3$ at 25 °C; [Rh(tta)(CO)(PPh_3)] = 0.0271 mol dm^{-3}, [MeI] = 0.267 mol dm^{-3}. Indicated is the disappearance of both Rh(I) isomers A and B (**pink**, k_{obs} = 0.00030(4) s^{-1} and 0.00039(3) s^{-1}).

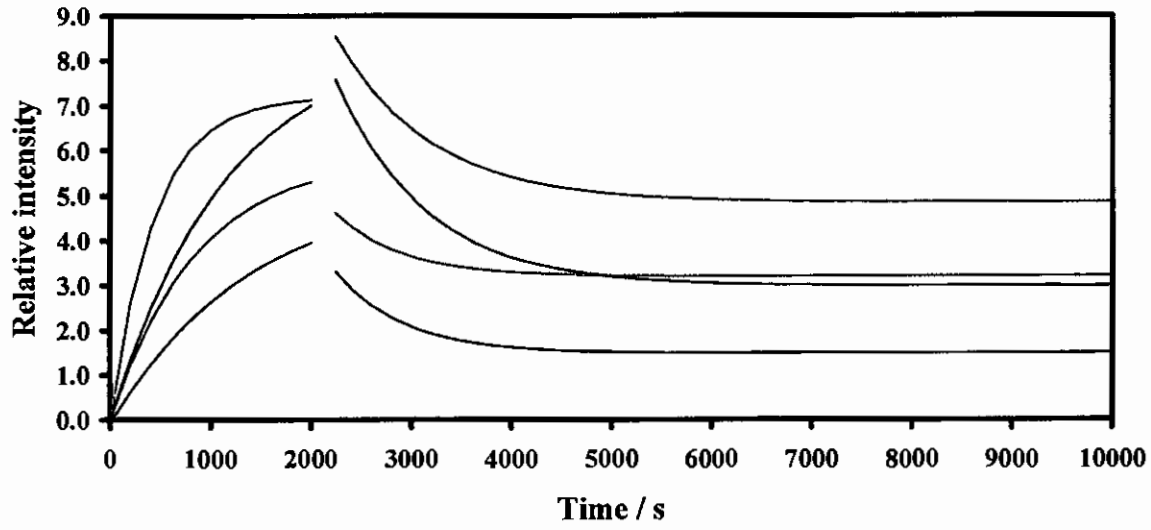

Figure 3.50: Relative intensity *vs* time data of the oxidative addition reaction between MeI and [Rh(tta)(CO)(PPh_3)], as monitored by ^{31}P NMR spectroscopy at 33.50, 34.42, 37.51 and 37.93 ppm in $CDCl_3$ at 25 °C; [Rh(tta)(CO)(PPh_3)] = 0.0271 mol dm^{-3}, [MeI] = 0.267 mol dm^{-3}. Indicated is the appearance of two Rh(III)-alkyl1 isomers (**yellow**, k_{obs} = 0.00118(9) and 0.00225(5) s^{-1}) and two Rh(III)-acyl1 isomers (**blue**, k_{obs} = 0.0007(5) and 0.00086(1) s^{-1}), during the *first reaction* { Rh(I) + MeI ⇌ [Rh(III)-alkyl1 ⇌ Rh(III)-acyl1] }, followed by the disappearance of the two Rh(III)-alkyl1 isomers (**yellow**, k_{obs} = 0.0015(3) and 0.00107(4) s^{-1}) and the two Rh(III)-acyl1 isomers (**blue**, k_{obs} = 0.0015(3) and 0.00111(2) s^{-1}), during the *second reaction* { [Rh(III)-alkyl1 ⇌ Rh(III)-acyl1] → Rh(III)-alkyl2 }.

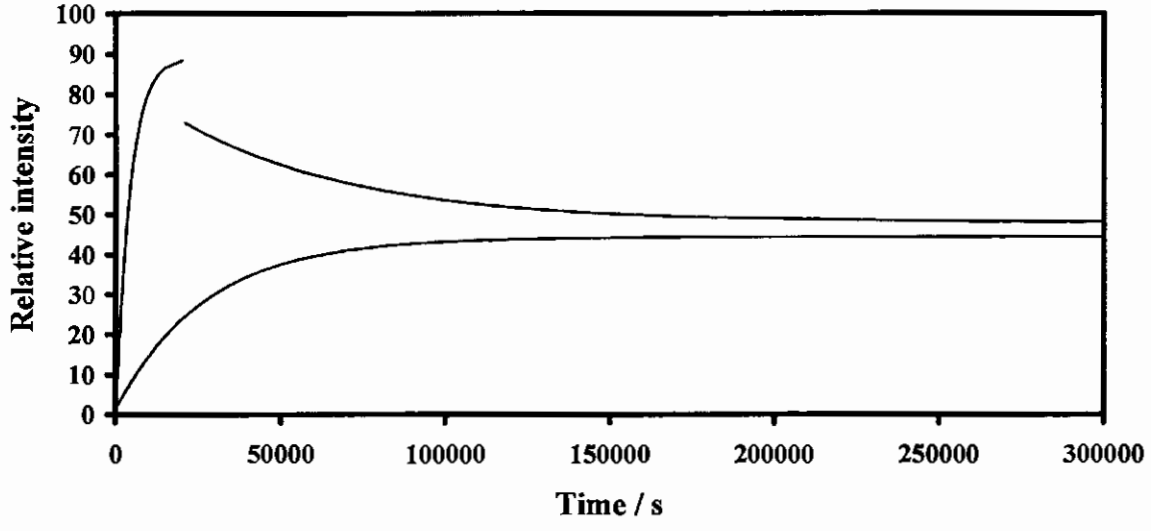

Figure 3.51: Relative intensity *vs* time data of the oxidative addition reaction between MeI and [Rh(tta)(CO)(PPh_3)], as monitored by ^{31}P NMR spectroscopy at 27.07 and 28.74 ppm in $CDCl_3$ at 25 °C; [Rh(tta)(CO)(PPh_3)] = 0.0271 mol dm^{-3}, [MeI] = 0.267 mol dm^{-3}. Indicated is the appearance of two Rh(III)-alkyl2 isomers (**green**), during the *second reaction* { [Rh(III)-alkyl1 ⇌ Rh(III)-acyl1] → Rh(III)-alkyl2 }. Note that the one isomer increases to a maximum (k_{obs} = 0.00024(3) s^{-1}) and then decreases to an equilibrium position with k_{obs} = 0.000019(3) s^{-1}. For the other isomer, k_{obs} = 0.000037(3) s^{-1}.

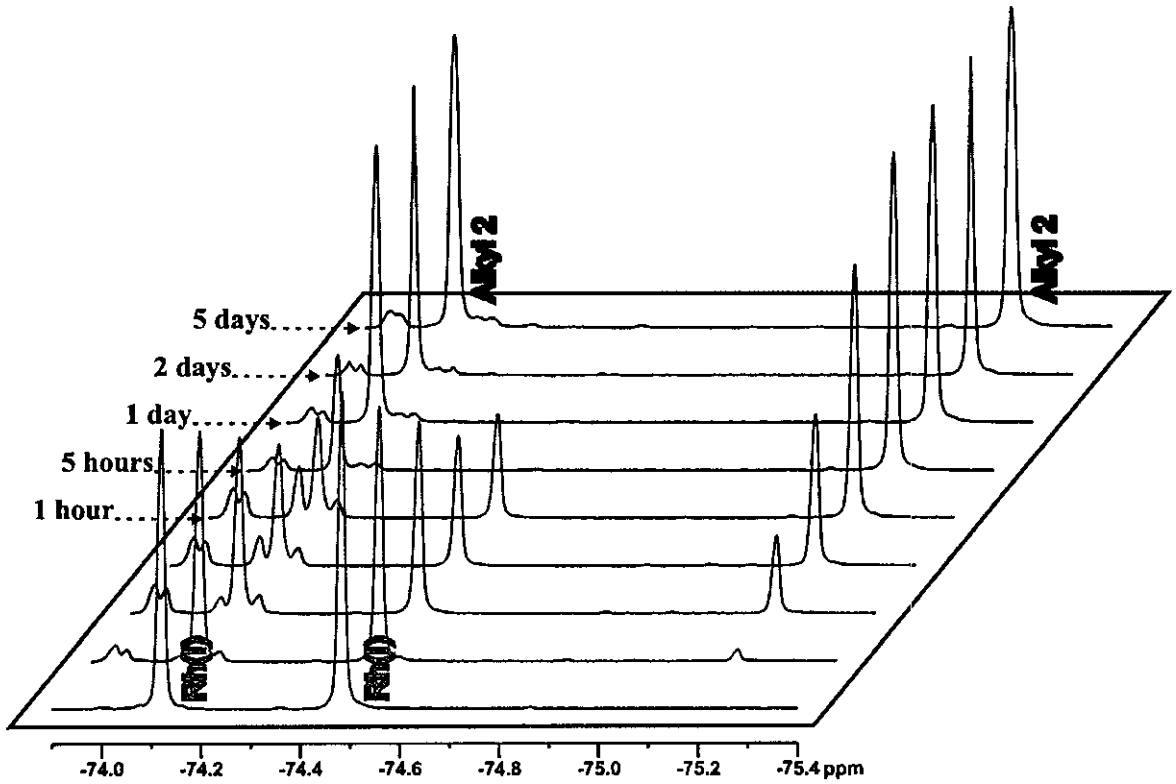

Figure 3.52: Illustration of the oxidative addition reaction between MeI and [Rh(tta)(CO)(PPh_3)], as monitored by ^{19}F NMR spectroscopy in $CDCl_3$ at 25 °C; [Rh(tta)(CO)(PPh_3)] = 0.0271 mol dm^{-3}, [MeI] = 0.271 mol dm^{-3}. The three equivalent fluorine atoms on the CF_3 group of tta give rise to a singlet for each isomer. Two isomers for each species can be observed. The *first reaction* is indicated by the disappearance of Rh(I) at -74.48 and -74.12 ppm (**pink**) and the simultaneous appearance of Rh(III)-alkyl1 and Rh(III)-acyl1 at -74.16, -74.12, -73.97 and -73.94 ppm (**black**). It was not possible to distinguish between the Rh(III)-alkyl1 and Rh(III)-acyl1 signals. Furthermore, the signal at -74.12 ppm overlaps with the Rh(I) signal and the kinetics of that signal could not be followed. The *second reaction* is indicated by the simultaneous disappearance of Rh(III)-alkyl1 and Rh(III)-acyl1 and the formation of a Rh(III)-alkyl2 species at -75.20 and -74.08 ppm (**green**). The first spectrum was recorded before mixing and the rest of the illustrated spectra were recorded after mixing at the indicated time intervals. The signals are colour coded for better clarity.

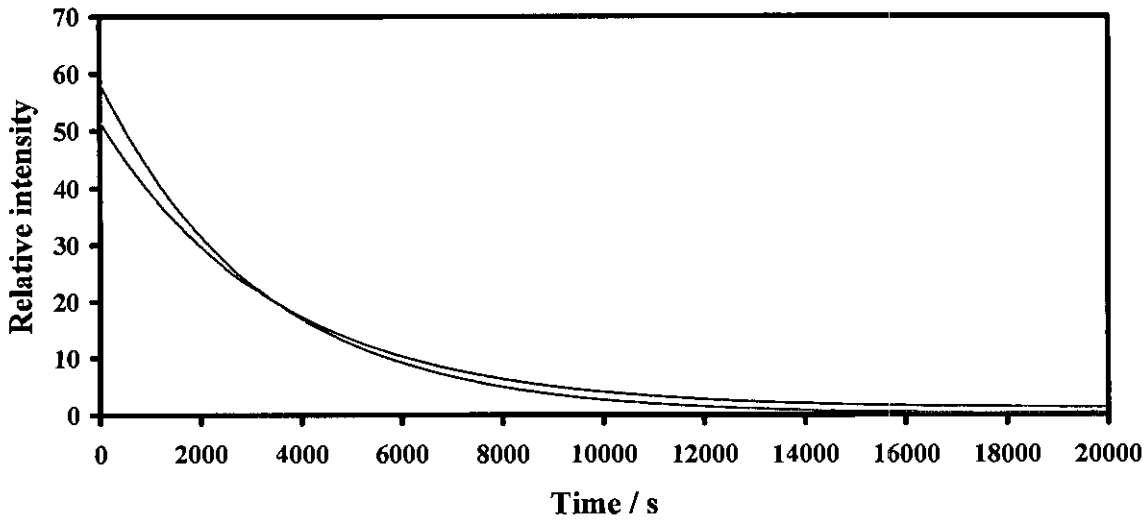

Figure 3.53: Relative intensity *vs* time data of the oxidative addition reaction between MeI and [Rh(tta)(CO)(PPh_3)], as monitored by ^{19}F NMR spectroscopy at -74.48 and -74.12 ppm in $CDCl_3$ at 25 °C; [Rh(tta)(CO)(PPh_3)] = 0.0271 mol dm^{-3}, [MeI] = 0.271 mol dm^{-3}. Indicated is the disappearance of both Rh(I) isomers A and B (pink, k_{obs} = 0.00028(1) s^{-1} and 0.00031(1) s^{-1}).

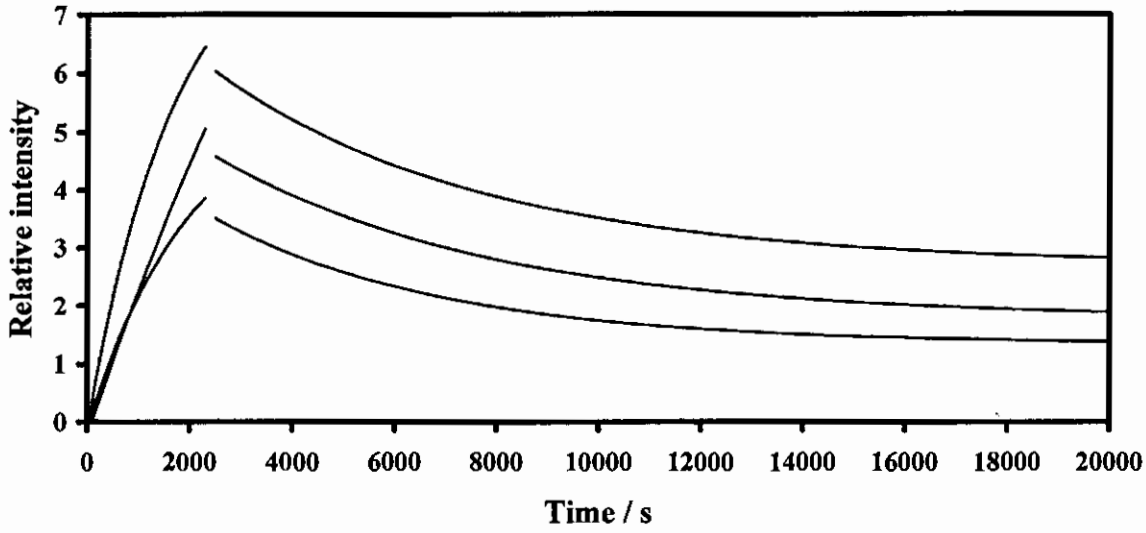

Figure 3.54: Relative intensity *vs* time data of the oxidative addition reaction between MeI and [Rh(tta)(CO)(PPh$_3$)], as monitored by ^{19}F NMR spectroscopy at -74.16, -73.97 and -73.94 ppm in $CDCl_3$ at 25 °C; [Rh(tta)(CO)(PPh$_3$)] = 0.0271 mol dm^{-3}, [MeI] = 0.271 mol dm^{-3}. It was not possible to distinguish between the Rh(III)-alkyl1 and Rh(III)-acyl1 signals. Furthermore, the signal at -74.12 ppm that represents the other Rh(III)-alkyl1/Rh(III)-acyl1 isomer, overlaps with the Rh(I) signal and the kinetics of that signal could therefore not be followed. Indicated is the appearance of Rh(III)-alkyl1 isomer(s) and Rh(III)-acyl1 isomer(s) (k_{obs} = 0.0006(2), 0.0001(3) and 0.0005(3)), during the *first reaction* { Rh(I) + MeI ⇌ [Rh(III)-alkyl1 ⇌ Rh(III)-acyl1] }, followed by the disappearance of the Rh(III)-alkyl1 isomer(s) and the Rh(III)-acyl1 isomer(s) (0.00019(1), 0.00018(1) and 0.00022(2)), during the *second reaction* { [Rh(III)-alkyl1 ⇌ Rh(III)-acyl1] → Rh(III)-alkyl2 }.

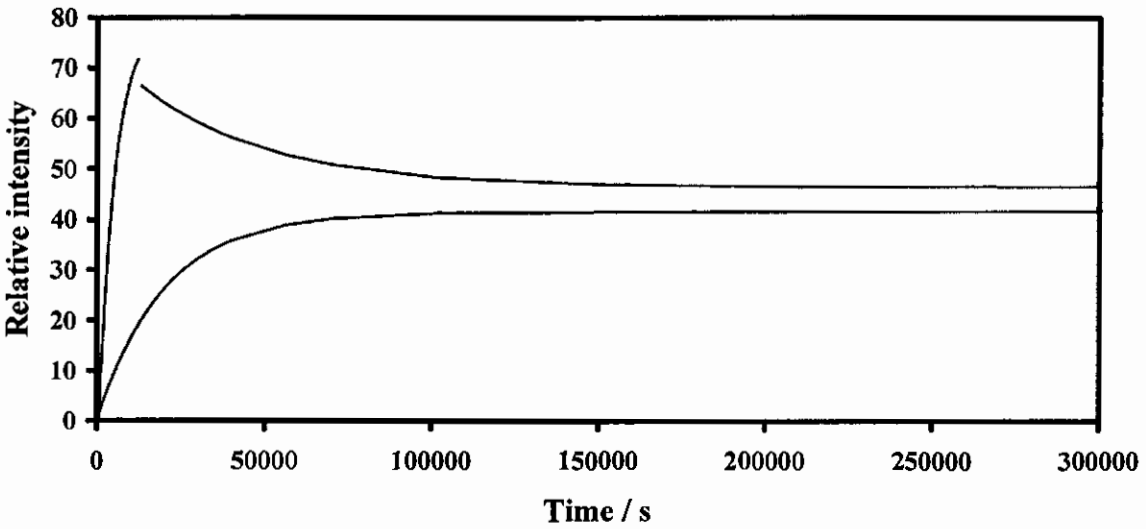

Figure 3.55: Relative intensity *vs* time data of the oxidative addition reaction between MeI and [Rh(tta)(CO)(PPh$_3$)], as monitored by ^{19}F NMR spectroscopy at -75.20 and -74.08 ppm in $CDCl_3$ at 25 °C; [Rh(tta)(CO)(PPh$_3$)] = 0.0271 mol dm^{-3}, [MeI] = 0.271 mol dm^{-3}. Indicated is the appearance of two Rh(III)-alkyl2 isomers (**green**), during the *second reaction* { [Rh(III)-alkyl1 ⇌ Rh(III)-acyl1] → Rh(III)-alkyl2 }. Note that the one isomer increases to a maximum (k_{obs} = 0.00022(3) s^{-1}) and then decreases to an equilibrium position with k_{obs} = 0.0000266(8) s^{-1}. For the other isomer, k_{obs} = 0.000050(1) s^{-1}.

The same reaction sequence as observed with the UV/vis and IR spectrophotometry, was observed with the ^{1}H, ^{31}P and ^{19}F NMR spectroscopy. The new feature introduced by the NMR study is the existence of more than one isomer for each intermediate. The two main isomers observed for each intermediate will be referred to as A and B, for example Rh(III)-alkyl1A and Rh(III)-alkyl1B, the choice of the labels is arbitrary and has no significance. The A and B isomers of each species exist in a fast equilibrium with each other, because the observed rate constant for the disappearance or formation of an A and a B isomer of the same species was found to be, within experimental error, the same, except for Rh(III)-alkyl2. Rh(III)-alkyl2A increases to a maximum and then decreases to an equilibrium point. The kinetic stable Rh(III)-alkyl2 product is thus Rh(III)-alkyl2A which forms faster than Rh(III)-alkyl2B, presumably with a lower activation energy than Rh(III)-alkyl2B. Rh(III)-alkyl2B, however, is the thermodynamic more stable product, since after the initial formation of Rh(III)-alkyl2A, it decreases slowly until an 1:1 equilibrium between Rh(III)-alkyl2A and Rh(III)-alkyl2B sets in. Once the equilibrium sets in, it showed no dynamic character in the temperature range -10 to 55 °C in $CDCl_3$ or acetone-d_6 (**paragraph 3.4.1.3**).

Rate constants obtained from ^{1}H, ^{31}P and ^{19}F NMR are summarized in **Table 3.21** (page 135). It can be seen that a good agreement exists between the kinetic rate constants obtained by utilizing UV/vis and IR spectrophotometric and ^{1}H, ^{31}P and ^{19}F NMR spectroscopic methods.

The Rh(III)-alkyl2 isomers were isolated in solid form and there structures were solved by ^{1}H NOESY and ^{1}H TOCSY experiments, as discussed in **paragraph 3.4.1.3**.

Taking into account that there exist two main isomers of each reactant and reaction product, the complete proposed reaction mechanism for the oxidative addition of MeI to [Rh(tta)(CO)(PPh_3)] is therefore:

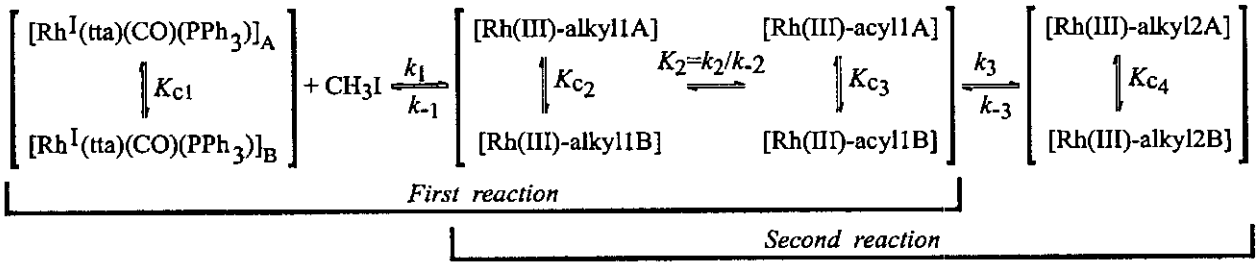

Scheme 3.8: Proposed reaction mechanism for the oxidative addition of MeI to [Rh(tta)(CO)(PPh_3)].

3.5.3.4 Correlation of the kinetic rate constants of the reaction between MeI and [Rh(tta)(CO)(PPh$_3$)] {7} as obtained by various spectrophotometric and spectroscopic methods.

A reasonable correlation has been obtained for the kinetic rate constants of the oxidative addition reaction between MeI and [Rh(tta)(CO)(PPh$_3$)] as determined from data obtained by various spectrophotometric and spectroscopic methods. The data are summarized in **Table 3.21**.

Table 3.21: The kinetic rate constants of the oxidative addition reaction between MeI and [Rh(tta)(CO)(PPh$_3$)] as obtained by various spectrophotometric and spectroscopic methods in chloroform at 25 °C. k_1 and k_3 are the rate constants associated with the *first* and the *second reactions* of the oxidative addition reaction between MeI and [Rh(tta)(CO)(PPh$_3$)] as indicated in **Scheme 3.8**.

Method	[MeI] / mM	1st reaction			
		Rh(I) disappearance		Rh(III)-alkyl 1 appearance	Rh(III)-acyl 1 appearance
		k_{obs} / s^{-1}	k_1 / $dm^3\ mol^{-1}\ s^{-1}$	k_{obs} / s^{-1}	k_{obs} / s^{-1}
IR	81	0.000144(1)	0.00178(1)	0.00106(2)	0.00151(9)
IR	452	0.000675(1)	0.001492(2)	0.00176(1)	0.0014(1)
IR	1000	0.00153(1)	0.00153(1)	0.0027(2)	0.0024(2)
^{1}H NMR [a]	267	0.00041(8) 0.00044(6)	0.0015(3) 0.0017(2)	0.003(1) 0.004(5)	0.0015(2) 0.0024(2)
^{19}F NMR [a]	271	0.00028(1) 0.00031(1)	0.00103(4) 0.00114(4)	0.0001(3) [b] 0.0005(3) [b] 0.0006(2) [b]	
^{31}P NMR [a]	267	0.00030(4) 0.00039(3)	0.0011(2) 0.0015(1)	0.00118(9) 0.00225(5)	0.0007(5) 0.00086(1)
Method	**[MeI] / mM**	**2nd reaction [d]**			
		Rh(III)-alkyl 1 disappearance		**Rh(III)-acyl 1 disappearance**	**Rh(III)-alkyl 2 appearance**
		k_{obs} / s^{-1}		k_{obs} / s^{-1}	k_{obs} / s^{-1}
IR	81	-		-	0.000126(2)
IR	452	0.000423(5)		0.000459(6)	0.00023(1)
IR	1000	0.00087(2)		0.00090(2)	0.00080(2)
^{1}H NMR [a]	267	0.0007(2) 0.0003(1)		0.00050(4) 0.00044(2)	0.000038(7) 0.00039(6), 0.000031(4) [c]
^{19}F NMR [a]	271	0.00018(1) [b] 0.00022(2) [b] 0.00019(1) [b]			0.000050(1) 0.00022(3), 0.0000266(8) [c]
^{31}P NMR [a]	267	0.0015(3) 0.00107(4)		0.0015(3) 0.00111(2)	0.000037(3) 0.00024(3), 0.000019(3) [c]

a Two isomers observed for each product

b Not able to distinguish between Rh(III)-alkyl 1 and Rh(III)-acyl 1 peaks, fourth peak under the signal of Rh(I)

c One isomer increases and then decreases to point of equilibrium, as indicated in **Figure 3.47**, **Figure 3.51** and **Figure 3.55**

d k_{obs} for the 2nd reaction corresponds to k_3 in **Scheme 3.8**, as determined on UV/vis, **Table 3.20** (page 121)

3.5.4 The oxidative addition between MeI and [Rh(bth)(CO)(PPh$_3$)] {6}.

The kinetic rate constants for the oxidative addition reaction between iodomethane (MeI) and [Rh(bth)(CO)(PPh$_3$)] were determined by UV/vis and IR spectrophotometry and NMR spectroscopy under pseudo first-order conditions. Rate constants, obtained by each of these techniques, were consistent and are summarized in **Table 3.22** (page 139) and **Table 3.23** (page 150).

3.5.4.1 The UV/vis monitored reaction between MeI and [Rh(bth)(CO)(PPh$_3$)] {6}.

The UV/vis scans of the oxidative addition reaction between iodomethane (MeI) and [Rh(bth)(CO)(PPh$_3$)] were recorded from 350 nm to 550 nm in chloroform. The spectral changes during the reaction were used to identify how many different reactions occur until the most stable rhodium(III) reaction product is formed. Overlay spectra are given in **Figure 3.56**, **Figure 3.57** and **Figure 3.58**.

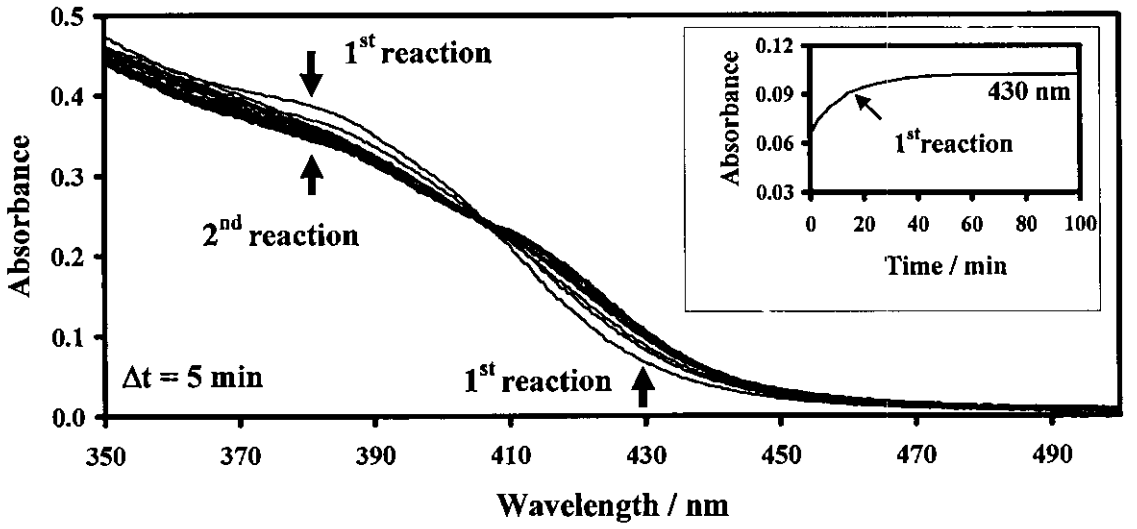

Figure 3.56: Spectrum of the oxidative addition reaction between MeI and [Rh(bth)(CO)(PPh$_3$)], as monitored on the UV/vis spectrophotometer between 350 – 550 nm in chloroform at 25 °C; [Rh(bth)(CO)(PPh$_3$)] = 0.00004 mol dm^{-3}, [MeI] = 0.052 mol dm^{-3}. Illustrated are the *first* and the *second reactions* with a time interval between scans of 5 min. **The insert:** Absorbance *vs* time data for the UV/vis monitored oxidative addition reaction of MeI to [Rh(bth)(CO)(PPh$_3$)] in chloroform at 430 nm illustrating the *first reaction*. The *first reaction* was monitored at this wavelength.

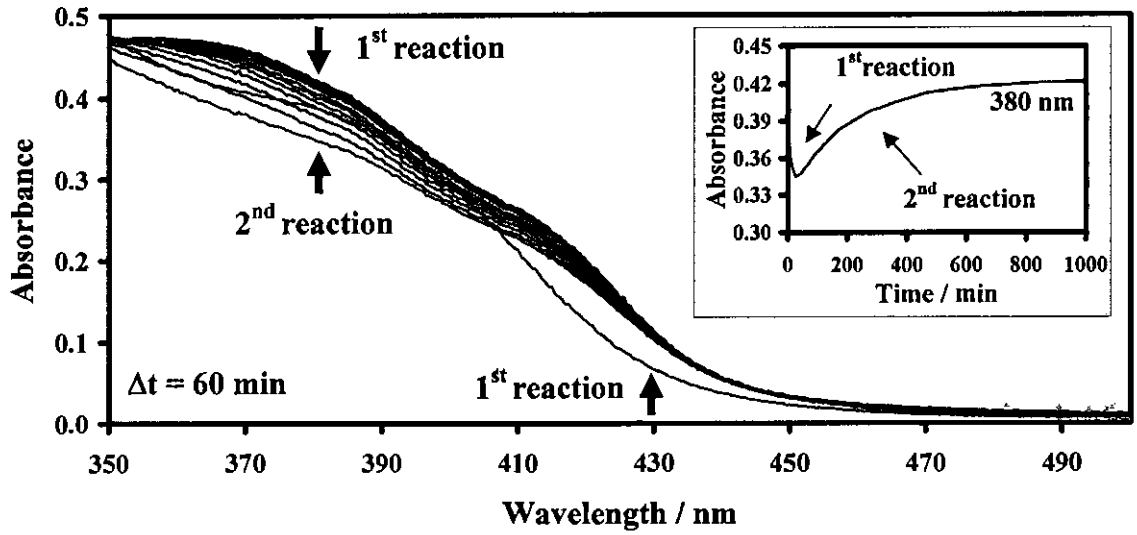

Figure 3.57: Spectrum of the oxidative addition reaction between MeI and [Rh(bth)(CO)(PPh$_3$)], as monitored on the UV/vis spectrophotometer between 350 – 550 nm in chloroform at 25 °C; [Rh(bth)(CO)(PPh$_3$)] = 0.00004 mol dm^{-3}, [MeI] = 0.052 mol dm^{-3}. Illustrated are the *first* and the *second reactions* with a time interval between scans of 60 min. **The insert:** Absorbance *vs* time data for the UV/vis monitored oxidative addition reaction of MeI to [Rh(bth)(CO)(PPh$_3$)] in chloroform at 380 nm illustrating the *first* and the *second reactions*. The *second reaction* was monitored at this wavelength.

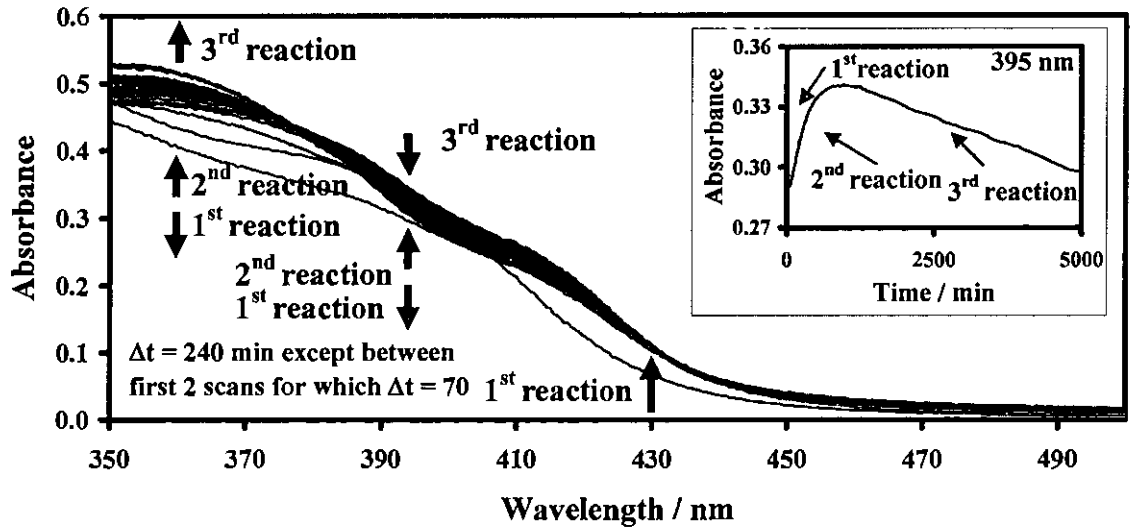

Figure 3.58: Spectrum of the oxidative addition reaction between MeI and [Rh(bth)(CO)(PPh$_3$)], as monitored on the UV/vis spectrophotometer between 350 – 550 nm in chloroform at 25 °C; [Rh(bth)(CO)(PPh$_3$)] = 0.00004 mol dm^{-3}, [MeI] = 0.052 mol dm^{-3}. Illustrated are the *first*, the *second* and the *third reactions* with a time interval of 70 min between the first two scans and 240 min between the successive scans. **The insert:** Absorbance *vs* time data for the UV/vis monitored oxidative addition reaction of MeI to [Rh(bth)(CO)(PPh$_3$)] in chloroform at 395 nm illustrating the *first*, the *second* and the *third reactions*. The *third reaction* was monitored at this wavelength.

From the overlay spectra recorded during the oxidative addition reaction between MeI and [Rh(bth)(CO)(PPh$_3$)] and the subsequent carbonyl insertion and deinsertion reactions illustrated

in the above figures, it is clear that there are at least three different reactions. The *first reaction* is best followed at 430 nm, the *second reaction* at 380 nm and the *third reaction* at 395 nm. The inserts in the above figures illustrate the absorbance *vs* time data for the three reactions at selected wavelengths. The rate constants for the three reactions are summarized in **Table 3.22** (page 139).

The temperature and [MeI] dependence of the *first reaction* of the oxidative addition reaction between MeI and [Rh(bth)(CO)(PPh_3)], as monitored by UV/vis spectrophotometry at 430 nm in chloroform, is demonstrated by **Figure 3.59**. The *second* and the *third reactions* are [MeI] independent and gave constant rate constants at different concentrations. Data are summarized in **Table 3.22** (page 139).

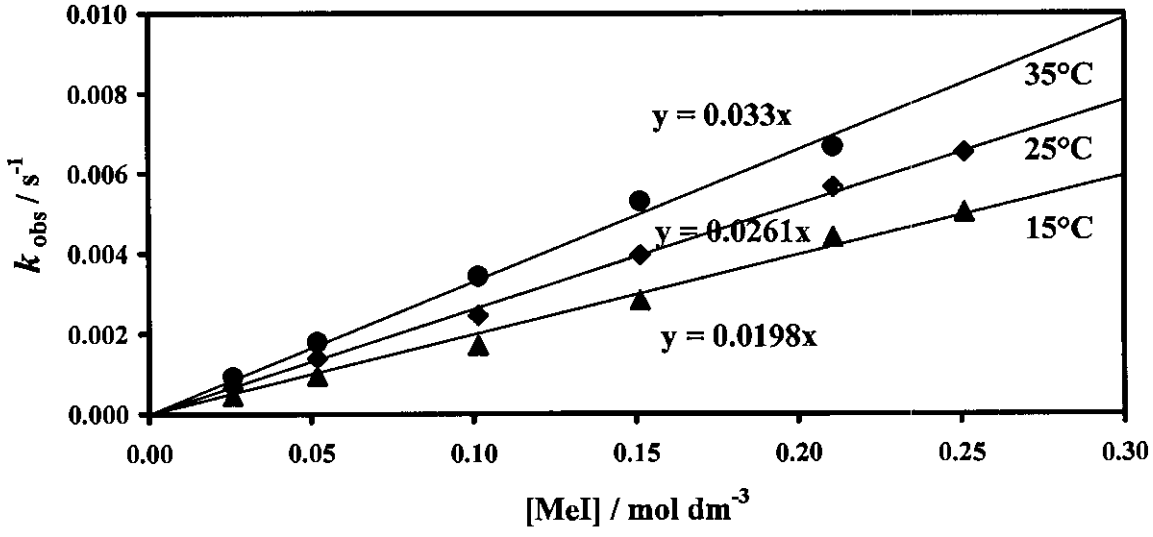

Figure 3.59: Temperature and MeI concentration dependence of the oxidative addition of MeI to [Rh(bth)(CO)(PPh_3)], as monitored on the UV/vis spectrophotometer at 430 nm in chloroform, for the *first reaction* { Rh(I) + MeI ⇌ [Rh(III)-alkyl] ⇌ Rh(III)-acyl] }.

The activation parameters $\Delta H^{\ddagger}$ (activation enthalpy) and $\Delta S^{\ddagger}$ (activation entropy), for the *first reaction* at 25 °C are summarized in **Table 3.22** (page 139). The linear Eyring relationship[54] between ln(k/T) and T^{-1} is illustrated in **Figure 3.60**.

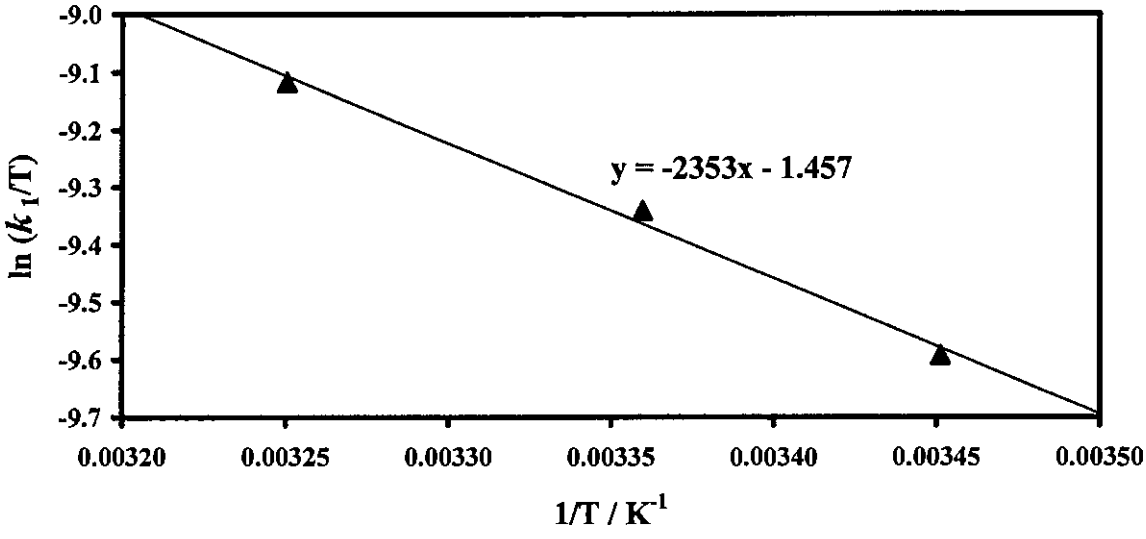

Figure 3.60: The Eyring curve of ln(k_1/T) *vs* 1/T for the *first reaction* { Rh(I) + MeI ⇌ [Rh(III)-alkyl1 ⇌ Rh(III)-acyl1] } of the oxidative addition reaction between MeI and [Rh(bth)(CO)(PPh$_3$)], as monitored on the UV/vis spectrophotometer in chloroform.

Table 3.22: Temperature dependent kinetic rate constants and activation parameters for the oxidative addition between MeI and [Rh(bth)(CO)(PPh$_3$)], as monitored on the UV/vis spectrophotometer in chloroform. k_1, k_3 and k_4 are the rate constants associated with the *first*, the *second* and the *third reactions* of this oxidative addition reaction.

T / °C	1st reaction				
	k_1 / dm^3 mol^{-1} s^{-1}	k_{-1} / s^{-1}	ΔH^* / kJ mol^{-1}	ΔS^* / J mol^{-1} K^{-1}	ΔG^* / kJ mol^{-1} [a]
16.6	0.021(1)	0.0000(2)	16.8(8)	-218(3)	82(2)
24.5	0.0265(6)	0.0000(1)			
34.5	0.0337(8)	0.0000(1)			
T / °C	2nd reaction				
	k_3 / s^{-1}		ΔH^* / kJ mol^{-1}	ΔS^* / J mol^{-1} K^{-1}	ΔG^* / kJ mol^{-1}
24.5	0.000059(3)		-	-	-
T / °C	3rd reaction				
	k_4 / s^{-1}		ΔH^* / kJ mol-1	ΔS^* / J mol^{-1} K^{-1}	ΔG^* / kJ mol^{-1}
24.5	0.000003(2)		-	-	-

a At 25 °C

Results of the UV/vis study of the reaction between MeI and [Rh(bth)(CO)(PPh$_3$)] are interpreted to imply the same as the UV/vis study of the reaction between MeI and [Rh(tta)(CO)(PPh$_3$)], with the difference that there is a *third reaction* observed. Since the *third reaction*, like the *second reaction*, is independent of [MeI] one may deduce that this reaction either involves solvent exchange with any of the ligands of the newly formed Rh(III) complex or it may be isomerization from a Rh(III)-alkyl to a Rh(III)-acyl product (or *vice versa*). Based on the UV/vis study alone one may write a preliminary reaction sequence:

$[Rh^{I}(bth)(CO)(PPh_3)] + MeI$

$k_{-1} \Updownarrow k_1$

[Rh(III)-oxidative addition product X]

$\Updownarrow$ (isomerization or solvent exchange)

[different Rh(III)-product Y]

$\Updownarrow$ (isomerization or solvent exchange)

[different Rh(III)-product Z]

To obtain more insight on the nature of the Rh(III)-products X, Y and Z, an IR and a NMR study of the reaction was conducted.

3.5.4.2 The IR monitored reaction between MeI and [Rh(bth)(CO)(PPh$_3$)] {6}.

Since the carbonyl stretching frequencies (ν_{CO}) are very sensitive to the metal environment and substitution reactions, as described in **paragraph 2.3.4, Chapter 2**, structural information that cannot be obtained from UV/vis spectrophotometry, can be obtained from IR spectrophotometry. An illustration of the oxidative addition reaction between MeI and [Rh(bth)(CO)(PPh$_3$)], as monitored on the IR spectrophotometer between 1600 – 2200 cm^{-1} in chloroform at 25 °C, is given in **Figure 3.61**. **Figure 3.62, Figure 3.63** and **Figure 3.64** give the absorbance *vs* time data of the indicated species for the *first* and the *second reactions*. The *third reaction* was observed with IR spectrophotometry, but the kinetics could not be followed. Rate constants are summarized in **Table 3.23** (page 150).

The concentration dependence of the *first reaction* of the oxidative addition reaction between MeI and [Rh(bth)(CO)(PPh$_3$)], as monitored on the IR spectrophotometry at 1983 cm^{-1} in chloroform, is illustrated in **Figure 3.65**.

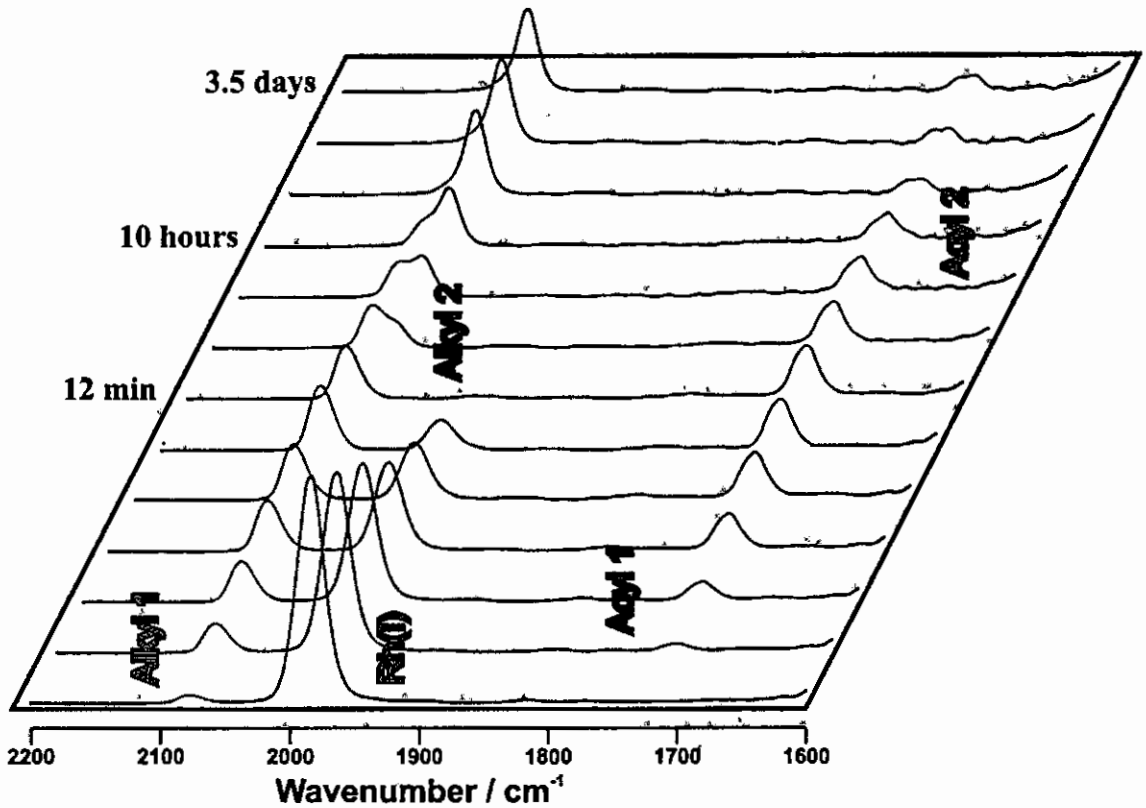

Figure 3.61: Illustration of the oxidative addition reaction between MeI and [Rh(bth)(CO)(PPh_3)], as monitored on the IR spectrophotometer between 1600 – 2200 cm^{-1} in chloroform at 25 °C; [Rh(bth)(CO)(PPh_3)] = 0.0080 mol dm^{-3}, [MeI] = 0.353 mol dm^{-3}. The *first reaction* is indicated by the disappearance of Rh(I) at 1983 cm^{-1} (**pink**) and the simultaneous appearance of Rh(III)-alkyl1 at 2079 cm^{-1} (**yellow**) and Rh(III)-acyl1 at 1720 cm^{-1} (**blue**). The *second reaction* is indicated by the simultaneous disappearance of Rh(III)-alkyl1 and Rh(III)-acyl1 and the formation of a Rh(III)-alkyl2 species at 2056 cm^{-1} (**green**). The *third reaction* is indicated by the disappearance of Rh(III)-alkyl2 and the formation of a Rh(III)-acyl2 species at 1709 cm^{-1} (**orange**). Unfortunately the kinetics of this *third reaction* could not be followed. The first spectrum was recorded 55 s after mixing and the rest of the illustrated spectra were recorded at the indicated time intervals. The signals are colour coded for better clarity.

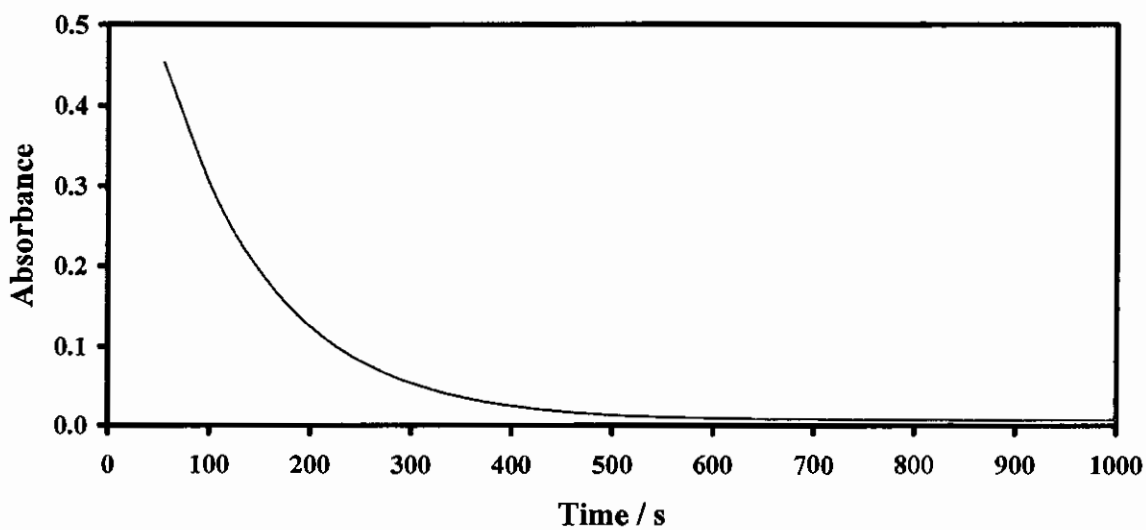

Figure 3.62: Absorbance *vs* time data of the oxidative addition reaction between MeI and [Rh(bth)(CO)(PPh_3)], as monitored on the IR spectrophotometer at 1983 cm^{-1} in chloroform at 25 °C; [Rh(bth)(CO)(PPh_3)] = 0.0080 mol dm^{-3}, [MeI] = 0.353 mol dm^{-3}. Indicated is the disappearance of Rh(I) (**pink**, k_{obs} = 0.00916(1) s^{-1}).

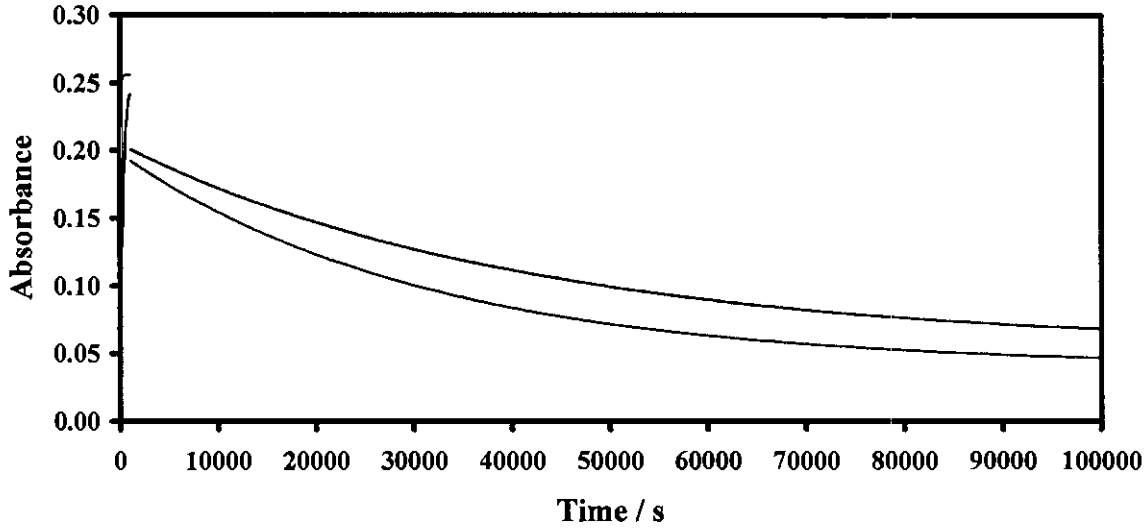

Figure 3.63: Absorbance *vs* time data of the oxidative addition reaction between MeI and [Rh(bth)(CO)(PPh_3)], as monitored on the IR spectrophotometer at 2079 and 1720 cm^{-1} in chloroform at 25 °C; [Rh(bth)(CO)(PPh_3)] = 0.0080 mol dm^{-3}, [MeI] = 0.353 mol dm^{-3}. Indicated is the appearance of Rh(III)-alkyl1 (**yellow**, k_{obs} = 0.00175(3) s^{-1}) and Rh(III)-acyl1 (**blue**, k_{obs} = 0.0032(5) s^{-1}), during the *first reaction* { Rh(I) + MeI ⇌ [Rh(III)-alkyl1 ⇌ Rh(III)-acyl1] }, followed by the disappearance of Rh(III)-alkyl1 (**yellow**, k_{obs} = 0.0000320(2) s^{-1}) and Rh(III)-acyl1 (**blue**, k_{obs} = 0.0000243(1) s^{-1}), during the *second reaction* { [Rh(III)-alkyl1 ⇌ Rh(III)-acyl1] → Rh(III)-alkyl2 }.

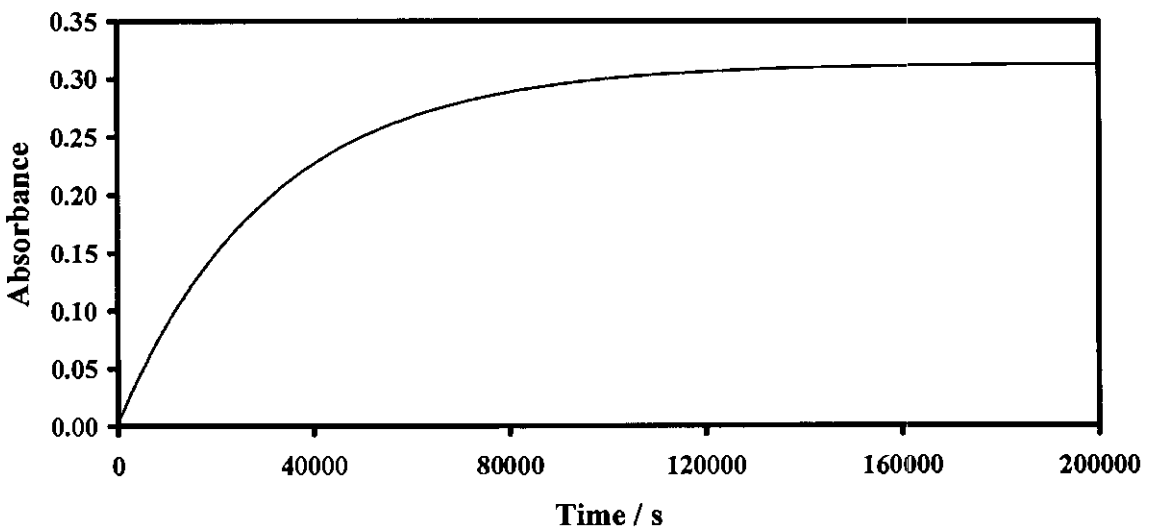

Figure 3.64: Absorbance *vs* time data of the oxidative addition reaction between MeI and [Rh(bth)(CO)(PPh_3)], as monitored on the IR spectrophotometer at 2056 cm^{-1} in chloroform at 25 °C; [Rh(bth)(CO)(PPh_3)] = 0.0080 mol dm^{-3}, [MeI] = 0.353 mol dm^{-3}. Indicated is the appearance of Rh(III)-alkyl2 (**green**, k_{obs} = 0.0000320(1) s^{-1}), during the *second reaction* { [Rh(III)-alkyl1 ⇌ Rh(III)-acyl1] → Rh(III)-alkyl2 }.

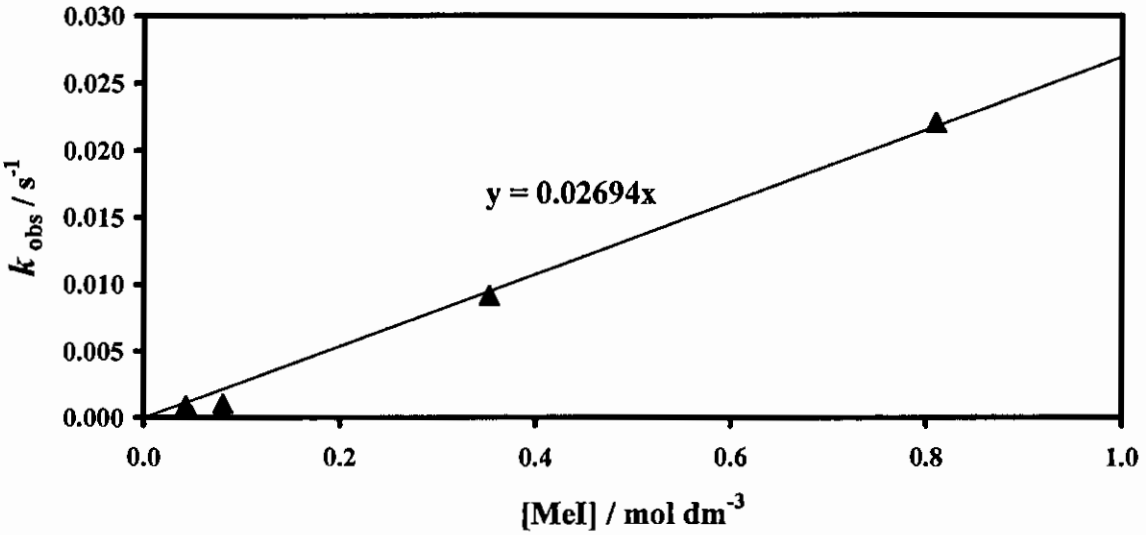

Figure 3.65: MeI concentration dependence of the oxidative addition of MeI to [Rh(bth)(CO)(PPh_3)], as monitored on IR spectrophotometer at 1983 cm^{-1} in chloroform, for the *first reaction* { Rh(I) + MeI ⇌ [Rh(III)-alkyl1 ⇌ Rh(III)-acyl1] }.

The *first* and the *second reactions* of the reaction between MeI and [Rh(bth)(CO)(PPh_3)] are interpreted to imply the same as the IR study of the reaction between MeI and [Rh(tta)(CO)(PPh_3)]. The *second reaction*, however, was followed by a very slow [MeI]-independent *third reaction* ($t_{1/2} \approx 64$ hours from UV/vis results) and corresponds to the slow disappearance of the Rh^{III}-alkyl2 species at 2056 cm^{-1} and the appearance of a new Rh^{III}-acyl2 species at 1709 cm^{-1}. The long half-life of the third reaction implied that it was not practical to follow as solvent evaporation became difficult to control. Inclusion of the third reaction into the general reaction sequence, give:

$$\text{Rh(I)} + \text{MeI} \underset{k_{-1}}{\overset{k_1}{\rightleftharpoons}} \{\text{[Rh(III)-alkyl1]} \underset{k_{-2}}{\overset{K_2, k_2}{\rightleftharpoons}} \text{[Rh(III)-acyl1]}\} \underset{k_{-3}}{\overset{k_3}{\rightleftharpoons}} \text{[Rh(III)-alkyl2]} \underset{k_{-4}}{\overset{k_4}{\rightleftharpoons}} \text{[Rh(III)-acyl2]}$$

First reaction

Second reaction

Third reaction

3.5.4.3 The ^{1}H and ^{31}P NMR monitored reaction between MeI and [Rh(bth)(CO)(PPh_3)] {6}.

The reaction between MeI and [Rh(bth)(CO)(PPh_3)] was monitored by ^{1}H and ^{31}P NMR. As with [Rh(tta)(CO)(PPh_3)], it is also best to look at either the methine or the methyl signals of the Rh(I), Rh(III)-alkyl and Rh(III)-acyl species when following the oxidative addition reaction on the ^{1}H NMR, due to overlapping of the signals in the aromatic region. On the ^{31}P NMR, each isomer is presented as a doublet due to the Rh-P coupling. By carefully comparing the positions and integrals of the different signals, the spectral parameters of the different isomers could be identified. An illustration of the oxidative addition reaction between MeI and [Rh(bth)(CO)(PPh_3)], as monitored by ^{1}H NMR spectroscopy in $CDCl_3$ at 25 °C, is given in **Figure 3.66**. An illustration of the reaction monitored by ^{31}P NMR spectroscopy in $CDCl_3$ at 25 °C, is given in **Figure 3.70**. Both illustrations are followed by the graphs of the relative intensity *vs* time data of the relative experiment and species for the *first* and the *second reactions*. The *third reaction* was observed with NMR spectroscopy, but the kinetics could not be followed due to the long reaction time and subsequent solvent evaporation. Rate constants are summarized in **Table 3.23** (page 150).

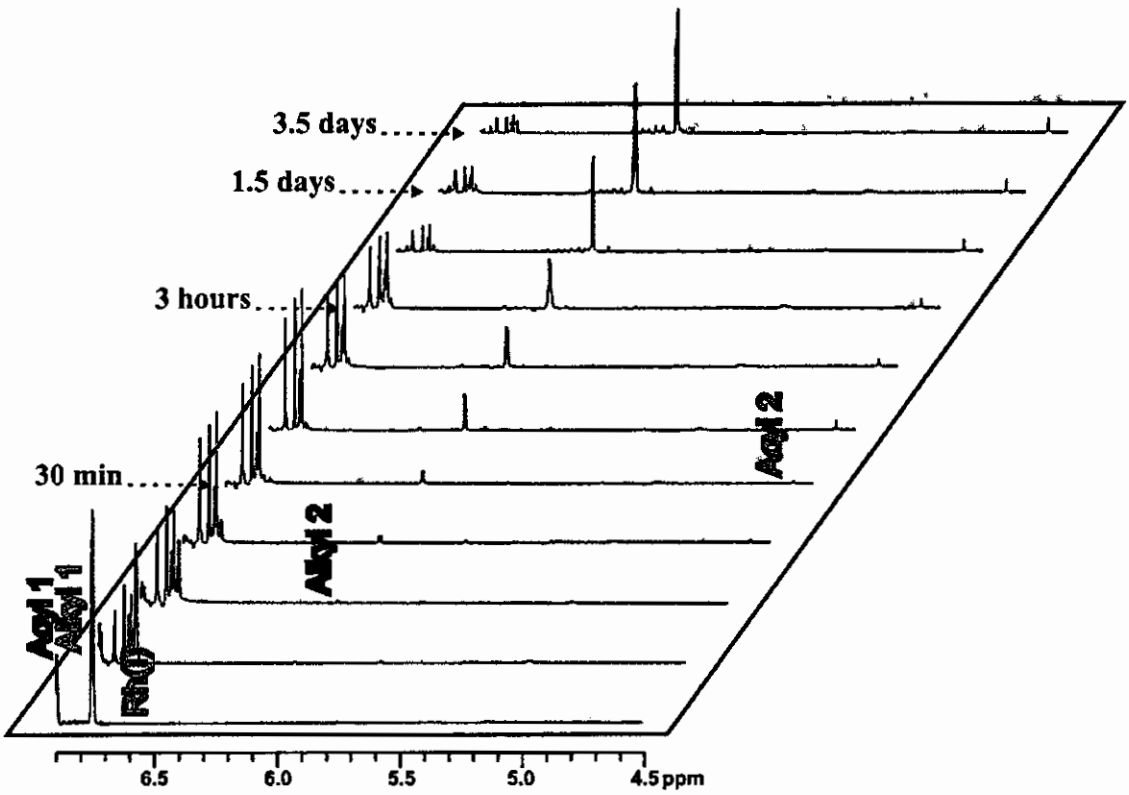

Figure 3.66: A fragment of the ^{1}H NMR spectra of the oxidative addition reaction between MeI and [Rh(bth)(CO)(PPh$_3$)], as monitored by ^{1}H NMR spectroscopy in $CDCl_3$ at 25 °C; [Rh(bth)(CO)(PPh$_3$)] = 0.0262 mol dm^{-3}, [MeI] = 0.159 mol dm^{-3}. Two isomers for each species can be observed. The *first reaction* is indicated by the disappearance of Rh(I) at 6.74 and 6.75 ppm (**pink**) and the simultaneous appearance of Rh(III)-alkyl1 at 6.76 and 6.78 ppm (**yellow**) and Rh(III)-acyl1 at 6.80 and 6.83 ppm (**blue**). The *second reaction* is indicated by the simultaneous disappearance of Rh(III)-alkyl1 and Rh(III)-acyl1 and the formation of a Rh(III)-alkyl2 species at 6.09 and 6.10 ppm (**green**). The *third reaction* is indicated by the disappearance of Rh(III)-alkyl2 and the formation of a Rh(III)-acyl2 species at 4.58 and 4.59 ppm (**orange**). Unfortunately the kinetics of this *third reaction* could not be followed. The first spectrum was recorded before mixing and the rest of the illustrated spectra were recorded after mixing at the indicated time intervals. The signals are colour coded for better clarity.

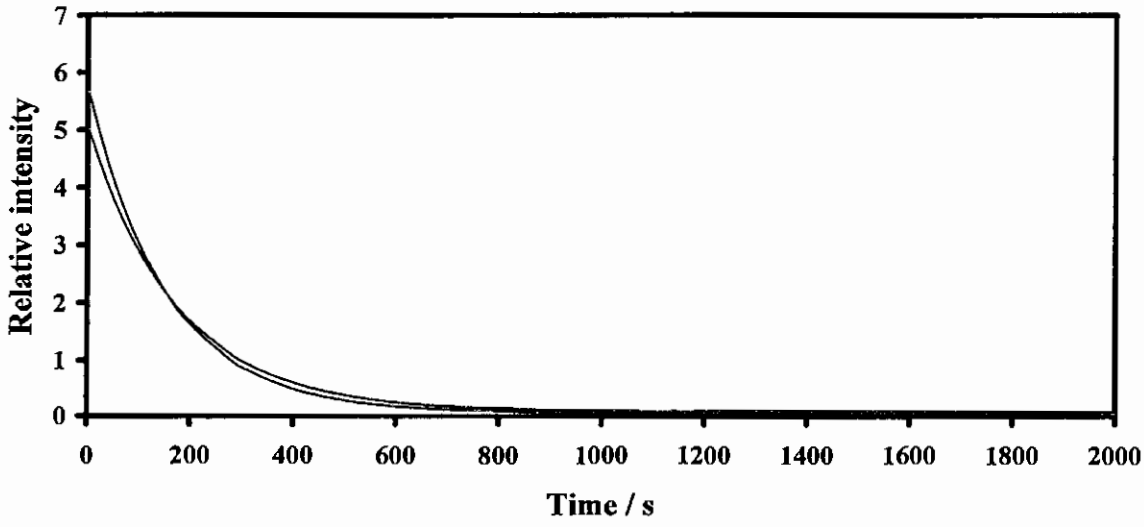

Figure 3.67: Relative intensity *vs* time data of the oxidative addition reaction between MeI and [Rh(bth)(CO)(PPh$_3$)], as monitored by ^{1}H NMR spectroscopy at 6.74 and 6.75 ppm in $CDCl_3$ at 25 °C; [Rh(bth)(CO)(PPh$_3$)] = 0.0262 mol dm^{-3}, [MeI] = 0.267 mol dm^{-3}. Indicated is the disappearance of both Rh(I) isomers A and B (pink, k_{obs} = 0.0057(3) s^{-1} and 0.0064(4) s^{-1}).

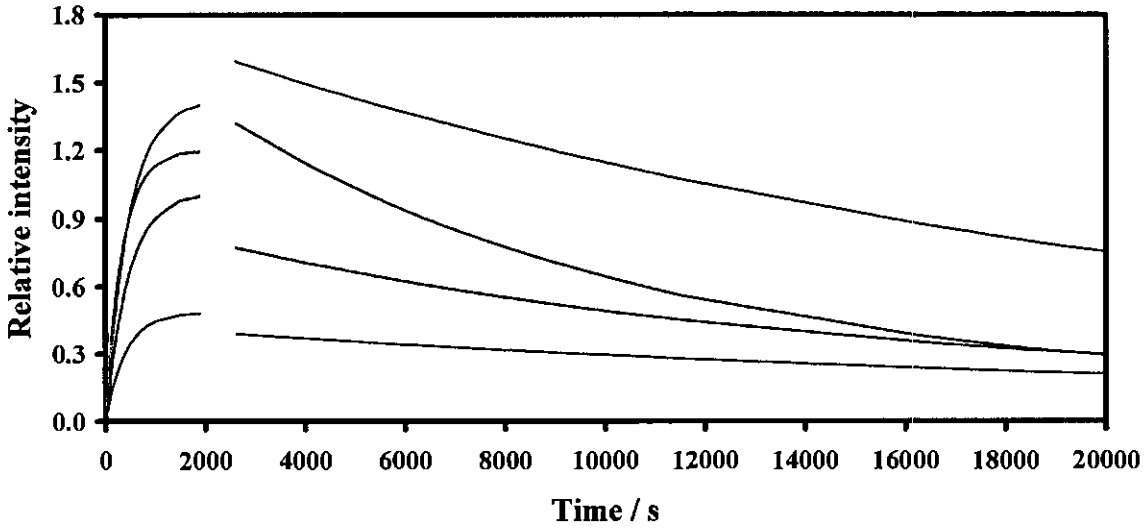

Figure 3.68: Relative intensity *vs* time data of the oxidative addition reaction between MeI and [Rh(bth)(CO)(PPh_3)], as monitored by ^1H NMR spectroscopy at 6.76, 6.78, 6.80 and 6.83 ppm in $CDCl_3$ at 25 °C; [Rh(bth)(CO)(PPh_3)] = 0.0262 mol dm^{-3}, [MeI] = 0.267 mol dm^{-3}. Indicated is the appearance of two Rh(III)-alkyl1 isomers (**yellow**, k_{obs} = 0.0025(3) and 0.0021(3) s^{-1}) and two Rh(III)-acyl1 isomers (**blue**, k_{obs} = 0.0025(8) and 0.0024(3) s^{-1}), during the *first reaction* { Rh(I) + MeI ⇌ [Rh(III)-alkyl1 ⇌ Rh(III)-acyl1] }, followed by the disappearance of the two Rh(III)-alkyl1 isomers (**yellow**, k_{obs} = 0.000051(3) and 0.00005(1) s^{-1}) and the two Rh(III)-acyl1 isomers (**blue**, k_{obs} = 0.000049(4) and 0.000055(6) s^{-1}), during the *second reaction* { [Rh(III)-alkyl1 ⇌ Rh(III)-acyl1] → Rh(III)-alkyl2 }.

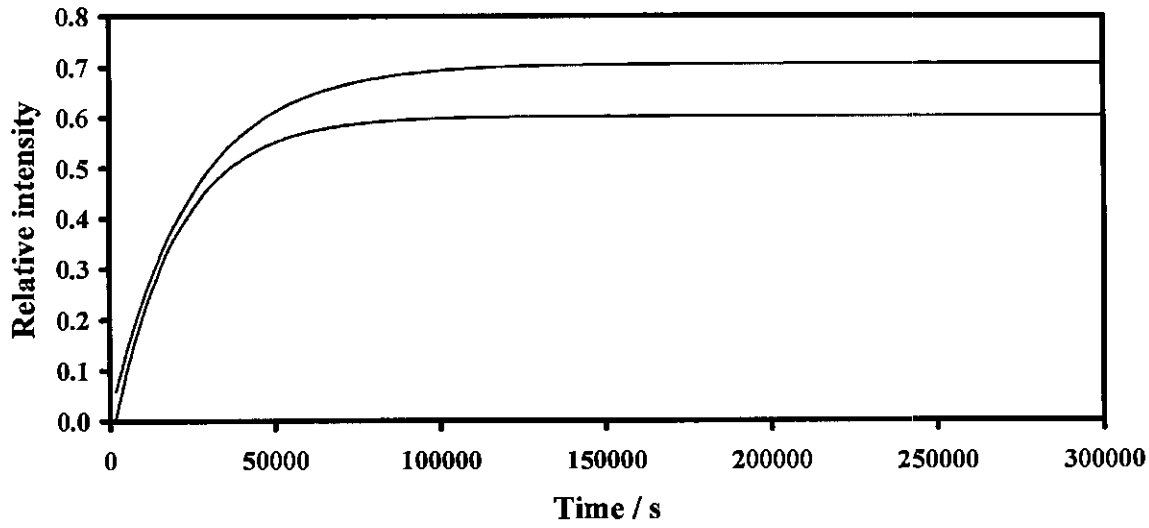

Figure 3.69: Relative intensity *vs* time data of the oxidative addition reaction between MeI and [Rh(bth)(CO)(PPh_3)], as monitored by ^1H NMR spectroscopy at 6.09 and 6.10 ppm in $CDCl_3$ at 25 °C; [Rh(bth)(CO)(PPh_3)] = 0.0262 mol dm^{-3}, [MeI] = 0.267 mol dm^{-3}. Indicated is the appearance of two Rh(III)-alkyl2 isomers (**green**, k_{obs} = 0.000051(9) and 0.000040(7) s^{-1}), during the *second reaction* { [Rh(III)-alkyl1 ⇌ Rh(III)-acyl1] → Rh(III)-alkyl2 }.

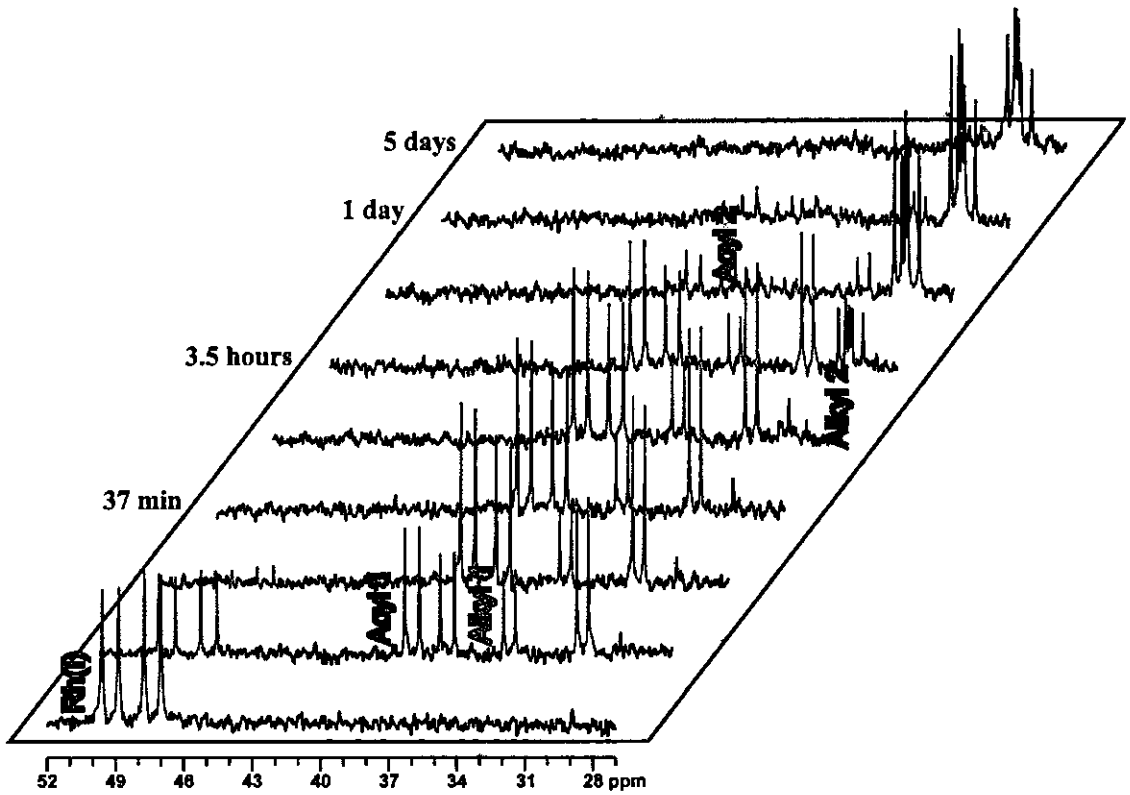

Figure 3.70: Illustration of the oxidative addition reaction between MeI and [Rh(bth)(CO)(PPh_3)], as monitored by ^{31}P NMR spectroscopy in $CDCl_3$ at 25 °C; [Rh(bth)(CO)(PPh_3)] = 0.0273 mol dm^{-3}, [MeI] = 0.106 mol dm^{-3}. The phosphorus atom on the PPh_3 group gives rise to a doublet for each isomer (due to Rh-P coupling). Two isomers for each species can be observed. The *first reaction* is indicated by the disappearance of Rh(I) at 47.41 and 49.21 ppm (**pink**) and the simultaneous appearance of Rh(III)-alkyl1 at 31.03 and 34.21 ppm (**yellow**) and Rh(III)-acyl1 at 36.89 and 38.40 ppm (**blue**). The *second reaction* is indicated by the simultaneous disappearance of Rh(III)-alkyl1 and Rh(III)-acyl1 and the formation of a Rh(III)-alkyl2 species at 28.62 and 29.21 ppm (**green**). The *third reaction* is indicated by the disappearance of Rh(III)-alkyl2 and the formation of a Rh(III)-acyl2 species at 35.16 and 35.81 ppm (**orange**). Unfortunately the kinetics of this *third reaction* could not be followed. The first spectrum was recorded before mixing and the rest of the illustrated spectra were recorded after mixing at the indicated time intervals. The signals are colour coded for better clarity.

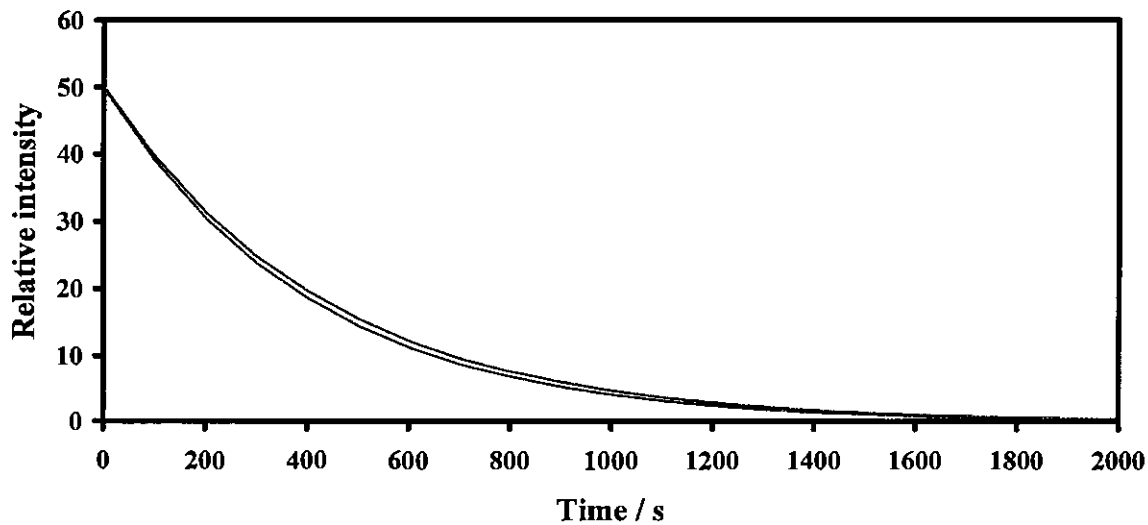

Figure 3.71: Relative intensity *vs* time data of the oxidative addition reaction between MeI and [Rh(bth)(CO)(PPh_3)], as monitored by ^{31}P NMR spectroscopy at 47.41 and 49.21 ppm in $CDCl_3$ at 25 °C; [Rh(bth)(CO)(PPh_3)] = 0.0273 mol dm^{-3}, [MeI] = 0.106 mol dm^{-3}. Indicated is the disappearance of both Rh(I) isomers A and B (pink, k_{obs} = 0.00244(4) and 0.00232(2) s^{-1}).

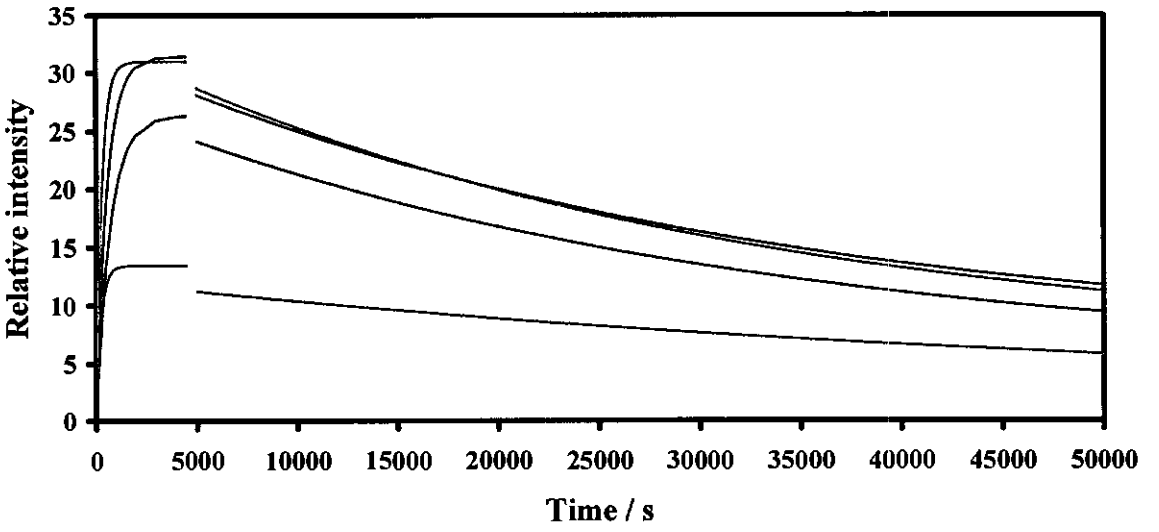

Figure 3.72: Relative intensity *vs* time data of the oxidative addition reaction between MeI and [Rh(bth)(CO)(PPh_3)], as monitored by ^{31}P NMR spectroscopy at 31.03, 34.21, 36.89 and 38.40 ppm in $CDCl_3$ at 25 °C; [Rh(bth)(CO)(PPh_3)] = 0.0273 mol dm^{-3}, [MeI] = 0.106 mol dm^{-3}. Indicated is the appearance of two Rh(III)-alkyl1 isomers (**yellow**, k_{obs} = 0.0041(2) and 0.00344(3) s^{-1}) and two Rh(III)-acyl1 isomers (**blue**, k_{obs} = 0.0018(2) and 0.00138(9) s^{-1}), during the *first reaction* { Rh(I) + MeI ⇌ [Rh(III)-alkyl1 ⇌ Rh(III)-acyl1] }, followed by the disappearance of the two Rh(III)-alkyl1 isomers (**yellow**, k_{obs} = 0.000019(4) and 0.000032(4) s^{-1}) and the two Rh(III)-acyl1 isomers (**blue**, k_{obs} = 0.000031(4) and 0.000032(6) s^{-1}), during the *second reaction* { [Rh(III)-alkyl1 ⇌ Rh(III)-acyl1] → Rh(III)-alkyl2 }.

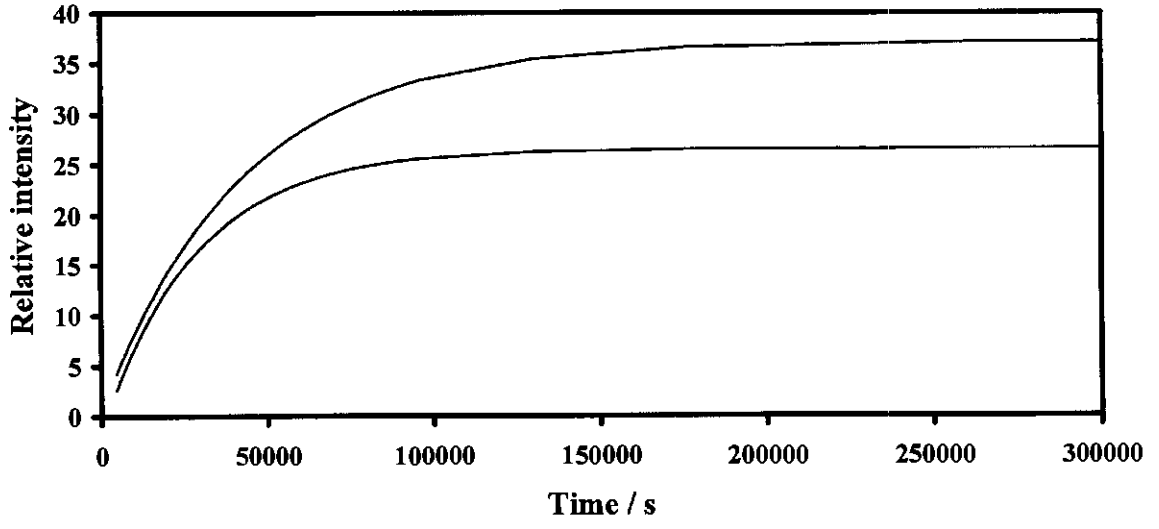

Figure 3.73: Relative intensity *vs* time data of the oxidative addition reaction between MeI and [Rh(bth)(CO)(PPh_3)], as monitored by ^{31}P NMR spectroscopy at 28.62 and 29.21 ppm in $CDCl_3$ at 25 °C; [Rh(bth)(CO)(PPh_3)] = 0.0273 mol dm^{-3}, [MeI] = 0.106 mol dm^{-3}. Indicated is the appearance of two Rh(III)-alkyl2 isomers (**green**, k_{obs} = 0.000024(2) and 0.000035(2) s^{-1}), during the *second reaction* { [Rh(III)-alkyl1 ⇌ Rh(III)-acyl1] → Rh(III)-alkyl2 }.

The same reaction sequence as observed with the UV/vis and IR spectrophotometry, was observed with the ^{1}H and ^{31}P NMR spectroscopy. As with the oxidative addition reaction with [Rh(tta)(CO)(PPh_3)], two isomers for each intermediate were also observed.

Results of the ^{1}H and ^{31}P NMR study of the reaction between MeI and [Rh(bth)(CO)(PPh_3)] are interpreted to imply the same reaction sequence as the ^{1}H and ^{31}P NMR study of the reaction between MeI and [Rh(tta)(CO)(PPh_3)], with the difference that *third reaction* is observed. Consistent with the IR results, the *third reaction* is identified as the slow disappearance of the Rh^{III}-alkyl2 species and the appearance of a new Rh^{III}-acyl2 species. Unfortunately, the kinetics of this reaction was too slow to follow effectively.

Rate constants obtained from ^{1}H and ^{31}P NMR are summarized in **Table 3.23** (page 150). It can be seen that a good agreement exists between the kinetic rate constants obtained by utilizing UV/vis and IR spectrophotometric and ^{1}H and ^{31}P NMR spectroscopic methods.

The structures of the Rh(III)-alkyl1, Rh(III)-acyl1 and Rh(III)-alkyl2 isomers were explored *in situ* during the reaction process by ^{1}H NOESY and will be discussed in **paragraph 3.5.4.5.**

Taking into account that there exist two main isomers of each reactant and reaction product, the complete proposed reaction mechanism for the oxidative addition of MeI to [Rh(bth)(CO)(PPh_3)] is therefore:

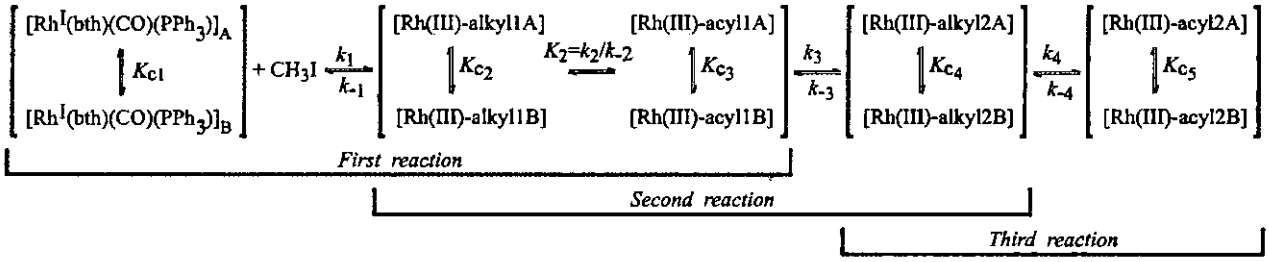

Scheme 3.9: Proposed reaction mechanism for the oxidative addition of MeI to [Rh(bth)(CO)(PPh_3)].

3.5.4.4 Correlation of the kinetic rate constants of the reaction between MeI and [Rh(bth)(CO)(PPh$_3$)] {6} as obtained by various spectrophotometric and spectroscopic methods.

A reasonable correlation has been obtained for the kinetic rate constants of the oxidative addition reaction between MeI and [Rh(bth)(CO)(PPh$_3$)] as determined from data obtained by various spectrophotometric and spectroscopic methods. The data are summarized in **Table 3.23**.

Table 3.23: The kinetic rate constants of the oxidative addition reaction between MeI and [Rh(bth)(CO)(PPh$_3$)] as obtained by various spectrophotometric and spectroscopic methods in chloroform at 25 °C. k_1 and k_3 are the rate constants associated with the *first* and the *second reactions* of the oxidative addition reaction between MeI and [Rh(bth)(CO)(PPh$_3$)] as indicated in **Scheme 3.9**.

Method	[MeI] / mM	1st reaction			
		Rh(I) disappearance		Rh(III)-alkyl 1 appearance	Rh(III)-acyl 1 appearance
		k_{obs} / s^{-1}	k_1 / $dm^3\ mol^{-1}\ s^{-1}$	k_{obs} / s^{-1}	k_{obs} / s^{-1}
IR	43	0.000926(6)	0.0215(1)	0.00117(2)	0.001027(7)
IR	81	0.001063(2)	0.01312(2)	0.00242(6)	0.00072(3)
IR	353	0.00916(1)	0.02595(3)	0.00175(3)	0.0032(5)
IR	810	0.0221(6)	0.0273(7)	0.018(4)	0.004(1)
^{1}H NMR [a]	159	0.0057(3) 0.0064(4)	0.036(2) 0.040(3)	0.0025(3) 0.0021(3)	0.0025(8) 0.0024(3)
^{31}P NMR [a]	106	0.00244(4) 0.00232(2)	0.0232(2) 0.0219(2)	0.0041(2) 0.00344(3)	0.0018(2) 0.00138(9)

Method	[MeI] / mM	2nd reaction [b]		
		Rh(III)-alkyl 1 disappearance	Rh(III)-acyl 1 disappearance	Rh(III)-alkyl 2 appearance
		k_{obs} / s^{-1}	k_{obs} / s^{-1}	k_{obs} / s^{-1}
IR	43	0.0000286(3)	0.000039(1)	0.0000277(1)
IR	81	0.00001887(8)	0.0000181(1)	0.0000129(4)
IR	353	0.0000320(2)	0.0000243(1)	0.0000320(1)
IR	810	0.000043(2)	0.000038(2)	0.0000372(9)
^{1}H NMR [a]	159	0.000051(3) 0.00005(1)	0.000049(4) 0.000055(6)	0.000051(9) 0.000040(7)
^{31}P NMR [a]	106	0.000019(4) 0.000032(4)	0.000031(4) 0.000032(6)	0.000024(2) 0.000035(2)

Method	[MeI] / mM	3rd reaction	
		Rh(III)-alkyl 2 disappearance	Rh(III)-acyl 2 appearance
		k_{obs} / s^{-1}	k_{obs} / s^{-1}
The disappearance of the Rh(III)-alkyl 2 and the appearance of the Rh(III)-acyl 2 were observed, but the kinetics could not be followed with IR spectrophotometry and NMR spectroscopy.			

a Two isomers observed for each product

b k_{obs} for the 2nd reaction corresponds to k_3 in **Scheme 3.9**, as determined on UV/vis, **Table 3.22** (page 139)

3.5.4.5 Spectroscopic identification of [Rh^{III}(bth)(CO)(PPh_3)(Me)(I)]-alkyl isomers.

1D ^{1}H NOESY's were recorded *in situ* during the oxidative addition reaction, to establish the relative dispositions of the ligands in [Rh^{III}(bth)(CO)(PPh_3)(Me)(I)]-alkyl1, [Rh^{III}(bth)(CO)(PPh_3)(Me)(I)]-acyl1 and [Rh^{III}(bth)(CO)(PPh_3)(Me)(I)]-alkyl2 and are given in **Figure 3.74** and **Figure 3.75**. As mentioned before (**paragraph 3.4.1.3**), twelve different Rh(III)-alkyl isomer products (excluding enantiomers) are possible. The goal of this experiment is to give more insight into the stereo arrangements of the Rh(III)-alkyl reaction products.

Irradiation of the Me resonance on the Rh(III)-alkyl1 (*ca* 1.6 ppm), resulted in an NOE coupling with the methine, phenyl, PPh_3 and thienyl groups as well with the methyl signal of Rh(III)-acyl1, see the 1D ^{1}H NOESY in **Figure 3.74**. This result is only possible if the Me group of the Rh(III)-alkyl1 isomer is below (or above) the square planar plane (formed by the two oxygens of the β-diketonato ligands and the other two groups), with the Me group adjacent to the PPh_3 group. The NOE coupling to the methine proton rules out the possibility of the Me group being in a position in the square planar plane. From the 1D ^{1}H NOESY spectra it is not possible to establish whether the CO group or the I is adjacent to the Me group, since these groups do not contain any protons.

An exceptional result is that as the Me resonance of Rh(III)-alkyl1 is irradiated, it converts into the Rh(III)-acyl1 product on the time scale of the NMR, showing an increased intensity for the signal of the methyl group on the Rh(III)-acyl1 at *ca* 3 ppm. This result is indicative of the fast equilibrium [Rh(III)-alkyl1 ⇌ Rh(III)-acyl1].

Irradiation of the methine proton resonance of the Rh(III)-alkyl2 (*ca* 6.1 ppm), resulted in a NOE coupling with the phenyl, PPh_3 and thienyl groups, see the 1D ^{1}H NOESY in **Figure 3.75** (top). This result is only possible if the PPh_3 group is below (or above) the square planar plane (formed by the two oxygens of the β-diketonato ligands and the other two groups). This rules out the possibility of the Me group being in the position above (or below) the plane. Irradiation of the Me resonance of the Rh(III)-alkyl2 resulted in an NOE coupling with the phenyl signals, see the 1D ^{1}H NOESY in **Figure 3.75** (second spectrum). This result is consistent with the Me group being in the square planar plane. Results obtained for the [Rh^{III}(bth)(CO)(PPh_3)(Me)(I)]-alkyl2 isomer are consistent with the results of the possible structure of the

[Rh^{III}(tta)(CO)(PPh_3)(Me)(I)]-alkyl2 isomers as discussed in **paragraph 3.4.1.3**. The absence of a phenyl group on the β-diketonato ligand, in the case of the [Rh^{III}(tta)(CO)(PPh_3)(Me)(I)]-alkyl2 isomers, gives a clear picture of the only possible structures of the [Rh^{III}(tta)(CO)(PPh_3)(Me)(I)]-alkyl2 isomers as given in **Figure 3.24** (**paragraph 3.4.1.3**).

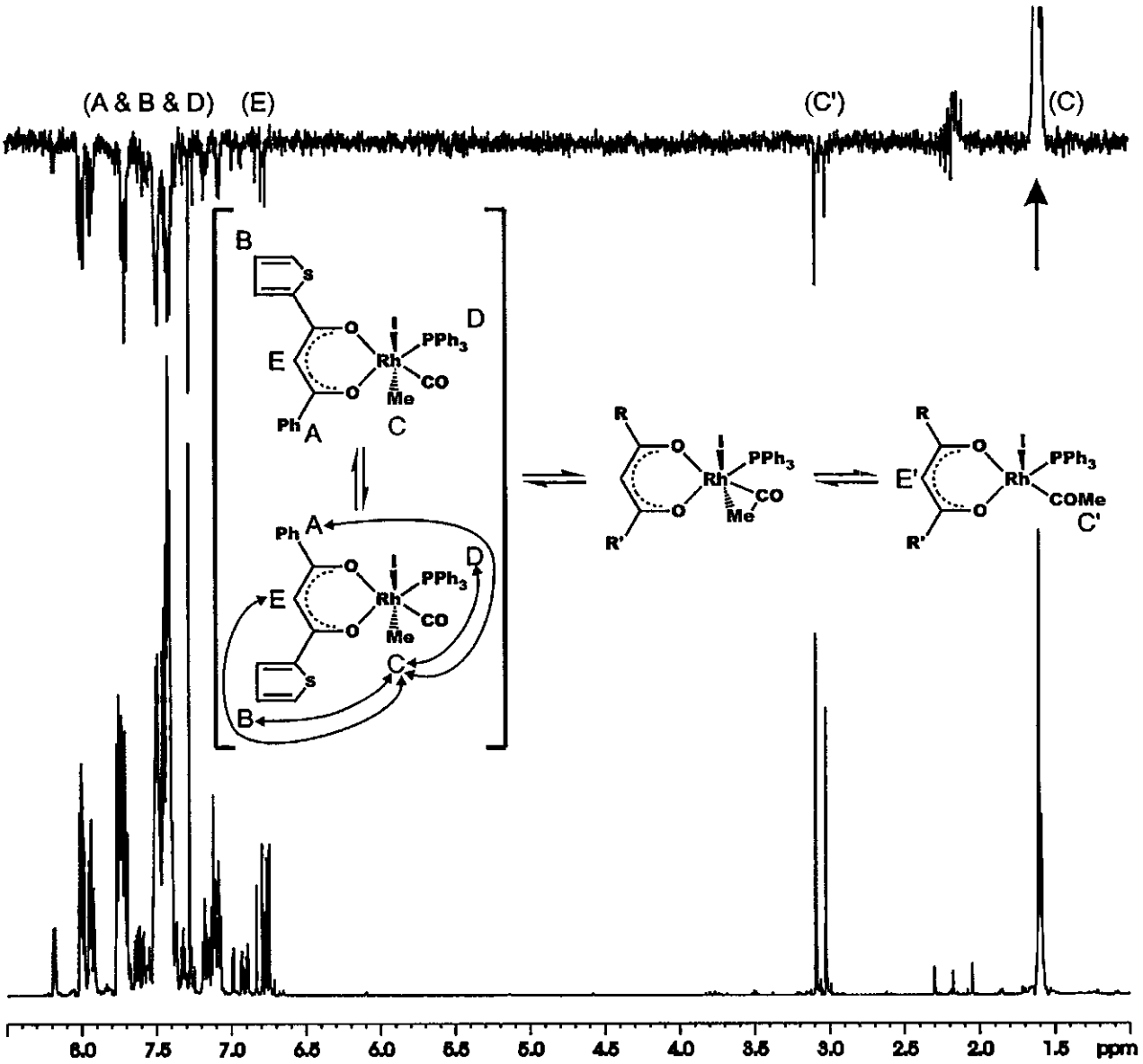

Figure 3.74: 1D ^{1}H NOESY (**top**) of [Rh^{III}(bth)(CO)(PPh_3)(Me)(I)]-alkyl1, pulsing on the methyl group as indicated by the blue arrow.. ^{1}H NMR spectrum (**bottom**) of [Rh^{III}(bth)(CO)(PPh_3)(Me)(I)]-alkyl1 ⇌ [Rh^{III}(bth)(CO)(PPh_3)(Me)(I)]-acyl1. MeI peak is suppressed for clarity.

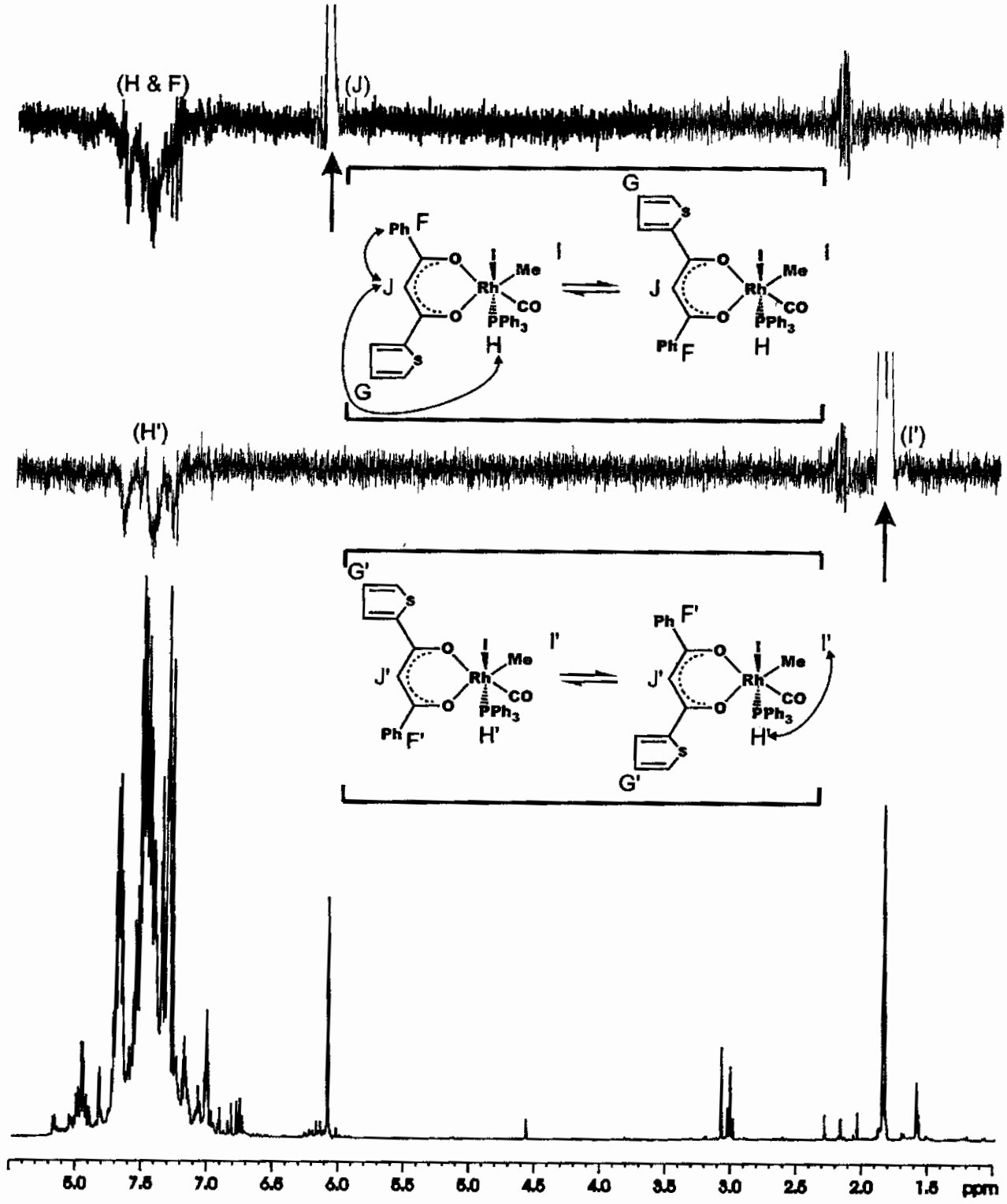

Figure 3.75: 1D ^{1}H NOESY (**top**) of [Rh^{III}(bth)(CO)(PPh$_3$)(Me)(I)]-alkyl2, pulsing on the methine proton (top) and methyl group (bottom) as indicated by the blue arrows. ^{1}H NMR spectrum (**bottom**) of [Rh^{III}(bth)(CO)(PPh$_3$)(Me)(I)]-alkyl2. Peaks are as indicated. MeI peak is suppressed for clarity. Also in solution are Rh(III)-alkyl1 and Rh(III)-acyl1 during the reaction [Rh^{III}(bth)(CO)(PPh$_3$)(Me)(I)]-alkyl1 ⇌ [Rh^{III}(bth)(CO)(PPh$_3$)(Me)(I)]-acyl1⇌ [Rh^{III}(bth)(CO)(PPh$_3$)(Me)(I)]-alkyl2.

3.5.5 The oxidative addition between MeI and [Rh(dtm)(CO)(PPh$_3$)] {8}.

The kinetic rate constants for the oxidative addition reaction between iodomethane (MeI) and [Rh(dtm)(CO)(PPh$_3$)] were determined by UV/vis and IR spectrophotometry and NMR spectroscopy under pseudo first-order conditions. Rate constants, obtained by each of these techniques, were consistent and are summarized in **Table 3.24** (page 158) and **Table 3.25** (page 167).

3.5.5.1 The UV/vis monitored reaction between MeI and [Rh(dtm)(CO)(PPh$_3$)] {8}.

The overlay UV/vis spectra of the reaction between MeI and [Rh(dtm)(CO)(PPh$_3$)] were recorded from 350 nm to 550 nm in chloroform to monitor the reaction progress. Overlay spectra is given in **Figure 3.76, Figure 3.77** and **Figure 3.78.**

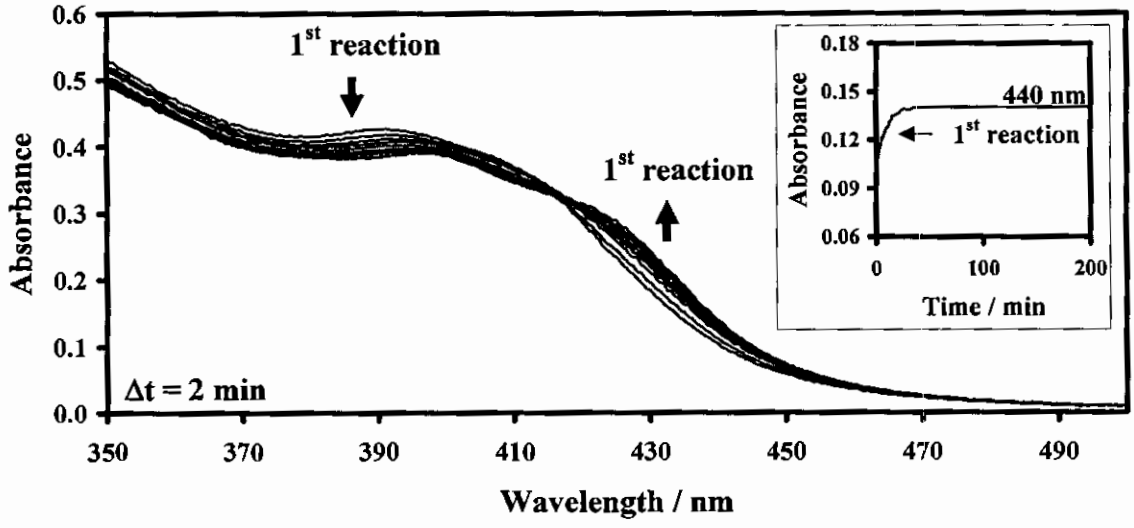

Figure 3.76: Spectrum of the oxidative addition reaction between MeI and [Rh(dtm)(CO)(PPh$_3$)], as monitored on the UV/vis spectrophotometer between 350 – 550 nm in chloroform at 25 °C; [Rh(dtm)(CO)(PPh$_3$)] = 0.00006 mol dm^{-3}, [MeI] = 0.056 mol dm^{-3}. The overlay spectra recorded for 24 minutes with a time interval of 2 min between successive scans illustrate the *first reaction.* **The insert:** Absorbance *vs* time data up to 200 min for the UV/vis monitored oxidative addition reaction of MeI to [Rh(dtm)(CO)(PPh$_3$)] in chloroform at 440 nm illustrating the *first reaction.* The *first reaction* was monitored at this wavelength.

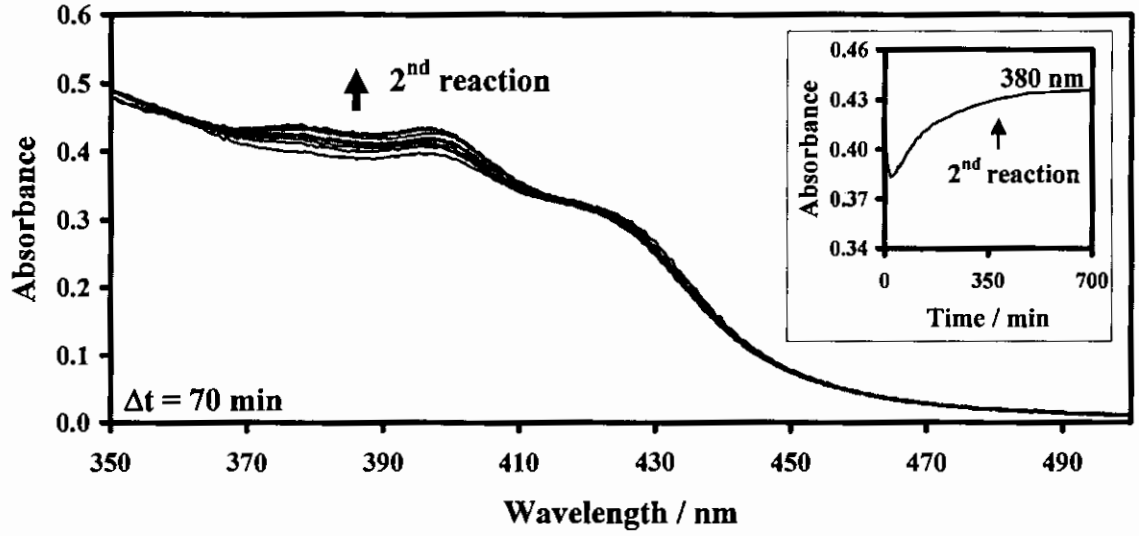

Figure 3.77: Spectrum of the oxidative addition reaction between MeI and [Rh(dtm)(CO)(PPh_3)], as monitored on the UV/vis spectrophotometer between 350 – 550 nm in chloroform at 25 °C; [Rh(dtm)(CO)(PPh_3)] = 0.00006 mol dm^{-3}, [MeI] = 0.056 mol dm^{-3}. Illustrated is the *second reaction* from 70 to 700 minutes with a time interval of 70 min between successive scans. **The insert:** Absorbance *vs* time data for the UV/vis monitored oxidative addition reaction of MeI to [Rh(dtm)(CO)(PPh_3)] in chloroform at 380 nm illustrating the *second reaction*. The *second reaction* was monitored at this wavelength. The change in absorbance for the *first reaction* at this wavelength is too small to give accurate results.

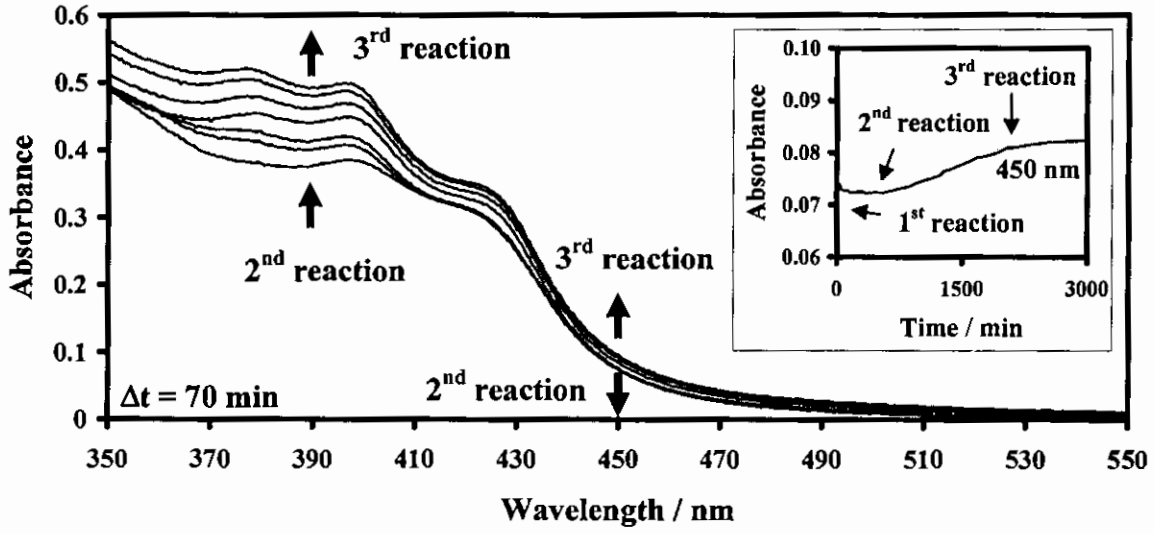

Figure 3.78: Spectrum of the oxidative addition reaction between MeI and [Rh(dtm)(CO)(PPh_3)], as monitored on the UV/vis spectrophotometer between 350 – 550 nm in chloroform at 25 °C; [Rh(dtm)(CO)(PPh_3)] = 0.00006 mol dm^{-3}, [MeI] = 0.056 mol dm^{-3}. Illustrated are the *second* and the *third reactions* from 70 to 4600 minutes with a time interval of 70 min between successive scans. **The insert:** Absorbance *vs* time data for the UV/vis monitored oxidative addition reaction of MeI to [Rh(dtm)(CO)(PPh_3)] in chloroform at 450 nm up to 3000 min illustrating the *first*, the *second* and the *third reactions*. The *third reaction* was monitored at this wavelength.

From the above figures, it is clear that there are three different reactions for oxidative addition process between MeI and [Rh(dtm)(CO)(PPh_3)] and subsequent CO insertion and deinsertion reactions. The *first reaction* is best followed at 440 nm, the *second reaction* at 380 nm and the *third reaction* at 450 nm. The inserts in the above figures illustrate the absorbance *vs* time data for the three reactions at selected wavelengths. The rate constants for the three reactions are summarized in **Table 3.24** (page 158).

The temperature and [MeI] dependence of the *first reaction* of the oxidative addition reaction between MeI and [Rh(bth)(CO)(PPh_3)], as monitored on the UV/vis spectrophotometry at 440 nm in chloroform, are demonstrated by **Figure 3.79**. The *second* and the *third reactions* are [MeI] independent and gave constant rate constants at different concentrations. Data are summarized in **Table 3.24** (page 158).

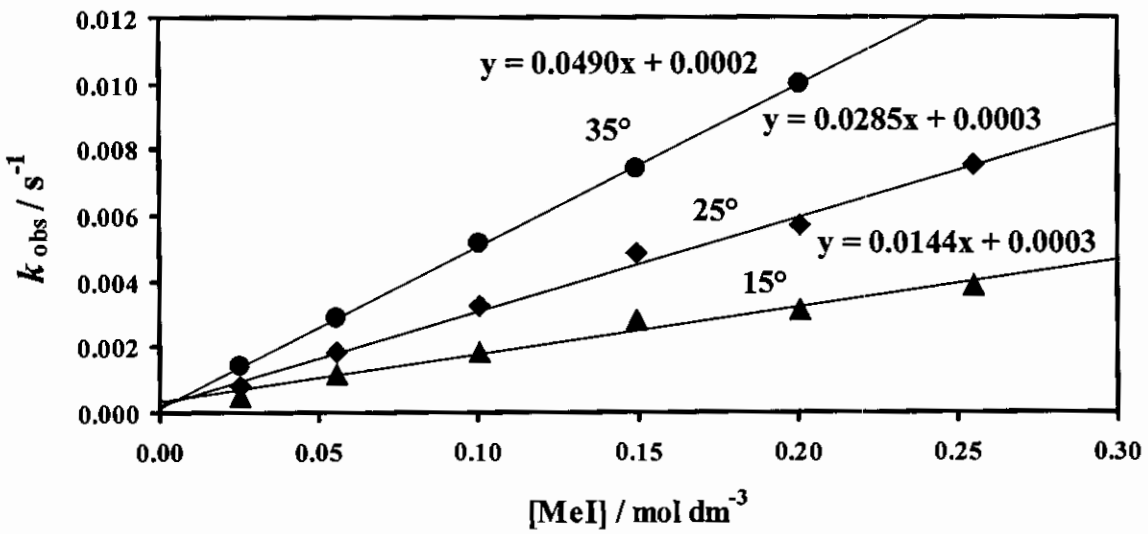

Figure 3.79: Temperature and MeI concentration dependence of the oxidative addition of MeI to [Rh(dtm)(CO)(PPh_3)], as monitored on the UV/vis spectrophotometer at 440 nm in chloroform, for the *first reaction* { Rh(I) + MeI ⇌ [Rh(III)-alkyl] ⇌ Rh(III)-acyl] }.

The linear Eyring relationship (**Equation 3.8**) for the *first* and the *second reactions* is given in **Figure 3.80** and **Figure 3.81** respectively. The activation parameters are summarized in **Table 3.24** (page 158).

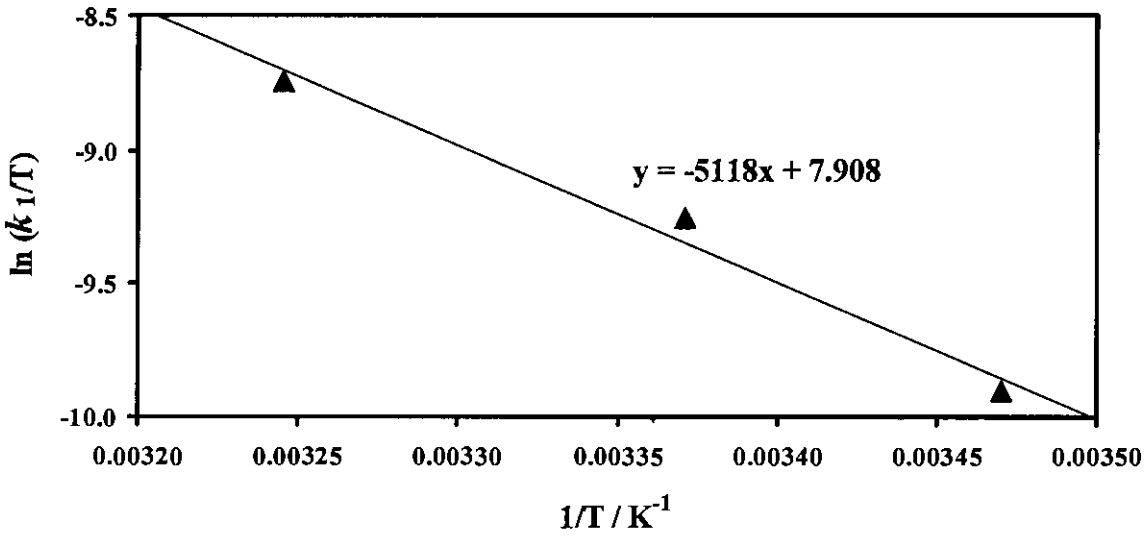

Figure 3.80: The Eyring curve of ln(k_1/T) *vs* 1/T for the *first reaction* { Rh(I) + MeI ⇌ [Rh(III)-alkyl1 ⇌ Rh(III)-acyl1] } of the oxidative addition reaction between MeI and [Rh(dtm)(CO)(PPh_3)], as monitored on the UV/vis spectrophotometer in chloroform.

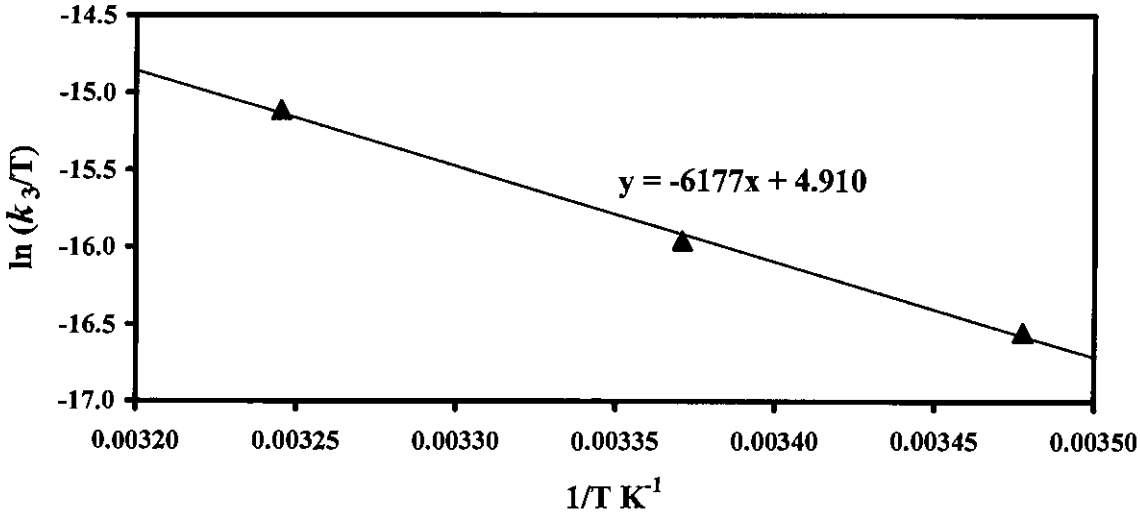

Figure 3.81: The Eyring curve of ln(k_3/T) *vs* 1/T for the *second reaction* { [Rh(III)-alkyl1 ⇌ Rh(III)-acyl1] → Rh(III)-alkyl2 } of the oxidative addition reaction between MeI and [Rh(dtm)(CO)(PPh_3)], as monitored on the UV/vis spectrophotometer in chloroform.

Table 3.24: Temperature dependent kinetic rate constants and activation parameters for the oxidative addition between MeI and [Rh(dtm)(CO)(PPh$_3$)], as monitored on the UV/vis spectrophotometer in chloroform. k_1, k_3 and k_4 are the rate constants associated with the *first*, the *second* and the *third reactions* of this oxidative addition reaction.

T / °C	1st reaction				
	k_1 / dm^3 mol^{-1} s^{-1}	k_{-1} / s^{-1}	ΔH^* / kJ mol^{-1}	ΔS^* / J mol^{-1} K^{-1}	ΔG^* / kJ mol^{-1} [a]
14.4	0.014(1)	0.0003(2)	40(6)	-130(20)	80(3)
23.5	0.029(1)	0.0002(2)			
35.0	0.0490(4)	0.00015(4)			
T / °C	2nd reaction				
	k_3 / s^{-1}		ΔH^* / kJ mol^{-1}	ΔS^* / J mol^{-1} K^{-1}	ΔG^* / kJ mol^{-1} [a]
14.4	0.000019(4)		50(6)	-160(20)	100(10)
23.5	0.0000349(5)				
35.0	0.00008(1)				
T / °C	3rd reaction				
	k_4 / s^{-1}		ΔH^* / kJ mol^{-1}	ΔS^* / J mol^{-1} K^{-1}	ΔG^* / kJ mol^{-1} [a]
23.5	0.000005(1)		-	-	-

a At 25 °C

Results of the UV/vis study of the reaction between MeI and [Rh(dtm)(CO)(PPh$_3$)] are interpreted to imply the same as the UV/vis study of the reaction between MeI and [Rh(bth)(CO)(PPh$_3$)]. Based on the UV/vis study alone one may thus write the same preliminary reaction sequence as was proposed for [Rh^I(bth)(CO)(PPh$_3$)] in **paragraph 3.5.4.1**:

[Rh^I(dtm)(CO)(PPh$_3$)] + MeI

k_{-1} ⇅ k_1

[Rh(III)-oxidative addition product X]

⇅ (isomerization or solvent exchange)

[different Rh(III)-product Y]

⇅ (isomerization or solvent exchange)

[different Rh(III)-product Z]

A NMR study was conducted to obtain more insight into the nature of these Rh(III)-products.

3.5.5.2 The IR monitored reaction between MeI and [Rh(dtm)(CO)(PPh$_3$)] {8}.

An illustration of the oxidative addition reaction between MeI and [Rh(dtm)(CO)(PPh$_3$)], as monitored on the IR spectrophotometer between 1600 – 2200 cm^{-1} in chloroform at 25 °C, is given in **Figure 3.82.** In accordance with the UV/vis study of this reaction, three reactions are observed on IR. **Figure 3.83, Figure 3.84** and **Figure 3.85** give the absorbance *vs* time data of the indicated species for the *first*, the *second* and the *third reactions.* Rate constants are summarized in **Table 3.25** (page 167).

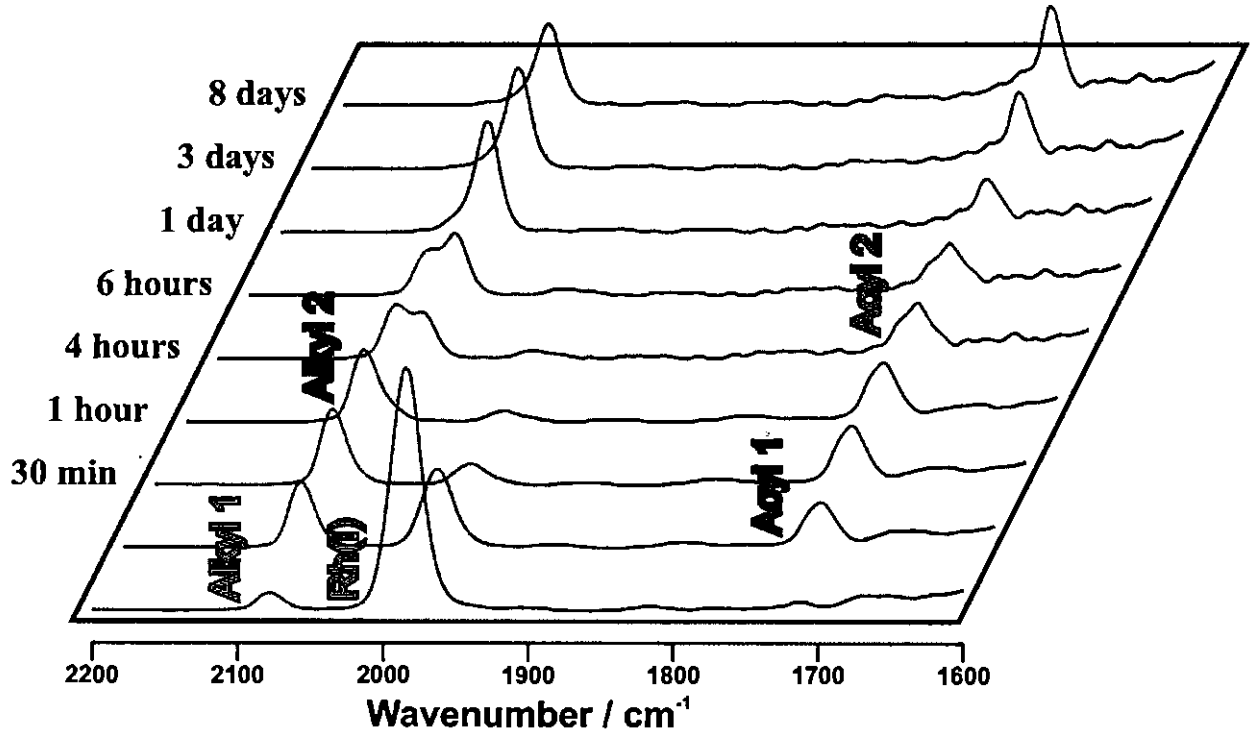

Figure 3.82: Illustration of the oxidative addition reaction between MeI and [Rh(dtm)(CO)(PPh_3)], as monitored on the IR spectrophotometer between 1600 – 2200 cm^{-1} in chloroform at 25 °C; [Rh(dtm)(CO)(PPh_3)] = 0.0091 mol dm^{-3}, [MeI] = 0.087 mol dm^{-3}. The *first reaction* is indicated by the disappearance of Rh(I) at 1987 cm^{-1} (**pink**) and the simultaneous appearance of Rh(III)-alkyl1 at 2079 cm^{-1} (**yellow**) and Rh(III)-acyl1 at 1720 cm^{-1} (**blue**). The *second reaction* is indicated by the simultaneous disappearance of Rh(III)-alkyl1 and Rh(III)-acyl1 and the formation of a Rh(III)-alkyl2 species at 2056 cm^{-1} (**green**). The *third reaction* is indicated by the disappearance of Rh(III)-alkyl2 and the formation of a Rh(III)-acyl2 species at 1713 cm^{-1} (**orange**). The first spectrum was recorded 70 s after mixing and the rest of the illustrated spectra were recorded at the indicated time intervals. The signals are colour coded for better clarity.

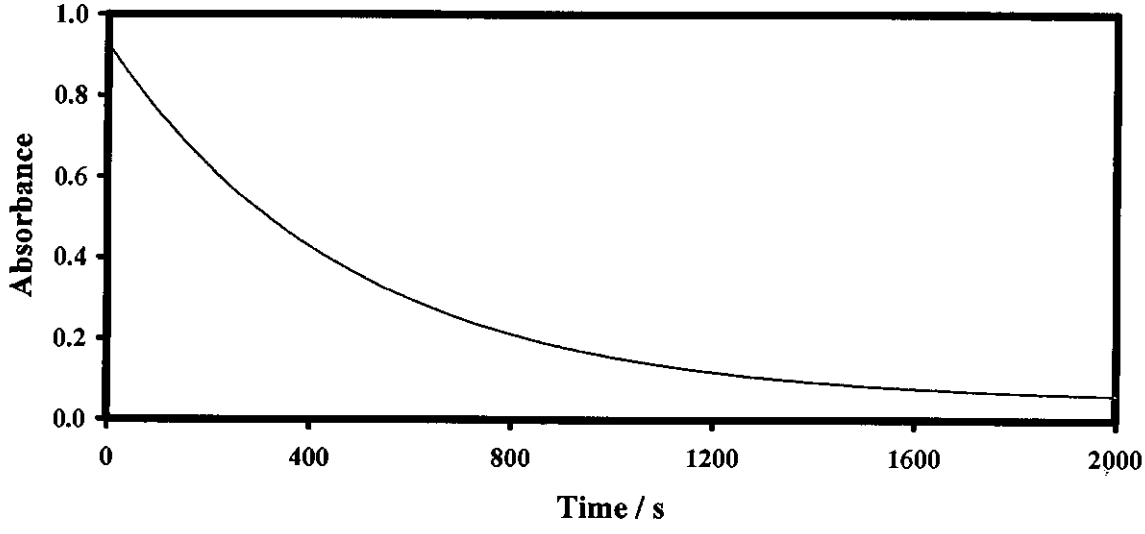

Figure 3.83: Absorbance *vs* time data of the oxidative addition reaction between MeI and [Rh(dtm)(CO)(PPh_3)], as monitored on the IR spectrophotometer at 1987 cm^{-1} in chloroform at 25 °C; [Rh(dtm)(CO)(PPh_3)] = 0.0091 mol dm^{-3}, [MeI] = 0.087 mol dm^{-3}. Indicated is the disappearance of Rh(I) (**pink**, k_{obs} = 0.00210(4) s^{-1}).

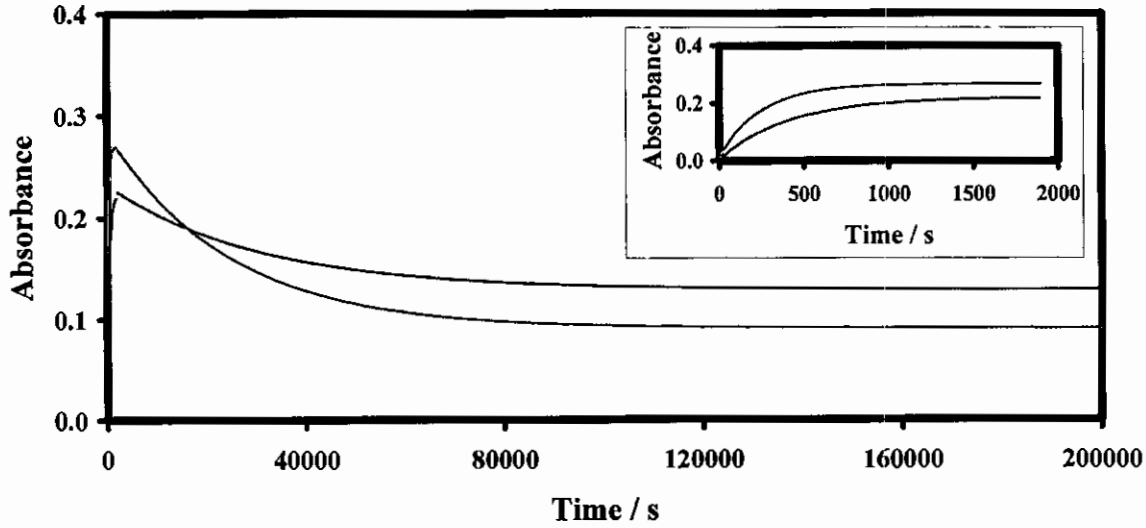

Figure 3.84: Absorbance *vs* time data of the oxidative addition reaction between MeI and [Rh(dtm)(CO)(PPh_3)], as monitored on the IR spectrophotometer at 2079 and 1720 cm^{-1} in chloroform at 25 °C; [Rh(dtm)(CO)(PPh_3)] = 0.0091 mol dm^{-3}, [MeI] = 0.087 mol dm^{-3}. Indicated is the appearance of Rh(III)-alkyl1 (yellow, k_{obs} = 0.0040(2) s^{-1}) and Rh(III)-acyl1 (**blue**, k_{obs} = 0.00243(7) s^{-1}), during the *first reaction* { Rh(I) + MeI ⇌ [Rh(III)-alkyl1 ⇌ Rh(III)-acyl1] }, followed by the disappearance of Rh(III)-alkyl1 (yellow, k_{obs} = 0.000041(1) s^{-1}) and Rh(III)-acyl1 (**blue**, k_{obs} = 0.000032(1) s^{-1}), during the *second reaction* { [Rh(III)-alkyl1 ⇌ Rh(III)-acyl1] → Rh(III)-alkyl2 }.

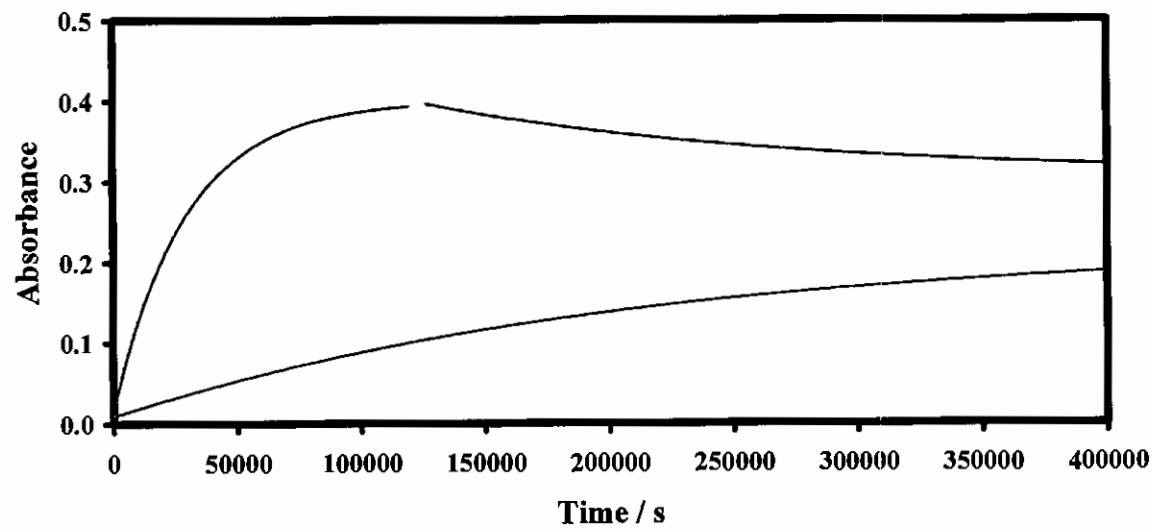

Figure 3.85: Absorbance *vs* time data of the oxidative addition reaction between MeI and [Rh(dtm)(CO)(PPh_3)], as monitored on the IR spectrophotometer at 2056 and 1713 cm^{-1} in chloroform at 25 °C; [Rh(dtm)(CO)(PPh_3)] = 0.0091 mol dm^{-3}, [MeI] = 0.087 mol dm^{-3}. Indicated is the appearance of Rh(III)-alkyl2 (**green**, k_{obs} = 0.0000339(4) s^{-1}), during the *second reaction* { [Rh(III)-alkyl1 ⇌ Rh(III)-acyl1] → Rh(III)-alkyl2 }, followed by the disappearance of Rh(III)-alkyl2 (**green**, k_{obs} = 0.0000034(3) s^{-1}) and the appearance of Rh(III)-acyl2 (**orange**, k_{obs} = 0.0000047(2) s^{-1}), during the *third reaction* { Rh(III)-alkyl2 → Rh(III)-acyl2 }.

The *first* and the *second reactions* of the reaction between MeI and [Rh(dtm)(CO)(PPh_3)] are interpreted to imply the same as the IR study of the reaction between MeI and [Rh(bth)(CO)(PPh_3)]. The overall reaction sequence for the *first* and the *second reactions* for this oxidative addition reaction can therefore also be represented as:

$$\text{Rh(I)} + \text{MeI} \underset{k_{-1}}{\overset{k_1}{\rightleftharpoons}} \left\{\text{[Rh(III)-alkyl1]} \underset{k_{-2}}{\overset{K_2, k_2}{\rightleftharpoons}} \text{[Rh(III)-acyl1]}\right\} \underset{k_{-3}}{\overset{k_3}{\rightleftharpoons}} \text{[Rh(III)-alkyl2]}$$

The *second reaction* was followed by a very slow ($t_{1/2} \approx 57$ hours) [MeI]-independent *third reaction* that corresponds to the slow first-order disappearance of the Rh(III)-alkyl2 species ($k_4 = 0.0000034(3)\ s^{-1}$) at 2056 cm^{-1} and the appearance, at the same rate, of a new Rh(III)-acyl2 species at 1713 cm^{-1} ($k_4 = 0.0000047(2)\ s^{-1}$) (**Figure 3.85**). The long half-life of the third reaction implied that it could not be followed with great accuracy, as solvent evaporation became difficult to control. The kinetic data of the *third reaction* are consistent with an $A \underset{k_{-4}}{\overset{k_4}{\rightleftharpoons}} B$ type of reaction with $k_{-4} <<< k_4$ as shown in:

$$\text{[Rh(III)-alkyl2]} \underset{k_{-4}}{\overset{k_4}{\rightleftharpoons}} \text{[Rh(III)-acyl2]}$$

The overall reaction sequence, for this oxidative addition reaction, is therefore presented as:

$$\text{Rh(I)} + \text{MeI} \underset{k_{-1}}{\overset{k_1}{\rightleftharpoons}} \left\{\text{[Rh(III)-alkyl1]} \underset{k_{-2}}{\overset{K_2, k_2}{\rightleftharpoons}} \text{[Rh(III)-acyl1]}\right\} \underset{k_{-3}}{\overset{k_3}{\rightleftharpoons}} \text{[Rh(III)-alkyl2]} \underset{k_{-4}}{\overset{k_4}{\rightleftharpoons}} \text{[Rh(III)-acyl2]}$$

3.5.5.3 The ^1H and ^{31}P NMR monitored reaction between MeI and [Rh(dtm)(CO)(PPh_3)] {8}.

An illustration of the oxidative addition reaction between MeI and [Rh(dtm)(CO)(PPh_3)], as monitored by ^1H NMR spectroscopy in $CDCl_3$ at 25 °C, is given in **Figure 3.86**. An illustration of the reaction monitored by ^{31}P NMR spectroscopy in $CDCl_3$ at 25 °C, is given in **Figure 3.90**. Both illustrations are followed by the graphs of the relative intensity *vs* time data of the relative experiment and species for the *first* and the *second reactions*. The *third reaction* could not be identified on the ^1H and ^{31}P NMR. Since the β- diketonato ligand, dtm, is symmetrical, only one isomer for each species can be observed with NMR spectroscopy for the oxidative addition reaction. Rate constants are summarized in **Table 3.25** (page 167).

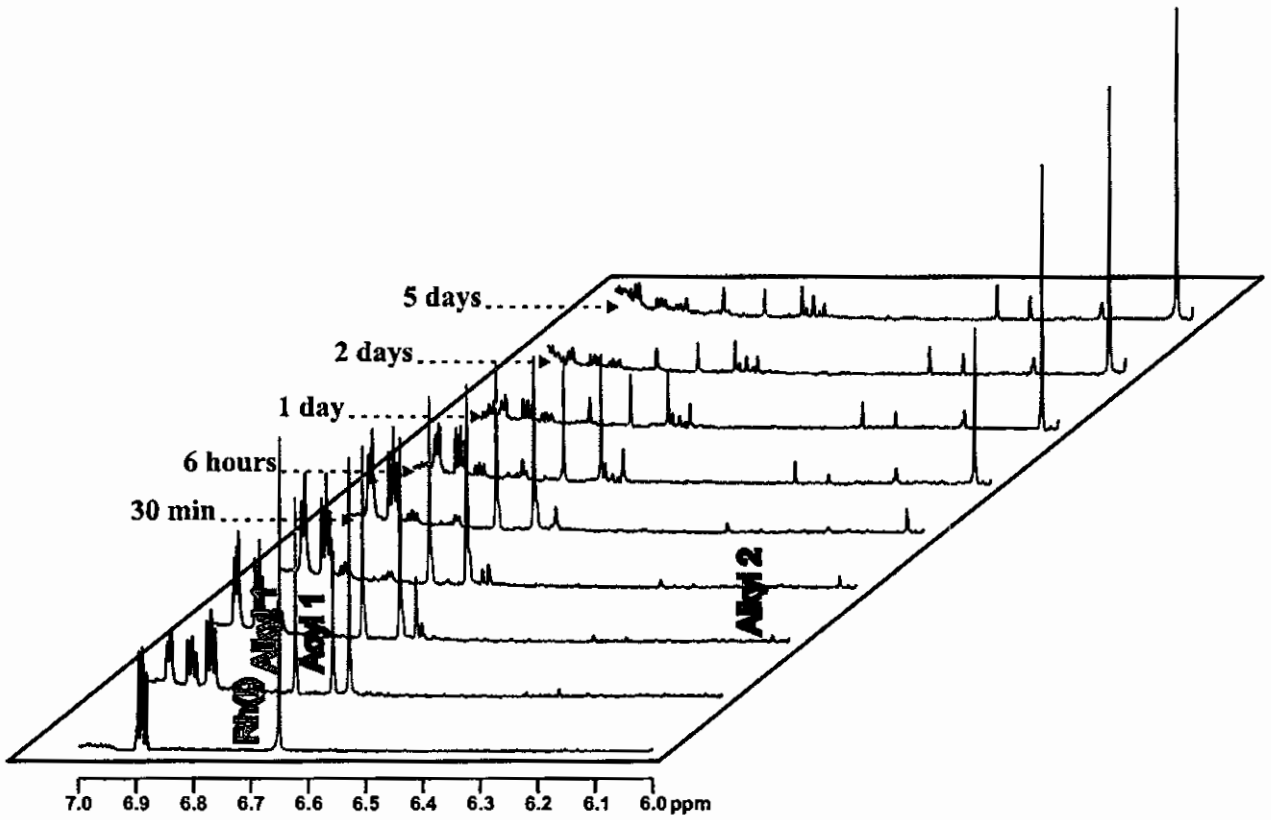

Figure 3.86: A fragment of the ^{1}H NMR spectra of the oxidative addition reaction between MeI and [Rh(dtm)(CO)(PPh$_3$)], as monitored by ^{1}H NMR spectroscopy in $CDCl_3$ at 25 °C; [Rh(dtm)(CO)(PPh$_3$)] = 0.0268 mol dm^{-3}, [MeI] = 0.150 mol dm^{-3}. One isomer for each species can be observed. The *first reaction* is indicated by the disappearance of Rh(I) at 6.65 ppm (**pink**) and the simultaneous appearance of Rh(III)-alkyl1 at 6.74 ppm (**yellow**) and Rh(III)-acyl1 at 6.68 ppm (**blue**). The *second reaction* is indicated by the simultaneous disappearance of Rh(III)-alkyl1 and Rh(III)-acyl1 and the formation of a Rh(III)-alkyl2 species at 6.03 ppm (**green**). The *third reaction* could not be identified on the ^{1}H NMR. The first spectrum was recorded before mixing and the rest of the illustrated spectra were recorded after mixing at the indicated time intervals. The signals are colour coded for better clarity. The signals 6.9 ppm and lower field represent the aromatic resonances of [Rh(dtm)(CO)(PPh$_3$)].

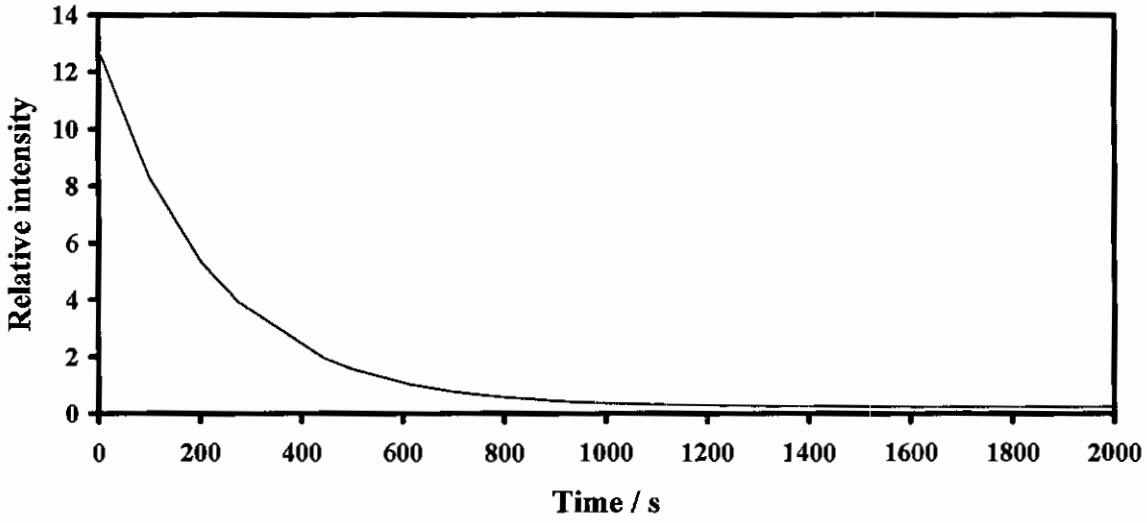

Figure 3.87: Relative intensity *vs* time data of the oxidative addition reaction between MeI and [Rh(dtm)(CO)(PPh$_3$)], as monitored by ^{1}H NMR spectroscopy at 6.65 ppm in $CDCl_3$ at 25 °C; [Rh(dtm)(CO)(PPh$_3$)] = 0.0268 mol dm^{-3}, [MeI] = 0.150 mol dm^{-3}. Indicated is the disappearance of the Rh(I) isomer (**pink**, k_{obs} = 0.00444(3) s^{-1}).

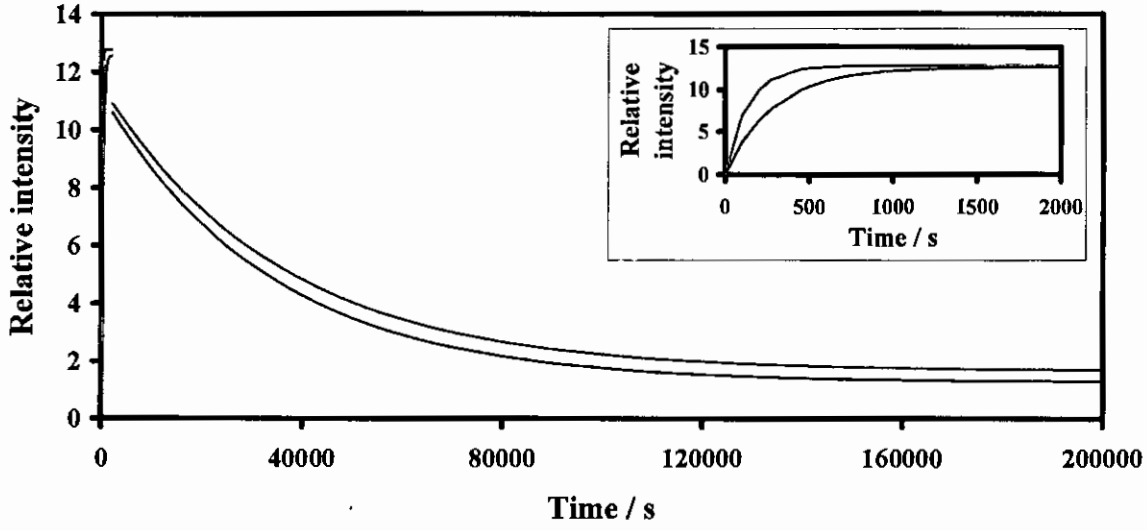

Figure 3.88: Relative intensity *vs* time data of the oxidative addition reaction between MeI and [Rh(dtm)(CO)(PPh_3)], as monitored by ^1H NMR spectroscopy at 6.68 and 6.74 ppm in $CDCl_3$ at 25 °C; [Rh(dtm)(CO)(PPh_3)] = 0.0268 mol dm^{-3}, [MeI] = 0.150 mol dm^{-3}. Indicated is the appearance of the Rh(III)-alkyl1 isomer (yellow, k_{obs} = 0.0076(2) s^{-1}) and the Rh(III)-acyl1 isomer (**blue**, k_{obs} = 0.0035(3) s^{-1}), during the *first reaction* { Rh(I) + MeI ⇌ [Rh(III)-alkyl1 ⇌ Rh(III)-acyl1] }, followed by the disappearance of the Rh(III)-alkyl1 isomer (**yellow**, k_{obs} = 0.000028(2) s^{-1}) and the Rh(III)-acyl1 isomer (**blue**, k_{obs} = 0.000030(2) s^{-1}), during the *second reaction* { [Rh(III)-alkyl1 ⇌ Rh(III)-acyl1] → Rh(III)-alkyl2 }.

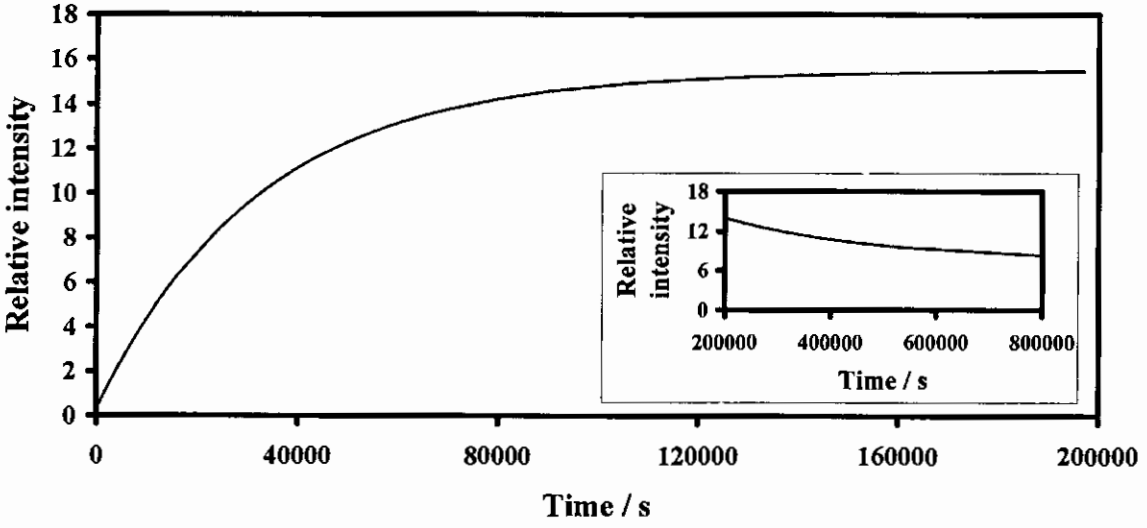

Figure 3.89: Relative intensity *vs* time data of the oxidative addition reaction between MeI and [Rh(dtm)(CO)(PPh_3)], as monitored by ^1H NMR spectroscopy at 6.03 ppm in $CDCl_3$ at 25 °C; [Rh(dtm)(CO)(PPh_3)] = 0.0268 mol dm^{-3}, [MeI] = 0.150 mol dm^{-3}. Indicated is the appearance of the Rh(III)-alkyl2 isomer (**green**, k_{obs} = 0.000031(2) s^{-1}), during the *second reaction* { [Rh(III)-alkyl1 ⇌ Rh(III)-acyl1] → Rh(III)-alkyl2 }. **The insert:** The disappearance of the Rh(III)-alkyl2 isomer was observed with k_{obs} = 0.0000034(8) s^{-1}, as part of the *third reaction.*

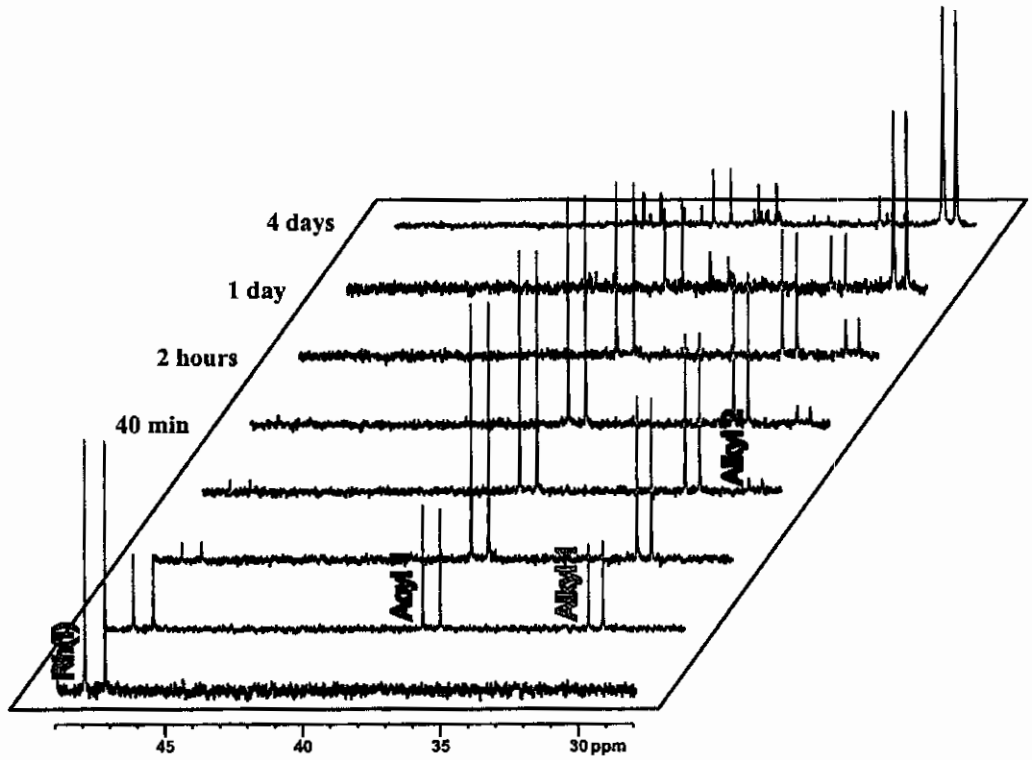

Figure 3.90: Illustration of the oxidative addition reaction between MeI and [Rh(dtm)(CO)(PPh_3)], as monitored by ^{31}P NMR spectroscopy in $CDCl_3$ at 25 °C; [Rh(dtm)(CO)(PPh_3)] = 0.0263 mol dm^{-3}, [MeI] = 0.133 mol dm^{-3}. The phosphorus atom on the PPh_3 group gives rise to a doublet for each isomer (due to Rh-P coupling). One isomer for each species can be observed. The *first reaction* is indicated by the disappearance of Rh(I) at 47.61 ppm (**pink**) and the simultaneous appearance of Rh(III)-alkyl1 at 31.22 ppm (**yellow**) and Rh(III)-acyl1 at 37.16 ppm (**blue**). The *second reaction* is indicated by the simultaneous disappearance of Rh(III)-alkyl1 and Rh(III)-acyl1 and the formation of a Rh(III)-alkyl2 species at 28.93 ppm (**green**). The *third reaction* could not be identified on the ^{31}P NMR. The first spectrum was recorded before mixing and the rest of the illustrated spectra were recorded after mixing at the indicated time intervals. The signals are colour coded for better clarity.

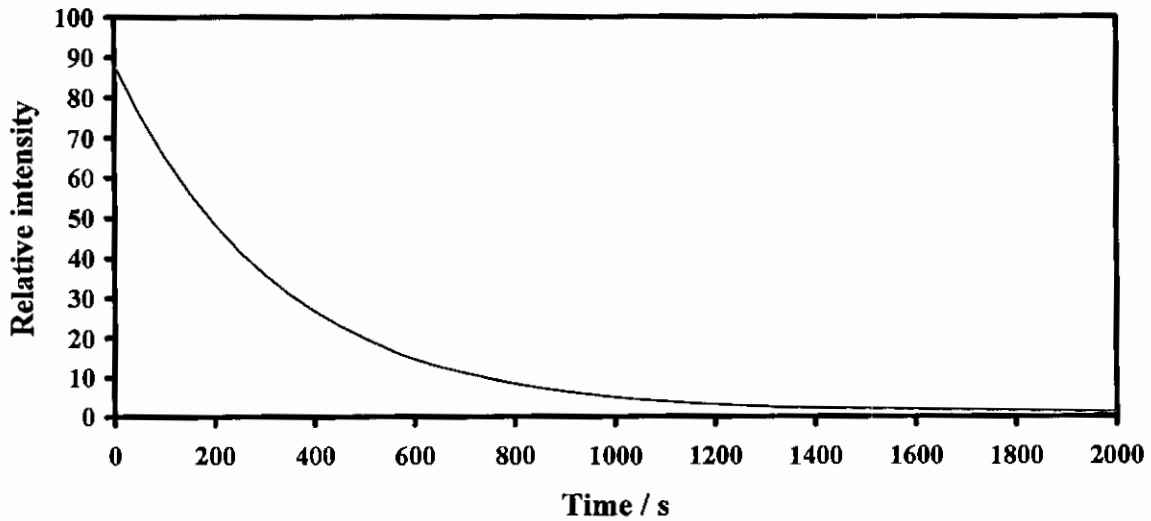

Figure 3.91: Relative intensity *vs* time data of the oxidative addition reaction between MeI and [Rh(dtm)(CO)(PPh_3)], as monitored by ^{31}P NMR spectroscopy at 47.61 ppm in $CDCl_3$ at 25 °C; [Rh(dtm)(CO)(PPh_3)] = 0.0263 mol dm^{-3}, [MeI] = 0.133 mol dm^{-3}. Indicated is the disappearance of the Rh(I) isomer (**pink**, k_{obs} = 0.0030(3) s^{-1}).

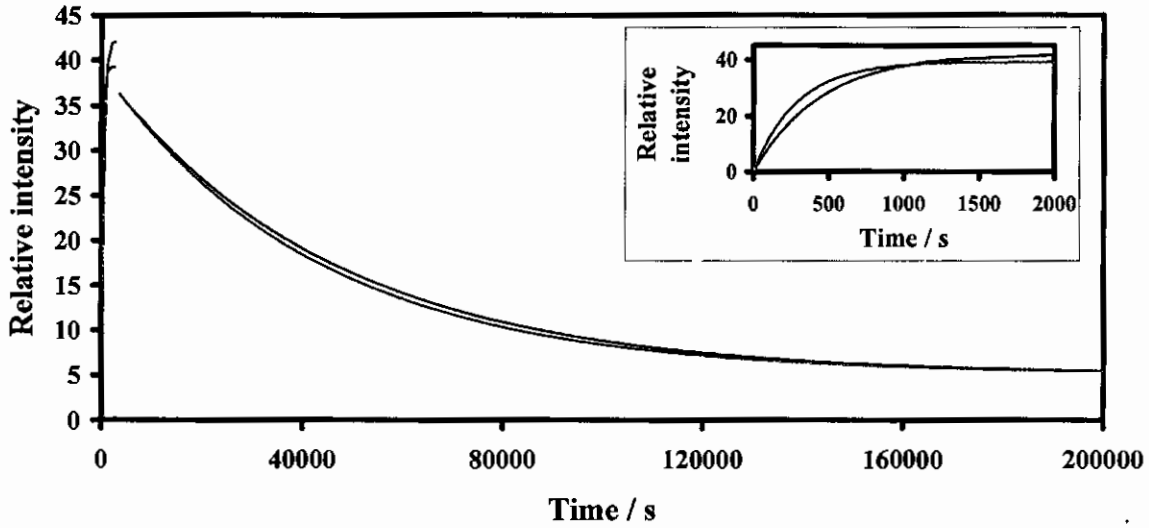

Figure 3.92: Relative intensity *vs* time data of the oxidative addition reaction between MeI and [Rh(dtm)(CO)(PPh_3)], as monitored by ^{31}P NMR spectroscopy at 31.22 and 37.16 ppm in $CDCl_3$ at 25 °C; [Rh(dtm)(CO)(PPh_3)] = 0.0263 mol dm^{-3}, [MeI] = 0.133 mol dm^{-3}. Indicated is the appearance of the Rh(III)-alkyl1 isomer (yellow, k_{obs} = 0.0023(6) s^{-1}) and the Rh(III)-acyl1 isomer (**blue**, k_{obs} = 0.0035(4) s^{-1}), during the *first reaction* { Rh(I) + MeI ⇌ [Rh(III)-alkyl1 ⇌ Rh(III)-acyl1] }, followed by the disappearance of the Rh(III)-alkyl1 isomer (**yellow**, k_{obs} = 0.000023(1) s^{-1}) and the Rh(III)-acyl1 isomer (**blue**, k_{obs} = 0.0000218(9) s^{-1}), during the *second reaction* { [Rh(III)-alkyl1 ⇌ Rh(III)-acyl1] → Rh(III)-alkyl2 }. **The insert:** Enlargement of the first 2000 s of the reaction.

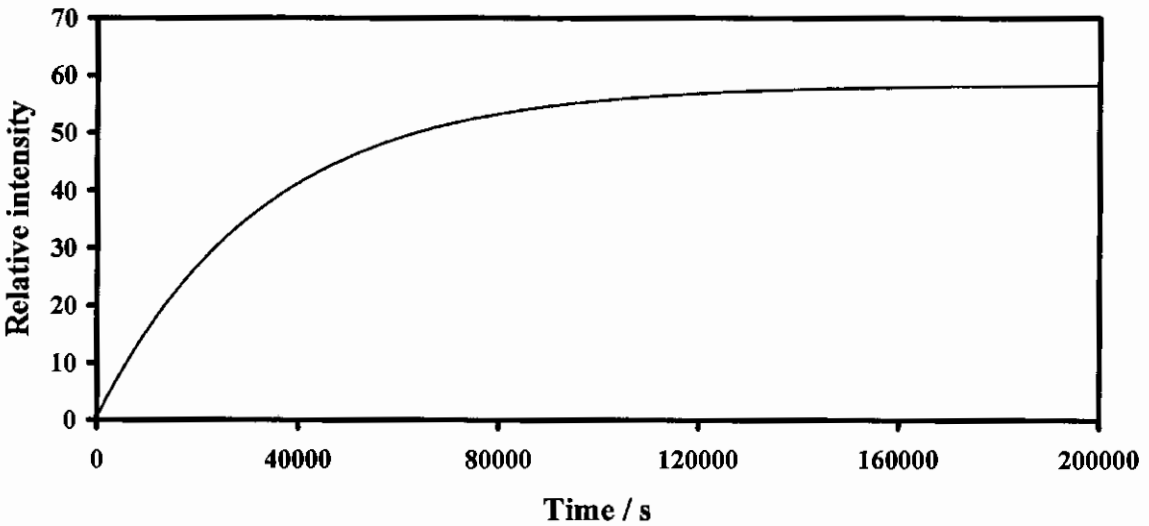

Figure 3.93: Relative intensity *vs* time data of the oxidative addition reaction between MeI and [Rh(dtm)(CO)(PPh_3)], as monitored by ^{31}P NMR spectroscopy at 28.93 ppm in $CDCl_3$ at 25 °C; [Rh(dtm)(CO)(PPh_3)] = 0.0263 mol dm^{-3}, [MeI] = 0.133 mol dm^{-3}. Indicated is the appearance of the Rh(III)-alkyl2 isomer (**green**, k_{obs} = 0.000031(2) s^{-1}), during the *second reaction* { [Rh(III)-alkyl1 ⇌ Rh(III)-acyl1] → Rh(III)-alkyl2 }.

The same reaction sequence as observed with the UV/vis and IR spectrophotometry, was observed with the ^{1}H and ^{31}P NMR spectroscopy. In this case, only one isomer for each intermediate was observed since the β-diketonato ligand, dtm, is symmetrical.

Results of the ^{1}H and ^{31}P NMR study of the reaction between MeI and [Rh(dtm)(CO)(PPh_3)] are interpreted to imply the same as the ^{1}H and ^{31}P NMR study of the reaction between MeI and [Rh(bth)(CO)(PPh_3)].

Rate constants obtained from ^{1}H and ^{31}P NMR are summarized in **Table 3.25** (page 167). It can be seen that a good agreement exist between the kinetic rate constants obtained by utilizing IR spectrophotometric and ^{1}H and ^{31}P NMR spectroscopic methods.

Taking into account that there exist only one main isomer of each reactant and reaction product, the complete proposed reaction mechanism for the oxidative addition of MeI to [Rh(dtm)(CO)(PPh_3)] is therefore:

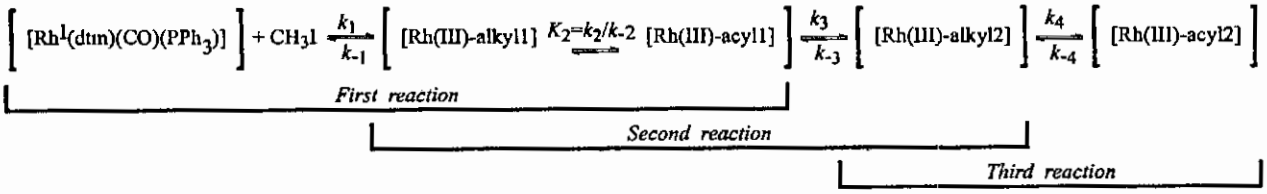

Scheme 3.10: Proposed reaction mechanism for the oxidative addition of MeI to [Rh(dtm)(CO)(PPh_3)].

3.5.5.4 Correlation of the kinetic rate constants of the reaction between MeI and [Rh(dtm)(CO)(PPh_3)] {8} as obtained by various spectrophotometric and spectroscopic methods.

A reasonable correlation has been obtained for the kinetic rate constants of the oxidative addition reaction between MeI and [Rh(dtm)(CO)(PPh_3)] as determined from data obtained by various spectrophotometric and spectroscopic methods. The data are summarized in **Table 3.25.**

Table 3.25: The kinetic rate constants of the oxidative addition reaction between MeI and [Rh(dtm)(CO)(PPh_3)] as obtained by various spectrophotometric and spectroscopic methods in chloroform at 25 °C. k_1, k_3 and k_4 are the rate constants associated with the *first*, the *second* and the *third reactions* of the oxidative addition reaction between MeI and [Rh(dtm)(CO)(PPh_3)] as indicated in **Scheme 3.10**.

Method	[MeI] / mM	1st reaction			
		Rh(I) disappearance		Rh(III)-alkyl 1 appearance	Rh(III)-acyl 1 appearance
		k_{obs} / s^{-1}	k_1 / $dm^3\ mol^{-1}\ s^{-1}$	k_{obs} / s^{-1}	k_{obs} / s^{-1}
IR	87	0.00210(4)	0.0241(5)	0.0040(2)	0.00243(7)
IR	390	0.01105(8)	0.0283(2)	0.015(1)	0.0038(5)
^{1}H NMR [a]	150	0.00444(3)	0.0296(2)	0.0076(2)	0.0035(3)
^{31}P NMR [a]	133	0.0030(3)	0.023(2)	0.0023(6)	0.0035(4)

Method	[MeI] / mM	2nd reaction		
		Rh(III)-alkyl 1 disappearance	Rh(III)-acyl 1 disappearance	Rh(III)-alkyl 2 appearance
		k_{obs} / s^{-1}	k_{obs} / s^{-1}	k_{obs} / s^{-1}
IR	87	0.000041(1)	0.000032(1)	0.0000339(4)
IR	390	0.000031(1)	0.000087(3)	0.0000233(2)
^{1}H NMR [a]	150	0.000028(2)	0.000030(2)	0.000031(2)
^{31}P NMR [a]	133	0.000023(1)	0.0000218(9)	0.000031(2)

Method	[MeI] / mM	3rd reaction	
		Rh(III)-alkyl 2 disappearance	Rh(III)-acyl 2 appearance
		k_{obs} / s^{-1}	k_{obs} / s^{-1}
IR	87	0.0000036(3)	0.0000047(2)
IR	390	-	0.0000039(5)
^{1}H NMR [a]	150	0.0000034(8)	-
^{31}P NMR [a]	133	-	-

a One isomer observed for each product
b k_{obs} for the 2nd reaction corresponds to k_3 in **Scheme 3.10**, as determined on UV/vis, **Table 3.24** (page 158)

3.5.6 Correlation of the reaction between iodomethane and [Rh(β-diketonato)(CO)(PPh_3)] complexes with one another and with other related complexes.

The UV/vis and IR results for the oxidative addition of MeI to the three complexes [Rh(β-diketonato)(PPh_3)(CO)], where β-diketonato = tta, dtm and bth, are summarized in **Table 3.26**. The *first reaction*, the k_1 oxidative addition step, was approximately 20 times slower for [Rh(tta)(PPh_3)(CO)] than for the other two complexes, [Rh(bth)(PPh_3)(CO)] and

[Rh(dtm)(PPh_3)(CO)]. The rate of the *second reaction*, the k_3 step, however, was 10 times faster for the [Rh(tta)(PPh_3)(CO)] complex than for the [Rh(bth)(PPh_3)(CO)] and [Rh(dtm)(PPh_3)(CO)] complexes. No *third reaction*, the k_4 step, was observed for [Rh(tta)(PPh_3)(CO)]. The rate of the *third reaction*, the k_4 step, observed for the [Rh(bth)(PPh_3)(CO)] and [Rh(dtm)(PPh_3)(CO)] complexes, is very slow in the order of 10^{-6} s^{-1}.

For [Rh(tta)(PPh_3)(CO)] the Rh(III)-alkyl2 isomers formed at different rates, the kinetic more stable Rh(III)-alkyl2A isomer formed faster than the thermodynamic stable Rh(III)-alkyl2B isomer, but after the initial formation of Rh(III)-alkyl2A, it decreases slowly until an 1:1 equilibrium between Rh(III)-alkyl2A and Rh(III)-alkyl2B sets in. For [Rh(bth)(PPh_3)(CO)], however, the Rh(III)-alkyl2 isomers formed at the same rates in a 0.86:1 equilibrium throughout the reaction.

The large negative ΔS* values for the oxidative addition step (k_1 step, **Table 3.26**) for all three complexes [Rh(β-diketonato)(PPh_3)(CO)] indicate an associative activation.

Table 3.26: The kinetic rate constants of the oxidative addition reaction between MeI and [Rh(β-diketonato)(CO)(PPh_3)] as obtained by various spectrophotometric and spectroscopic methods in chloroform at 25 °C for β-diketonato = tta, bth and dtm. k_1, k_3 and k_4 are the rate constants associated with the *first, second and third stages* of the reaction of MeI to [Rh(β-diketonato)(CO)(PPh_3)].

[Rh(tta)(CO)(PPh_3)]							
Method	k_1 / $dm^3mol^{-1}s^{-1}$	k_{-1} / s^{-1}	k_3 / s^{-1}	k_4 / s^{-1}	$\Delta H^*(k_1)$ / kJ mol^{-1}	$\Delta S^*(k_1)$ / J mol^{-1} K^{-1}	$\Delta G^*(k_1)$ / kJ mol^{-1}
IR	0.00152(4)	0.00001(2)	0.0009(4)	-	31.1(5)	-193(2)	89(1)
UV/vis	0.00171(4)	0.000023(6)	0.0008(3)	-			
^{1}H NMR	0.0016(1)	-	0.0004(2)	-			
^{19}F NMR	0.0011(1)	-	0.00019(2)	-			
^{31}P NMR	0.0013(3)	-	0.0011(3)	-			
[Rh(dtm)(CO)(PPh_3)]							
Method	k_1 / $dm^3mol^{-1}s^{-1}$	k_{-1} / s^{-1}	k_3 / s^{-1}	k_4 / s^{-1}	$\Delta H^*(k_1)$ / kJ mol^{-1}	$\Delta S^*(k_1)$ / J mol^{-1} K^{-1}	$\Delta G^*(k_1)$ / kJ mol^{-1}
IR	0.026(3)	-	0.000032(6)	0.000004(1)	40(6)	-130(20)	80(3)
UV/vis	0.029(1)	0.0002(2)	0.0000349(5)	0.000005(1)			
^{1}H NMR	0.0296(2)	-	0.000030(2)	0.0000034(8)			
^{31}P NMR	0.023(2)	-	0.000025(5)	-			
[Rh(bth)(CO)(PPh_3)]							
Method	k_1 / $dm^3mol^{-1}s^{-1}$	k_{-1} / s^{-1}	k_3 / s^{-1}	k_4 / s^{-1}	$\Delta H^*(k_1)$ / kJ mol^{-1}	$\Delta S^*(k_1)$ / J mol^{-1} K^{-1}	$\Delta G^*(k_1)$ / kJ mol^{-1}
IR	0.022(6)	0.0000(2)	0.000029(9)	-	16.8(8)	-218(3)	82(2)
UV/vis	0.0265(6)	0.0000(1)	0.000059(3)	0.000003(2)			
^{1}H NMR	0.038(3)	-	0.000049(5)	-			
^{31}P NMR	0.0226(9)	-	0.000029(6)	-			

For all the complexes of the type $[Rh(R^1COCHCOR^2)(CO)(PPh_3)]$ it is clear that the group electronegativity of the R groups on the β-diketonato ligand directly influences the electron density on the metal centre. Since the change in electron density on the metal is reflected by parameters such as the kinetic rate constants, carbonyl stretching frequencies and pK_a, a relationship between these parameters and group electronegativities of R^1 and R^2 should exist. **Table 3.27** gives a summary of these parameters.

Table 3.27: Kinetic rate constants for the oxidative addition step in chloroform and carbonyl stretching frequencies of $[Rh(R^1COCHCOR^2)(CO)(PPh_3)]$, as well as pK_a and group electronegativities of the R substituents of the free uncoordinated β-diketone. See List of abbreviations for a list of the β-diketonato ligands.

β-diketonato ligand $(R^1COCHCOR^2)^-$					$[Rh(R^1COCHCOR^2)(CO)(PPh_3)]$	
abreviation	**R^1**	**R^2**	**$(\chi_{R1} + \chi_{R2})$ / (Gordy scale) [a]**	**pK_a [b]**	**ν_{CO} [c] / cm^{-1}**	**k_1 [f] / $mol^{-1}\ dm^3\ s^{-1}$**
dfcm	Fc	Fc	3.74	13.1	1977	0.155
bfcm	Fc	C_6H_5	4.08	10.41	1977	0.077
dtm	Th	Th	4.20	8.893(3)	1971	0.029(1)
fca	Fc	CH_3	4.21	10.01	1980	0.065
bth	Th	Ph	4.31	9.006(8)	1970, 1980	0.0265(6)
dbm	C_6H_5	C_6H_5	4.42	9.35	1979	0.00961 [d]
bav	C_6H_5	$CH_2CH_2CH_2CH_3$	4.43	9.33	1983	0.0332
bap	C_6H_5	CH_2CH_3	4.52	9.33	1982	0.0337
ba	C_6H_5	CH_3	4.55	8.70	1980	0.00930 [d]
bab	C_6H_5	$CH_2CH_2CH_3$	4.62	9.23	1981	0.0454
acac	CH_3	CH_3	4.68	8.95	1978	0.024 [e]
fctfa	Fc	CF_3	4.88	6.56	1986	0.00611
tta	CF_3	Th	5.11	6.491(8)	1981	0.00171(4)
tfba	C_6H_5	CF_3	5.22	6.30	1983	0.00112 [d]
tfaa	CF_3	CH_3	5.35	6.30	1983	0.00146 [d]
hfaa	CF_3	CF_3	6.02	4.71	-	0.00013(1)

a group electronegativities of this study, **paragraph 3.2** and reference[57]

b pK_a of this study, **paragraph 3.3.3** and from reference[58]

c ν_{CO} this study, **paragraph 3.4.1** and reference[59]

d value in acetone

e value in 1,2-dichloroethane

f rate constants from this study and references [60,61,50,62]

---

[57] W.C. du Plessis, J.C. Erasmus, G.J. Lamprecht, J. Conradie, T.S. Cameron, M.A.S. Aquino, J.C. Swarts, Can. J. Chem. 77 (1999) 378.

[58] W. C. du Plessis, T. G. Vosloo, J. C. Swarts, J. Chem. Soc., Dalton Trans. (1998) 2507.

[59] J. Conradie, G.J. Lamprecht, S. Otto, J.C. Swarts, Inorg. Chim. Acta. 328 (2002) 191.

[60] D. Lamprecht, Electrochemical, Kinetic and Molecular Mechanic Aspects of Rhodium(I) and Rhodium(III) Complexes, Ph. D. Thesis, University of the Orange Free State, R.S.A., 1998.

Figure 3.94 illustrates that the sum of the group electronegativities of R^1 and R^2 of the β-diketonato ligand $(R^1COCHCOR^2)^-$ coordinated to [Rh(β-diketonato)(CO)(PPh_3)] and [Rh(β-diketonato)($POPh_3$)$_2$] is linearly dependent on logk_1. k_1 is the rate constant for the oxidative addition of iodomethane to these rhodium complexes. This result is expected since the metal atom Rh acts as a nucleophile when it undergoes oxidative addition. The nucleophilicity (or basicity) of the metal will influence the rate of oxidative addition reactions. Any influence of a ligand bonded to the metal, that will increase the electron density on the metal centre, will thus lead to an increased rate of oxidative addition, assuming all other influences, factors and parameters remain constant. From the linear relationship in **Figure 3.94** it follows that the sum of the group electronegativities R^1 and R^2 of the β-diketonato ligand $(R^1COCHCOR^2)^-$ coordinated to [Rh(β-diketonato)(CO)(PPh_3)] gives a good indication of the electron density (nucleophilicity) of rhodium in each complex.

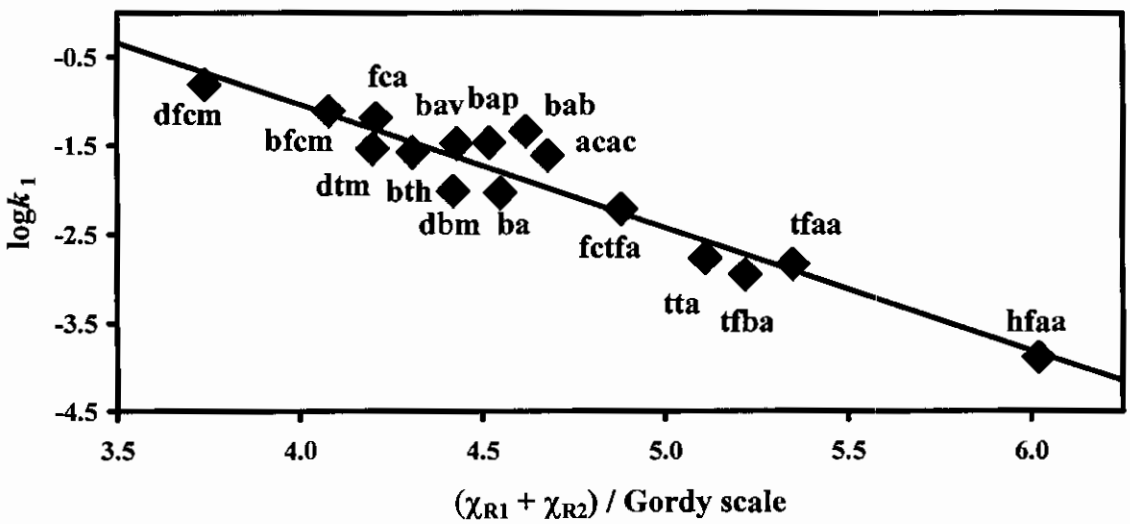

Figure 3.94: Relationship between logk_1, the second-order rate constant for the first step of oxidative addition of iodomethane to [Rh($R^1COCHCOR^2$)(CO)(PPh_3)] and the sum of the group electronegativities of R^1 and R^2, $(\chi_{R1} + \chi_{R2})$, of the β-diketonato ligand $(R^1COCHCOR^2)^-$ coordinated to the rhodium complexes. The β-diketonato ligands are as indicated.

[61] S.S. Basson, J.G. Leipoldt, J.T. Nel, Inorg. Chim. Acta 84 (1984). 167.

[62] M.F. Stuurman, Synthesis, Chemical Kinetics, Thermodynamic and Structural Properties of Phenyl-containing β-diketonato Complexes of Rhodium(I), M.Sc. Thesis, University of the Free State, R.S.A., 2007.

3.5.7 Mechanistic implications and conclusions

From the spectroscopic identification of the [Rh^{III}(bth)(CO)(PPh_3)(Me)(I)]-alkyl1 isomers in **paragraph 3.5.4.5** (page 151), it followed that the initial products of the oxidative addition reaction, the Rh(III)-alkyl1 isomers, have the Me group in the axial position below (or above) the square planar plane, adjacent to the PPh_3 group and it is not possible to establish whether the CO group or the I is adjacent to the Me group. For the observed methyl migration reaction to take place, to form the Rh(III)-acyl1 isomers, a *cis* configuration of -CH_3 and -CO relative to one another is needed. The result is thus consistent with the Rh(III)-alkyl1 isomers having the Me group below (or above) the square planar plane (from 1D ^{1}H NOESY **Figure 3.74** top), adjacent to the PPh_3 group (from 1D ^{1}H NOESY **Figure 3.74** middle) and adjacent to the Me group (for Me migration to take place). If the I is adjacent to the Me group, the CO has to be in a position *trans* to Me and then methyl migration is not possible.

The large negative ΔS* values for the oxidative addition step (k_1 step, **Table 3.26**) for all three complexes [Rh(β-diketonato)(PPh_3)(CO)] indicate an associative activation in terms a possible linear transitional state, especially in view of the fact that Rh(III)-acyl1 product is formed from the Rh(III)-alkyl1 product of oxidative addition. For the Rh(III)-acyl1 species to form, a *cis* configuration of -CH_3 and -CO relative to one another is preferable in the Rh(III)-alkyl species, and such a coordination mode is probable from a *trans* addition of MeI.

A proposed reaction mechanism for the *first reaction* of the oxidative addition of MeI to [Rh^I(bth)(CO)(PPh_3)], consistent with experimental results, involves a linear attack by [Rh^I(bth)(CO)(PPh_3)] on methyl iodide to form ionic five-coordinate methyl [Rh(bth)(CO)(PPh_3)(Me)]$^+$ complex and a free iodide ion as proposed by Basson *et al.*,[49] followed by the fast formation of an octahedral Rh(III)-alkyl1 species with Me and I in the apical position as illustrated in **Scheme 3.11**.

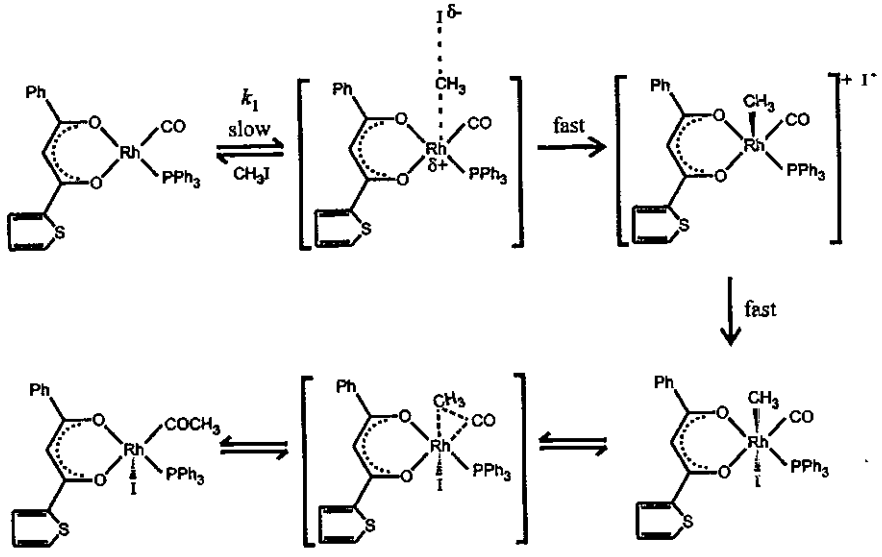

Scheme 3.11: Proposed mechanism for *first reaction* of the MeI addition to [Rh^{I}(bth)(CO)(PPh$_3$)]. (Only one isomer shown.)

From the spectroscopic identification of the [Rh^{III}(tta)(CO)(PPh$_3$)(Me)(I)]-alkyl2 isomers in **paragraph 3.4.1.3** and the [Rh^{III}(bth)(CO)(PPh$_3$)(Me)(I)]-alkyl2 isomers in **paragraph 3.5.4.5**, it follows that the Rh(III)-alkyl2 isomers have the PPh$_3$ group in the axial position below (or above) the square planar plane, adjacent to the Me group and it is not possible to establish whether the CO group or the I is adjacent to the PPh$_3$ group. See also **Figure 3.24** (**paragraph 3.4.1.3**) for the possible structures of [Rh^{III}(tta)(CO)(PPh$_3$)(Me)(I)]-alkyl2. A proposed reaction mechanism for the *second reaction* of the oxidative addition of MeI to [Rh^{I}(bth)(CO)(PPh$_3$)], the decarbonylation reaction to form the Rh(III)-alkyl2 isomers, consistent with experimental results, is given in **Scheme 3.12**.

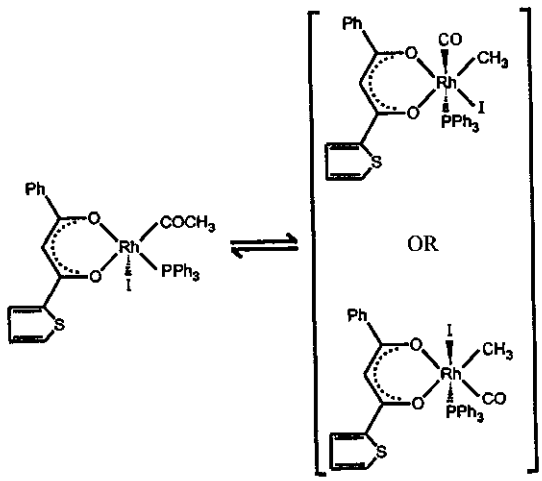

Scheme 3.12: Proposed mechanism for *second reaction* of the MeI addition to [Rh^{I}(bth)(CO)(PPh$_3$)]. This mechanism is also valid for [Rh^{I}(tta)(CO)(PPh$_3$)].)]. (Only one isomer shown.)

The proposed mechanism for the *first* and the *second reactions* of the MeI addition to [Rh(β-diketonato)(PPh_3)(CO)] complexes with thienyl-containing β-diketonato = tta, dtm and bth is consistent with the general reaction mechanism as given in **Scheme 3.13.**

From the presented NMR results in this study, it is clear that different isomers of the same species react at the same rate and are in fast equilibrium with each other. IR and NMR results indicated that the Rh(III)-alkyl1 and Rh(III)-acyl1 species are in a fast equilibrium with each other. For all complexes studied the equilibrium between the Rh(III)-alkyl1 and Rh(III)-acyl1 was fast enough to be maintained during the slow conversion of Rh(III)-acyl1 to Rh(III)-alkyl2. The final proposed reaction mechanism for the oxidative addition of iodomethane to [Rh(β-diketonato)(PPh_3)(CO)] complexes with thienyl-containing β-diketonato = tta, dtm and bth is as given in **Scheme 3.13.** The rate constants k_{-3} and k_{-4} in all cases were too small to be detected, except for k_{-1}. It was not possible to determine k_2 or k_{-2} separately in this study as no clear cut saturation kinetics, even at 1.000 mol dm^{-3} [MeI] could be observed. The equilibrium constants in **Scheme 3.13** that could be determined, are summarized in **Table 3.28** together with spectral parameters of the different reaction products.

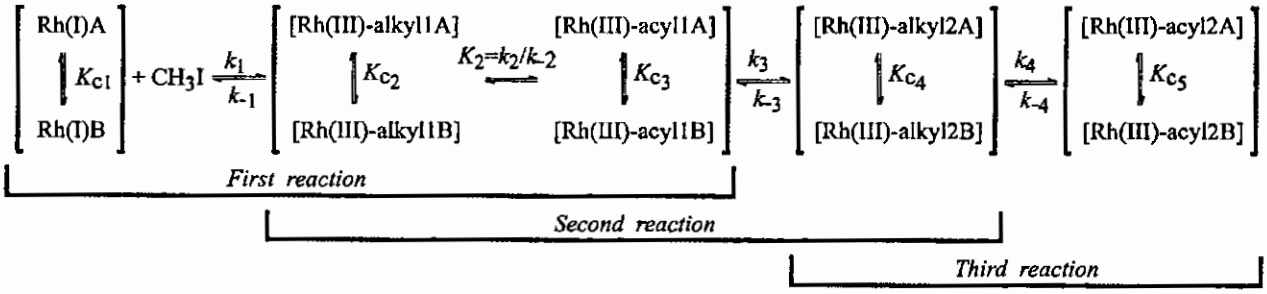

Scheme 3.13: A complete general reaction mechanism for the oxidative addition of iodomethane to [Rh(β-diketonato)(PPh_3)(CO)] complexes.

Table 3.28: ^{1}H, ^{19}F, ^{31}P NMR and IR spectral parameters of the different isomeric forms of [Rh(tta)(CO)(PPh_3)] and the Rh(III) complexes formed during the oxidative addition reaction of MeI to [Rh(tta)(CO)(PPh_3)]. K_c = [RhB-species]/[RhA-species].

$[Rh^{I}(tta)(CO)(PPh_3)]$									
	^{31}P NMR			^{1}H NMR			^{19}F NMR		IR
compound	$\delta^{31}P$ / ppm	$^{1}J(^{31}P$-$^{103}Rh)$ / Hz	Ratio isomers on ^{31}P NMR	$\delta^{1}H$ methine proton β-diketone ligand/ppm	$\delta^{1}H$ CH_3-group from MeI/ppm	Ratio isomers on ^{1}H NMR	$\delta^{19}F$ CF_3-group	Ratio isomers on ^{19}F NMR	ν_{CO} / cm^{-1}
Rh(I)A	47.61	177	K_{c1} = 1.0	6.42	-	K_{c1} = 1.05	-74.16	1.0	1991
Rh(I)B	47.66	177		6.43	-		-74.12		
Rh(III)-alkyl 1A	33.50	125	K_{c2} = 0.7	6.44	1.54	K_{c2} = 0.7	*	*	2079
Rh(III)-alkyl 1B	34.42	125		6.49	1.55		-74.16		
Rh(III)-acyl 1A	37.51	155	K_{c3} = 0.4	6.43	2.99	K_{c3} = 0.5	-74.12 -73.97 -73.94		1728
Rh(III)-acyl 1B	37.93			6.45	3.07				
Rh(III)-alkyl 2A	27.07	113	K_{c4} = 1.0**	5.72	1.90	K_{c4} = 1.0**	-75.20	1.0**	2064
Rh(III)-alkyl 2B	28.74	113		5.80	1.90		-74.08		

$[Rh^{I}(bth)(CO)(PPh_3)]$							
	^{31}P NMR			^{1}H NMR			IR
compound	$\delta^{31}P$ / ppm	$^{1}J(^{31}P$-$^{103}Rh)$ / Hz	Ratio isomers on ^{31}P NMR	$\delta^{1}H$ methine proton β-diketone ligand/ppm	$\delta^{1}H$ CH_3-group from MeI/ppm	Ratio isomers on ^{1}H NMR	ν_{CO} / cm^{-1}
Rh(I)A	47.41	176	K_{c1} = 1.0	6.74	-	K_{c1} = 1.0	1983
Rh(I)B	49.21	177		6.75	-		
Rh(III)-alkyl 1A	31.03	128	K_{c2} = 0.4	6.67	1.6	K_{c2} = 0.4	2079
Rh(III)-alkyl 1B	34.21	128		6.78	1.6		
Rh(III)-acyl 1A	38.50	154	K_{c3} = 0.8	6.80	3.02	K_{c3} = 0.8	1720
Rh(III)-acyl 1B	36.89	154		6.83	3.10		
Rh(III)-alkyl 2A	28.62	121	K_{c4} = 1.3	6.10	1.85	K_{c4} = 1.4	2056
Rh(III)-alkyl 2B	29.21	121		6.09	1..85		
Rh(III)-acyl 2A	35.16	156	-	4.58	-	-	1709
Rh(III)-acyl 2B	35.81	160		4.59	-		

$[Rh^{I}(dtm)(CO)(PPh_3)]$					
	^{31}P NMR		^{1}H NMR		IR
compound	$\delta^{31}P$ / ppm	$^{1}J(^{31}P$-$^{103}Rh)$ / Hz	$\delta^{1}H$ methine proton β-diketone ligand/ppm	$\delta^{1}H$ CH_3-group from MeI / ppm	ν_{CO} / cm^{-1}
Rh(I)	47.61	176	6.65	-	1987
Rh(III)-alkyl 1	31.22	126	6.74	1.60	2079
Rh(III)-acyl 1	37.16	154	6.68	3.04	1720
Rh(III)-alkyl 2	28.93	117	6.03	1.84	2056
Rh(III)-acyl 2	35.5	159	*	3.05	1713

* Peaks could not uniquely be identified due to excessive overlapping

** at equilibrium

3.6 Quantum computational chemistry.

3.6.1 Introduction.

The main purpose of this quantum computational study is to obtain more information on the stereochemistry of the different rhodium(III) reaction products of the reaction between iodomethane (MeI) and thienyl containing β-diketonato [Rh^{I}(β-diketonato)(CO)(PPh_3)] complexes. Only a few [Rh^{III}(β-diketonato)(CO)(PPh_3)(CH_3)(I)] and [Rh^{III}(β-diketonato)($COCH_3$)(PPh_3)(I)] crystal structures exist (**paragraph 2.3.7.3, Chapter 2**) and up to date, to the knowledge of the author, only speculation exists about the stereochemistry of these products during the oxidative addition reaction and subsequent carbonyl insertion and deinsertion reactions. Various ^{1}H NMR techniques used in this study did give insight into these products (**paragraph 3.4.1.3** and **paragraph 3.5.4.5**), but the complete structures could not be solved. The synthesis of the most stable Rh(III) reaction products was successful, but the intermediate products could not be isolated and all attempts to obtain crystals of the final product, suitable for X-ray single crystal determination, failed. It was therefore decided to follow the quantum computational approach to address as much of the structurally based unanswered questions as possible.

To make the quantum computational study as meaningful as possible, within the borders of this M.Sc. research program, some goals were set.

a. The quantum computational approach had to be validated as accurate. This was addressed by theoretically solving the structures of Hbth **{1}** and [Rh(tta)(CO)(PPh_3)] **{7}** and then comparing the calculated data with the structural data of these compounds which were experimentally determined by means of single crystal X-ray diffraction methods.
b. Having then proved that the quantum computational approach gives structures for Hbth **{1}** and [Rh(tta)(CO)(PPh_3)] **{7}** that almost exactly correspond to the experimentally determined structures, the structures of [Rh(bth)($CO)_2$] **{3}**, [Rh(tta)($CO)_2$] **{4}**, [Rh(dtm)($CO)_2$] **{5}**, [Rh(bth)(CO)(PPh_3)] **{6}** and [Rh(dtm)(CO)(PPh_3)] **{8}** were solved by theoretical means.
c. The quantum computational optimized structures of [Rh^{I}(β-diketonato)($CO)_2$] complexes **{3}**-**{5}** and [Rh^{I}(β-diketonato)(CO)(PPh_3)] complexes **{6}**-**{8}** were then used to predict the IR stretching frequencies (ν) by utilizing TDDFT (time-dependent Density Function Theory)

calculations. The calculated data of the carbonyl stretching frequencies (ν_{CO}) were then compared with the experimentally obtained data, which gave excellent correlations. This once again validates the accuracy of the quantum computational approach.

d. Finally, calculations were done to obtain the stereochemistry of the Rh(III) reaction products of the reaction between MeI and thienyl containing β-diketonato [Rh^{I}(β-diketonato)(CO)(PPh_3)] complexes. This was done by comparing overall molecular energies.

All calculations were done with the ADF (Amsterdam Density Functional)[63] 2005.01 program system, the PW91 (Perdew-Wang, 1991)[64] generalized gradient approximation (GGA) for both exchange and correlation, Slater-type TZP (Triple ζ polarized) basis sets, tight criteria for SCF convergence and geometry optimization. No symmetry limitations were imposed, in other words, all calculations were done in the C1 (no symmetry) mode. The calculations were preformed in the gas phase and no solvent effects were taken into account.

3.6.2 Hbth {1} and [Rh(tta)(CO)(PPh_3)] {7}: a computational and crystallographic study.

Figure 3.95 gives graphical illustrations, comparing ADF quantum computational bond lengths and bond angles to experimental X-ray crystal data of Hbth **{1}** and [Rh(tta)(CO)(PPh_3)] **{7}**. R values are given as a measure of the average accuracy of all the computed (gas phase) bond lengths and angles under consideration, with the numerical value of one being representative of results that agree with experimental crystal data (solid state). A comparison of the data of [Rh(dtm)$(CO)_2$)] **{5}** is not included, since the refinement of the data crystal data (**paragraph 3.4.4**) did not give satisfactory results.

The following expression was used to calculate R values:

$$R = n^{-1} \times \sum \left[x_{ei} - |x_{ci} - x_{ei}| / x_{ei} \right] \quad , \quad i = 1 \rightarrow n$$

with n = number of data points, x_{ei} = experimental data point i and x_{ci} = calculated data point i.

---

63 G.T. Velde, F.M. Bickelhaupt, E.J. Baerends, C.F. Guerra, S.J.A. Van Gisbergen, J.G. Snijders, T.J. Ziegler, J. Comp. Chem. 22 (2001) 931.

64 J. P. Perdew, J. A. Chevary, S. H. Vosko, K. A. Jackson, M. R. Perderson, D. J. Singh, C. Fioihais, Phys. Rev. B 46 (1992) 6671.

The numbering system used is illustrated in **Figure 3.96**. **Table 3.29** lists the most important X-ray structural data and calculated parameters obtained from ADF geometry optimizations of the complexes. This selected data were used to calculate the R values.

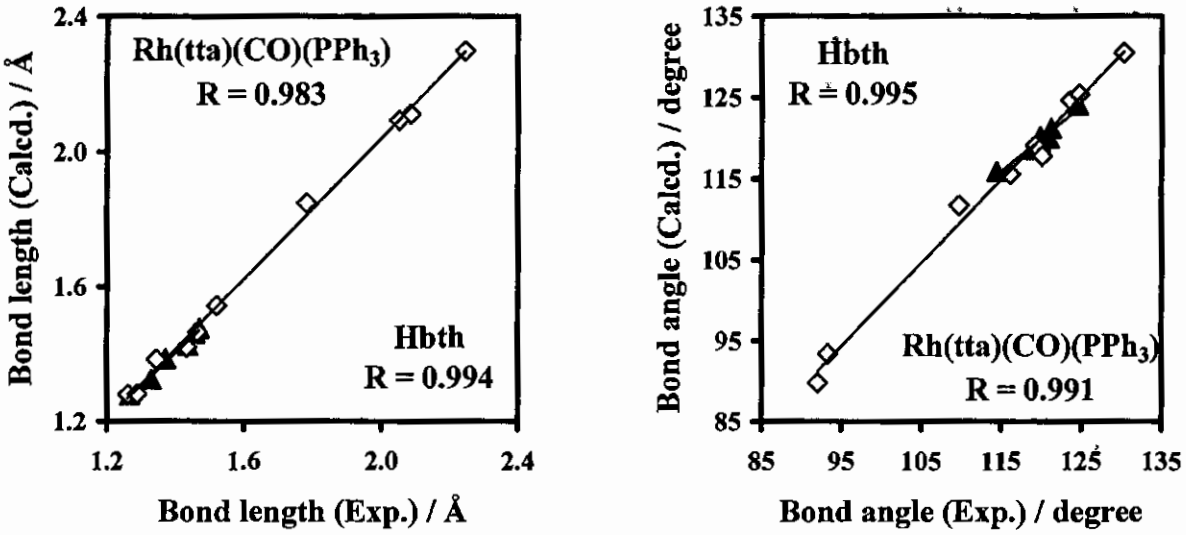

Figure 3.95: Plots of experimental *vs* calculated bond lengths (Å) and bond angles (°) of Hbth {1} (▲) and [Rh(tta)(CO)(PPh$_3$)] {7} (◊), using ADF(PW91)/TZP. Data points correspond to values in **Table 3.29**.

The figures above are an indication of the general degree of accuracy of the given computational data. All the R values correspond to an average accuracy ≥ 98%.

Figure 3.96: Structures of Hbth {1} **(left)** and [Rh(tta)(CO)(PPh$_3$)] {7} **(right)** indicating the numbering system.

Table 3.29: X-ray crystal data and calculated bond lengths and bond angles of Hbth {1} and [Rh(tta)(CO)(PPh_3)] {7}.

	Hbth {1}		Rh(tta)(CO)(PPh_3) {7}	
	Crystal	ADF	Crystal	ADF
Bond lengths / Å				
C1-C2	1.457	1.462	1.463	1.464
C2-C3	1.436	1.427	1.432	1.421
C3-C4	1.371	1.387	1.345	1.385
C4-C5	1.469	1.475	1.520	1.542
C2-O1	1.267	1.279	1.261	1.280
C4-O2	1.330	1.326	1.288	1.282
O1-Rh	-	-	2.085	2.111
O2-Rh	-	-	2.052	2.093
C6-Rh	-	-	1.781	1.847
P-Rh	-	-	2.245	2.298
Bond angles / °				
C1-C2-C3	119.9	120.2	119.2	119.1
C2-C3-C4	119.9	119.6	123.6	124.6
C3-C4-C5	124.6	124.1	120.1	117.8
O1-C2-C1	118.9	118.6	116.1	115.5
O1-C2-C3	121.2	121.2	124.7	125.4
O2-C4-C3	121.0	120.0	130.3	130.5
O2-C4-C5	114.4	115.9	109.7	111.7
O1-Rh-C6	-	-	92.0	89.8
O2-Rh-P	-	-	93.3	93.4

From the above table it can be seen that the calculated bond lengths and bond angles are in excellent agreement with the crystal data. The calculated bond lengths are constantly slightly larger than the crystal data, with the exception of the C2-C3 and C4-O2 bond lengths for both Hbth {1} and [Rh(tta)(CO)(PPh_3)] {7}. The bonds around the Rh atom deviate slightly more from the crystal data (0.026 - 0.066 Å) than the other bond lengths (0.0001 - 0.022 Å). It must be pointed out that all computations done in this study simulated gas phase conditions with the consequent exclusion of intermolecular interactions and forces. The result is that bond lengths, in general, tend to be longer in the gas phase computational optimizations, than in the corresponding solid state crystal structures. Furthermore, the DFT program takes electronic effects into account, but not the resonance effect as discussed in **paragraph 2.2.2.2, Chapter 2,** which explains why the calculated C2-C3 and C4-O2 bond lengths are too short.

No specific tendency in bond angle size was observed. The largest deviation is seen for the O1-Rh-C6 and the C3-C4-C5 bond angles of [Rh(tta)(CO)(PPh_3)] {7}. The O1-Rh-C6 bond angle was calculated as 89.8°, while the crystallographic value is 92.0°. This bond includes a

carbonyl group which has less movement restrictions than the other groups. In general, the bond angles agreed closely to the crystal data.

Evidence presented in this section illustrated the relatively high degree of accuracy attained by the use of the quantum computational program ADF in geometry optimizations of thienyl containing β-diketones and β-diketonato Rh complexes. Whether artificially generated atomic coordinates or coordinates obtained from X-ray data were used in the input files, the relevant calculated molecular geometries and energies always converged to the same values. Structural data computed for related compounds may therefore be presented with an extrapolative equally high degree of accuracy.

3.6.3 [Rh(bth)(CO)$_2$] {3}, [Rh(tta)(CO)$_2$] {4}, [Rh(dtm)(CO)$_2$] {5}, [Rh(bth)(CO)(PPh$_3$)] {6} and [Rh(dtm)(CO)(PPh$_3$)] {8}: a computational study.

3.6.3.1 Geometrical study of thienyl containing Rh(I) complexes.

The optimized structures of the thienyl containing square planar Rh(I) complexes are presented in the figures below with selected bond distance and bond angles as indicated. The other isomer of [Rh(tta)(CO)(PPh$_3$)] {7}, that was not discussed in **paragraph 3.6.2**, is also included.

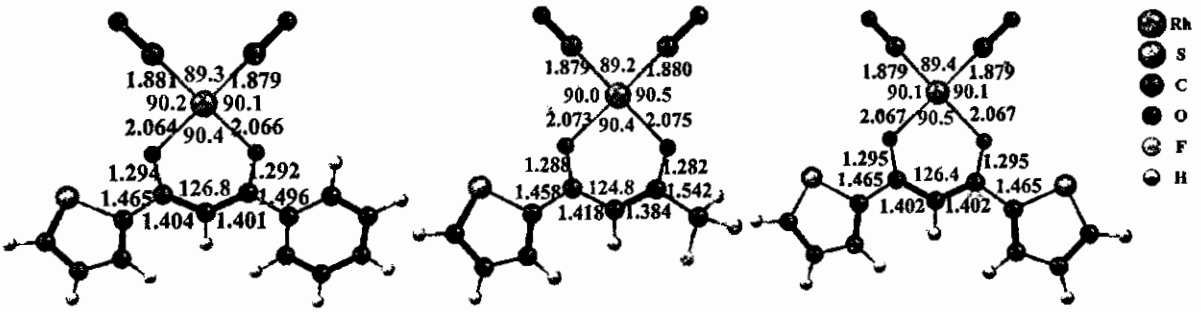

Figure 3.97: The calculated structures of [Rh(bth)(CO)$_2$] {3}, [Rh(tta)(CO)$_2$] {4} and [Rh(dtm)(CO)$_2$] {5}. Angles (degree) (**blue**) and bonds (Å) (**black**) are as indicated.

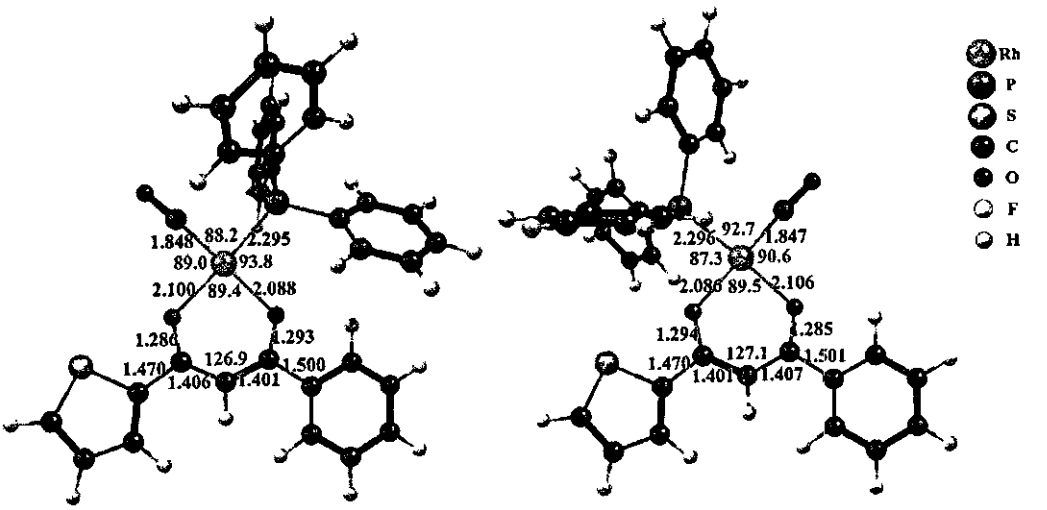

Figure 3.98: The calculated structures both isomers A and B of [Rh(bth)(CO)(PPh$_3$)] {6}. Angles (degree) (**blue**) and bonds (Å) (**black**) are as indicated.

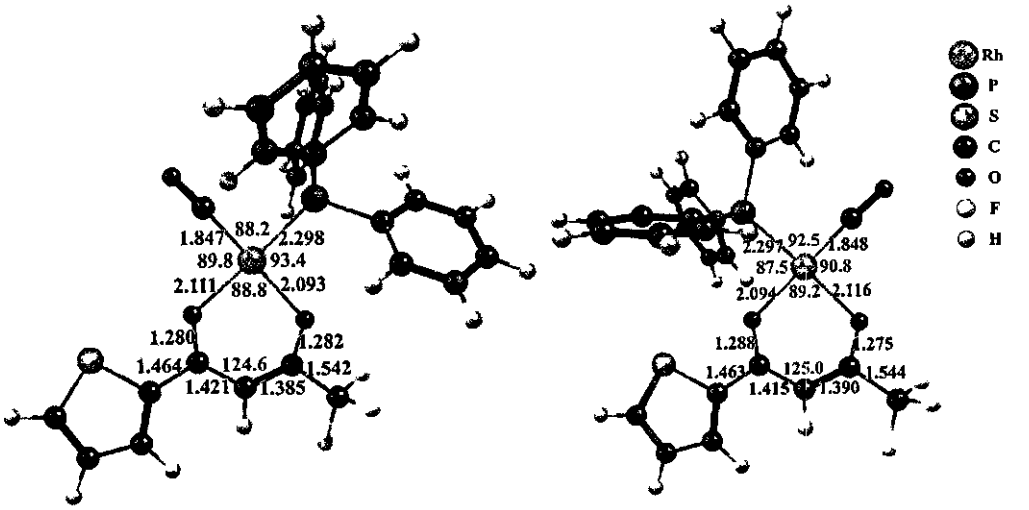

Figure 3.99: The calculated structures of both isomers A and B of [Rh(tta)(CO)(PPh$_3$)] {7}. Angles (degree) (**blue**) and bonds (Å) (**black**) are as indicated.

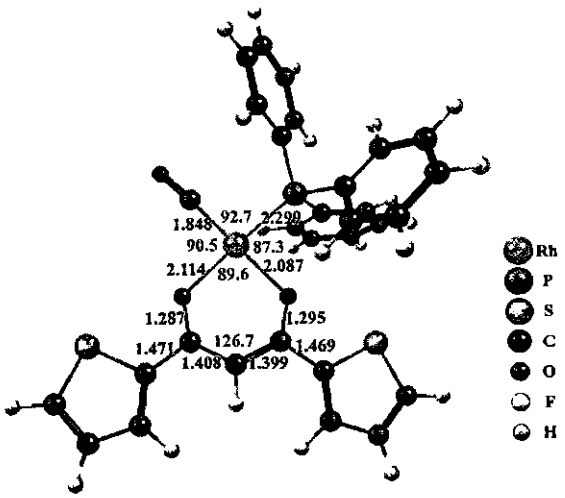

Figure 3.100: The calculated structures of the one isomer of [Rh(dtm)(CO)(PPh$_3$)] {8}. Angles (degree) (**blue**) and bonds (Å) (**black**) are as indicated.

All optimized structures resulted in a square planar arrangement. One would expect a slight twist in the aromatic rings when these molecules are packed in a crystal system. The bond lengths and bond angles are in agreement with complexes of this type (**Table 2.6** and **Table 2.7** in **paragraph 2.3.7, Chapter 2**). The different isomers of [Rh(bth)(CO)(PPh_3)] **{6}** and [Rh(tta)(CO)(PPh_3)] **{7}** had, within experimental error, the same relative molecular energy. This means that, in the gas phase, both isomers will exist in a 1:1 ratio. This is consistent with the experimental data, in solution of $CDCl_3$. The equilibrium constants (K_{c1}) in $CDCl_3$ at 25 °C for both [Rh(bth)(CO)(PPh_3)] **{6}** and [Rh(tta)(CO)(PPh_3)] **{7}** were found to be 1.0 (**Table 3.15, paragraph 3.4.3**).

3.6.3.2 IR carbonyl stretching frequency (ν_{CO}) study of thienyl containing Rh(I) complexes.

The dicarbonyl complexes give an IR spectrum with two distinctive singlet ν_{CO} peaks - one for the symmetrical and one for the asymmetrical carbonyl stretching. Replacement of one of these CO groups with PPh_3 results in a monocarbonyl phosphine [Rh^I(β-diketonato)(CO)(PPh_3)] complex. Subsequently only one ν_{CO} peak is observed, represented by the one CO group. TDDFT calculations were preformed on the optimized structures to obtain the ν_{CO}. The calculated and experimental carbonyl stretching frequencies (ν_{CO}) are tabulated in **Table 3.30** and illustrated graphically for [Rh(tta)(CO)(PPh_3)] **{7}** in **Figure 3.101**. See **paragraph 3.4.1.2** for a discussion on the results obtained experimentally. The calculated carbonyl stretching frequencies are in excellent agreement with the experimentally obtained values.

Table 3.30: Calculated and experimental carbonyl stretching frequencies (ν_{CO}) of thienyl containing Rh(I) complexes.

	Calculated DFT [a] ν_{CO} / cm^{-1}	**Experimental** [b] ν_{CO} / cm^{-1}
[Rh^I(β-diketonato)($CO)_2$]		
bth **{3}**	1996 2056	1996 2058
tta **{4}**	2007 2066	2008, 2026, 2033, 2078, 2098
dtm **{5}**	1998 2057	1992 2057
[Rh^I(β-diketonato)(CO)(PPh_3)] [c]		
bth **{6}**	1974, 1977	1970, 1980 (1983) [d]
tta **{7}**	1981, 1986	1981 (1991) [c]
dtm **{8}**	1977	1971 (1987) [c]

a Unscaled
b In chloroform
c Two isomers each, except for complex **{8}** which is symmetrical
c In solid state, solution ν_{CO} in brackets

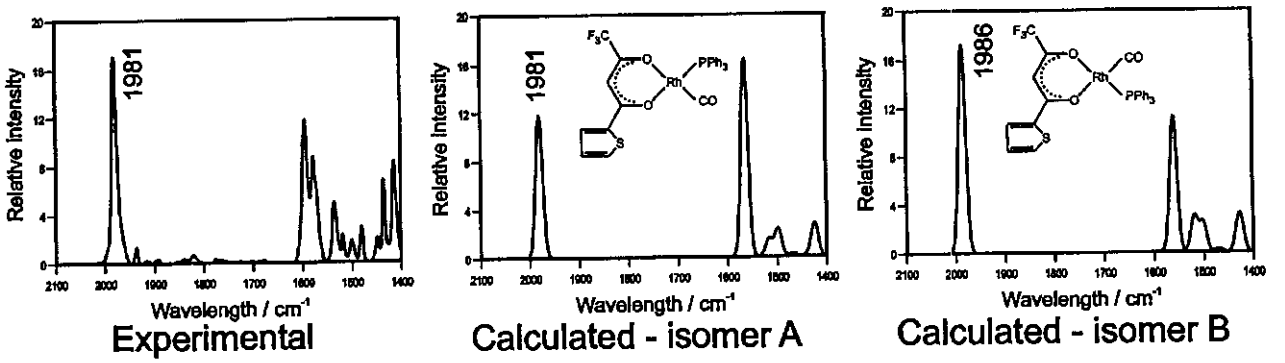

Figure 3.101: IR spectrum for [Rh(tta)(CO)(PPh$_3$)] {7}, experimental (left) and calculated (middle and right for the two isomers) The crystal structure of {7} corresponds to the geometry of the calculated isomer in the middle.

3.6.4 Rh(III) oxidative addition products.

Mathematically calculated, the different arrangements of the groups bonded to the Rh give rise to a theoretical possibility of 24 different octahedral Rh(III)-alkyl isomers and 12 different square pyramidal Rh(III)-acyl isomers. Since the enantiomers (12 Rh(III)-alkyl and 6 Rh(III)-acyl mirror images) display the same computational and chemical properties, they can be excluded from this discussion. This leaves one with 12 different Rh(III)-alkyl isomers and 6 different Rh(III)-acyl isomers. The structures of these possibilities are given in **Figure 3.102** and **Figure 3.103**. The possibility of trigonal bipyramidal Rh(III)-acyl isomers was also inspected, but resulted in such high relative molecular energies, that they were discarded from this study.

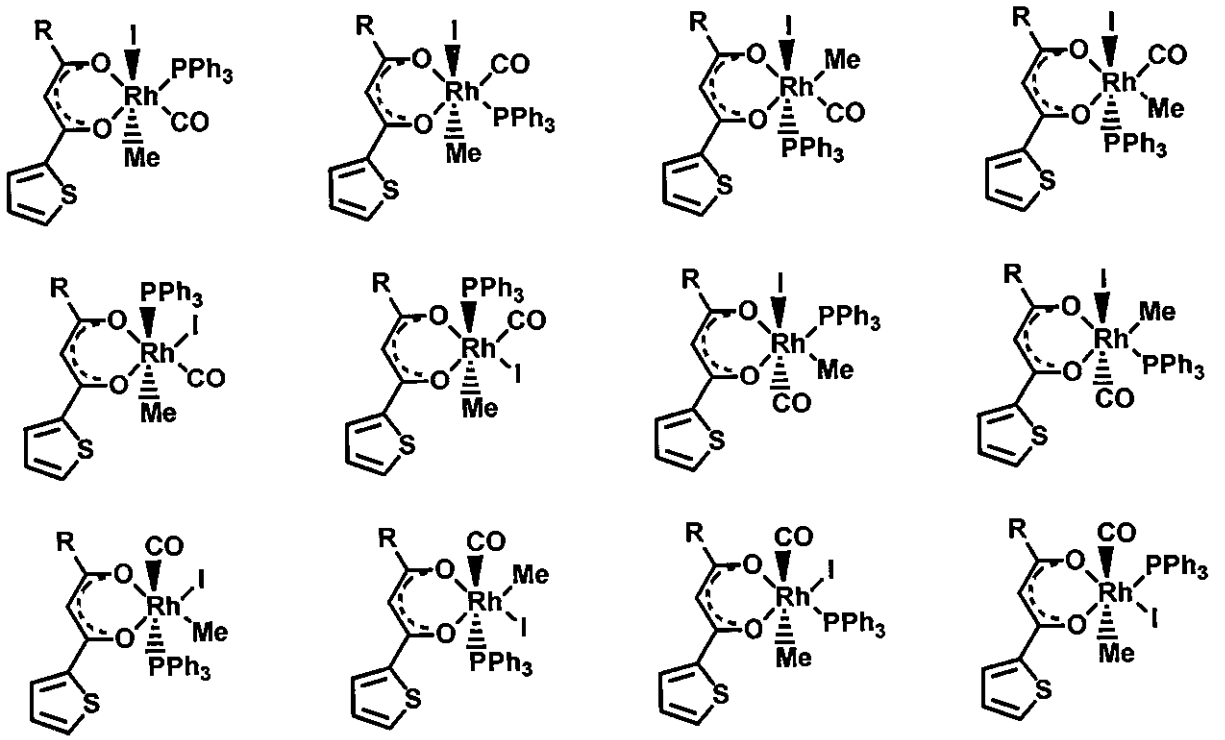

Figure 3.102: Twelve theoretical possible octahedral Rh(III)-alkyl species, excluding the enantiomers.

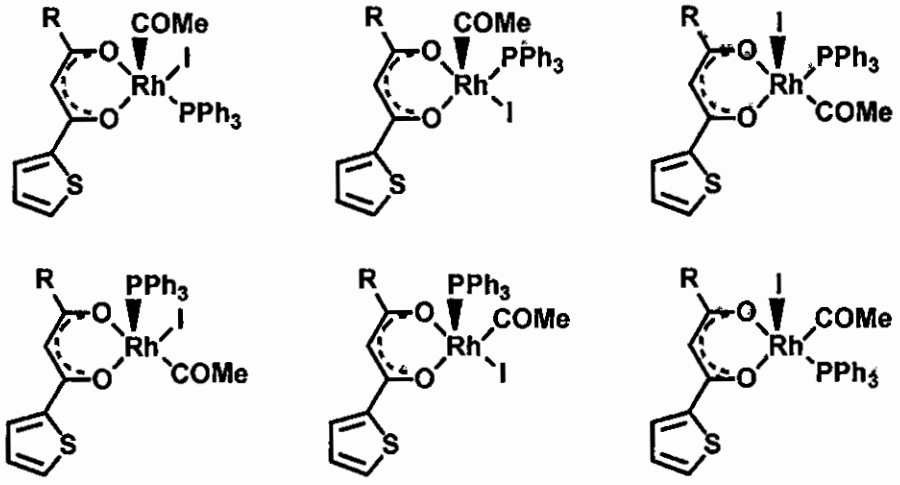

Figure 3.103: Six theoretical possible square pyramidal Rh(III)-acyl species, excluding the enantiomers.

To obtain a better insight into the relative stability of these possible reaction products during the oxidative addition reaction between MeI and square planar Rh(I) complexes, the structures in **Figure 3.102** and **Figure 3.103** were submitted to a computational study. Graphical representations of the relative molecular energies of the reaction products of [Rh(bth)(CO)(PPh_3)] **{6}**, [Rh(tta)(CO)(PPh_3)] **{7}** and [Rh(dtm)(CO)(PPh_3)] **{8}** with MeI are given in **Figure 3.104**, **Figure 3.105** and **Figure 3.106** respectively.

When comparing the relative energies of the different Rh(III) complexes in **Figure 3.104**, **Figure 3.105** and **Figure 3.106**, one can discard the upper 6 Rh(III)-alkyl isomers and the upper 2 Rh(III)-acyl isomers, since they are energetically not favoured. MeI will either be added *cis* or *trans* to the square planar Rh(I) complex. The *cis* addition products have similar or slightly lower energies than the lowest energy *cis* addition products. Calculations done by Griffin *et al.*[65] for the transition state (TS) in the oxidative addition of iodomethane to *cis*-$[Rh(CO)_2I_2]^-$, indicated that the linear TS is strongly favoured over a bent *cis* TS. The same conclusion, namely linear S_n2-like TS, was made by Feliz *et al.*[66] from a DFT study of the activation parameters of the iodomethane oxidative addition to Rh(I) complexes. A theoretical study of the TS of the oxidative addition of iodomethane to [Rh(bth)(CO)(PPh_3)] **{6}**, [Rh(tta)(CO)(PPh_3)] **{7}** and [Rh(dtm)(CO)(PPh_3)] **{8}** does not fall within the borders of this M.Sc. research program and is part of the prospective studies. *Trans* addition of iodomethane to

[65] T.R. Griffin, D.B. Cook, A. Haynes, J.M. Pearson, D. Monti, G.E. Morris, J. Am. Chem. Soc. 118 (1996) 3029.

[66] M. Feliz, Z. Freixa, P.W.N.M. van Leeuwen, C. Bo, Organometallics 24 (2005) 5718.

[Rh(bth)(CO)(PPh_3)] {**6**}, [Rh(tta)(CO)(PPh_3)] {**7**} and [Rh(dtm)(CO)(PPh_3)] {**8**} is consistent with the experimental results of this study, see **paragraph 3.5.7**.

Both the experimental results of this study and the theoretical calculations by Griffin *et al.*[65] and Feliz *et al.*[66] are thus consistent with *trans* addition of iodomethane to square planar Rh(I) complexes. Assuming *trans* addition and ignoring the two lowest energy *cis* addition products, leaves one with only two sets of Rh(III)-alkyl isomers and two sets of Rh(III)-acyl isomers.

The stereochemistry of the two sets of Rh(III)-alkyl isomers is illustrated in the top row of **Figure 3.102**. Close inspection of the stereochemistry of the two sets of Rh(III)-alkyl isomers reveals that it can be described as:

Type 1: The methyl and the iodide are above and below the square planar plane (the *trans* oxidative addition products to the two isomers of the Rh(I) complex, the first two structures in **Figure 3.102**).

Type 2: The PPh_3 and the iodide are above and below the square planar plane (the third and fourth figures in **Figure 3.102**).

These two types correspond exactly to the two classes of octahedral Rh(III)-alkyl complexes characterized by crystallography as described in **paragraph 2.3.7.3 (Chapter 2)**. These two sets of Rh(III)-alkyl isomers and the lowest energy two sets of Rh(III)-acyl isomers are used to propose a reaction path that include steriochemistry for the oxidative addition reaction of iodomethane to the [Rh(β-diketonato)(CO)(PPh_3)] complexes of this study.

3.6.5 Proposed reaction path of oxidative addition of iodomethane (MeI) to [Rh(β-diketonato)(CO)(PPh_3)].

As a representative example, the proposed reaction path of the oxidative addition reaction between MeI and [Rh(bth)(CO)(PPh_3)] {**6**}, with specific stereochemistry, is given in **Figure 3.107**. Only one isomer is illustrated since the reaction path of the other isomer is similar. One starts off with a square planar Rh(I) complex to which MeI is added. As the MeI is added, it goes through a transition state (not calculated) to form the *trans* addition octahedral Rh(III)-alkyl1 (type 1) product which is in equilibrium with a square pyramidal Rh(III)-acyl1 product. These first Rh(III)-alkyl1 and Rh(III)-acyl1 products that form then transform into a

second set of Rh(III)-alkyl2 (type 2) and Rh(III)-acyl2 products. The small difference in energy makes the equilibrium between the Rh(III) products possible. Note that the stereochemistry of the final Rh(III)-acyl2 product with the acyl moiety in the apical position, corresponds to the stereochemistry of the all the square pyramidal Rh(III)-acyl crystal structures solved (**paragraph 2.3.7.3, Chapter 2**).

The reaction mechanism proposed on experimental grounds for the first two steps of the MeI addition to $[Rh^{I}(bth)(CO)(PPh_3)]$ in **Scheme 3.11** and **3.12** in **paragraph 3.5.7,** is consistent with the theoretically calculated reaction path in **Figure 3.107** for $[Rh^{I}(bth)(CO)(PPh_3)]$. The spectroscopic identification of $[Rh^{III}(bth)(CO)(PPh_3)(Me)(I)]$-alkyl1 and -alkyl2 isomers (**paragraph 3.5.4.5**) is consistent with the stereochemistry calculated for the $[Rh^{III}(bth)(CO)(PPh_3)(Me)(I)]$-alkyl1 and -alkyl2 isomers in **Figure 3.107**. The Rh(III)-alkyl1 product corresponds thus to the type 1 group of crystal structures solved and the Rh(III)-alkyl2 product corresponds thus to the type 2 group of crystal structures solved (**Figure 2.19, paragraph 2.3.7.3, Chapter 2**).

For $[Rh^{I}(tta)(CO)(PPh_3)]$ it was experimentally found that the *third reaction* does not occur and a stable Rh(III)-alkyl2 product was isolated. The $[Rh^{III}(tta)(CO)(PPh_3)(Me)(I)]$ **{10}** product, as explored by NMR techniques (**paragraph 3.4.1.3**), was found to have the I (or CO) and PPh_3 groups above and below the plane. The first option (I and PPh_3 in the apical positions) is consistent with the stereochemistry of the theoretically calculated lowest energy Rh(III)-alkyl2 or type 2 geometry. All calculations in the current study were done in the gas phase. Future studies will explore the effects of solvents on the theoretically calculated energies of the different Rh(III) products, the TS of the oxidative addition process and the proposed reaction path.

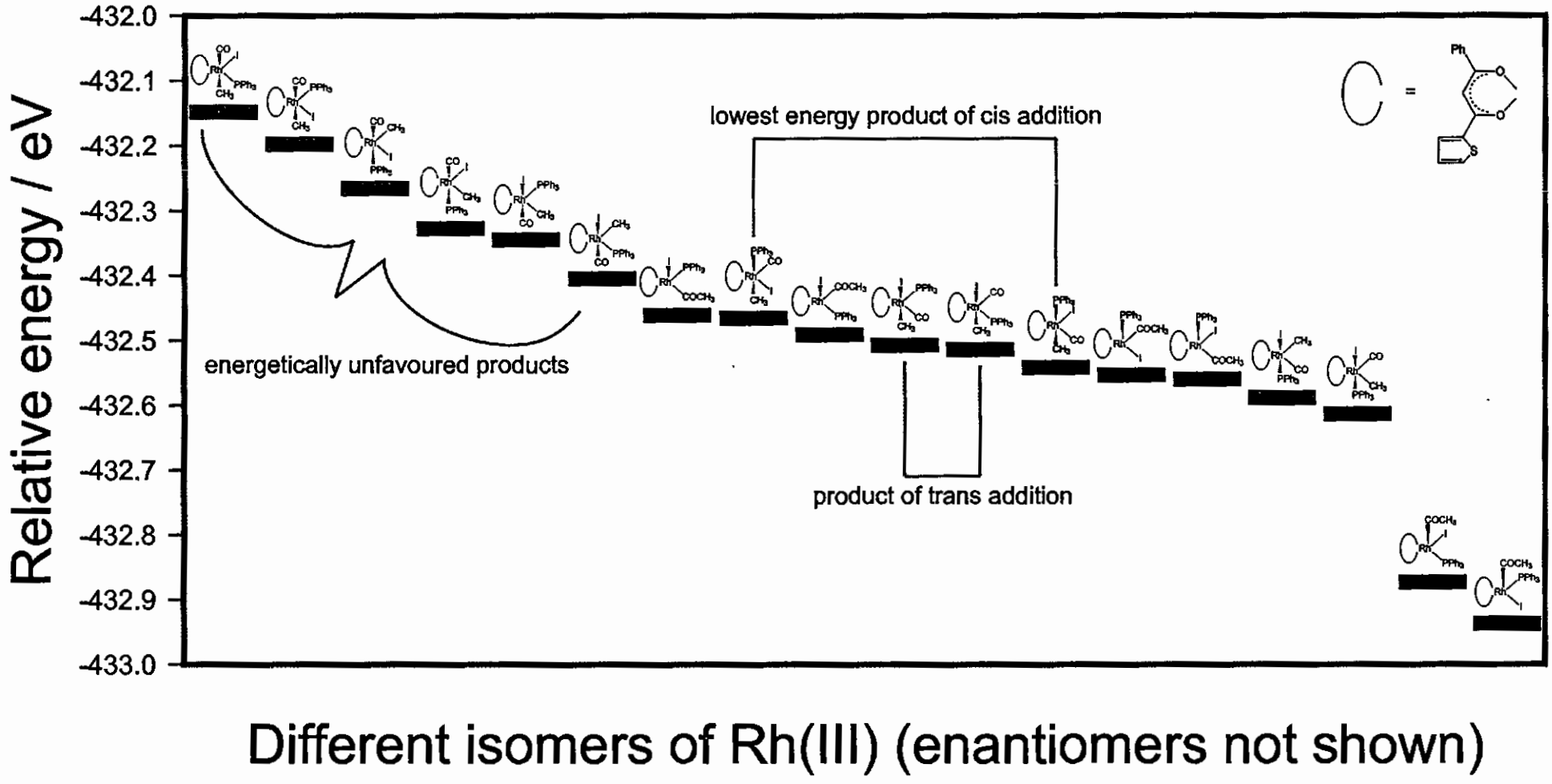

Figure 3.104: A graphical representation of the relative energies of the 12 possible Rh(III)-alkyl isomers (purple lines) and the 6 possible Rh(III)-acyl isomers (brown lines) during the reaction between MeI and [Rh(bth)(CO)(PPh_3)] {**6**}. Note that the absolute values of the energies shown along the vertical axis are meaningless.

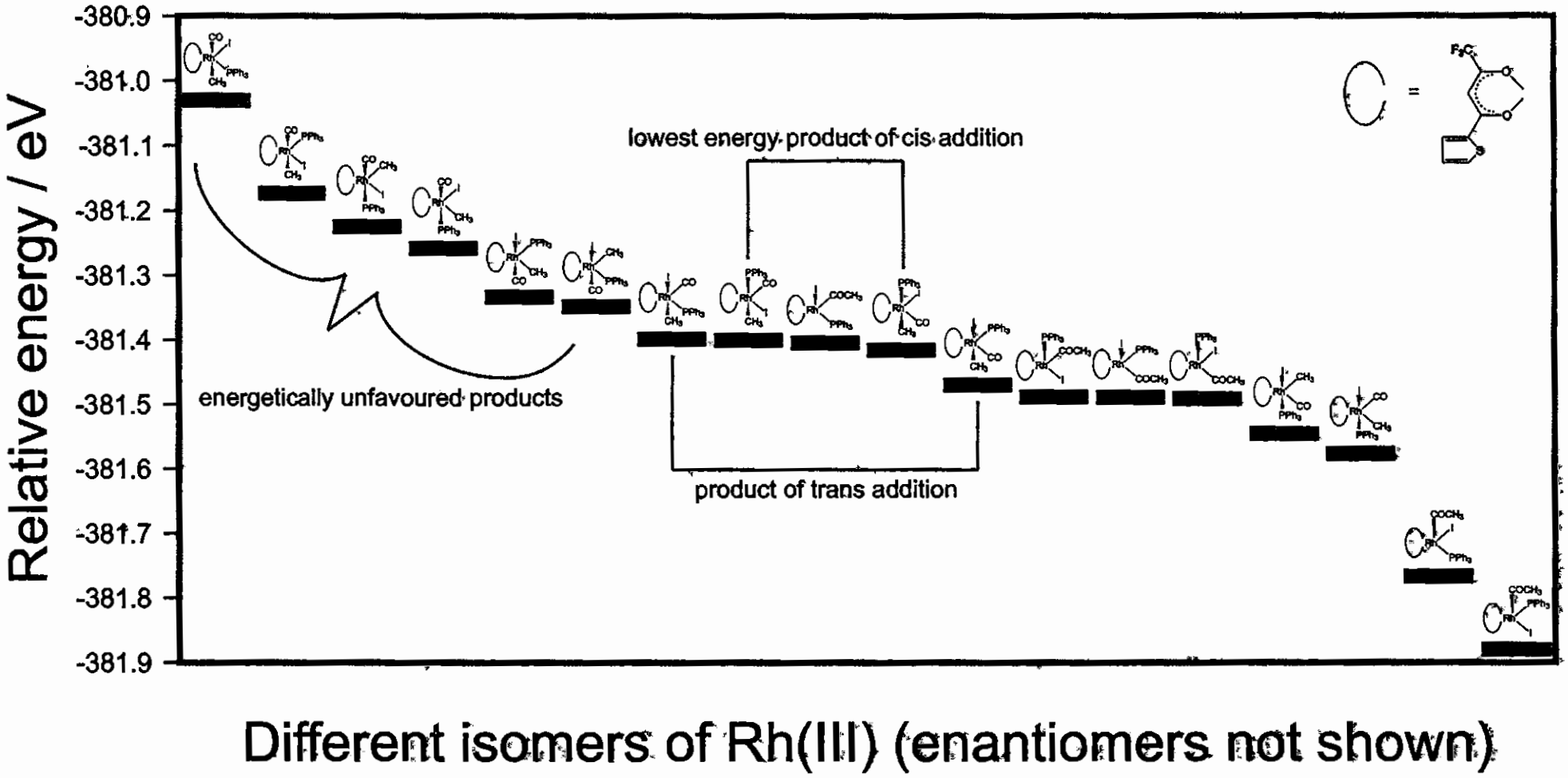

Figure 3.105: A graphical representation of the relative energies of the 12 possible Rh(III)-alkyl isomers (purple lines) and the 6 possible Rh(III)-acyl isomers (brown lines) during the reaction between MeI and [Rh(tta)(CO)(PPh_3)] {7}. Note that the absolute values of the energies shown along the vertical axis are meaningless.

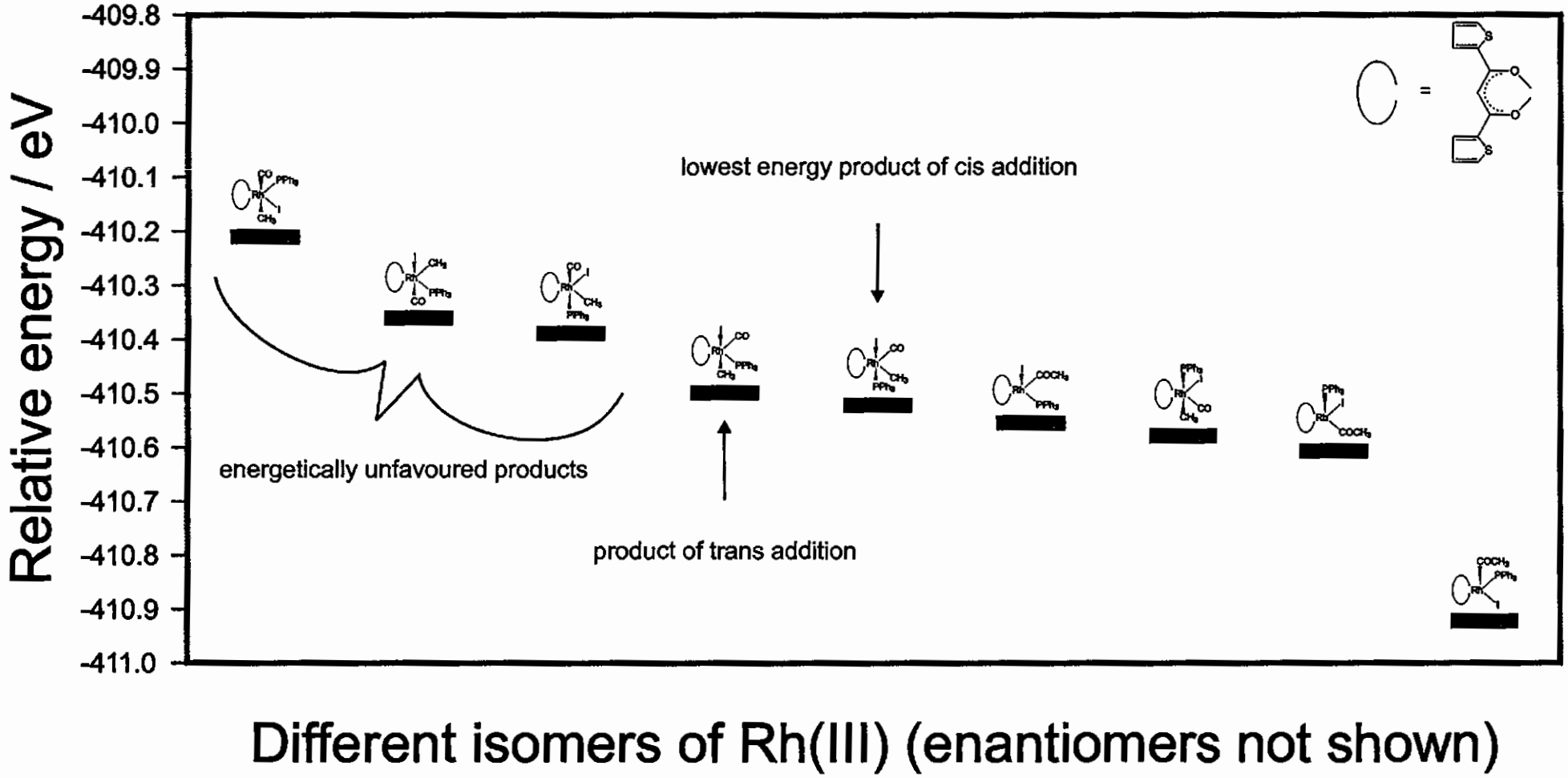

Figure 3.106: A graphical representation of the relative energies of the 12 possible Rh(III)-alkyl isomers (purple lines) and the 6 possible Rh(III)-acyl isomers (brown lines) during the reaction between MeI and [Rh(dtm)(CO)(PPh_3)] **{8}**. Note that the absolute values of the energies shown along the vertical axis are meaningless.

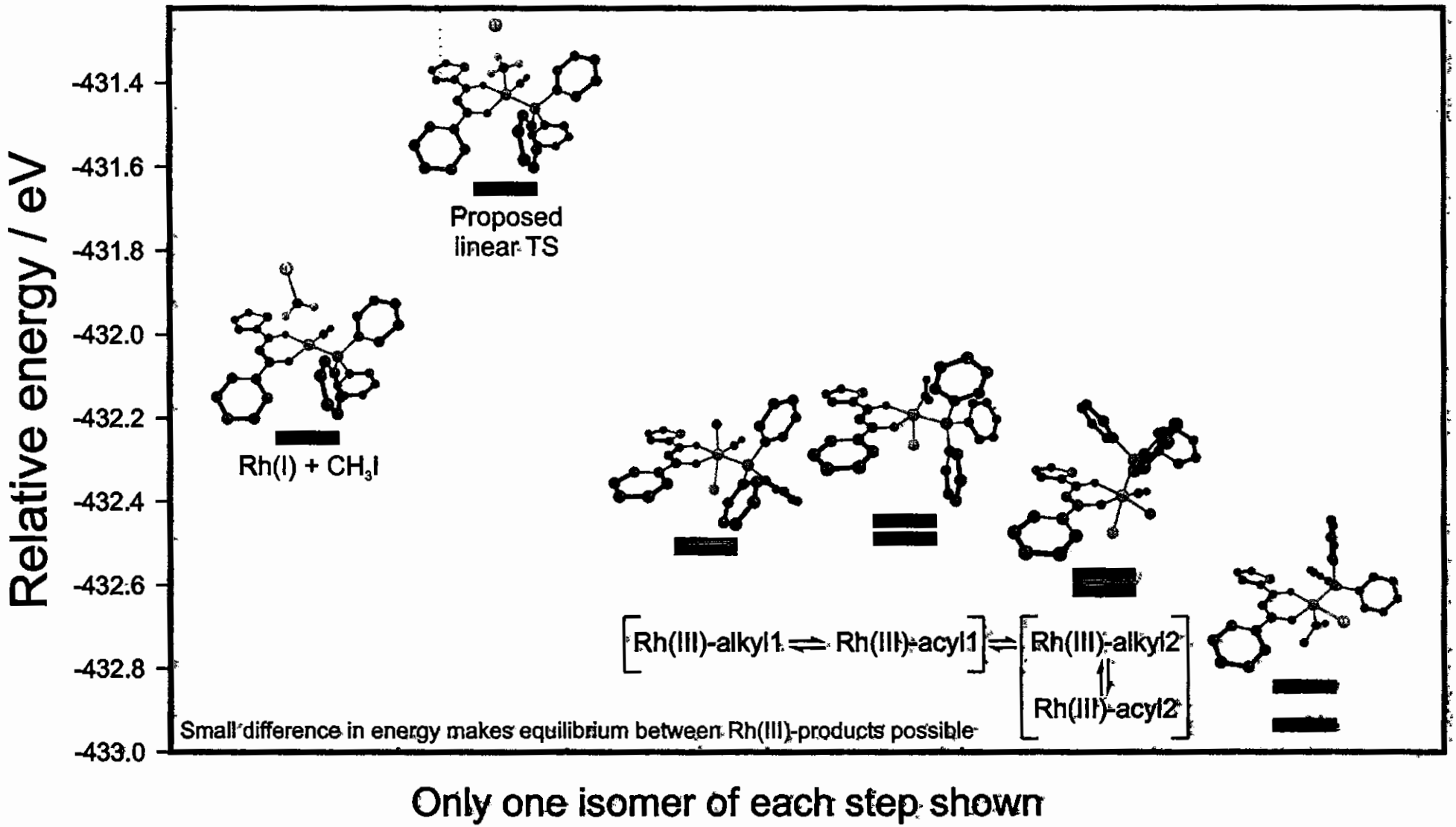

Figure 3.107: Proposed reaction path for the oxidative addition reaction between MeI and [Rh(bth)(CO)(PPh$_3$)] **{6}** with specific stereochemistry. Note that the absolute values of the energies shown along the vertical axis are meaningless.

4 Experimental

4.1 Introduction.

In this chapter all experimental procedures, reaction conditions and techniques are described.

4.2 Materials.

Solid reagents used in preparations (Merck, Aldrich and Fluka) were used without further purification. Liquid reactants and solvents were distilled prior to use; water was doubly distilled. Organic solvents were dried according to published methods.[1] Melting points (m.p.) were determined with an Olympus BX51 system microscope assembled on top of a Linkam THMS600 stage and connected to a Linkam TMS94 temperature programmer.

4.3 Synthesis.

4.3.1 β-diketones {1}-{2}.

4.3.1.1 1-phenyl-3-(2-thenoyl)-1,3-propanedione (Hbth) {1}.

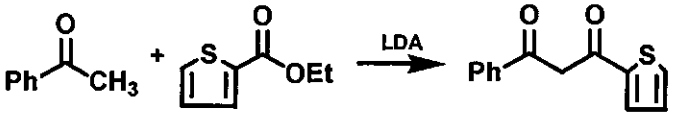

{1}

The system was flame dried and degassed with Ar for 30 min. The Ar was maintained during the reaction. 98% Acetophenone (1.2260 g, 10.00 mmol) was mixed with THF (1.0 ml) and stirred for a few minutes. LDA (6.70 ml of a 1.5 M solution in hexane, 10.0 mmol) was added while stirring and kept cool on an ice-bath. The transparent brown solution was allowed to stir a

[1] B.S. Furniss, A.J. Hannaford, P.W.G. Smith, A.R. Tatchell, Vogel's Textbook of Practical Organic Chemistry, Fifth edtion., Longman Scientific & Technical, John Wiley & Sons, New York, Chapter 4, pp. 395–469.

further 20 min at 0°C. 95% Ethyl 2-thiophenecarboylate (1.6442 g, 10.00 mmol) was added and the reaction mixture was allowed to stir overnight at room temperature (± 25°C) resulting in a milky yellow-orange solution. Diethyl ether was added resulting in a thick olive green suspension. The cream coloured precipitate was filtered off. The precipitate was acidified by dissolving it in HCl (50 ml, 0.3 M). The product was extracted with diethyl ether (3 x 50ml). The combined extracts were thoroughly washed with water, dried ($MgSO_4$) and solvent removed under reduced pressure. Recrystallisation with diethyl ether gave spectroscopically pure Hbth {1} as light brown crystals (0.4329 g, 18.8% yield); m.p. 80.3-81.3 °C; δ_H(600 MHz, $CDCl_3$): 4.57 (2H, s, keto CH_2), 6.71 (1H, s, enol CH), 7.17 (1H, dd, ^3J = 5 Hz, ^3J = 4 Hz, keto CH), 7.19 (1H, dd, ^3J = 5 Hz, ^3J = 4 Hz, enol CH), 7.51 (2H, m, keto + enol CH), 7.59 (1H, m, keto + enol CH), 7.66 (1H, dd, ^3J = 5 Hz, ^4J = 1 Hz, enol CH), 7.71 (1H, dd, ^3J = 5 Hz, ^4J = 1 Hz, keto CH), 7.83 (1H, dd, ^3J = 4 Hz, ^4J = 1 Hz, enol CH), 7.86 (1H, dd, ^3J = 4 Hz, ^4J = 1 Hz, keto CH), 7.97 (2H, m, enol CH), 8.06 (2H, m, keto CH).

4.3.1.2 1,3-di(2-thenoyl)-1,3-propanedione (Hdtm) {2}.

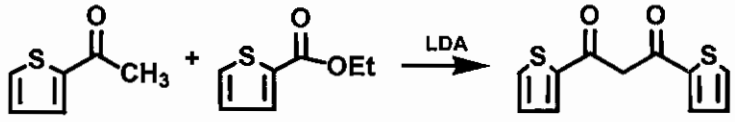

{2}

2-Acetylthiophene was prepared *via* acylation according to published procedure.[2] The system was flame dried and degassed with Ar for 30 min. The Ar was maintained during the reaction. 2-Acetylthiophene (1.2618 g, 10.00 mmol) was mixed with THF (1.0 ml) and stirred for a few minutes. LDA (5.60 ml of a 1.8 M solution in hexane, 10.0 mmol) was added while stirring and kept cool on an ice-bath. The transparent brown solution was allowed to stir a further 15 min at 0°C. 95% Ethyl 2-thiophenecarboylate (1.6442 g, 10.00 mmol) was added and the reaction mixture was allowed to stir overnight at room temperature (± 30°C) resulting in a milky brown-yellow solution. Diethyl ether was added resulting in a thick brown suspension. The brown precipitate was filtered off. The precipitate was acidified by dissolving it in HCl (50 ml, 0.3 M). The product was extracted with diethyl ether (3 x 50ml). The combined extracts were thoroughly washed with water, dried ($MgSO_4$) and solvent removed under reduced pressure. Spectroscopically pure Hdtm {2} brown product was obtained (0.4360 g, 18.5% yield); m.p. 99.5 – 100.2 °C; δ_H(600 MHz, $CDCl_3$): 4.49 (2H, s, keto CH_2), 6.56 (1H, s, enol CH),

[2] H.D. Hartough, A.I. Kosak, J. Am. Chem. Soc. 69 (1947) 1012.

7.17 (2H, dd, ^3J = 5 Hz, ^3J = 4 Hz, keto CH), 7.18 (2H, dd, ^3J = 5 Hz, ^3J = 4 Hz, enol CH), 7.63 (2H, dd, ^3J = 5 Hz, ^4J = 1 Hz, enol CH), 7.72 (2H, dd, ^3J = 5 Hz, ^4J = 1 Hz, keto CH), 7.79 (2H, dd, ^3J = 4 Hz, ^4J = 1 Hz, enol CH), 7.91 (1H, dd, ^3J = 4 Hz, ^4J = 1 Hz, keto CH).

4.3.1.3 4,4,4-trifluoro-1-(2-thenoyl)-1,3-propanedione (Htta).

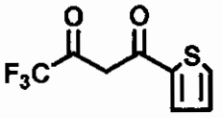

The β-diketone Htta (thenoyltrifluoroacetone or 4,4,4-trifluoro-1-(2-thenoyl)-1,3-propanedione) was bought from Aldrich for use in this study; m.p. 42.1 – 43.0 °C; δ_H(600 MHz, $CDCl_3$): 4.95 (2H, s, keto CH_2), 6.47 (1H, s, enol CH), 7.22 (2H, dd, ^3J = 5 Hz, ^3J = 4 Hz, keto CH), 7.23 (2H, dd, ^3J = 5 Hz, ^3J = 4 Hz, enol CH), 7.78 (2H, dd, ^3J = 5 Hz, ^4J = 1 Hz, enol CH), 7.82 (2H, dd, ^3J = 5 Hz, ^4J = 1 Hz, keto CH), 7.84 (1H, dd, ^3J = 4 Hz, ^4J = 1 Hz, keto CH), 7.86 (2H, dd, ^3J = 4 Hz, ^4J = 1 Hz, enol CH).

4.3.2 [Rh(β-diketonato)$(CO)_2$] complexes {3}-{5}.

4.3.2.1 Dicarbonyl(1-phenyl-3-(2-thenoyl)-1,3-propanedionato-κ^2O,O')rhodium(I) [Rh(bth)$(CO)_2$] {3}.

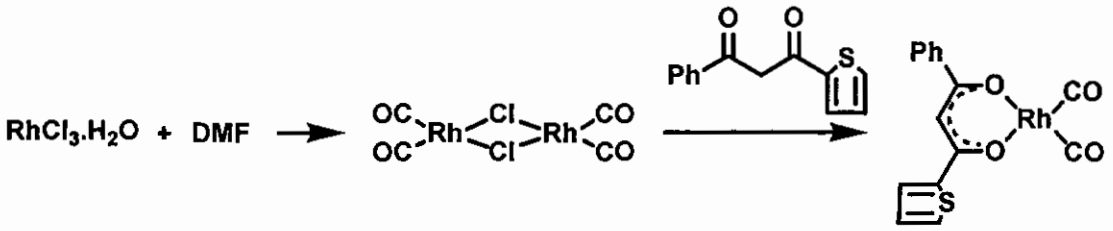

{1} {3}

$RhCl_3.3H_2O$ (0.1001 g, 0.38 mmol) was dissolved in water (3 drops) and refluxed in DMF (3 ml) for *ca* 30 minutes until light yellow. The solution was allowed to cool on ice. An equivalent amount of solid Hbth {1} (0.0875 g, 0.38 mmol) was slowly added to a stirred solution. After 30 min of stirring the crude product [Rh(bth)$(CO)_2$] {3} was precipitated with an excess of water and suction filtered. Recrystallisation with hexane gave spectroscopically pure [Rh(bth)$(CO)_2$] {3} as maroon feathery crystals (0.1187 g, 80.5% yield); m.p. 147.2-148.8 °C; ν (C=O)/cm^{-1} = 1996 and 2058; δ_H(600 MHz, $CDCl_3$): 6.85 (1H, s, CH), 7.13 (1H, dd, ^3J = 5 Hz, ^3J = 4 Hz, CH), 7.47 (2H, m, CH), 7.53 (1H, m, CH), 7.58 (1H, dd, ^3J = 5 Hz, ^4J = 1 Hz, CH), 7.75 (1H, dd, ^3J = 4 Hz, ^4J = 1 Hz, CH), 7.93 (2H, m, CH).

4.3.2.2 Dicarbonyl(thenoyltrifluoroacetonato-κ^2O,O')rhodium(I) [Rh(tta)(CO)$_2$] {4}.

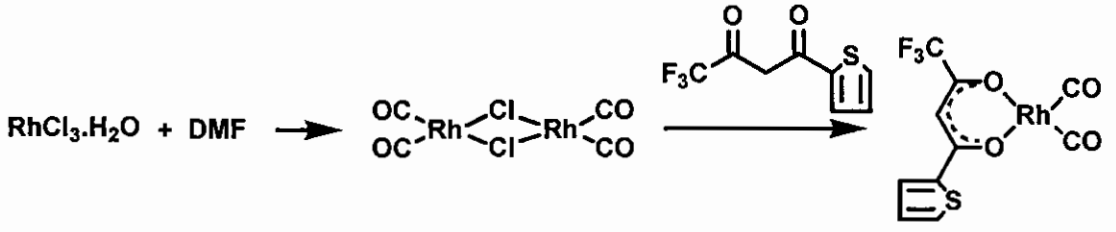

{4}

$RhCl_3.3H_2O$ (0.1001 g, 0.38 mmol) was dissolved in water (3 drops) and refluxed in DMF (3 ml) for *ca* 30 minutes until light yellow. The solution was allowed to cool on ice. An equivalent amount of solid Htta (0.0844 g, 0.38 mmol) was slowly added to a stirred solution. After 30 min of stirring the crude product [Rh(tta)(CO)$_2$] {4} was precipitated with an excess of water and suction filtered. Recrystallisation with hexane gave spectroscopically pure [Rh(tta)(CO)$_2$] {4} as red hairy crystals (0.1294 g, 89.6% yield); m.p. 143.3-134.7 °C; ν (C=O)/cm^{-1} = 2008, 2026, 2708 and 2098; δ_H(300 MHz, $CDCl_3$): 6.58 (1H, s, CH), 7.18 (1H, dd, ^3J = 5 Hz, ^3J = 4 Hz, CH), 7.72 (1H, dd, ^3J = 5 Hz, ^4J = 1 Hz, CH), 7.80 (1H, dd, ^3J = 4 Hz, ^4J = 1 Hz, CH).

4.3.2.3 Dicarbonyl(1,3-di(2-thenoyl)-1,3-propanedionato-κ^2O,O')rhodium(I) [Rh(dtm)(CO)$_2$] {5}.

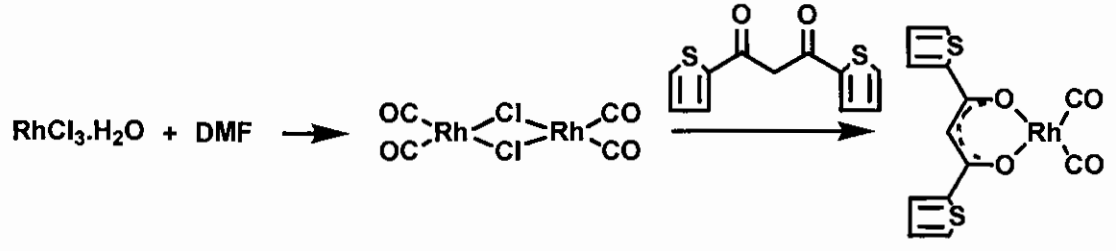

{2} {5}

$RhCl_3.3H_2O$ (0.1001 g, 0.38 mmol) was dissolved in water (3 drops) and refluxed in DMF (3 ml) for *ca* 30 minutes until light yellow. The solution was allowed to cool on ice. An equivalent amount of solid Hdtm {2} (0.0898 g, 0.38 mmol) was slowly added to a stirred solution. After 30 min of stirring the crude product [Rh(dtm)(CO)$_2$] {5} was precipitated with an excess of water and suction filtered. Recrystallisation with chloroform gave spectroscopically pure [Rh(dtm)(CO)$_2$] {5} as blue-purple crystals (0.0858 g, 57.3% yield); m.p. 149.2-149.9 °C; ν (C=O)/cm^{-1} = 1992 and 2057; δ_H(600 MHz, $CDCl_3$): 6.75 (1H, s, CH), 7.13 (2H, dd, ^3J = 5 Hz, ^3J = 4 Hz, CH), 7.56 (2H, dd, ^3J = 5 Hz, ^4J = 1 Hz, CH), 7.72 (2H, dd, ^3J = 4 Hz, ^4J = 1 Hz, CH).

4.3.3 [Rh(β-diketonato)(CO)(PPh_3)] complexes {6}-{8}.

4.3.3.1 Carbonyl(1-phenyl-3-(2-thenoyl)-1,3-propanedionato-κ^2O,O')triphenylphosphine-rhodium(I) [Rh(bth)(CO)(PPh_3)] {6}.

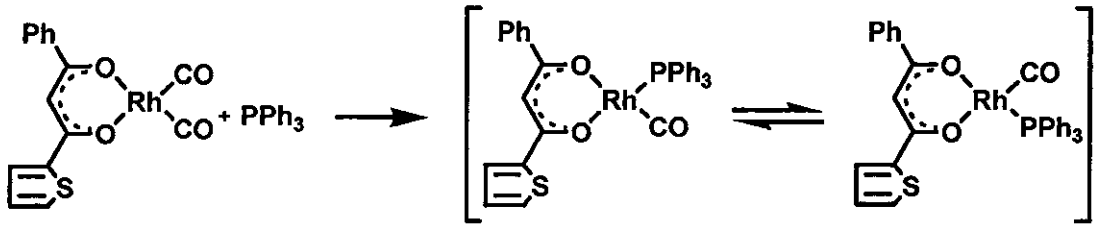

{3} {6A} {6B}

To a solution of [Rh(bth)$(CO)_2$] {3} (0.0776 g, 0.20 mmol) in warm hexane (3 ml) was added an equivalent amount of solution of PPh_3 (0.0525 g, 0.20 mmol) in warm hexane (3 ml). After 1 min of stirring the product [Rh(bth)(CO)(PPh_3)] {6} precipitated. The solvent was removed by decantation, resulting in spectroscopically pure [Rh(bth)(CO)(PPh_3)] {6} as a yellow powder (0.0830 g, 66.7% yield); m.p. 149.1-189.5 °C; ν (C=O)/cm^{-1} = 1970; δ_H(600 MHz, $CDCl_3$): 6.75 (1H, s, isomer A CH), 6.75 (1H, s, isomer B CH), 6.89 (1H, dd, ^3J = 5 Hz, ^3J = 4 Hz, isomer B CH), 7.10 (3H, m, isomer A CH), 7.10 (1H, dd, ^3J = 4 Hz, ^4J = 1 Hz, isomer B CH), 7.11 (1 H, dd, ^3J = 5 Hz, ^3J = 4 Hz, isomer A CH), 7.27 (1H, dd, ^3J = 5 Hz, ^4J = 1 Hz, isomer B CH), 7.42 (14H, m, CH), 7.47 (9H, m, CH), 7.52 (1H, dd, ^3J = 5 Hz, ^4J = 1 Hz, isomer A CH), 7.75 (12H, m, CH), 7.76 (1H, dd, ^3J = 4 Hz, ^4J = 1 Hz, isomer A CH), 8.01 (2H, m, isomer B CH).

4.3.3.2 Carbonyl(thenoyltrifluoroacetonato-κ^2O,O')triphenylphosphine-rhodium(I) [Rh(tta)(CO)(PPh_3)] {7}.

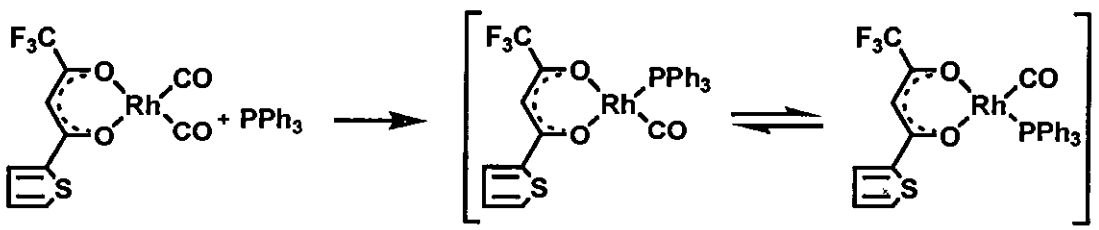

{3} {7A} {7B}

To a solution of [Rh(tta)$(CO)_2$] {4} (0.0760 g, 0.20 mmol) in warm hexane (3 ml) was added an equivalent amount of solution of PPh_3 (0.0535 g, 0.20 mmol) in warm hexane (3 ml). After 1 min of stirring the product [Rh(tta)(CO)(PPh_3)] {7} precipitated. The solvent was removed by

decantation, resulting in spectroscopically pure [Rh(tta)(CO)(PPh_3)] {7} as a yellow powder (0.0493 g, 40.1% yield); m.p. 181.9-182.4 °C; ν (C=O)/cm^{-1} = 1981; δ_H(600 MHz, $CDCl_3$): 6.42 (1H, s, isomer A CH), 6.43 (1H, s, isomer B CH), 6.92 (1H, dd, ^3J = 5 Hz, ^3J = 4 Hz, isomer B CH), 7.13 (1H, dd, ^3J = 5 Hz, ^3J = 4 Hz, isomer A CH), 7.18 (1H, dd, ^3J = 4 Hz, ^4J = 1 Hz, isomer B CH), 7.37 (1H, dd, ^3J = 5 Hz, ^4J = 1 Hz, isomer B CH), 7.43 (12H, m, CH), 7.48 (6H, m, CH), 7.63 (1H, dd, ^3J = 5 Hz, ^4J = 1 Hz, isomer A CH), 7.69 (12H, m, CH), 7.76 (1H, dd, ^3J = 4 Hz, ^4J = 1 Hz, isomer A CH).

4.3.3.3 Dicarbonyl(1,3-di(2-thenoyl)-1,3-propanedionato-κ^2O,O')triphenylphosphine-rhodium(I) [Rh(dtm)(CO)(PPh_3)] {8}.

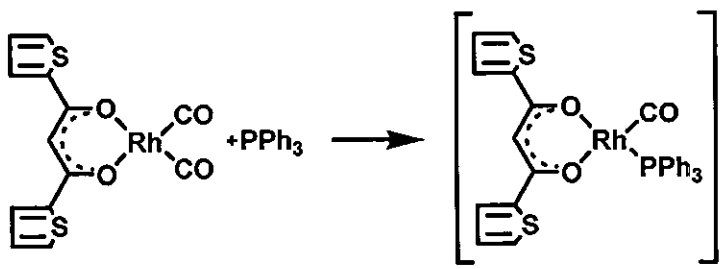

{5} {8}

To a solution of [Rh(dtm)$(CO)_2$] {5} (0.0394 g, 0.10 mmol) in chloroform (3 ml) was added an equivalent amount of solution of PPh_3 (0.0262 g, 0.10 mmol) in chloroform (3 ml). The solvent was removed by evaporation, resulting in spectroscopically pure [Rh(dtm)(CO)(PPh_3)] {8} as a yellow powder (0.0331 g, 52.7% yield); m.p. 180.0-184.5 °C; ν (C=O)/cm^{-1} = 1971; δ_H(600 MHz, $CDCl_3$): 6.65 (1H, s, CH), 6.89 (1H, dd, ^3J = 5 Hz, ^3J = 4 Hz, ring B CH), 7.08 (1H, dd, ^3J = 4 Hz, ^4J = 1 Hz, ring B CH), 7.11 (1H, dd, ^3J = 5 Hz, ^3J = 4 Hz, ring A CH), 7.27 (1H, dd, ^3J = 5 Hz, ^4J = 1 Hz, ring B CH), 7.41 (6H, m, CH), 7.45 (3H, m, CH), 7.52 (1H, dd, ^3J = 5 Hz, ^4J = 1 Hz, ring A CH), 7.73 (1H, dd, ^3J = 4 Hz, ^4J = 1 Hz, ring A CH), 7.74 (6H, m, CH).

4.4 Spectroscopic, spectrophotometric, equilibrium constants (K_c), acid dissociation constants (pK_a) and kinetic measurements.

NMR measurements at 298 K were recorded on a Bruker Advance DPX 300 NMR spectrometer [^{1}H (300.130 MHz) and ^{31}P (121.495 MHz)] and a Bruker Advance II 600 NMR spectrometer [^{1}H (600.130 MHz), ^{19}F (564.686 MHz) and ^{31}P (242.937 MHz)]. The chemical shifts were reported relative to $SiMe_4$ (0.00 ppm) for the ^{1}H spectra, relative to $CFCl_3$ (0.00 ppm) for the ^{19}F spectra and relative to 85% H_3PO_4 (0 ppm) for the ^{31}P spectra. Positive values indicate downfield shift and negative values correspond to upfield shifts.

IR spectra were recorded on a Digilab FTS 2000 infrared spectrophotometer utilizing a He-Ne laser at 632.6 nm.

Acid dissociation was monitored on a Cary 50 Probe UV/vis spectrophotometer. pH-measurements were done on a Hanna instruments model HI 9321, fitted with a glass electrode. The pH-meter was calibrated with buffers at a pH of 4.01, 7.01 and 10.01 respectively.

Kinetic measurements were monitored on a Digilab FTS 2000 Fourier transform infrared spectrophotometer utilizing a He-Ne laser at 632.6 nm, a Cary 50 Probe UV/vis spectrophotometer, a Bruker Advance DPX 300 NMR spectrometer [^{1}H (300.130 MHz) and ^{31}P (121.495 MHz)] and a Bruker Advance II 600 NMR spectrometer [^{1}H (600.130 MHz), ^{19}F (564.686 MHz) and ^{31}P (242.937 MHz)].

4.4.1 Calculation of % keto isomer and equilibrium constant (K_c) determination.

^{1}H NMR spectra of thiophene containing β-diketones were recorded at 298 K with concentrations ≅ 0.012 mol dm^{-3} in $CDCl_3$. Integration of spectra was done in such a way that the methine proton, thiophene-CO-C**H**=C(OH)-R at *ca* 6.47 – 6.71 ppm was always assigned an integral value of one. The % keto was calculated using **Equation 4.1**.

Equation 4.1: % keto isomer = (*I* of keto signal)/{(*I* of keto signal)+(*I* of enol signal)}x100%

with *I* = integral value. Once the % keto isomer was known, the equilibrium constant can be determined as illustrated in **Equation 4.2** and **Equation 4.3**.

Equation 4.2: $K_c = \frac{[\text{thiophene} - \text{CO} - \text{CH} = \text{C(OH)} - \text{R}]}{[\text{thiophene} - \text{CO} - \text{CH}_2 - \text{CO} - \text{R}]} = \frac{k_{enol}}{k_{keto}}$, applicable to equilibrium

$$\text{thiophene} - \text{CO} - \text{CH}_2 - \text{CO} - \text{R} \underset{}{\overset{K_c}{\rightleftharpoons}} \text{thiophene} - \text{CO} - \text{CH} = \text{C(OH)} - \text{R}$$

Equation 4.3: K_c = (% enol isomer)/(% keto isomer) = (100 - % keto isomer)/(% keto isomer)

with K_c = equilibrium constant, k_{enol} = forward rate constant and k_{keto} = backward rate constant.

4.4.2 Acid dissociation constant (K_a) determinations.

The pK_a values were determined by measuring the absorbance at different pH's during an acid-base titration in acetonitrile-water mixtures, 1:9 by volume, μ = 0.100 mol dm^{-3} ($NaClO_4$) at 25.0(5) ^{0}C. β-Diketone concentrations were ≅ 0.07 mmol dm^{-3}. A linear response by the pH meter (Hanna instruments model HI 9321), fitted with a glass electrode, was ensured by calibration with commercial buffers at pH = -log a_{H^+} = 4.01, 7.01 and 10.01 respectively (where a_{H^+} = activity of H^+). A test pK_a determination was then performed by titrating the well characterized compound acetylacetone (Hacac) with sodium hydroxide. A least squares fit of the obtained UV/vis absorbance/pH data for this titration using **Equation 4.4**, utilising the fitting program MINSQ,[4] resulted in a pK_a of 8.95(8) in acetonitrile-water mixtures, 1:9 by volume. The pK_a obtained was within experimental error the same as the best available published pK_a for acetylacetone (Hacac) in water (8.878(5) when μ = 1 mol dm^{-3} and 8.98 when μ = 0.0172 mol dm^{-3}).[3] It was therefore concluded that the electrode was calibrated to measure hydrogen ion activity under the conditions used. It is not expected that the electrode would behave differently for any of the other pK_a determinations because only pK_a values of a series of β-diketones were determined. The pK_a values were determined by measuring the UV/vis absorbance/pH data with titration from high to low as well as from low to high pH and a least squares fit of the absorbance/pH data using **Equation 4.4**.

---

[3] J. Starý, The Solvent Extraction of Metal Chelates, MacMillan Company, New York, 1964, Appendix.

Equation 4.4: $$A_T = \frac{A_{HA}10^{-pH} + A_A 10^{-pK_a}}{10^{-pH} + 10^{-pK_a}}$$

with A_T = total absorbance, A_{HA} the absorbance of the β-diketone in the protonated form and A_A the absorbance of the β-diketone in the deprotonated (basic) form.

4.4.3 Oxidative addition reactions.

Oxidative addition reactions were monitored on the IR (by monitoring formation and disappearance of the carbonyl peaks), UV/vis (by monitoring the change in absorbance at the specified wavelength) and NMR (by monitoring the change in integration units of the specified signals) spectrophotometers. All kinetic measurements were monitored under pseudo-first-order conditions with [MeI] six to hundred times the concentration of the [Rh(β-diketonato)(CO)(PPh_3)] complex in the specified solution. The concentration [Rh(β -diketonato)(CO)(PPh_3)] ≅ 0.00005 mol dm^{-3} for UV/vis measurements, ≅ 0.008 mol dm^{-3} for IR measurements and ≅ 0.014 mol dm^{-3} for NMR measurements. Kinetic measurements under pseudo-first-order conditions for different concentrations of a [Rh(β-diketonato)(CO)(PPh_3)] complex, for a constant [MeI] confirmed that the concentration [Rh(β-diketonato)(CO)(PPh_3)] did not influence the value of the observed kinetic rate constant. The observed first-order rate constants were obtained from least-squares fits of absorbance (IR and UV/vis) or integration units (NMR) *vs* time data.[4]

The activation parameters ΔH^* (activation enthalpy) and ΔS^* (activation entropy), for the oxidative addition reactions were determined from least-squares fits[4] of the reaction rate constants *vs* temperature data according to the Eyring relationship,[5] **Equation 4.5**, or rewritten in the linear form as **Equation 4.6**. The activation free energy $\Delta G^* = \Delta H^* - T\Delta S^*$.

[4] MINSQ, Least squares parameter Estimation, Version 3.12, MicroMath, 1990.

[5] H. Espenson, Chemical Kinetics and Reaction Mechanisms, Second edition, McGraw-Hill, New York, 1995, p. 156.

Equation 4.5: $$k = \frac{k_B T}{h} e^{\frac{-\Delta H^*}{RT}} e^{\frac{\Delta S^*}{R}}$$

Equation 4.6: $$\ln k/T = -\frac{\Delta H^*}{RT} + \frac{\Delta S^*}{R} + \ln\frac{k_B}{h}$$

with k = rate constant, k_B = Boltzmann's constant = 1.3806 x 10^{-23} J K^{-1}, T = temperature, h = Planck's constant = 6.625 x 10^{-34} J s, and R = universal gas constant = 8.314 J mol^{-1} K^{-1}.

4.5 Crystallography.

4.5.1 Structure determination of Hbth {1}.

Crystals of Hbth {1} were obtained by recrystallizing from diethyl ether. The light brown crystal was mounted on a glass fibre and used for the X-ray crystallographic analysis. The X-ray intensity data were measured on a Bruker X8 Apex II 4K Kappa CCD diffractometer area detector system equipped with a graphite monochromator and Mo K_α fine-focus sealed tube (λ = 0.71073 Å) operated at 1.5 KW power (50 KV, 30 mA). The detector was placed at a distance of 4.3 cm from the crystal. Crystal temperature during the data collection was kept constant at 100(2) K using an Oxford 700 series cryostream cooler.

The initial unit cell and data collection were achieved by the Apex2 software[6] utilizing COSMO[7] for optimum collection of more than a hemisphere of reciprocal space. A total of 1128 frames were collected with a scan width of 0.5° in φ and ω and an exposure time of 10 $s.frame^{-1}$. The frames were integrated using a narrow-frame integration algorithm and reduced with the Bruker SAINT-Plus[8] and XPREP[8] software packages respectively. The integration of the data using a monoclinic cell yielded a total of 21300 reflections to a maximum θ angle of 28.32°, of which 2695 were independent with a R_{int} = 0.0290. Analysis of the data showed no significant decay during the data collection. Data were corrected for absorption effects using the multi-scan

[6] Apex2. (Version 1.0-27), Bruker AXS Inc., Madison, Wisconsin, USA, 2005.

[7] COSMO. Version 1.48, Bruker AXS Inc., Madison, Wisconsin, USA, 2003.

[8] SAINT-Plus. Version 7.12 (including XPREP), Bruker AXS Inc., Madison, Wisconsin, USA, 2004.

technique SADABS[9]) with minimum and maximum transmission coefficients of 0.9089 and 0.9674 respectively.

The structure was solved by the direct methods package SIR97[10] and refined using the WinGX software package[11] incorporating SHELXL.[12] The final anisotropic full-matrix least-squares refinement on F^2 with 143 variables converged at R1 = 0.0634 for the observed data and wR2 = 0.1705 for all data. The GOF was 1.063. The largest peak on the final difference electron density synthesis was 1.351 e.Å^{-3} at 0.45 Å from C13 and the deepest hole -0.822 e.Å^{-3} at 0.19 Å from C12.

The aromatic H atoms were placed in geometrically idealized positions (C–H = 0.95 Å) and constrained to ride on their parent atoms with $U_{iso}(H) = 1.2U_{eq}(C)$. The hydroxyl H was located from a Fourier difference map. Non-hydrogen atoms were refined with anisotropic displacement parameters. Atomic scattering factors were taken from the International Tables for Crystallography Volume C.[13] The molecular plot was drawn using the DIAMOND program[14] with a 50% thermal envelope probability for non-hydrogen atoms. Hydrogen atoms were drawn as arbitrary sized spheres with radius of 0.135 Å.

4.5.2 Structure determination of [Rh(dtm)(CO)$_2$] {5}.

Crystals of [Rh(dtm)(CO)$_2$] {5} were obtained by recrystallizing from chloroform. The blue-purple crystal was mounted on a glass fibre and used for the X-ray crystallographic analysis. The X-ray intensity data were measured on a Bruker X8 Apex II 4K Kappa CCD diffractometer area detector system equipped with a graphite monochromator and Mo K_α fine-focus sealed tube (λ = 0.71073 Å) operated at 1.5 KW power (50 KV, 30 mA). The detector was placed at a

---

[9] SADABS. Version 2004/1, Bruker AXS Inc., Madison, Wisconsin, USA, 1998.

[10] A. Altomare, M.C. Burla, M. Camalli, G.L. Cascarano, C. Giacovazzo, A. Guagliardi, A.G.G. Moliterni, G. Polidori, R. Spagna, J. Appl. Cryst. 32 (1999) 115.

[11] L.J. Farrugia, WinGX Version 1.70.01, J. Appl. Cryst. 32 (1999) 837.

[12] G.M. Sheldrick, SHELXL97 Program for crystal structure refinement. University of Göttingen, Germany, 1997.

[13] International Tables for Crystallography, vol C, Kluwer Academic Publishers, Dordrecht, The Netherlands, p. 1002.

[14] K. Brandenburg, H. Putz, DIAMOND, Release 3.1a. Crystal Impact GbR, Bonn, Germany 2005.

distance of 3.75 cm from the crystal. Crystal temperature during the data collection was kept constant at 100(2) K using an Oxford 700 series cryostream cooler.

The initial unit cell and data collection were achieved by the Apex2 software[6] utilizing COSMO[7] for optimum collection of more than a hemisphere of reciprocal space. A total of 880 frames were collected with a scan width of 0.5° in φ and ω and an exposure time of 30 s.frame^{-1}. The frames were integrated using a narrow-frame integration algorithm and reduced with the Bruker SAINT-Plus[8] and XPREP[8] software packages respectively. The integration of the data using a monoclinic cell yielded a total of 10495 reflections to a maximum θ angle of 26.36°, of which 2636 were independent with a R_{int} = 0.0447. Analysis of the data showed no significant decay during the data collection. Data were corrected for absorption effects using the multi-scan technique SADABS[9]) with minimum and maximum transmission coefficients of 0.5858 and 0.9272 respectively.

The structure was solved by the direct methods package SIR97[10] and refined using the WinGX software package[11] incorporating SHELXL.[12] The final anisotropic full-matrix least-squares refinement on F^2 with 181 variables converged at R1 = 0.0868 for the observed data and wR2 = 0.2236 for all data. The GOF was 1.144. The largest peak on the final difference electron density synthesis was 4.402 e.Å^{-3} at 1.25 Å from H13 and the deepest hole -1.576 e.Å^{-3} at 1.48 Å from H43.

The aromatic H atoms were placed in geometrically idealized positions (C–H = 0.93 Å) and constrained to ride on their parent atoms with $U_{iso}(H) = 1.2U_{eq}(C)$. Non-hydrogen atoms were refined with anisotropic displacement parameters. Atomic scattering factors were taken from the International Tables for Crystallography Volume C.[13] The molecular plot was drawn using the DIAMOND program[14] with a 50% thermal envelope probability for non-hydrogen atoms. Hydrogen atoms were drawn as arbitrary sized spheres with radius of 0.135 Å.

4.6 Computational.

ADF (Amsterdam Density Functional) calculations were carried out using DFT (Density Functional Theory)[15] with the PW91 (Perdew-Wang, 1991) exchange and correlation functional.[16] TZP (Triple ζ polarized) basis set, a fine mesh for numerical integration, a spin-restricted (gas-phase) formalism and full geometry optimization with tight convergence criteria as implemented in the ADF program system version 2005.01, were used. No symmetry limitations were imposed.

[15] G.T. Velde, F.M. Bickelhaupt, E.J. Baerends, C.F. Guerra, S.J.A. Van Gisbergen, J.G. Snijders, T.J. Ziegler, J. Comp. Chem. 22 (2001) 931.

[16] J. P. Perdew, J. A. Chevary, S. H. Vosko, K. A. Jackson, M. R. Perderson, D. J. Singh, C. Fioihais, Phys. Rev. B 46 (1992) 6671.

5 Summary, conclusions and future perspectives

Thienyl-containing β-diketones of the type $ThCOCH_2COR$, with R = Th (Hdtm), C_6H_5 (Hbth), have been prepared. The group electronegativity of the thienyl group is 2.107 (Gordy scale) as inferred from a linear methyl ester IR carbonyl stretching frequency – group electronegativity relationship. A single crystal X-ray determination of the structure of $ThCOCH_2COPh$ indicates, that the enolization in a direction away from the thienyl group, always dominates. Asymmetric enolisation, in the direction furthest from the thienyl group, was also observed for $ThCOCH_2COR$, with R = Th or CF_3 (Htta). This finding is considered to be the result of resonance driving forces rather than inductive electronic effects of substituents on the pseudo-aromatic β-diketone core. By increasing the temperature of the solvent ($CDCl_3$) from 0 to 50 °C, the percentage keto isomer at equilibrium of Htta (4.2 – 7.1%), Hbth (5.3 – 9.5%) and Hdtm (14.8–21.9%) increased. Slow conversion kinetics from the keto to the dominant enol isomer was monitored in $CDCl_3$ solution for Hbth and Hdtm. The keto-enol conversion for Htta was found to be too fast to measure. pK_a' values of the thienyl-containing β-diketones $ThCOCH_2COR$ were determined as 6.49 (Htta), 9.01 (Hbth) and 8.89 (Hdtm).

Synthetic routes to prepare new thienyl-containing β-diketonato rhodium(I) complexes of the type $[Rh^I(ThCOCHCOR)(CO)_2]$, $[Rh^I(ThCOCHCOR)(CO)(PPh_3)]$ and $[Rh^{III}(\beta\text{-diketonato})(CO)(PPh_3)(Me)(I)]$ with Th = thienyl and R = C_6H_5 (Ph), Th and CF_3 have been developed. The crystal structure of $[Rh(dtm)(CO)_2]$ was also solved. From ^1H and ^{31}P NMR studies, it is clear that for complexes of the type $[Rh^I(\beta\text{-diketonato})(CO)(PPh_3)]$ and $[Rh^{III}(\beta\text{-diketonato})(CO)(PPh_3)(Me)(I)]$, with an unsymmetrical β-diketonato ligand, at least two main isomers exist in solution. The equilibrium constant, K_c, which relates these two isomers in an equilibrium reaction, is concentration independent but temperature dependent for $[Rh^I(tta)(CO)(PPh_3)]$. $\Delta_r G$, $\Delta_r H$ and $\Delta_r S$ values for this equilibrium have been determined. However, changes in the temperature (-30 to 55 °C in $CDCl_3$) or concentration had little influence on the equilibrium constant of $[Rh^I(bth)(CO)(PPh_3)]$ and the $[Rh^{III}(\beta\text{-diketonato})(CO)(PPh_3)(Me)(I)]$ complexes of tta and bth.

The chemical kinetics of the oxidative addition reaction of CH_3I to [Rh(ThCOCHCOR)(CO)(PPh_3)] have been studied in detail utilizing IR, UV/vis, ^1H NMR, ^{19}F NMR and ^{31}P NMR techniques. The NMR studies revealed that the rate of oxidative addition of iodomethane to the different [Rh(ThCOCHCOR)(CO)(PPh_3)] isomers were the same. Three definite sets of reactions, involving at least two Rh(III)-alkyl (two isomers each) and two Rh(III)-acyl species (two isomers each), as shown in the reaction sequence below, were observed.

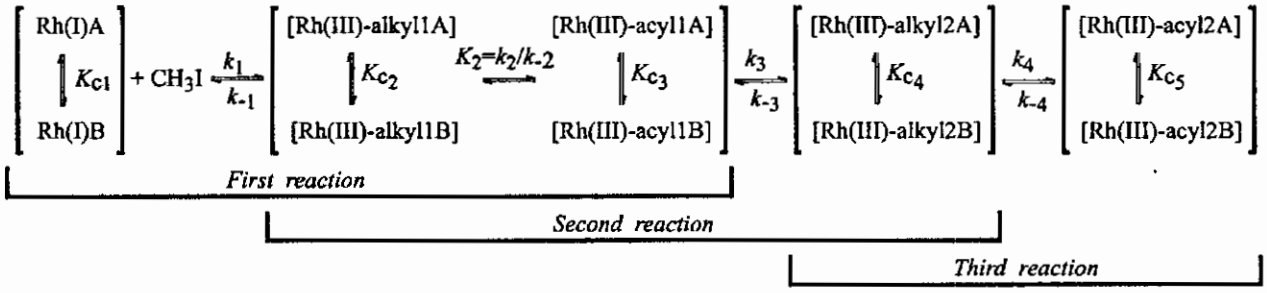

A quantum computational chemistry study, by means of DFT calculations, has been done on the thienyl-containing rhodium(I) and rhodium(III) complexes involved in the above reaction scheme. Excellent results, in agreement with experimental results, were obtained on the geometry optimization of Hdtm and [Rh(ThCOCHCOCF_3)(CO)(PPh_3)]. By comparing the relative energies of the optimized geometries of the 12 possible rhodium(III)-alkyl and 6 possible rhodium(III)-acyl products, the stereochemistry of the different alkyl1, alkyl2, acyl1 and acyl2 products in the above reaction scheme was proposed, as illustrated in the reaction mechanism below for the oxidative addition of iodomethane to [Rh(ThCOCHCOPh)(CO)(PPh_3)].

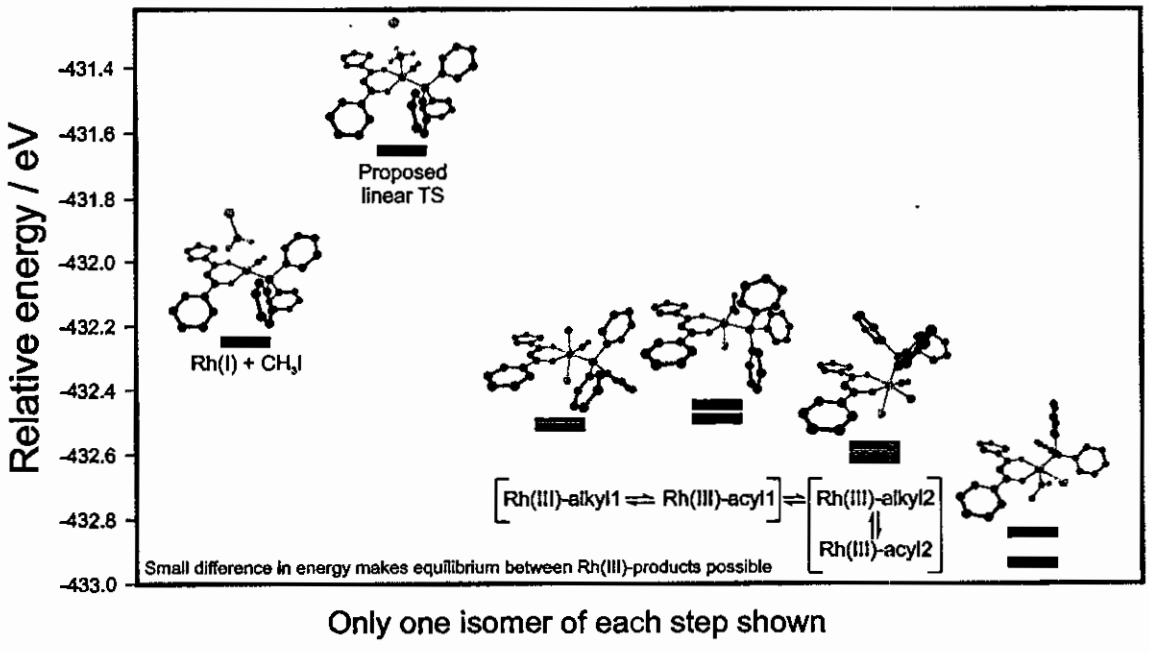

Experimental results, obtained on the stereochemistry of selected alkyl1 and alkyl2 reaction products by means of ^{1}H NOESY, were consistent with the stereochemistry proposed by the quantum chemistry calculations.

Future theoretical studies on the current topic will involve the determination of solvent effects on the relative energies of the optimized rhodium(III) products. The different transition states of the proposed reaction mechanism will also be determined. Future experimental studies involve the characterization of the rhodium(III) products, by means of single crystal X-ray crystallography.

A Appendix

^{1}H NMR

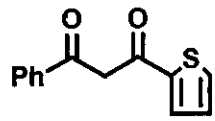

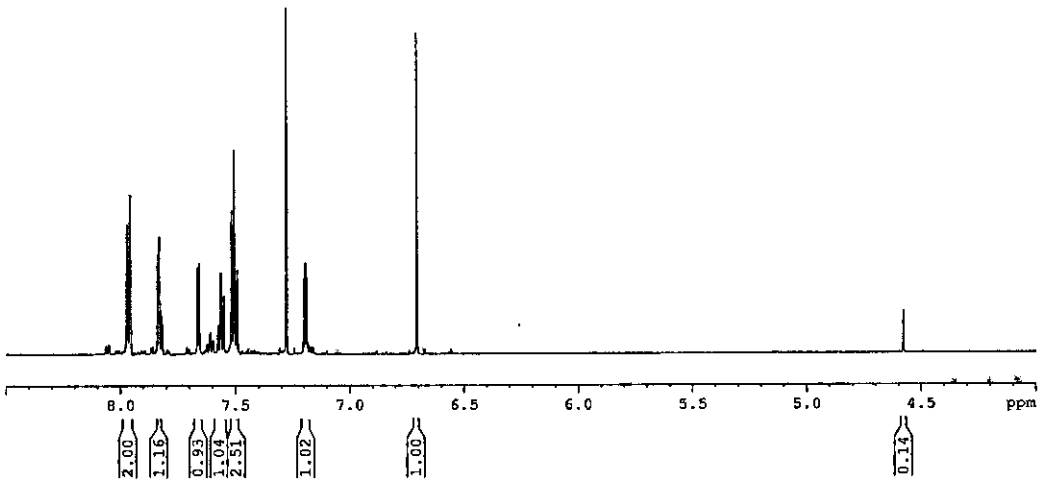

Spectrum 1: 1-phenyl-3-(2-thenoyl)-1,3-propanedione (Hbth) {1}

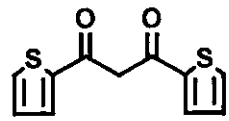

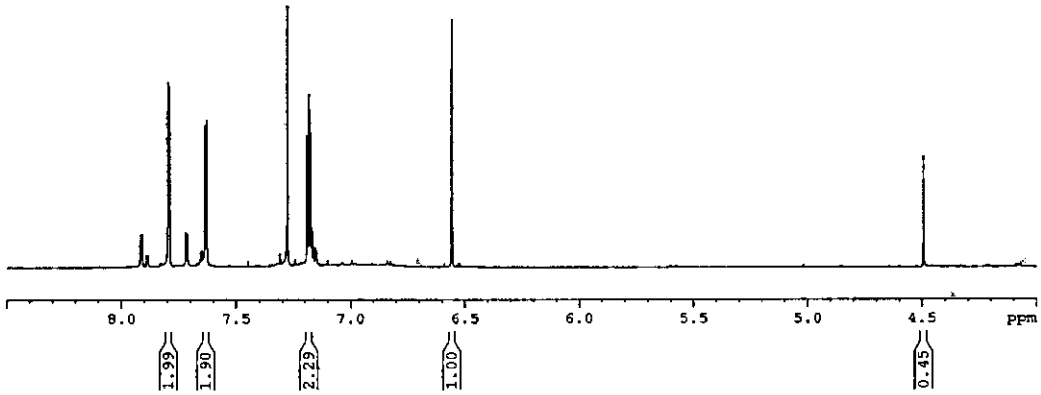

Spectrum 2: 1,3-di(2-thenoyl)-1,3-propanedione (Hdtm) {2}

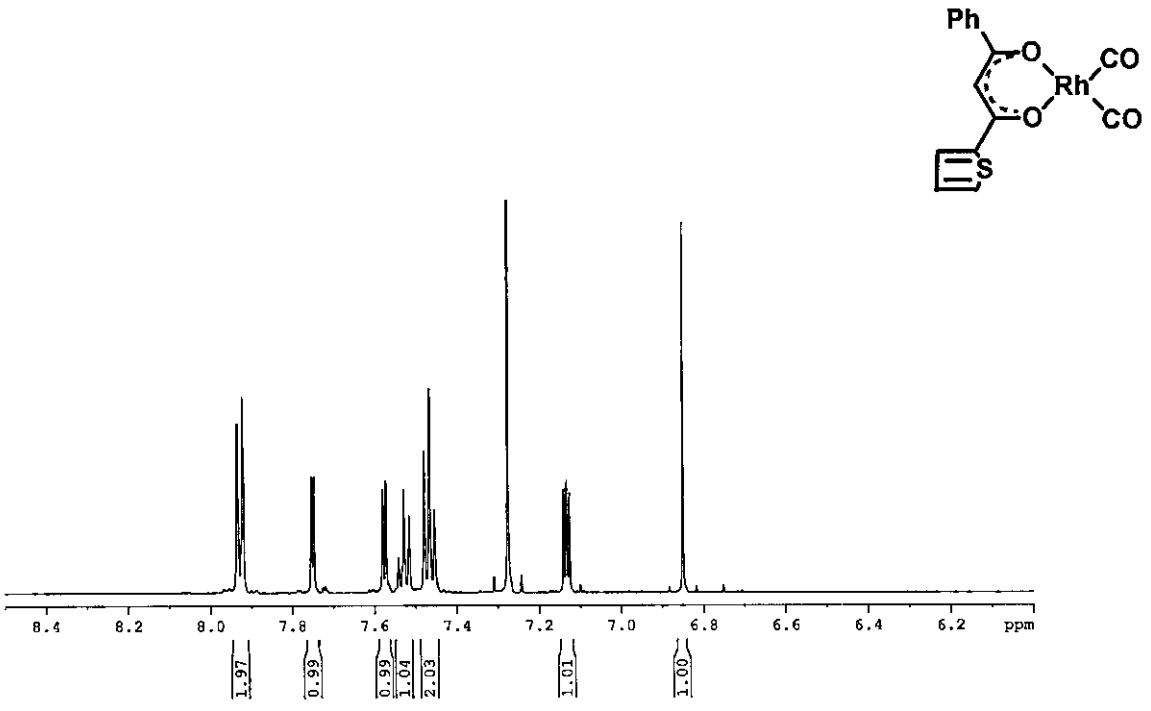

Spectrum 3: Dicarbonyl(1-phenyl-3-(2-thenoyl)-1,3-propanedionato-κ^2O,O')rhodium(I) [Rh(bth)$(CO)_2$] **{3}**

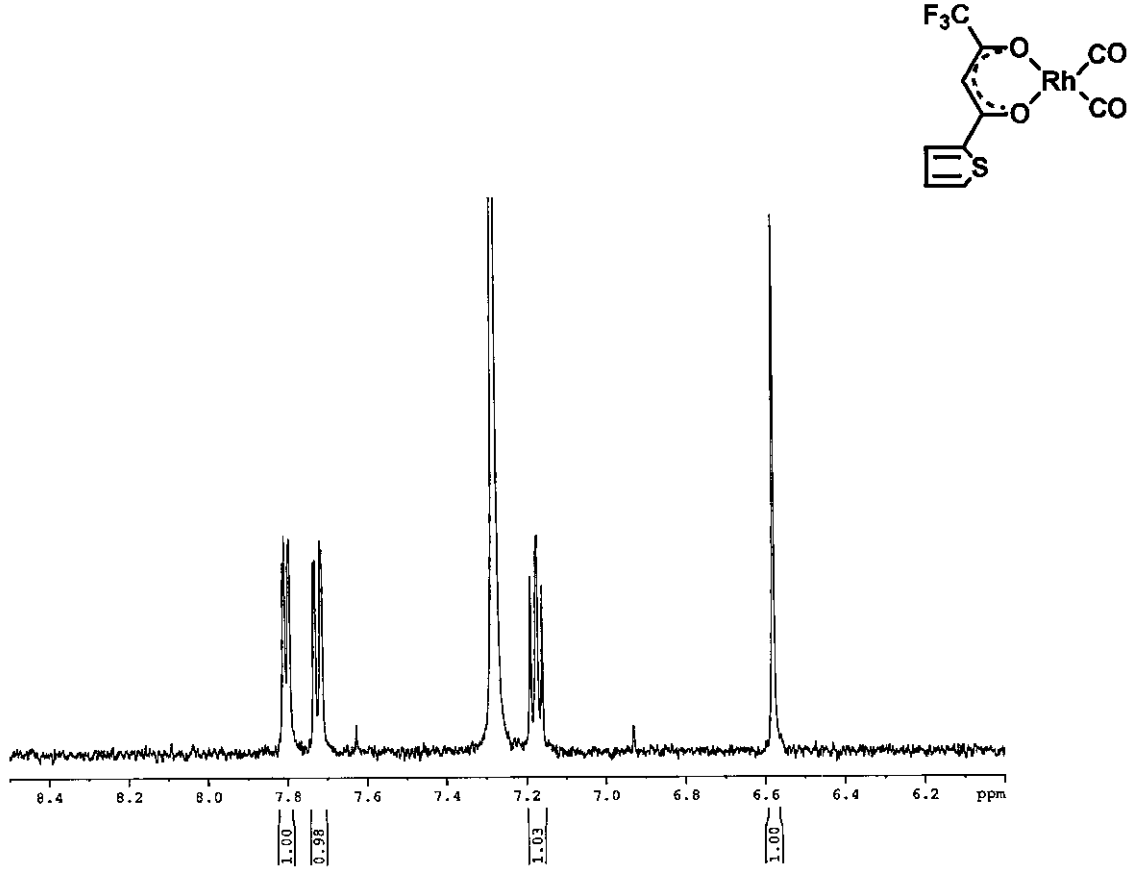

Spectrum 4: Dicarbonyl(thenoyltrifluoroacetonato-κ^2O,O')rhodium(I) [Rh(tta)$(CO)_2$] **{4}**

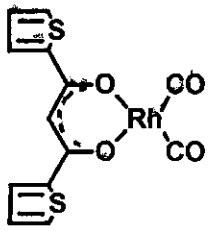

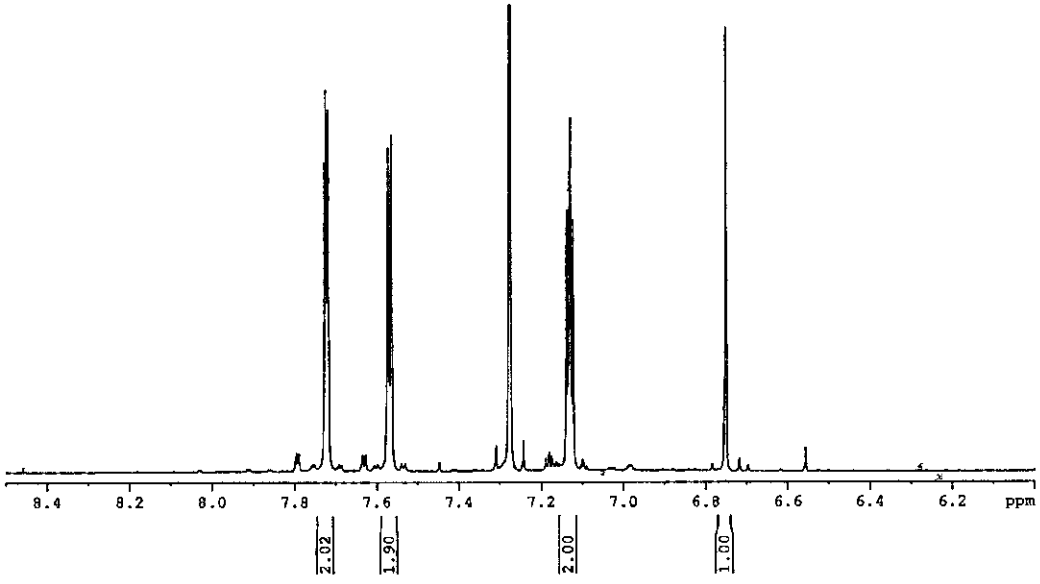

Spectrum 5: Dicarbonyl(1,3-di(2-thenoyl)-1,3-propanedionato-κ^2O,O')rhodium(I) [Rh(dtm)(CO)$_2$] **{5}**

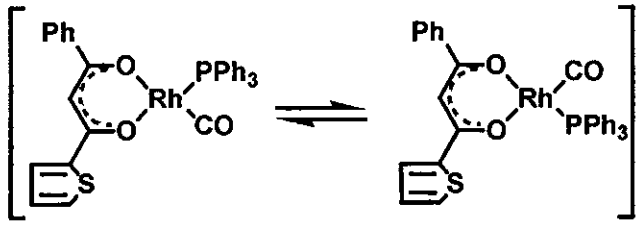

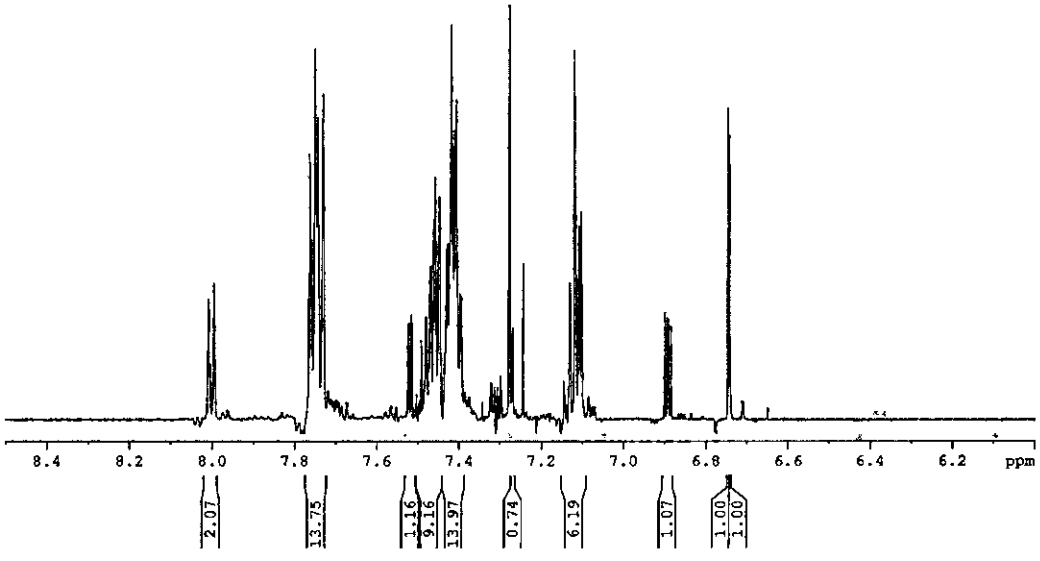

Spectrum 6: Carbonyl(1-phenyl-3-(2-thenoyl)-1,3-propanedionato-κ^2O,O')triphenylphosphine-rhodium(I) [Rh(bth)(CO)(PPh$_3$)] **{6}**

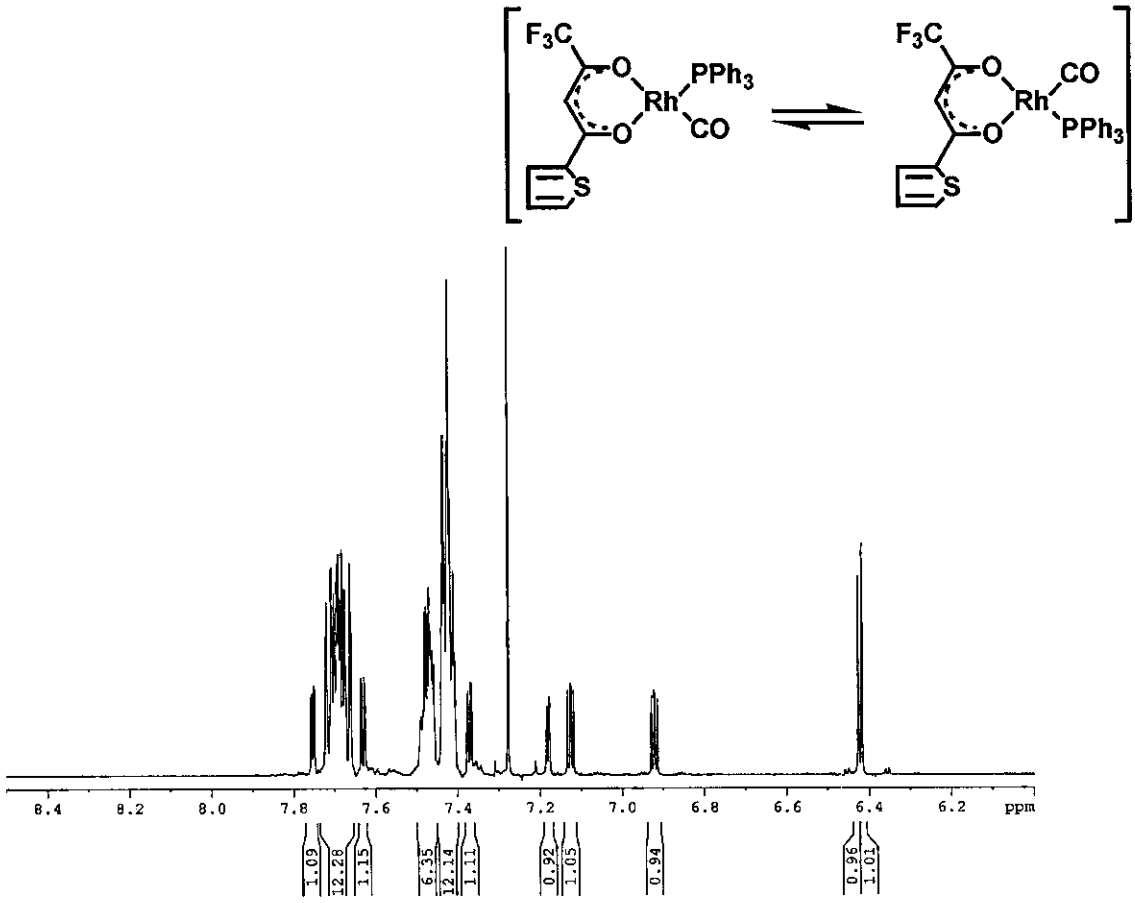

Spectrum 7: Carbonyl(thenoyltrifluoroacetonato-κ^2O,O')triphenylphosphine-rhodium(I) [Rh(tta)(CO)(PPh_3)] {7}

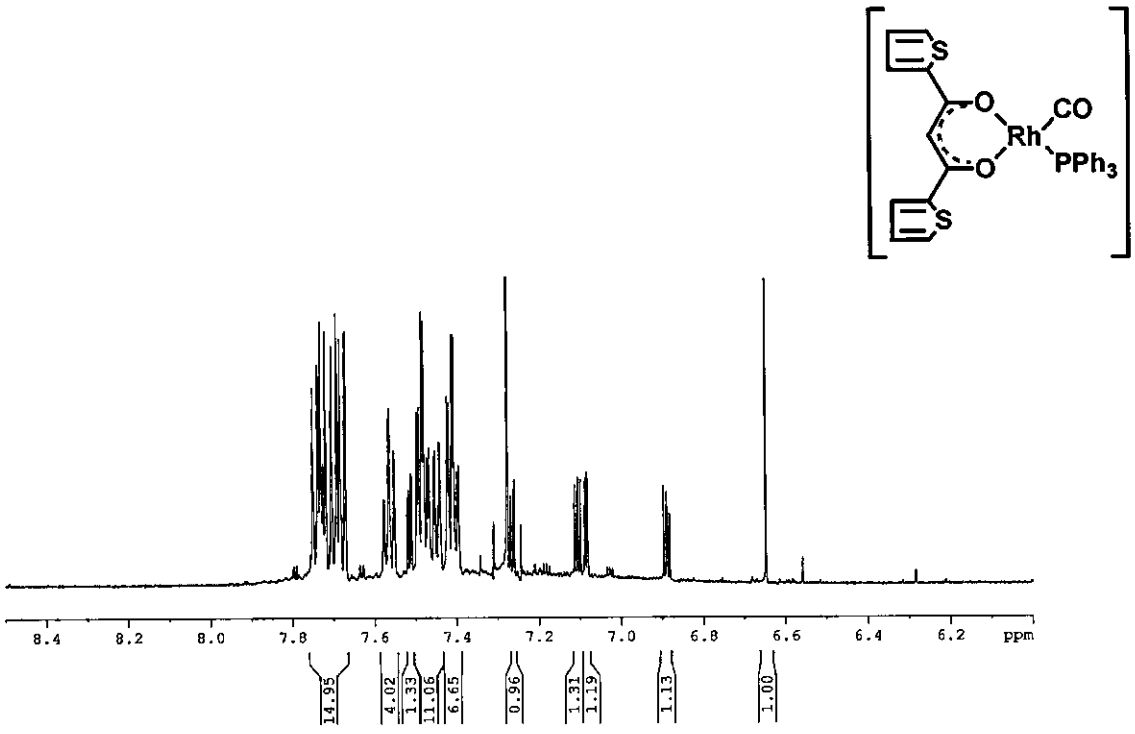

Spectrum 8: Dicarbonyl(1,3-di(2-thenoyl)-1,3-propanedionato-κ^2O,O')triphenylphosphine-rhodium(I) [Rh(dtm)(CO)(PPh_3)] {8}

^{31}P NMR

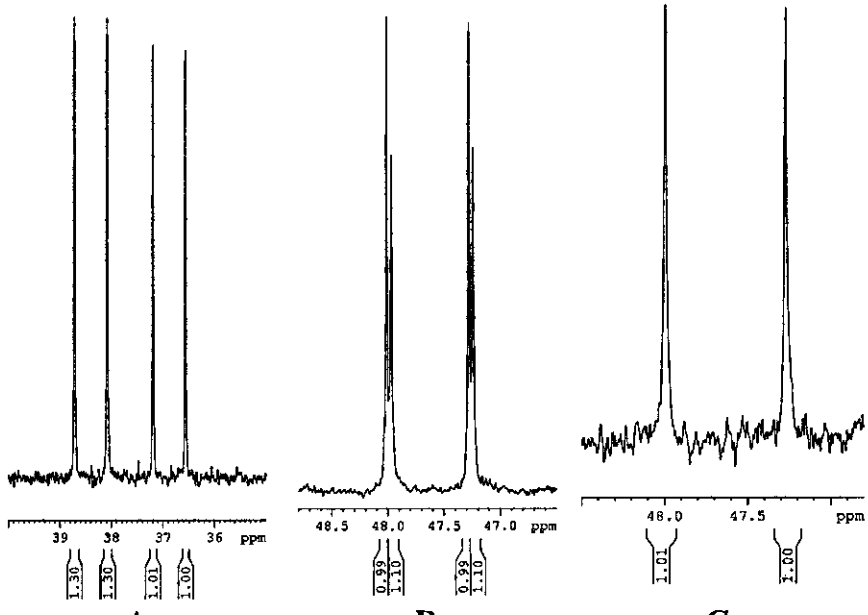

Spectrum 9: A [Rh(bth)(CO)(PPh_3)] **{6}, B** [Rh(tta)(CO)(PPh_3)] **{7}, C** [Rh(dtm)(CO)(PPh_3)] **{8}**

^{19}F NMR

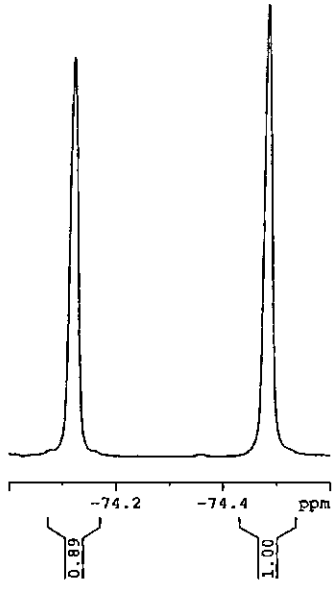

Spectrum 10: [Rh(tta)(CO)(PPh_3)] **{7}**

Summary

Thienyl-containing β-diketones of the type $ThCOCH_2COR$, with R = Th (Hdtm), C_6H_5 (Hbth), have been prepared. The group electronegativity of the thienyl group is 2.107 (Gordy scale) as inferred from a linear methyl ester IR carbonyl stretching frequency – group electronegativity relationship. A single crystal X-ray determination of the structure of $ThCOCH_2COPh$ indicates, that the enolization in a direction away from the thienyl group, always dominates. Asymmetric enolisation, in the direction furthest from the thienyl group, was also observed for $ThCOCH_2COR$, with R = Th or CF_3 (Htta). This finding is considered to be the result of resonance driving forces rather than inductive electronic effects of substituents on the pseudo-aromatic β-diketone core. By increasing the temperature of the solvent ($CDCl_3$) from 0 to 50 °C, the percentage keto isomer at equilibrium of Htta (4.2 – 7.1%), Hbth (5.3 – 9.5%) and Hdtm (14.8–21.9%) increased. Slow conversion kinetics from the keto to the dominant enol isomer was monitored in $CDCl_3$ solution for Hbth and Hdtm. The keto-enol conversion for Htta was found to be too fast to measure. pK_a' values of the thienyl-containing β-diketones $ThCOCH_2COR$ were determined as 6.49 (Htta), 9.01 (Hbth) and 8.89 (Hdtm).

Synthetic routes to prepare new thienyl-containing β-diketonato rhodium(I) complexes of the type $[Rh^I(ThCOCHCOR)(CO)_2]$, $[Rh^I(ThCOCHCOR)(CO)(PPh_3)]$ and $[Rh^{III}(\beta\text{-diketonato})(CO)(PPh_3)(Me)(I)]$ with Th = thienyl and R = C_6H_5 (Ph), Th and CF_3 have been developed. The crystal structure of $[Rh(dtm)(CO)_2]$ was also solved. From ^1H and ^{31}P NMR studies, it is clear that for complexes of the type $[Rh^I(\beta\text{-diketonato})(CO)(PPh_3)]$ and $[Rh^{III}(\beta\text{-diketonato})(CO)(PPh_3)(Me)(I)]$, with an unsymmetrical β-diketonato ligand, at least two main isomers exist in solution. The equilibrium constant, K_c, which relates these two isomers in an equilibrium reaction, is concentration independent but temperature dependent for $[Rh^I(tta)(CO)(PPh_3)]$. Δ_rG, Δ_rH and Δ_rS values for this equilibrium have been determined. However, changes in the temperature (-30 to 55 °C in $CDCl_3$) or concentration had little influence on the equilibrium constant of $[Rh^I(bth)(CO)(PPh_3)]$ and the $[Rh^{III}(\beta\text{-diketonato})(CO)(PPh_3)(Me)(I)]$ complexes of tta and bth.

SUMMARY

The chemical kinetics of the oxidative addition reaction of CH_3I to [Rh(ThCOCHCOR)(CO)(PPh_3)] have been studied in detail utilizing IR, UV/vis, ^1H NMR, ^{19}F NMR and ^{31}P NMR techniques. The NMR studies revealed that the rate of oxidative addition of iodomethane to the different [Rh(ThCOCHCOR)(CO)(PPh_3)] isomers were the same. Three definite sets of reactions, involving at least two Rh(III)-alkyl (two isomers each) and two Rh(III)-acyl species (two isomers each), as shown in the reaction sequence below, were observed.

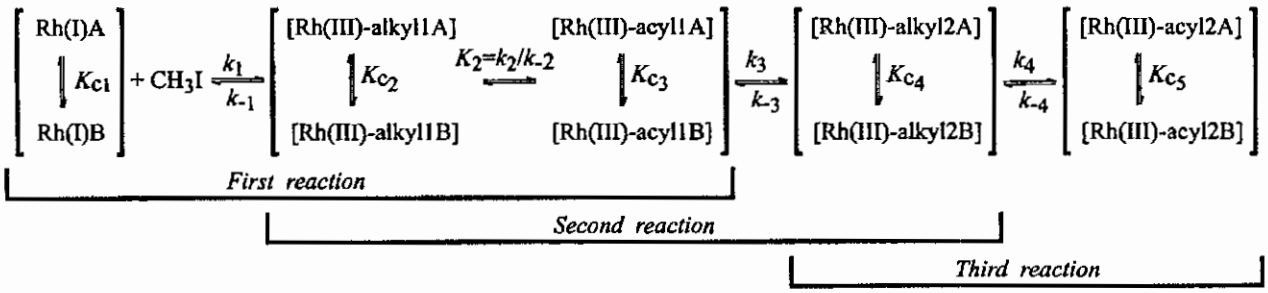

A quantum computational chemistry study, by means of Density Functional Theory (DFT) calculations was done on the thienyl-containing rhodium(I) and rhodium(III) complexes involved in the above reaction scheme. Excellent results, in agreement with experimental results were obtained on the geometry optimization of Hdtm and [Rh(ThCOCHCOCF_3)(CO)(PPh_3)]. By comparing the relative energies of the optimized geometries of the 12 possible rhodium(III)-alkyl and 6 possible rhodium(III)-acyl products, the stereochemistry of the different alkyl1, alkyl2, acyl1 and acyl2 products in the above reaction scheme was proposed. Experimental results obtained on the stereochemistry of the selected alkyl1 and alkyl2 reaction products, by means of ^1H NOESY, were consistent with the stereochemistry proposed by quantum chemistry calculations.

Keywords

β-diketone rhodium(I) rhodium(III) oxidative stereochemistry NOESY computational DFT

Opsomming

Tiëniel-bevattende β-diketone van die vorm $ThCOCH_2COR$, met R = Th (Hdtm), C_6H_5 (Hbth) is berei. Die groep-elektronegatiwiteit van die tiëniel-groep is as 2.107 (Gordy-skaal), bepaal vanaf 'n linieêre verband tussen die metiel ester IR karboniel strekkingsfrekwensie en die groep-elektronegatiwiteit. 'n Kristallografiese X-straal bepaling van die struktuur van $ThCOCH_2COPh$ het aangetoon dat enolisasie in 'n rigting weg van die tiëniel-groep domineer. Asimmetriese enolisasie in die rigting verste van die tiëniel-groep is ook waargeneem vir $ThCOCH_2COR$, met R = Th of CF_3 (Htta). Dit word geïnterpreteer as die resultaat van 'n resonansdryfkrag, eerder as die induktiewe elektroniese effek van die substituente op die pseudo-aromatiese β-diketoon kern. 'n Toename in die temperatuur van die oplosmiddel ($CDCl_3$) vanaf 0 na 50°C, toon 'n toename in die persentasie keto-isomeer by ewewig vir Htta (4.2 – 7.1%), Hbth (5.3 – 9.5%) en Hdtm (14.8 – 21.9%). Die stadige omsetting van die keto na die dominante enol-isomeer is in 'n $CDCl_3$ oplossing gemonitor vir Hbth en Hdtm. Die keto-enol omsetting van Htta was te vinnig om te meet. pK_a' waardes van tiëniel-bevattende β-diketone, $ThCOCH_2COR$, is bepaal as 6.49 (Htta), 9.01 (Hbth) en 8.89 (Hdtm).

Sintese roetes is ontwikkel om nuwe tiëniel-bevattende β-diketonatorodium(I)komplekse, van die vorm $[Rh^I(ThCOCHCOR)(CO)_2]$, $[Rh^I(ThCOCHCOR)(CO)(PPh_3)]$ en $[Rh^{III}(\beta\text{-diketonato})(CO)(PPh_3)(Me)(I)]$ met Th = tiëniel en R = C_6H_5 (Ph), Th en CF_3 te berei. Die kristalstruktuur van $[Rh(dtm)(CO)_2]$ is ook opgeklaar. ^1H en ^{31}P KMR-studies van die komplekse $[Rh^I(\beta\text{-diketonato})(CO)(PPh_3)]$ en $[Rh^{III}(\beta\text{-diketonato})(CO)(PPh_3)(Me)(I)]$, wat 'n asimmetriese β-diketonato-ligand bevat, het aangetoon dat daar minstens twee isomere van hierdie komplekse in oplossing bestaan. Die ewewigskonstante, K_c, tussen die twee isomere by ewewig, is konsentrasie-onafhanklik maar temperatuur-afhanklik vir $[Rh^I(tta)(CO)(PPh_3)]$. $\Delta_r G$, $\Delta_r H$ en $\Delta_r S$ is vir hierdie ewewig bereken. Verandering in temperatuur (-30 tot 55°C in $CDCl_3$) of konsentrasie het 'n minimale invloed op die ewewigskonstante van die $[Rh^I(bth)(CO)(PPh_3)]$- en die $[Rh^{III}(\beta\text{-diketonato})(CO)(PPh_3)(Me)(I)]$-komplekse van tta en bth gehad.

OPSOMMING

Die chemiese kinetika van die oksidatiewe addisie-reaksie tussen CH_3I en [Rh(ThCOCHCOR)(CO)(PPh_3)] is deur middel van IR, UV/sigbaar, ^1H KMR, ^{19}F KMR en ^{31}P KMR-spektroskopie ondersoek . Die KMR studies het aangetoon dat die tempo van oksidatiewe addisie van metieljodied tot die verkillende [Rh(ThCOCHCOR)(CO)(PPh_3)]-isomere dieselfde was. Drie reaksiestelle, wat minstens twee Rh(III)-alkielspesies (twee isomere elk) en twee Rh(III)-asielspesies (twee isomere elk) bevat, soos aangetoon in die onderstaande reaksieskema, is waargeneem.

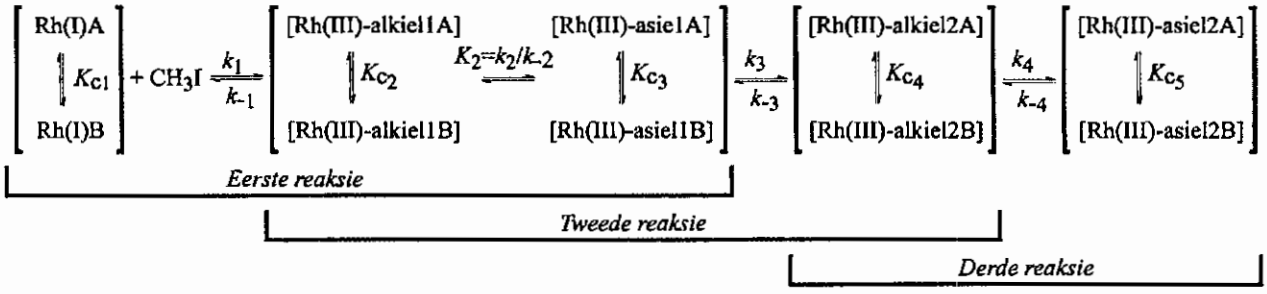

'n Kwantum berekeningschemie-studie, met behulp van DFT ("Density Functional Theory") berekeninge, is op die tiëniel-bevattende rodium(I)- en rodium(III)-komplekse betrokke in die bogenoemde reaksieskema uitgevoer. Uitstekende resultate, in ooreenstemming met eksperimentele resultate, is verkry vir die geoptimiseerde geometrie van Hdtm en [Rh(ThCOCHCOCF_3)(CO)(PPh_3)]. 'n Vergelyking van die relatiewe energieë van die geoptimiseerde geometrieë van die 12 moontlike rodium(III)-alkiel en 6 moontlike rodium(III)-asiel produkte het dit moontlik gemaak om die stereochemie van die verskillende alkiel1-, alkiel2-, asiel1- en asiel2-produkte in bogenoemde reaksieskema te voorspel. Eksperimentele resultate, met behulp van ^1H NOESY uitgevoer op geselekteerde alkiel1 en alkiel2 reaksieprodukte, stem ooreen met die stereochemie wat voorspel is deur die kwantum chemie berekeninge.